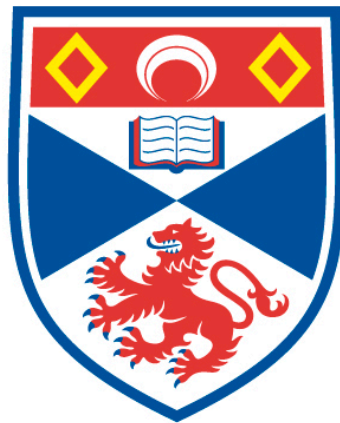


Towards mitochondrial targeting for the treatment of Alzheimer's Disease

Rana Abdul Razzak

A thesis submitted for the degree of PhD
at the
University of St Andrews



2019

Full metadata for this item is available in
St Andrews Research Repository
at:
<http://research-repository.st-andrews.ac.uk/>

Identifier to use to cite or link to this thesis:
DOI: <https://doi.org/10.17630/10023-18869>

This item is protected by original copyright

Candidate's declaration

I, Rana Abdul Razzak, do hereby certify that this thesis, submitted for the degree of PhD, which is approximately 39,006 words in length, has been written by me, and that it is the record of work carried out by me, or principally by myself in collaboration with others as acknowledged, and that it has not been submitted in any previous application for any degree.

I was admitted as a research student at the University of St Andrews in September 2014.

I received funding from an organisation or institution and have acknowledged the funder(s) in the full text of my thesis.

Date

Signature of candidate

Supervisor's declaration

I hereby certify that the candidate has fulfilled the conditions of the Resolution and Regulations appropriate for the degree of PhD in the University of St Andrews and that the candidate is qualified to submit this thesis in application for that degree.

Date

Signature of supervisor

Permission for publication

In submitting this thesis to the University of St Andrews we understand that we are giving permission for it to be made available for use in accordance with the regulations of the University Library for the time being in force, subject to any copyright vested in the work not being affected thereby. We also understand, unless exempt by an award of an embargo as requested below, that the title and the abstract will be published, and that a copy of the work may be made and supplied to any bona fide library or research worker, that this thesis will be electronically accessible for personal or research use and that the library has the right to migrate this thesis into new electronic forms as required to ensure continued access to the thesis.

I, Rana Abdul Razzak, confirm that my thesis does not contain any third-party material that requires copyright clearance.

The following is an agreed request by candidate and supervisor regarding the publication of this thesis:

Printed copy

Embargo on all of print copy for a period of 5 years on the following ground(s):

- Publication would preclude future publication

Supporting statement for printed embargo request

Data in the thesis will be used for future publications

Electronic copy

Embargo on all of electronic copy for a period of 5 years on the following ground(s):

- Publication would preclude future publication

Supporting statement for printed embargo request

Data in the thesis will be used for future publications

Title and Abstract

- I agree to the title and abstract being published.

Date

Signature of candidate

Date

Signature of supervisor

Underpinning Research Data or Digital Outputs

Candidate's declaration

I, Rana Abdul Razzak, hereby certify that no requirements to deposit original research data or digital outputs apply to this thesis and that, where appropriate, secondary data used have been referenced in the full text of my thesis.

Date

Signature of candidate

Acknowledgment

Warm and sincere gratitude to my beloved parents and sister for all the love and emotional and financial support they have been providing me with and for reinforcing the importance of good education in our lives.

I would like to sincerely thank Dr. Gordon Florence and Prof. Frank Gunn-Moore for offering me the opportunity to be a part of their groups. Special thanks for Dr. Eoin Gould, Dr. Laura Aitken and Dr. Fatma-Zohra Bioud for their great assistance and support. I also like to thank the whole Florence and Gunn-Moore groups for their assistance in the laboratory and for making this experience as enjoyable and fruitful as possible.

Many thanks to Dr. William Gabrielli, Dr. David Smith, Prof. Nicholas Westwood and his respected group members for their assistance with gel permeation chromatography. Many thanks to Prof. Rebecca Goss and her respected group-members for their assistance with reversed-phase high performance liquid chromatography techniques.

Many thanks to Madhima Dey for the training she provided me with in both cell culture techniques and cell viability assessment. Special thanks to Dr. Marcus Bischoff for the assistance and consultation he provided with the use of confocal microscopy imaging. Special thanks to Dr. Javier Tello for the guidance he provided with cell staining and use of fluorescence microscopy. Many thanks to Dr. Jonathan Nytk, Mr. Adria Escobet Montalban and M. Pengfei Liu for the help they provided with the two-photon fluorescence characterization of my fluorescent polymeric nano-architectures.

Special thanks to Prof. Robert H. Grubbs and his respective team members for their support and guidance in optimizing ring opening metathesis polymerization techniques.

I would like to thank the solution phase NMR service team; Dr. Tomas Lebl, Mrs. Melanja Smith and Dr. Siobhan Smith for their support. Many thanks to the mass spectrometry service team; Dr Catherine Botting, Dr. Sally Shirran, Dr. Silvia Synowsky and Mrs. Caroline Horsburgh for the support they provided with compound characterization.

Finally, special thanks to the University of St Andrews and St Andrews Education for Palestinian Students for the financial support.

Abbreviations

ADP	Adenosine Diphosphate
ATP	Adenosine Triphosphate
AD	Alzheimer's disease
ABAD	Amyloid Binding Alcohol Dehydrogenase
APP	Amyloid Precursor Protein
ADC	Antibody Drug Conjugates
Aβ	Amyloid Beta
BACE	β -site APP-cleaving enzyme
BBB	Blood Brain Barrier
CAA	Coumarin bearing Acryl-Amide
CoA	Co-enzyme A
d	Doublet
DCM	Dichloromethane
DMAP	4-Dimethylaminopyridine
DMF	Dimethylformamide
DMSO	Dimethyl Sulfoxide
EDCI	1-Ethyl-3-(3-dimethylaminopropyl)carbodiimide
EtOAc	Ethyl Acetate
EtOH	Ethanol
GIII	Grubbs Third-Generation Catalyst
GPC	Gel Permeation Chromatography
HyD	Hybrid Detector
IMM	Inner Mitochondrial Membrane
LBL	Lipid Bilayer
MeOH	Methanol

MM	Macro-monomer
Mn	Number Average Molecular Weight
MTM	Mitochondrial Targeting Moiety
Mw	Weight Average Molecular Weight
MWCNT	Multi-Walled Carbon Nano-Tubes
NAD	Nicotinamide Adenine Dinucleotide
NFTs	Neurofibrillary Tangles
Non-Tg	Non-Transgenic mouse
NPBA	Nanosopic Polymeric Brush Architectures
OMM	Outer Mitochondrial Membrane
PEG	Polyethylene Glycol
PMT	Photomultiplier
PNPs	Polymeric Nanoparticles
PPh₃	Triphenylphosphine
RAWM	Radial-Arm Water Maze
rHADH	Rat 3-hydroxyacyl-coenzyme dehydrogenase
ROMP	Ring Opening Metathesis Polymerization
ROS	Reactive Oxygen Species
RT	Room Temperature
S	Siglet
SCHAD	short chain L-3-hydroxyacyl-coenzyme dehydrogenase
SPs	Senile Plaques
t	triplet
TEG	Tetraethylene Glycol
Tg ABAD	Transgenic mouse overexpressing ABAD
Tg mAPP/ABAD	Transgenic mouse overexpressing mutant APP and ABAD
Tg mAPP	Transgenic mouse overexpressing mutant APP

THF	Tetrahydrofuran
TJs	Tight Junctions
Tol	Toluene
Tr-	Trityl protecting group

Abstract

Nanoparticles (NPs) have emerged as a promising approach to overcoming biological barriers imposed by the human body. Polymeric NPs offer a superior synthetic flexibility and advances in polymerization chemistries have made polymeric architectures with precisely tuned properties accessible. Ring opening metathesis polymerization (ROMP) has become a popular polymerization technique due to its mild conditions a tolerance to an array of functional groups. We successfully synthesized two generations of ROMP monomers that feature polymerizable group and a mitochondrial targeting ligand linked together via a hydrophilic spacer. This monomer can be *co*-polymerized with another ROMP monomer bearing a fluorescent molecule to enable the visualization of the polymeric NPs in the cell. The second-generation monomers have differs from the first-generation analogues by its three-fold longer hydrophilic linker. *Co*-polymers prepared from second-generation monomers show cellular up-take but no mitochondrial localization.

Contents

1	Targeted Drug Delivery and it's Potential in Alzheimer's Disease Therapy.....	12
1.1	Drug Delivery Hurdles and Approaches to Surpass Them	13
1.1.1	Nanoscope Materials: Structurally Diverse and Functionally Versatile Drug Delivery Vectors 18	
1.2	Applications of Targeted Drug Delivery	24
1.2.1	Alzheimer's disease	25
2	Project Aims	34
2.1	Hypothesis to be tested	34
2.2	Preliminary Design's Monomer Components.....	38
3	Synthesis of Heterotelechelic Oligoethylene Glycol Chains	40
3.1	Results and Discussion	40
3.1.1	Mono-Protection	41
3.1.2	Williamson Ether Synthesis.....	41
3.1.3	Deprotection.....	42
3.1.4	Purification.....	43
3.1.5	Molecular Weight Distribution Analysis	43
3.1.6	Summary	44
4	Ring Opening Metathesis Polymerization: Route to Homo- & Co-polymers.....	45
4.1	Introduction.....	45
4.1.1	Mechanism of Ring-Opening Metathesis Polymerization	48
4.1.2	Monomer Design Rationale	51
4.2	Synthesis and Characterization of First-Generation Homopolymers.....	69
4.2.1	Monomer Synthesis.....	70
4.2.2	Homopolymers Synthesis and Characterization	80
4.2.3	Biocompatibility of First-Generation Ring-Opening Metathesis Homopolymers	89
4.2.4	Summary	89
5	Revised Synthesis of Homo- and Co-polymers via Ring Opening Metathesis Polymerization	90
5.1	Revised Monomer Synthesis.....	91
5.2	Homo- and Co-Polymers Synthesis and Characterization	94
5.2.1	Homo-Polymerization ¹ H NMR Kinetics	94
5.2.2	Evaluation of Propagating Homo-Polymer Chains of Second-Generation Monomers	97
5.3	Biocompatibility of Second-Generation Ring-Opening Metathesis Homopolymers.....	100
5.4	Summary	102

6	Synthesis and Characterization of First-Generation <i>Co</i>-polymers	103
6.1	Summary	115
7	Conclusions and Future Considerations	116
8	Future Work.....	122
9	Experimental Section.....	126
9.1	General Considerations	126
9.2	Compound Characterization Techniques	126
9.3	Standard Procedure for Determining the Homo-Polymerization Kinetics of First-Generation Monomers Using ¹ H NMR	128
9.4	Standard Procedure for Determining the Homo-Polymerization Kinetics of Second-Generation Monomers Using ¹ H NMR.....	129
9.5	Standard Procedure for Evaluating the Progression of <i>M_n</i> and <i>D</i> of Propagating Homo-Polymer Chains of First- and Second-Generation Monomers Using GPC	132
9.6	Standard Homo-Polymerization Procedure of First-Generation Monomers.....	132
9.7	Standard Homo-Polymerization Procedure of Second-Generation Monomers	132
9.8	Standard Block- <i>Co</i> -Polymerization Procedure of Second-Generation Monomers.....	133
9.9	Determination of the Ratio of Second-Generation Monomers in the Structure of First-Generation <i>Co</i> -Polymers Using ¹ H NMR Spectroscopy	134
9.10	Cell Culture Methods	135
9.11	AlamarBlue® Cellular Viability Assay Protocol.....	135
9.12	MTT Cellular Viability Assay Protocol.....	135
9.12.1	Cell Density Optimization for MTT Assay Protocol	136
9.13	Cellular Uptake Assessment Protocol.....	137
9.14	Compound Synthesis Procedures.....	138
10	Spectra	173
11	References.....	217

1 Targeted Drug Delivery and it's Potential in Alzheimer's Disease Therapy

Nanomedicine is the science of designing, manufacturing and introducing nanoscopic material into the human body to diagnose, prevent or treat diseases on a cellular and subcellular level. (1) Its main objective is to lower the overall consumption of the therapeutic reagent by maximizing its bioavailability in the desired site of action. (1) Efficacy of drug targeting mediated by nanotechnology is largely dependent upon the nanocarriers' success in overcoming biological barriers, their efficiency at recognizing the targeted site and their success at the spatial and temporal release of their cargo. (2) Thus, nanocarriers have to be equipped with the necessary components that would enable them to face biological barriers and fulfil the intended purpose. (3) Nanoparticles, NPs, can take different shapes, be prepared from various materials and host a range of diagnostic or therapeutic reagents. (3)

Polymeric NPs enjoy a high degree of synthetic flexibility which is an attribute that can account for their widespread use in nanoparticle synthesis. (4) (5) (6) Advances in polymerization chemistries have made NPs with tunable physical, chemical and optical properties accessible. (4) (5) (6) Furthermore, the modular surface chemistry of polymeric materials allows orthogonal transformations that can enable the final architectures to perform versatile functionalities. (7) Polymeric NPs-based therapy has found many biomedical applications that can be exploited for the diagnosis and treatment of a wide range of diseases including cancer, diabetes and many more. (3) However, diseases associated with the brain remain quite challenging due to the presence of the blood brain barrier. (8) The blood brain barrier protects this vital organ by precisely controlling the passage of nutrients and efflux of waste maintaining brain homeostasis and preventing the disruption of synaptic transmission. (8)

Alzheimer's disease, AD, has become a global health crisis due to the increasing number of AD cases. (9) AD patients suffer from a complete social dependence causing an enormous strain on the patients' families and the health care system. (10) Causes of the disease are not fully understood, however, recent studies have linked this disease with unfavorable mitochondria-associated interaction between two proteins; amyloid beta and amyloid-beta binding alcohol dehydrogenase. (11) This interaction was shown to trigger several mitochondrial functional and morphological defects including elevation in levels of reactive oxygen species and a consequent increase in mitochondrial permeability, which can ultimately lead to neuronal death. (11) Inhibition of this interaction was shown to protect neurons from amyloid-beta induced toxicity. (11) Mitochondrial targeting of drugs provides the opportunity to approach the problem with the spatial precision it needs to confine drug targeting to the diseased subcellular site without interfering with any healthy cellular and subcellular processes taking place elsewhere. (12) (13) (14)

1.1 Drug Delivery Hurdles and Approaches to Surpass Them

Decades of dedicated efforts have led to scientific advances in understanding the physiology of many diseases and development of a wide range of therapeutic materials. To fulfil their intended purpose, these therapeutic materials must have adequate pharmacokinetics and dynamics that can allow them to accumulate in the diseased site in their therapeutically effective concentration, figure 1. (1)

Pharmacokinetic refers to how the host's body acts on the therapeutic material, figure 2. (15) The extent of this action is reflected by the therapeutic material's blood-circulation life time and the rate of its clearance from the host's body. (15) Drug clearance from the body can occur via two main routes; excretion or biotransformation, figure 1. (15) By excretion, chemically intact drug is filtered into urine, sweat or air by kidneys, skin and lungs respectively. (15) Clearance of the drug molecule by excretion depends on its molecular weight and susceptibility to enzymatic degradation, respectively. (15) By biotransformation, drugs can be chemically converted into metabolites upon degradation by proteolytic enzymes which can mainly be found in the liver, figure 1. (15)

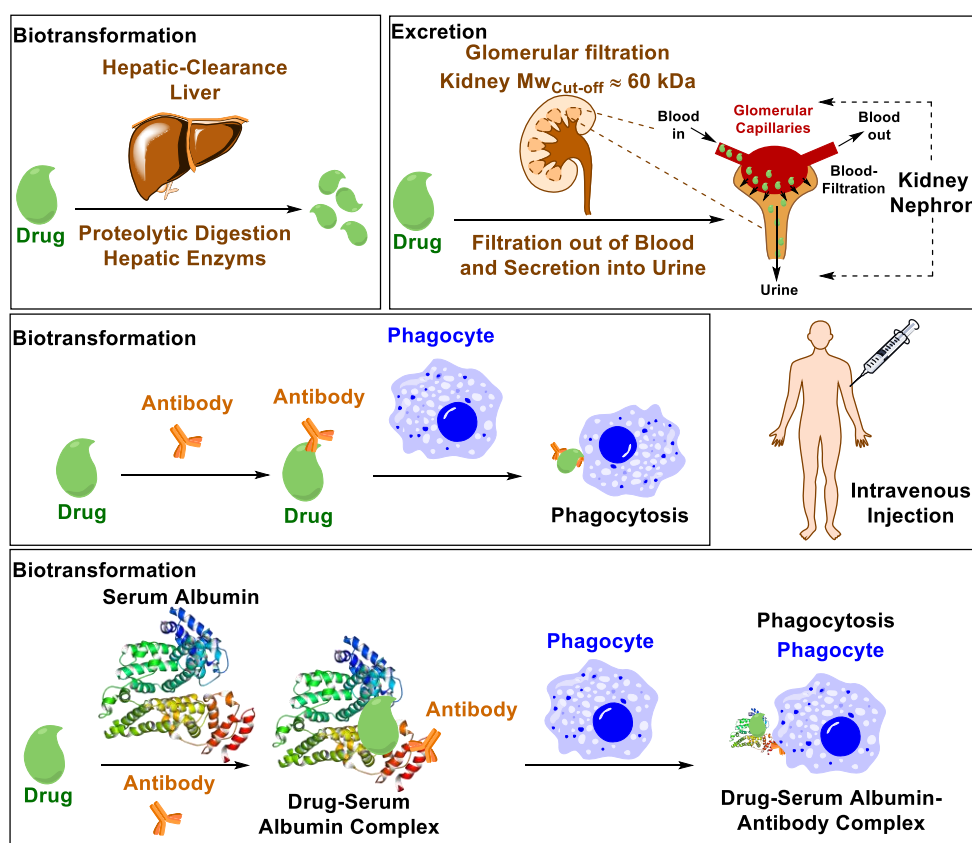


Figure 1: Biological barriers that the therapeutic material encounters upon intravenous injection that can reduce the blood-circulation life time of the therapeutic material. This can compromise the pharmacokinetic of the therapeutic material and ultimately its effectiveness. Biological barriers include; water-solubility in the blood stream (not shown), excretion by glomerular filtration, biotransformation by enzymatic degradation or/and clearance by immune system.

Another biotransformation clearance route is by the reticuloendothelial system, figure 1. (16) In this route, therapeutic material can be cleared via functional group-specific interactions with blood components through a process termed opsonization, figure 1. (16) Upon opsonization, the therapeutic material binds, covalently or non-covalently, to an antibody that can be recognized by the reticuloendothelial system constituents. (17) The reticuloendothelial system, or the mononuclear phagocytic system, is a part of the immune system and consists of phagocytic cells. (16) (17) These cells accumulate in several organs such as liver, spleen, lymph nodes and kidneys. (16) (17) Clearance by reticuloendothelial system is highly dependent on the drug's ability to bind to phagocytes via receptor- or electrostatic-mediated interactions. (16) (17) Such interactions can be facilitated by blood components such as antibodies and serum proteins. (16) (17) Clearance by any of these routes reduces the blood-circulation life time of the therapeutic material and prevents it from reaching its effectively therapeutic concentration at the diseased site. (16) (17)

Pharmacodynamics refers to how the therapeutic material acts on the host's body, figure 1. (18) The extent of this action is reflected by the therapeutic material's mechanism of its action and its therapeutically effective concentration. (18) The ability to specifically interact with the diseased site can boost the therapeutic material's pharmacodynamics and ultimately its performance. (18) Targeted drug delivery has emerged as a promising approach to improve the pharmacokinetic and/or dynamics without permanently altering the properties of the therapeutic material. (2) Targeted drug delivery platforms can be divided into two major categories; molecular and carrier approach. (2) In this section, we will review some examples of targeted drug delivery platforms, how they can improve the pharmacokinetic and/or dynamics and their advantages and limitations.

In the molecular approach, the therapeutic materials are coupled to a targeting ligand that can selectively recognize the targeted site. (2) The targeting ligand can improve the pharmacodynamics by promoting the adherence of the therapeutic materials to the membrane of the targeted site via receptor- or electrostatic-mediated interactions which can facilitate their uptake. (2)

Antibody drug conjugates is an example of receptor-mediated drug delivery. (19) The therapeutic reagent, such as the anticancer reagent calicheamicin, is coupled to an antibody, such as the monoclonal Immunoglobulin G4 anti-body (IgG4 mAb), figure 3. (19) The antibody can specifically recognize a receptor expressed on the membrane of the diseased cell, e.g. Immunoglobulin G4, . (19) Incorporation of degradable linkers, such as a disulfide linker, facilitates the intracellular liberation of the therapeutic reagent upon interaction with a component present in the biological environment within the cell, such as a reducing reagent like glutathione. (19)

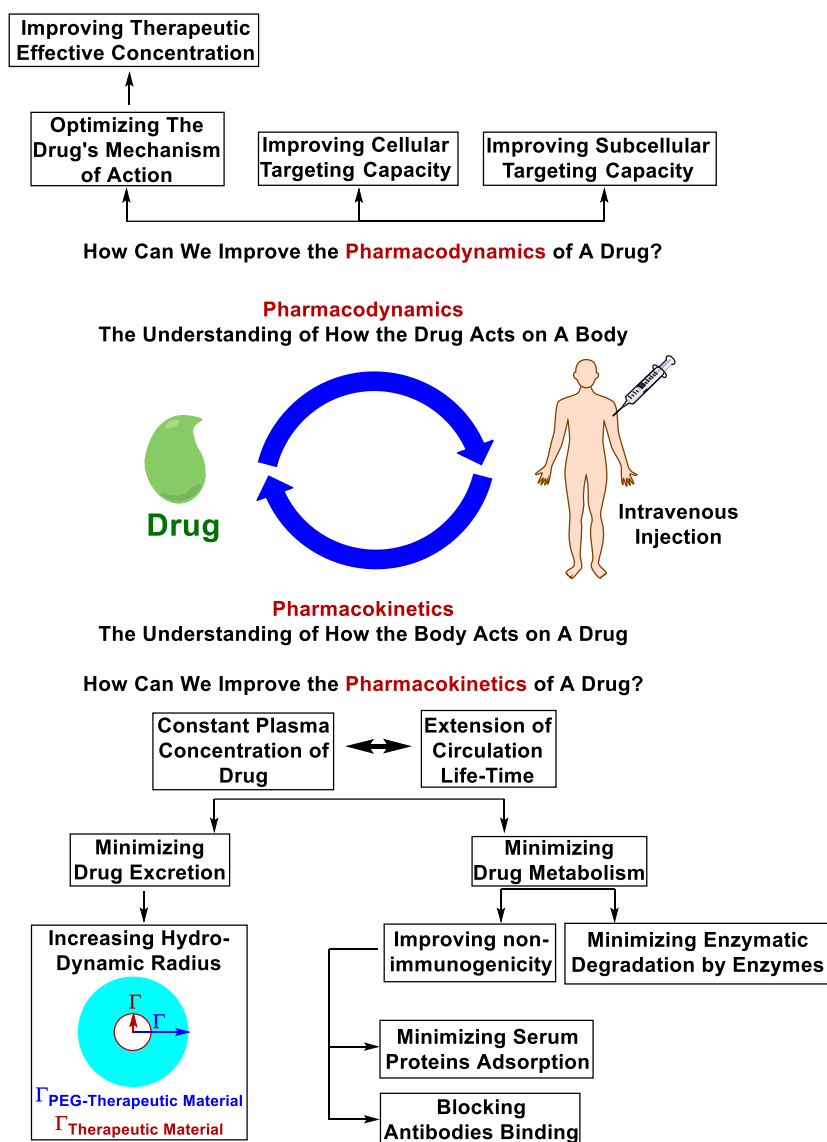


Figure 2: The pharmacokinetic and dynamic aspects that determine the fate of the therapeutic material and ability to accumulate in the diseased site at its therapeutically effective concentration. Figure adapted from Ref. (174)

Mitochondria-targeted bioactive molecules are an example of electrostatic-mediated drug delivery utilizing the molecular approach, though, at a subcellular level. Bioactive molecules, such as antioxidants, can be coupled to a lipophilic cationic ligand, such as a triphenylphosphonium cation, that can direct the uptake to the mitochondrial matrix as a response to its inner negative potential, figure 3. (20) The antioxidative component, without being released, can reduce the levels of reactive oxygen species, such as hydrogen peroxide or superoxide, and protect against ROS-mediated toxicity. (20)

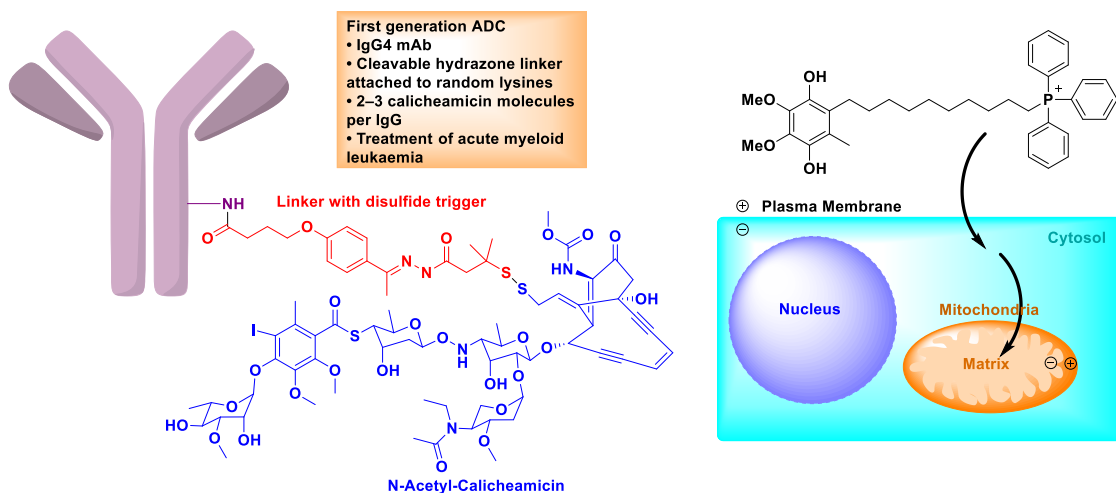


Figure 3: Antibody-drug conjugates for receptor-mediated drug delivery in cancer therapy (left) and mitochondria-targeted bioactive molecules for electrostatic mediated antioxidants delivery (right). Figures adapted from Ref. (19) and (20) respectively.

The main issue associated with this approach is that the targeting ligand can promote a competitive binding to the membrane of phagocytic cells via receptor- or electrostatic-mediated interactions. (3) This can accelerate the clearance of the therapeutic material by the reticuloendothelial system, as described above, reducing its circulation life time and ultimately compromising its pharmacokinetic. (3)

In the carrier approach, the therapeutic material is encapsulated within a nanoscopic vehicle the surface of which can be decorated with a targeting ligand. (2) As previously mentioned, the targeting ligand can drive the uptake via either electrostatic- or receptor-mediated endocytosis. (2) The surface of the carrier can also be conjugated to a hydrophilic and colloid-stabilizing polymer. (2)

Anti-cancer reagents such as paclitaxel can be encapsulated within transferrin-anchored nanoliposomes to enhance their water solubility, biocompatibility and biodistribution, figure 4. (21) Such liposomes can be prepared by self-assembly of biocompatible amphiphilic polymers functionalized with transferrin. (21) Transferrin is an iron-transporting protein that can internalize iron into cells via transferrin receptor-mediated endocytosis. (21) It is reported that transferrin receptors are upregulated in human cancer cells compared to healthy ones establishing transferrin-mediated endocytosis as a promising cellular targeting machinery in cancer therapy. (22) The liposomal vehicles presented in this communication were shown to be stable at physiological pH. (21) The therapeutic material can be released upon exposure to the acidic environment within the cancer cells. (21)

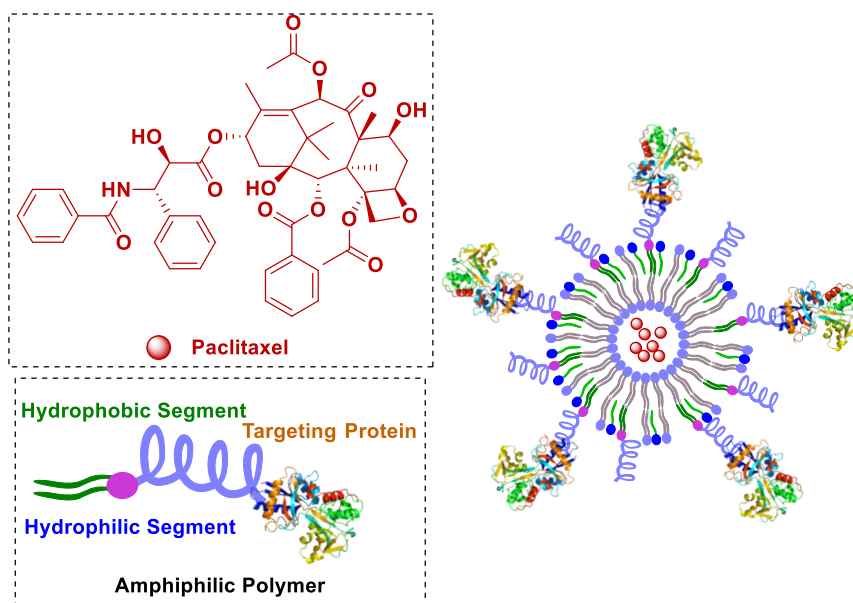


Figure 4: Paclitaxel-loaded liposomes functionalized with transferrin as receptor targeting nano-particles for the treatment of ovarian cancer. Figure adapted from Ref. (21)

Multi-walled carbon nanotubes, MWCNTs, have been exploited for the delivery of anticancer reagents, such as platinum IV cis-platin pro-drug, to the mitochondria, figure 5. (23) Mitochondrial targeting of such MWCNTs was achieved by evoking an electrostatic-response between the mitochondrial targeting fluorescent ligand, e.g. rhodamine-110, covalently bound to the surface of the MWCNTs and the mitochondrial matrix's inner negative potential. (24) The hydrophobic pro-drug can be loaded into the hydrophobic interior of the MWCNTs and retained there by means of π - π interactions between aromatic rings in the pro-drug and the MWCNTs. An *in situ* reduction of the platinum IV pro-drug, by interacting with a reducing reagent such as glutathione, into its more reactive and hydrophilic platinum II form can facilitate its extrusion from the hydrophobic interior to the biological milieu where it can act on the mitochondrial DNA inducing mitochondrial and ultimately cellular apoptosis. (25)

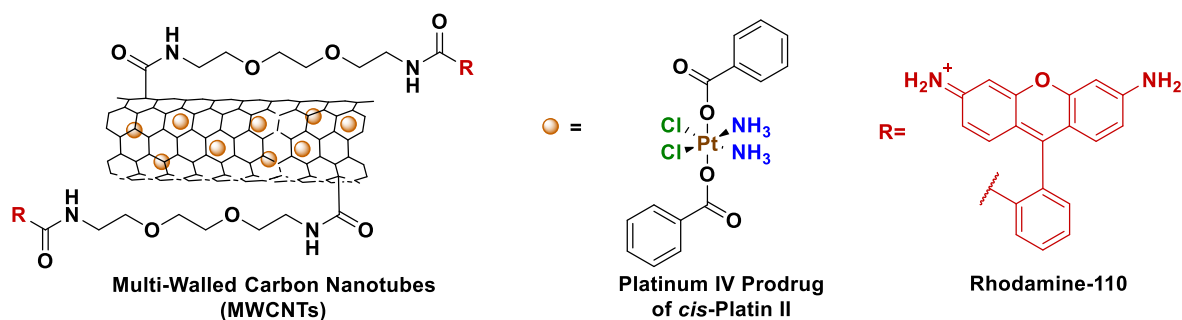


Figure 5: MWCNTs loaded with cis-platin pro-drug and coupled to rhodamine 110 for mitochondrial targeting. Figure adapted from Ref. (23)

The disadvantage of this approach is that the surface of the carrier tends to get over-crowded with the targeting ligands, hydrophilic polymers and occasionally fluorescent molecules that cellular up take becomes hampered by steric factors. (26) This jeopardizes pharmacodynamics of the therapeutic material and, ultimately, its efficacy at fulfilling its intended purpose. (26) Therefore, when attempting to design a drug delivery system, both pharmacokinetic and dynamic aspects need to be considered. The design should also be experimented with to find the ultimate balance between the two.

1.1.1 Nanoscopic Materials: Structurally Diverse and Functionally Versatile Drug Delivery Vectors

Of the two approaches described above, the carrier approach enables the drug delivery system to perform multiple functions. This capacity stems from the modular surfaces the carriers, henceforward referred to as nanoparticles, that follow this approach have. Nanoparticles, NPs, modular surface means the surface can be conjugated to different types of molecules ranging from fluorescence tags, receptor- or electrostatic- mediated targeting ligands, hydrophilic polymers, to stimuli-responsive linkers, figure 6. (21) (23) (27) NPs can be prepared from different types of material such as organic or inorganic and can adopt different morphologies, figure 6. (28) (29) (30) (31) (32) (33) With this greater modular composition and surface of the carrier approach comes the greater effort and time needed to find the balance between the both pharmacokinetic and dynamic aspects discussed previously.

Surface-Conjugated Molecule	Function NPs Can Perform	Reference
Fluorescence tag	Tracking of NPs mobility and localization in <i>in vitro</i> or <i>in vivo</i> studies	(23)
Targeting Protein or antibody	facilitate NPs receptor-mediated cellular uptake	(21)
Ionic targeting ligand	enhance NPs subcellular localization	(23)
Hydrophilic polymer	enhance their solubility in the blood stream	(27)
Degradable linker between carrier and loaded drug	promote specific spatial and temporal release of their cargo	(27)

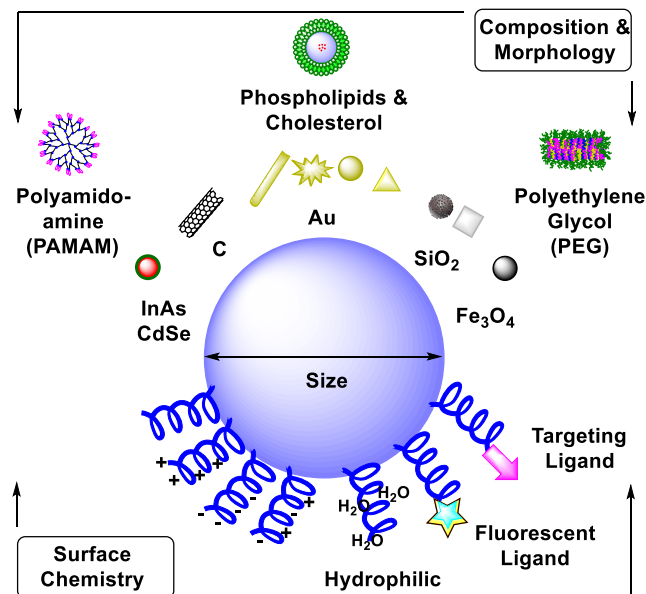


Figure 6: Tunable physical, chemical and optical properties of nanomaterials. Figure adapted from Ref. (3)

Polymeric nanoparticles have emerged as a good compromise between structure and efficiency. Water solubility, biocompatibility, non-immunogenicity and modular surface chemistry can all be combined in one skeleton. (27) (7) That leaves more room for optimizing other structural aspects that contribute to the overall performance such as morphology and core or surface chemistry.

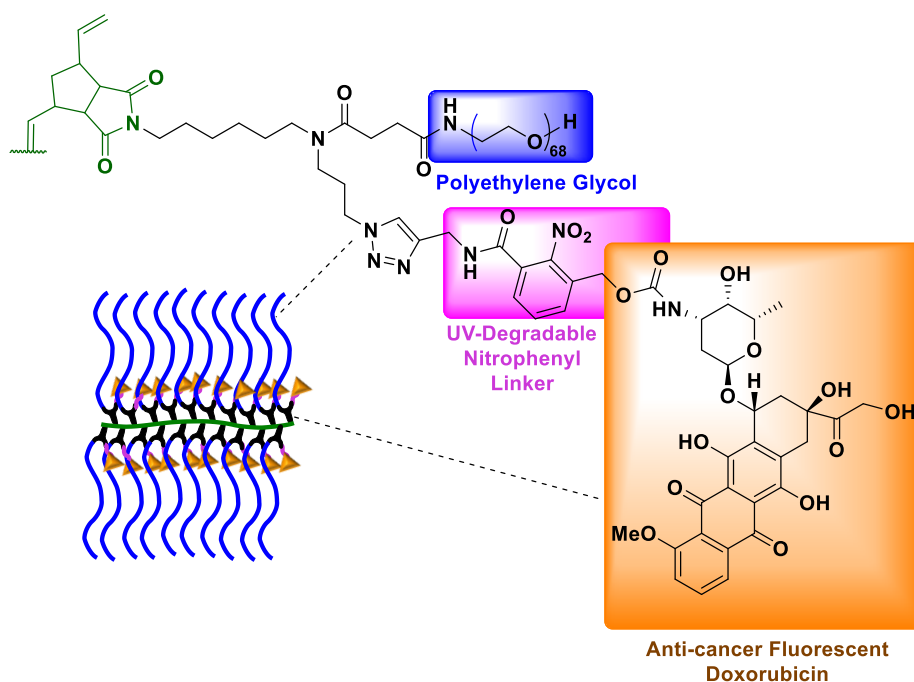
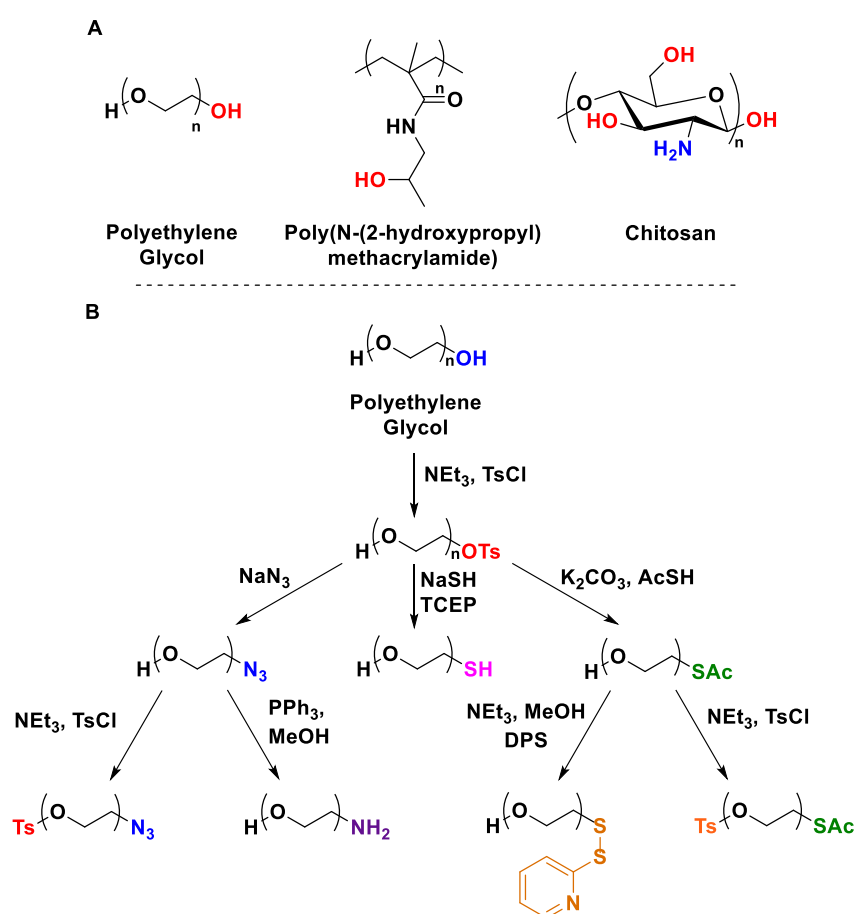


Figure 7: Schematic representation of the possible multimodal action the carrier approach can adopt. The nanoscopic carrier design can feature non-immunogenic capacity, photochemically-induced drug release and optical visualization associated with polyethylene glycol, nitrophenyl and the fluorescent doxorubicin respectively. Adapted from Ref. (7)

1.1.1.1 Polymers in Targeted Drug Delivery

Polymeric materials stand out owing to the presence of derivatizable groups in their structure, scheme 1. These functional groups can be asymmetrically derivatized to enable the precise covalent coupling to various molecules such as optical probes, targeting moieties or drug molecules, scheme 1. (34) Polyethylene glycol, poly(N-(2-hydroxypropyl)methacrylamide) and chitosan feature other essential properties for drug targeting such as hydrophilicity and non-immunogenicity, scheme 1. (4) (5) (6) Because polyethylene glycol has only two terminal functional groups, we envisioned that its desymmetrization and functionalization is practically more precise to accomplish and monitor.



Scheme 1: Structure of polymers used for the preparation of drug delivery vectors. Structure and synthesis pathways towards asymmetrically derivatized polyethylene glycol polymer chains. Adapted from Ref. (34)

Pegylation, which is the conjugation of polyethylene glycol chains, is one of the most commonly applied approaches to minimizing the clearance of therapeutic molecules. (35) (36) (37) Several pegylated therapeutics were approved by the Food and Drug Administration, FDA, and became commercially available, such as PegIntron® and Neulasta® which are prescribed as treatments for hepatitis C and

chemotherapy-induced neutropenia respectively. (35) (36) (37) Pegylation of drugs or protein-based therapeutics has been shown to enhance their overall pharmacokinetics by extending their blood-circulation life time and reducing the rate of their clearance from the host's body. (35) (36) (37)

PEG is a highly hydrated molecule. (38) consequently, it increases the hydrodynamic volume of the PEG-coupled therapeutic material. (38) This attribute which was confirmed both computationally and experimentally is believed to minimize the propensity of the therapeutic material to undergo excretion by glomerular filtration. (38) Pegylation was also shown to protect the *in vitro* catalytic activity of proteins against proteolytic digestion induced by enzymes such as trypsin, chymotrypsin or protease. (37)

Pegylation was shown to trigger a combination of attractive and repulsive forces against serum proteins using computational and experimental models. (39) (40) (41) The triumph of either form of forces depends on the model used to study these forces and the conditions under which these forces were examined. (39) (40) (41) This is a significantly important attribute considering that protein adsorption is a key step in phagocytosis of colloidal systems by opsonization. (39) (40) (41) From our own experience in the area, treatment of PEG-based nanoparticles with cell culture media, supplemented with 10% fetal bovine serum (FBS), caused turbidity which might be the product of dominating attractive forces. This turbidity was not observed when FBS-free cell culture media was used instead. The turbidity significantly scaled down as the concentration of pegylated nanoparticles in 10% FBS-media was decreased from 100-5 μM .

PEG is believed to bestow its non-immunogenic property upon its PEG-coupled therapeutic material by masking its functional groups that are detectable by the host's immune system under a shell of water molecules. (35) (36) (37) The non-immunogenic property of PEG was elucidated by *in vitro* experiments where therapeutics in their native and pegylated forms were treated with antibodies then immunoprecipitated. (35) (36) (37) Pegylation was shown to reduce the binding of antibodies to the therapeutic material. (35) (36) (37) (42) However, clinical trials of other FDA-approved pegylated-therapeutics have raised speculations about the replicability of the PEG non-immunogenic effect across a wide range of treatments. (36) In the clinical trial of krystexxa®, a pegylate protein for the treatment of chronic gout, 50% of the patients were unresponsive to the treatment and were hypersensitive to infusion. (36) Further *in vivo* experiments using animal models concluded that pegylation diminished the original immunogenicity of the PEG-coupled therapeutic material but triggered a new immunogenic reaction against the pegylated-therapeutic material. (36) These observations suggest that the non-immunogenicity of pegylated therapeutics may vary not only across the pegylated therapeutics themselves but also across living subjects. (36)

1.1.1.2 Approaches to Polymeric Nanoparticles Synthesis

Synthesis of polymeric nanoparticles falls under two major categories with respect to the type of bonds formed between monomers; self-assembly and covalent polymerization. In the former, the monomers are held together via noncovalent interactions such as hydrophobic, hydrophilic, π - π stacking, Van der Waals or electrostatic interactions. (43) Advantages of such interactions is their reversibility which maintains the identity and inherent properties of each individual component. (44) Because of the reversible nature of these noncovalent interactions, self-assembled amphiphiles face *in vivo* stability issues in addition to biological barrier such as phagocytosis, cellular selectivity and renal filtration. Self-assembled systems may undergo dissociation in the blood stream upon significant dilution after *in vivo* administration which is critical for their use as drug delivery vectors, figure 8. (45) The stability of self-assembled systems is determined by thermodynamic elements such as the critical micelle concentration, CMC, which is the concentration of monomer that dictates in which direction the equilibrium between monomeric and polymeric form is shifted and the kinetics of monomer dissociation at concentrations below CMC. (46) (47) (48)

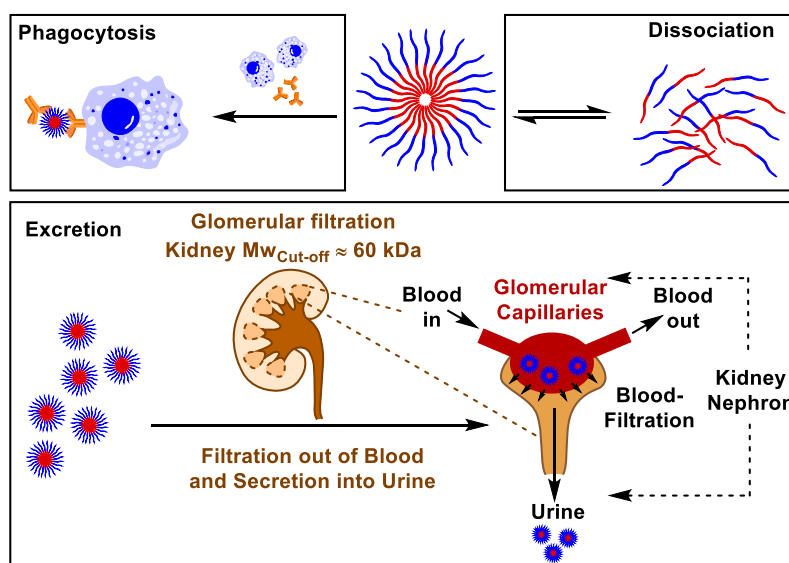


Figure 8: Biological barriers detrimental to the efficiency of self-assembled nanoparticles. Biological barriers include; water solubility of self-assembled nanoparticles in blood pool, recognition and attack by immune system, degradation by enzymes and selective uptake by cells at the diseased site. Dissociation upon dilution below CMC is an additional barrier that can affect their efficiency at delivering the therapeutic cargo.

Covalent polymerization techniques, such as ring-opening metathesis polymerization, ROMP, have emerged as an alternative approach to self-assembly for the synthesis of thermodynamically stable nanoparticles. Under carefully selected conditions, which will be discussed in chapter II, the equilibrium during their synthesis is shifted towards the polymeric form due to the relief of the ring strain associated

with the transformation. (49) In such techniques, monomers are held together via the more thermodynamically stable covalent bonds, and therefore, interlocked in the polymeric architecture.

ROMP initiated by the third generation Grubbs catalysts occurs with good control over molecular weight and molecular weight distribution of growing polymer chains, generating polymeric architectures with predictable molecular weights and narrow dispersity indices. (49) ROMP is a practical polymerization technique due to the mild conditions under which it operates and its compatibility with a wide range of functional groups. Its functional group tolerance facilitates the incorporation of an array of fluorescent molecules (50) (51), magnetic resonance imaging, MRI, contrast reagents (51) (52), hydrophilic polymers (27) (50) (51) receptor-mediated targeting ligands (50) or therapeutic reagents (27) in pre- or post-polymerization steps, figure 9. The major drawback of ROMP from a biological perspective is the cytotoxicity associated with ruthenium in the synthesis of polymeric drug delivery vectors. The issue is not being overlooked and significant efforts are dedicated to improve initiators design to promote optimal catalyst-polymer separation. (53) (54)

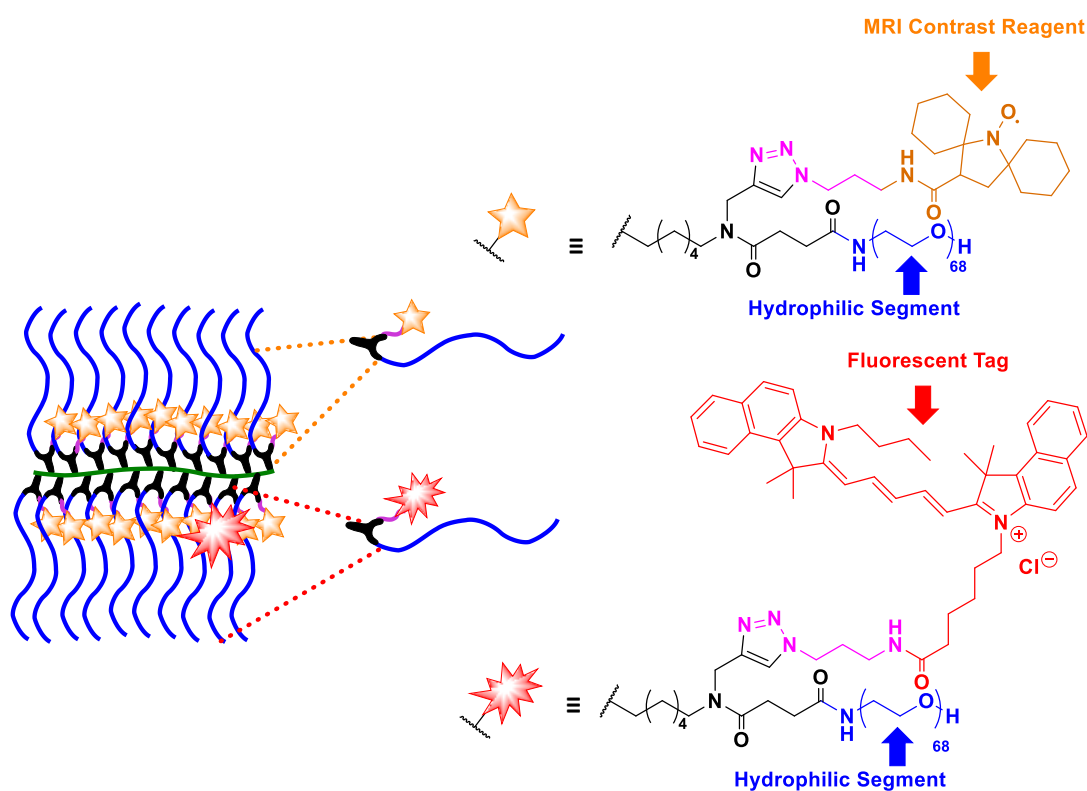


Figure 9: An example of nanoscopic brushes prepared via ROMP initiated by Grubbs III catalyst demonstrating the array of compatible functional groups. Various molecules such as the hydrophilic PEG, fluorescent Cy5 and the MRI contrast reagent were all incorporated into the polymeric vehicle in a pre-polymerization step without any reported complication. Figure adapted from Ref. (51)

1.2 Applications of Targeted Drug Delivery

Targeted drug delivery has found applications in the diagnosis and treatment of many diseases such as cancer (21), diabetes (55) and neurodegenerative diseases (2). As yet, neurodegenerative diseases remain an area where targeted drug delivery is most needed as surgical treatments are not usually an option and a treatment at a molecular level is needed. Additionally, therapeutic materials not only have to evade *en route* biological barriers such as solubility in the blood stream, stability against enzymatic and hydrolytic degradation and phagocytosis but also the blood brain barrier, BBB, figure 10.

The BBB protects the brain from micro-organisms, toxic compounds and fluctuations in the blood stream that can disrupt synaptic transmission allowing the brain to efficiently perform its vital functions. BBB's major contributor to its specific permeability are the endothelial cells that line the cerebral microvessels and the tight junctions between them, figure 10. (8) The BBB can account for why many neurological disorders remain untreated despite the advances in drug discovery in that area. (8)

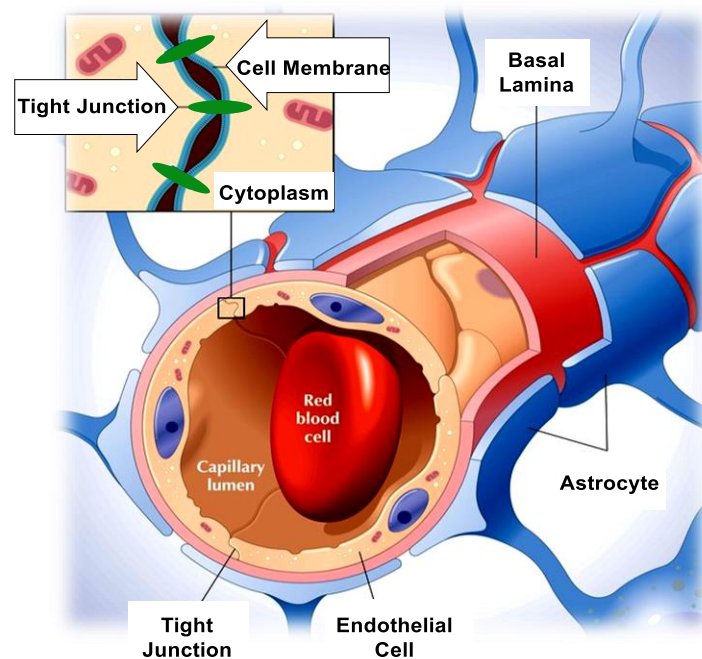


Figure 10: Illustration of the BBB. The BBB is an additional biological barrier neurotherapeutic reagents must overcome. The BBB protects the brain from micro-organisms, toxic compounds and fluctuations in the blood stream that can disrupt synaptic transmission allowing the brain to efficiently perform its vital functions BBB figure is taken from Ref. (161)

1.2.1 Alzheimer's disease

Alzheimer's disease, AD, is the most common form of neurodegeneration in the central nervous system. AD is becoming a global health crisis due to the increasing number of AD cases and the costs associated with the care provided for AD patients. (9) AD is associated with the occurrence of three major morphological brain abnormalities; extraneuronal deposits of amyloid-beta protein, $A\beta$, intraneuronal aggregates of a microtubule associated protein called tau in its hyperphosphorylated form and shrinkage in brain tissue, figure 11. (9) Occurrence of these morphological defects in areas of the brain that host language, memory and problem-solving centres can result in cognitive decline, memory impairment, behavioural changes as well as complete social dependence all of which are symptoms observed amongst AD patients. (10)

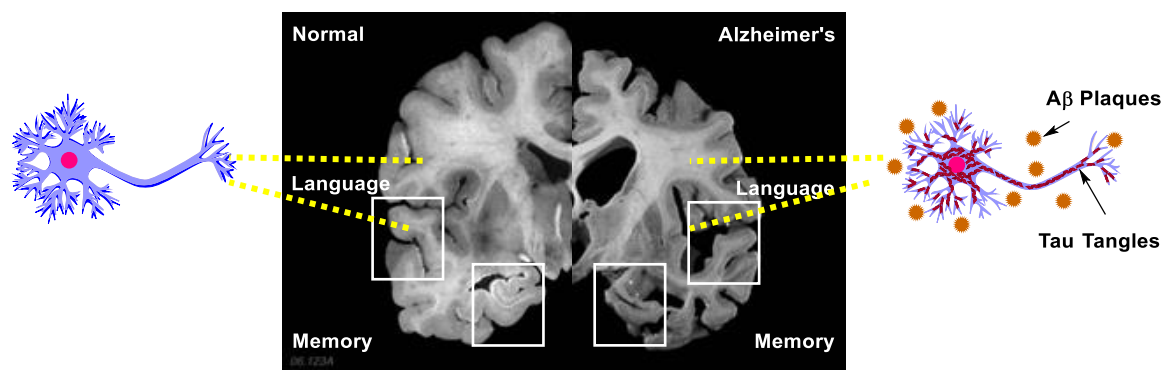


Figure 11: Morphological defects in the brain of AD patients, right, in comparison to non-demented age matched control, left. The morphological defects include shrinkage in brain size, intraneuronal deposits termed tau tangles and extraneuronal aggregates termed amyloid plaques. Figure adapted from Ref. (162)

1.2.1.1 Pathology of Alzheimer's Disease

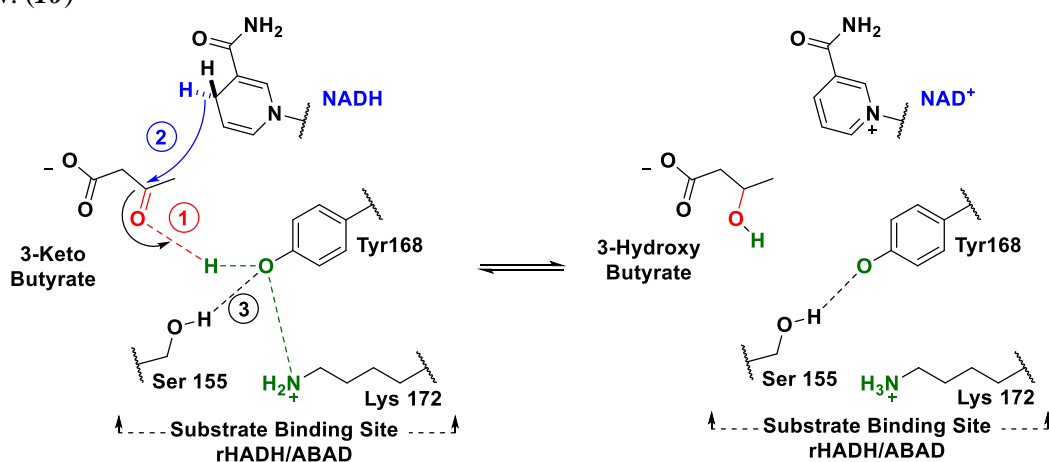
Several cascades have been implicated with the pathology of AD among which is a mitochondria-associated interaction between intraneuronal $A\beta$ and a mitochondrial protein termed amyloid-beta binding alcohol dehydrogenase, ABAD. (10) $A\beta$ is the product of the sequential cleavage of a membrane protein termed amyloid precursor protein (APP) by β - and γ -secretases. (56) Studies suggest that $A\beta$ production and subsequent intraneuronal accumulation precedes its extraneuronal deposition as senile plaques. (57) Intraneuronal $A\beta$ can interact with several vital proteins, amongst which is ABAD, triggering cytotoxic cascades that ultimately may lead to Alzheimer's disease. (10) ABAD is an enzyme expressed in several body tissue types including heart, liver and brain tissues. (58) ABAD is known by other names such as human brain short chain L-3-hydroxyacyl-coenzyme dehydrogenase, SCHAD, and 3-hydroxyacyl-coenzyme dehydrogenase type II, HADH II. (59) (11) Studies revealed that ABAD predominantly localizes in the mitochondria where, in conjunction with nicotinamide adenine

dinucleotide (NAD⁺), it catalyzes the third step of the fatty acid metabolism pathway: RCH(OH)-CH₂-CO-SCoA + NAD⁺ ↔ R-CO-CH₂-CO-SCoA + NADH. (10) (60) (61) (62) (63) Using protein crystallography, residues Ser¹⁵⁵, Tyr¹⁶⁸ and Lys¹⁷² were identified as the catalytic triad involved in ABAD enzymatic activity and were found to be conserved in both human and rat forms of the protein, figure 12. (10) (11)

	151		190
	βE →		←----- aE ----->
Rat Brain HADHII/ABAD	INTA S VAAFE	GQVGQAA Y SA	S KGGIVGMTL PIARDLAPIG
Mouse HADHII/ABAD	INTA S VAAFE	GQVGQAA Y SA	S KGGIDGMTL PIARDLAPTG
Bovin HADHII/ABAD	INTA S VAAFE	GQVGQAA Y SA	S KGGIVGMTL PIARDLAPMG
Human HADHII/ABAD	INTA S VAAFE	GQVGQAA Y SA	S KGGIVGMTL PIARDLAPIG
	βF	200	210
	IRVVTIAPGL	FATPLLTTLP
	IRVVTIAPGL	FATPLLTTLP
	IRVMTIAPGL	FGTPLLTTLP
	IRVMTIAPGL	FGTPLLTSLP

Figure 12: : Amino acid sequence from residue 151 to 210 of brain rHADH II/ABAD aligned with mouse, bovine and human forms. Residues in red, bold and italic are the catalytic triad believed to be involved in the enzymatic activity of the proteins. Figure adapted from Ref. (11)

The mechanism by which the triad residues can catalyse the reversible oxidation of alcohols into ketones was predicted by analysing the crystal structure of ABAD-NAD⁺ complex with 3-ketobutyrate. (11) The proposed mechanism begins with hydrogen bonding between Tyr¹⁶⁸ residue and the carbonyl of 3-ketobutyrate promoted due to the increased acidity of the hydroxyl group of Tyr¹⁶⁸ as a result of its coordination to the ammonium group of Lys¹⁷², scheme 2. (11) Subsequently, a simultaneous hydride transfer to the carbonyl group from the co-enzyme, NADH, and protonation of the resulting secondary alcohol by abstracting the Tyr¹⁶⁸ proton occurs. (11) The resulting Tyr¹⁶⁸ anion is stabilized via hydrogen bond formation with Ser¹⁵⁵ residue. The significance of the fatty acid metabolic pathway stems from its potential as an energy source for various organs including the brain when glucose levels are low. (10)



Scheme 2: The proposed mechanism of the catalytic activity of rHADH/ABAD drawn from the crystal structure of HADH II /ABAD-NADH complex with 3-ketobutyrate. Figures adapted from Ref. (11)

1.2.1.1.1 Consequences of ABAD-A β Interaction and Its Link to Alzheimer's Disease

Aging and associated neurodegenerative diseases were first linked to oxidative damage in 1950s when Denham Harman proposed that organisms age due to the build-up of reactive oxygen species. (64) (65) Reactive oxygen species (ROS) are oxygen containing entities, such as superoxide (O_2^\bullet), hydrogen peroxide (H_2O_2), and the highly reactive hydroxyl radical ($^\bullet OH$), that can react with reducible compounds. (66) Mitochondria generate most of endogenous ROS as toxic by-products of oxidative phosphorylation, figure 13. Free electrons can be donated directly to O_2 , as they are funnelled down the electron transport chain, to generate superoxide anion (O_2^\bullet) and other ROS at sites up stream of complex IV, in particular, complex I, II and III. (67) Complex I and II produce ROS in the mitochondrial matrix while complex III may form superoxide in either the matrix or intermembrane space. (68) Dismutation of (O_2^\bullet) into H_2O_2 may spontaneously occur by superoxide dismutase, figure 13. H_2O_2 can be reduced to H_2O by matrix enzymes such as peroxiredoxins, catalase or glutathione. (66) (69) ROS production is increased when electron movement from complexes I–III to complex IV is blocked or slowed down. This may occur as a result of inhibition of one or multiple respiratory chain complexes or electron carriers. Inefficient flow of electrons through the respiratory chain increases the residence time of electrons on sites accessible to O_2 which increases the probability of one electron reductions of O_2 to form (O_2^\bullet) and H_2O_2 . (67) (68)

ROS can cause oxidation of proteins' functional groups, such as sulfhydryl groups. Oxidation of sulfhydryl groups into sulfenic acid groups which can be readily converted to disulfides by reaction with an adjacent sulfhydryl residue can lead to intra-protein or inter-protein cross-linking. (70) (71) Cross-linking of proteins changes proteins' structure, conformation and ultimately their function. Additionally, ROS can cause lipid peroxidation of membranes, scheme 3, leading to membrane fragmentation and mislocalization of mitochondrial membrane and intermembrane space proteins such as the release of a component of the respiratory chain machinery, cytochrome c, from mitochondrial membrane space into the cytosol. (72) Such event leads to interruption of oxidative phosphorylation and ultimately energy production disorder. (68)

In vitro studies revealed that overexpression of ABAD in an A β -rich environment exacerbates A β -induced cytotoxicity by accentuating A β -mediated production of reactive oxygen species, ROS. (62) This observation was supported by the elevated levels of radicals, as shown by the sharp peak at 3410 G, detected in intact frozen brain samples taken from AD mouse models using electron paramagnetic resonance. (62)

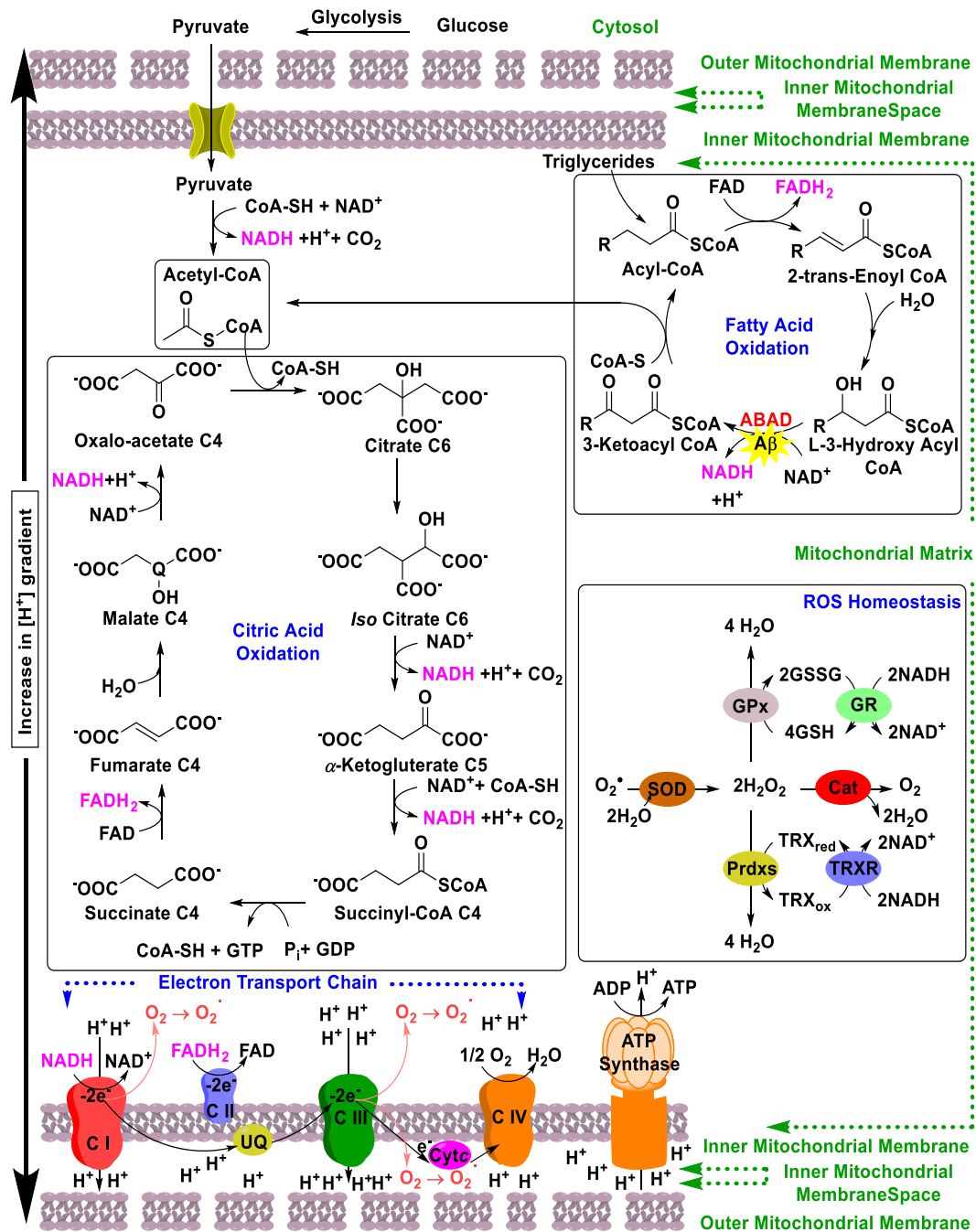
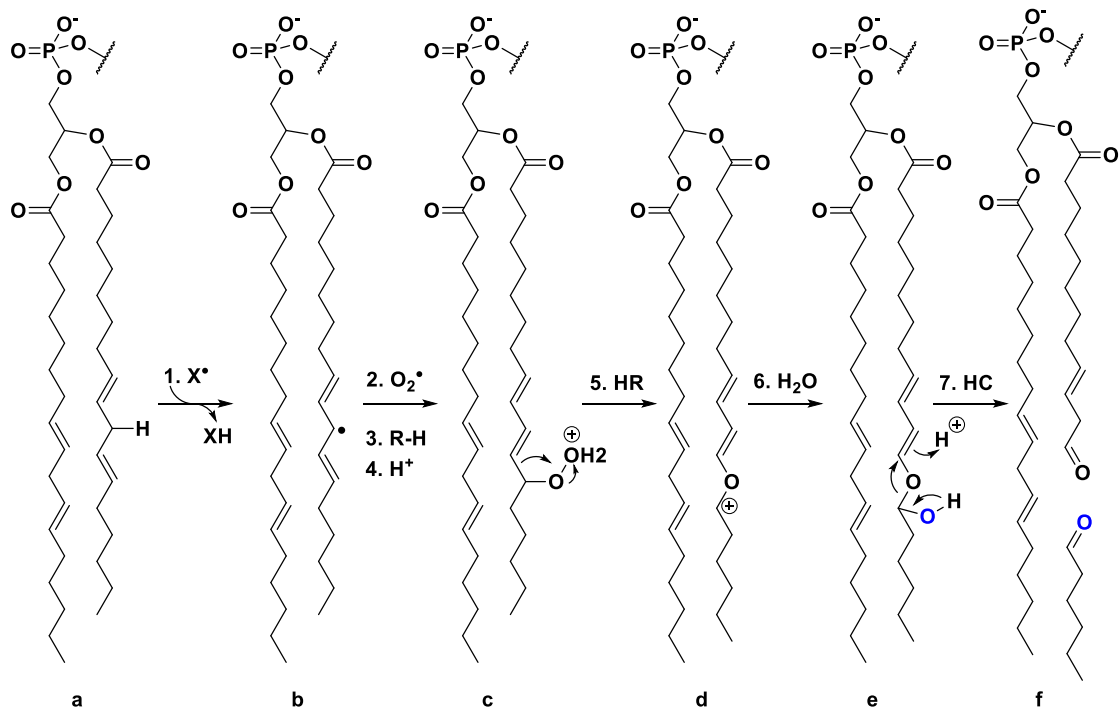


Figure 13: Energy production pathways. Glucose and triglycerides are metabolized into acetyl-CoA, and ultimately CO₂, through citric and fatty acid oxidation pathways generating NADH and FADH₂ as by-products. NADH and FADH₂ are used to fuel oxidative phosphorylation of ADP that leads to ATP synthesis. NADH and FADH₂ are oxidized back to NAD⁺ and FAD via complex I and II, respectively, which are constituents of the electron transport chain. The resulting electrons are transferred from CI and II to CIII via a lipid-soluble mobile carrier termed ubiquinone, UQ, via a series of redox reactions. The electrons then transferred from CII to CIV via cytochrome c, Cyt c, a water-soluble electron carrier located within the intermembrane space. At CIV, the electrons are used to reduce O₂ and form water. These series of redox reactions carried out by the electron transport chain are coupled to production of an electrochemical [H⁺] gradient across the inner membrane as a result of consumption of H⁺ during the redox reactions or their efflux by CI, III and IV. This electrochemical gradient is what drives the ATP synthesis by ATP synthase. ROS are generated at complex I and II and converted into H₂O₂ by superoxide dismutase (SOD). H₂O₂ is quenched by antioxidative enzymes such as peroxiredoxins (Prdxs), catalase (Cat) or glutathione peroxidase (GPx). Figure adapted from Ref. (12)



Scheme 3: Oxidation of unsaturated aliphatic chain followed by fragmentation into reactive aldehydes as one of the Consequences of overproduction of ROS. The transformation begins with an abstraction of an allylic hydrogen radical by X^\bullet which could be superoxide (O_2^\bullet) or hydroxyl radical ($^\bullet OH$) generating a reactive allylic radical **b**. This step is followed by an allylic oxidation to generate an alkyl hydrogen peroxide **c** which upon protonation and a subsequent Hock rearrangement it transforms into cationic intermediate **d** which undergoes nucleophilic attack by water and Hock cleavage to cause fragmentation into the unsaturated fatty acids in cell membranes, leading to the membrane's damage.

The downstream implications of overexpression of ABAD in an $A\beta$ rich environment were assessed in an animal behavioural experiment termed radial arm water maze, RAWM. AD transgenic mouse models overexpressing mutant APP and ABAD, Tg mAPP/ABAD, showed inferior spatial and temporal memory and learning capabilities compared to non-demented controls. (62) Tg mAPP/ABAD models showed no significant decrease in the number of errors committed as they mapped out maze looking for the submerged platform, figure 14. (62)

Additionally, on a molecular level, binding of ABAD to $A\beta$ triggers a conformational change in many regions in ABAD's structure including the catalytic triad. (10) (11) (62) (73) This can account for the inhibition of ABAD's *in vitro* catalytic activity as a reducing reagent for acetoacetyl-CoA (10) and an oxidizing reagent for octanol (10) in the presence of micromolar concentrations of $A\beta$.

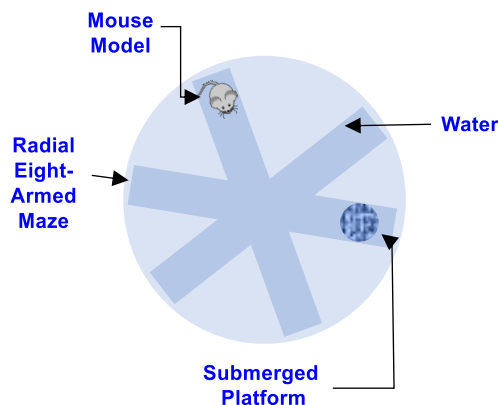
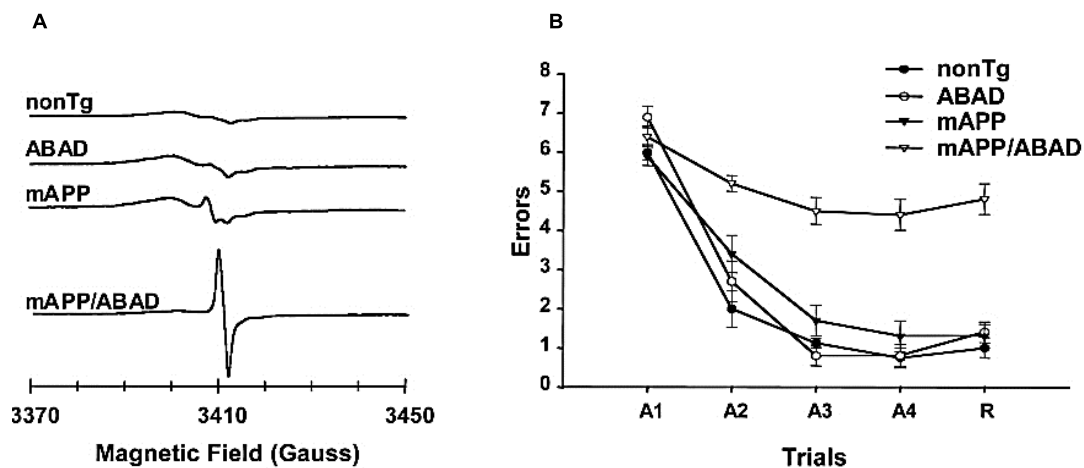


Figure 14: Consequences of overexpression of ABAD in an $A\beta$ -rich environment examined in *in vitro* (A) and *in vivo* (B) experiments. The over production of ROS has been linked to neuronal dysfunction and ultimately cognitive decline. (A) EPR spectra of intact frozen brain samples isolated from the brains of non-transgenic mouse and transgenic mouse models over expressing ABAD, mutant $A\beta$ -precursor protein (mAPP) or overexpressing both mAPP/ABAD. The stacked spectra show the elevation of ROS level, indicated by the peak at 3410 G, in the brains of mouse model over expressing both mAPP and ABAD. (B) Number of errors in finding the submerged platform in a RAWM vs. trials attempted by transgenic mouse models over expressing ABAD, mAPP or both mAPP/ABAD. The figure shows a superior temporal and spatial memory and learning capacity in non-Tg, Tg ABAD and Tg mAPP in comparison to Tg mAPP/ABAD. Figures adapted from Ref. (62)

1.2.1.1.2 Evidence of ABAD- $A\beta$ Interaction and its Location

The association of ABAD with $A\beta$ was demonstrated by co-immunoprecipitation using antibodies specific to $A\beta$, anti- $A\beta$, followed by immunoblotting using antibodies specific to ABAD, anti-ABAD as depicted in figure 15. (62) This approach facilitated the detection and isolation of ABAD- $A\beta$ complexes from cortical protein extracts taken from brains of candidates representing both demented and non-demented categories. (62) The results presented in figure 15 (left) highlight the overexpression

of ABAD in brain cells of AD patients (lane 1) in comparison to age matched controls (lane 2). (62) The same co-immunoprecipitation experiment, with the added immunoblotting of A β using anti-A β to enable the its visualization, conducted on mitochondrial fractions isolated from cortical brain samples of AD mouse models, over-expressing both ABAD and the mutant human form of APP (right, lane 2) or mAPP only (lane 3), and non-demented controls (lane 1) further validated the association of ABAD with A β . (62)

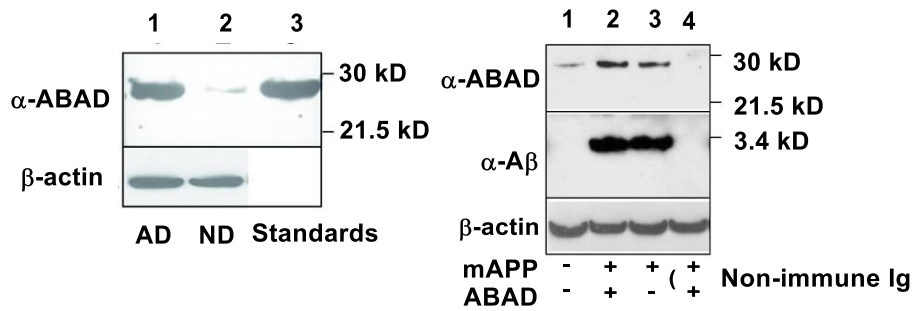


Figure 15: Co-immunoprecipitation followed by immunoblotting of cortical protein extracts taken from brains of human AD patients (left), mouse AD models (right) and age-matched and non-demented controls used for both. The β -actin panel shows no variation in protein loading across all lanes. Figures adapted from Ref. (62)

Immunostaining of cortical brain cells obtained from brain samples of AD patients, figure 16 (left), and Tg mAPP/ABAD mouse models, figure 16 (right), achieved by treatment with fluorescent antibodies specific to ABAD and antibodies specific to A β , followed by confocal microscopy further validated the association of ABAD with A β and established mitochondria as a promising sub-cellular site for the inhibition of ABAD-A β interaction. (62)

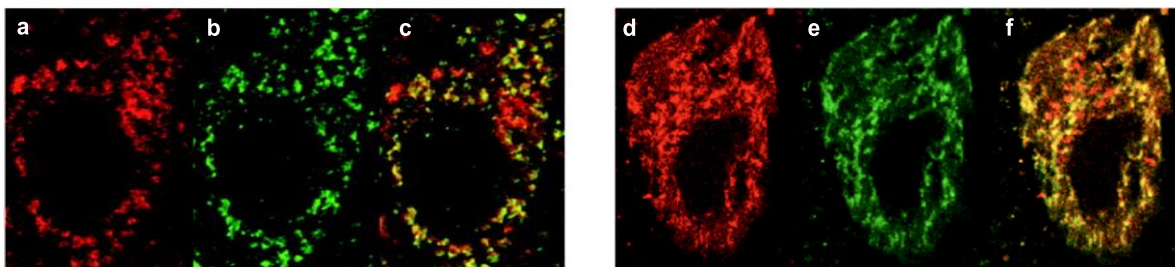
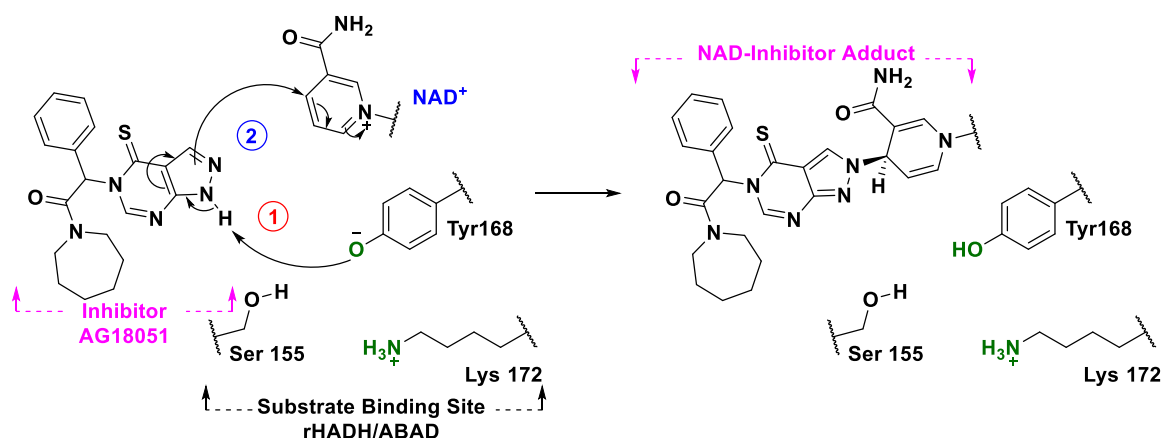


Figure 16: Colocalization of ABAD and A β in mitochondria in cortical brain samples taken from human AD patients (a-c) and tg mAPP/ABAD models (d-f). ABAD is shown in red (a, d), A β is shown in green (b, e). ABAD and A β fluorescence channels are merged in (c, f). Figures adapted from Ref. (62)

1.2.1.1.3 Inhibition of ABAD Preserves Mitochondrial Function

Protecting against ABAD-A β interaction can be achieved by inhibiting ABAD. Pre-treatment of cultured neurons overexpressing ABAD with an ABAD-inhibitor prior to exposure to A β showed attenuated levels of A β -mediated production of ROS. (73) The inhibitor was shown to covalently bind to ABAD's co-enzyme, NAD⁺. The mechanism of inhibition was drawn from the crystal structure of ABAD with the bound inhibitor and is believed to proceed similarly to the mechanism of ABAD-catalyzed oxidation of alcohols except that it is not reversible, scheme 4. (73)



Scheme 4: The proposed mechanism of the inhibition of AG18051 of the rHADH/ABAD enzyme drawn from the crystal structure of HADH II /ABAD-NAD⁺ complex with 3-ketobutyrate. Figures adapted from Ref. (73)

Several compounds were successfully synthesized and their capacity as micromolar inhibitors of the A β -ABAD interaction was tested, figure 17. The micromolar inhibitors demonstrated promising IC₅₀ values and octanol-water partition coefficients the latter is an indicative of their likelihood to cross the BBB.

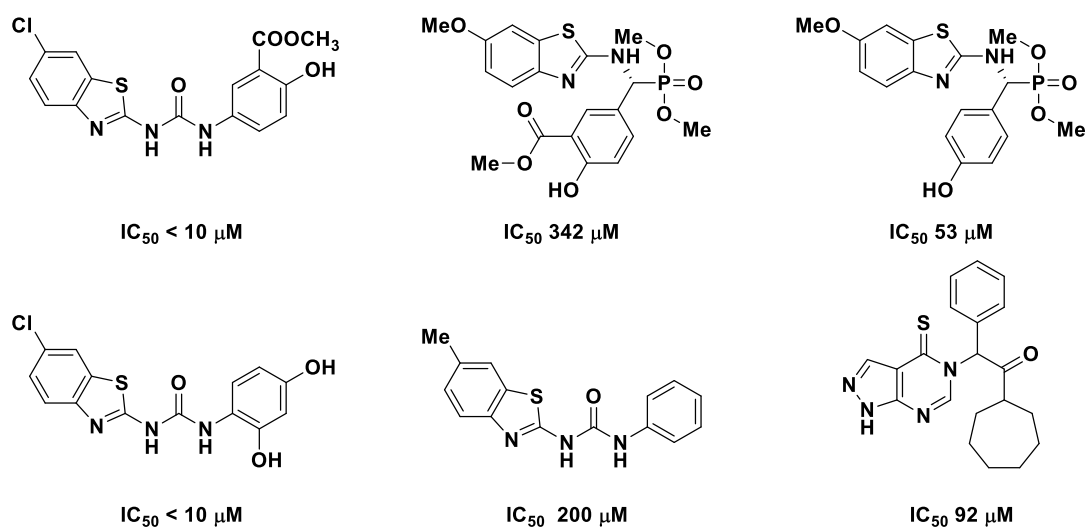


Figure 17: Structure of the compounds whose capacity as micromolar inhibitors of A β -ABAD interaction was tested in *in vitro* experiments. The inhibitors showed promising IC₅₀ values. (175)

It is important to note that ABAD is of a vital importance to mitochondrial activity for the reasons discussed earlier. Therefore, optimizing inhibitors design is still currently work under progress as the aim is to attenuate the over-expressed levels of ABAD not to completely inhibit it.

2 Project Aims

2.1 Hypothesis to be tested

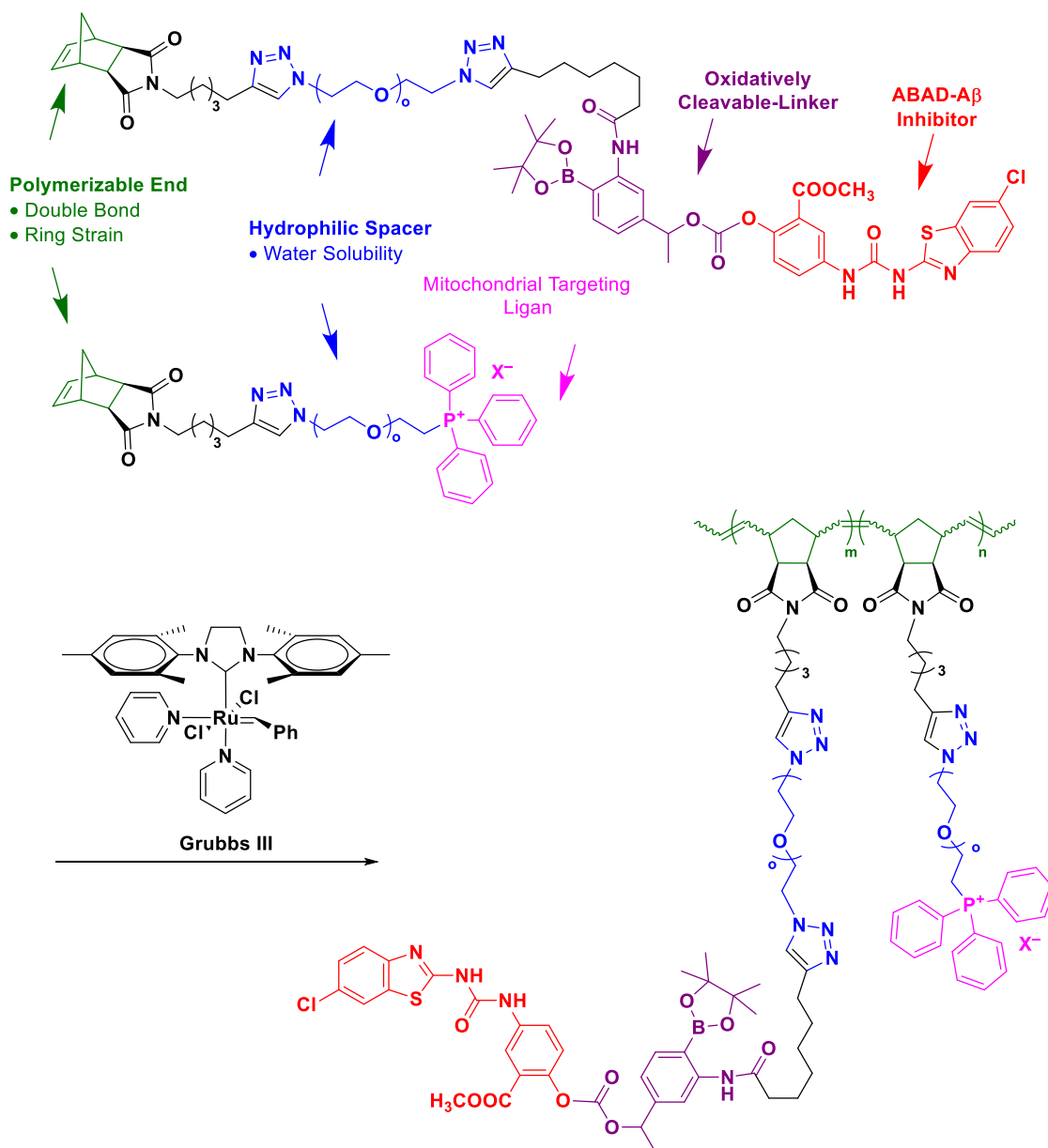
The brain relies on both the glucose and fatty acid metabolism pathways, taking place in the mitochondria, for energy production, figure 13. (74) We speculated that if ABAD's activity was reduced and, therefore, A β -ABAD interaction is suppressed, this will protect against ROS over-production associated with A β -ABAD interaction and ultimately boost energy production through glucose metabolism pathway. We reasoned that designing a mitochondrial targeting, delivery and stimulated release mechanism of A β -ABAD interaction inhibitors will to improve the latter's potency and help in achieving the aforementioned ultimate goal.

For this purpose, we aimed to prepare nanoscopic polymeric brush architectures (NPBA) via ROMP that can be used for mitochondrial delivery of ABAD inhibitors. The monomers used for the preparation of the NPBA design via ROMP feature a polymerizable end, a hydrophilic linker and a mitochondrial targeting ligand. The choice of each structural element of NPBA design is discussed in detail in the corresponding sections.

Briefly, the **polymerizable end**, *cis*-5-Norbornene-*exo*-2,3-dicarboximide, feature a strained olefinic group that drives the polymerization equilibrium towards polymer synthesis, scheme 5. *cis*-5-Norbornene-*exo*-2,3-dicarboximide derivative can be accessed from *cis*-5-Norbornene-*exo*-2,3-dicarboxylic anhydride and 6-amino hexanol both of which is commercially available. *cis*-5-Norbornene-*exo*-2,3-dicarboximide derivative can be prepared in 80-85% yields and easily separable by conventional column chromatography techniques. Costs associated with the use of *cis*-5-norbornene-*exo*-2,3-dicarboxylic anhydride as a precursor were considered. An attempt to prepare it in house was made via Diels-Alder reaction of cyclopentadiene and maleic anhydride. However, *cis*-5-norbornene-*endo*-2,3-dicarboxylic anhydride was the most consistently obtained Diels-Alder product. *cis*-5-norbornene-*endo*-2,3-dicarboxylic derivatives are less favorable precursor compared to their *cis*-5-norbornene-*exo*-2,3-dicarboxylic analogues as they tend to polymerize slower and produce polymeric products with broad dispersity indices. (75)

As for the **hydrophilic linker**, scheme 5, a range of hydrophilic polymers are commercially available such as chitosan, polyethylene glycol and poly(N-(2-hydroxypropyl)methacrylamide). Because polyethylene glycol has only two terminal functional groups, we envisioned that its functionalization is practically more precise to accomplish and monitor. Additionally, ethylene glycol oligomers and polymers of various lengths are commercially available. More importantly, ethylene glycol oligomers can be prepared in house in good yields and oligomeric purity via oligomerization of tetraethylene glycol.

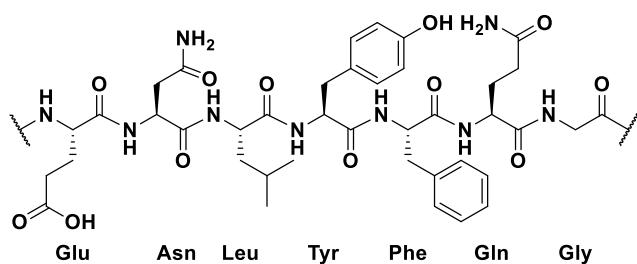
For **mitochondrial targeting**, we chose triphenylphosphonium iodide, scheme 5, as the targeting ligand exploiting the mitochondrial inner negative potential to stimulate mitochondrial up-take. Triphenylphosphonium iodide was chosen as the mitochondrial targeting ligand due to its economic and synthetic accessibility relative to mitochondrial targeting peptides and rhodamine chloride derivatives. (76) (77)



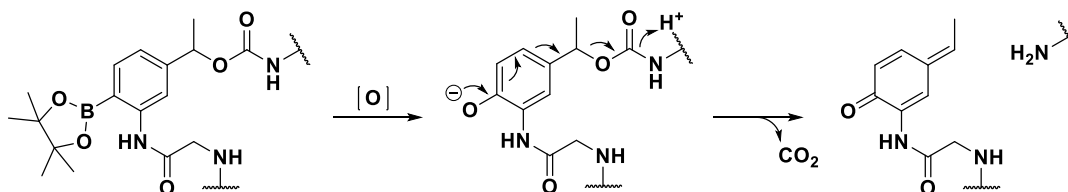
Scheme 5: Illustration of project goals which is the synthesis of polymeric brush-like nanoparticles that can be used for the mitochondrial delivery of ABAD-inhibitors. The monomers used for the preparation of the brush nanoparticles feature a polymerizable end, hydrophilic linker and a mitochondrial targeting ligand. The design features an oxidatively-cleavable linker which presents a promising approach for a stimulated drug release mechanism that exploits the elevated levels of ROS found in the mitochondria of AD affected neurons.

To stimulate the A β -ABAD interaction inhibitor's spatial and temporal release, a cleavable linker needs to be incorporated. The suitable **cleavable linker** needs to be stable in biological media prior to the event that leads to the cleavage event. Additionally, the linker needs to be biocompatible and needs to generate biocompatible metabolites after the cleavage event. Finally, the cleavable linker needs to be economically and synthetically accessible. An array of linkers can be considered to serve this purpose. Cleavable linkers can be responsive to endogenous or exogenous stimuli. (78) Endogenous stimuli range from enzymatic hydrolysis, oxidation to reduction, scheme 6. (78) Exogenous stimulation can be achieved by irradiation with light, scheme 6. (78) To this point of the project, the identity of the cleavable linker is yet to be determined, however, drawn from the literature's general observations, we speculated that **enzymatically-degradable linkers** are chemo-selective, yet, are synthetically laborious. **Oxidatively-cleavable linkers** are a promising choice due to the elevated levels of ROS in AD affected cells making them a distinguishably oxidizing environment. More information regarding their stability under physiological conditions and in the presence of nucleophiles and enzymes needs to be obtained. **Reductively-cleavable linkers** employing di-sulfide bonds may undergo a premature cleavage prior to their arrival to the mitochondria as di-sulfide reducing enzymes, such as glutathione, are synthesized into the cytosol and imported to several subcellular compartments such as mitochondria and endoplasmic reticulum. (79) **Photo-degradable linkers**, in particular ortho-nitrobenzyl derivatives, are the most heavily exploited for stimulated drug release in *in vitro* experiments as they are stable against enzymatic and nucleophilic conditions. (78) However, due to their short absorption wavelengths which lie near the UV range of the spectrum, 300-365 nm, they raise phototoxicity concerns and deep tissue penetration limitations. (80) (81)

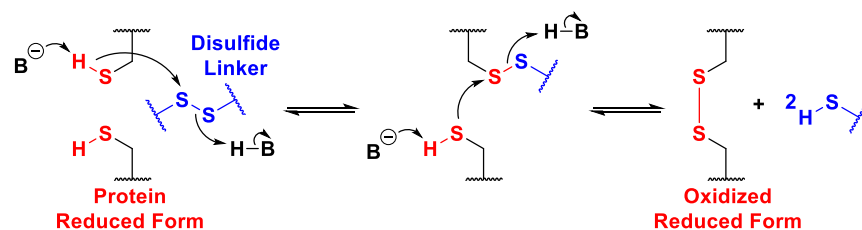
Enzymatically-Cleavable Linkers



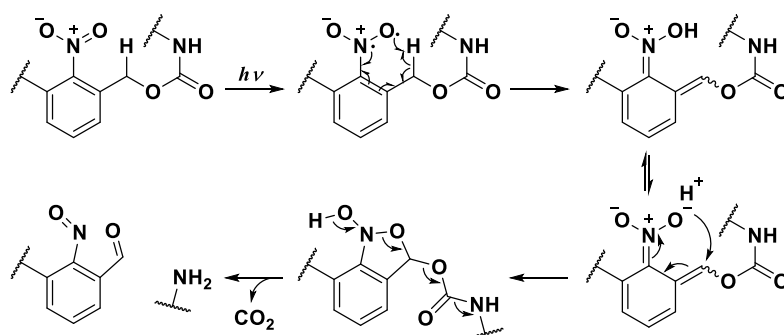
Oxidatively-Cleavable Linkers



Reductively-Cleavable Linkers



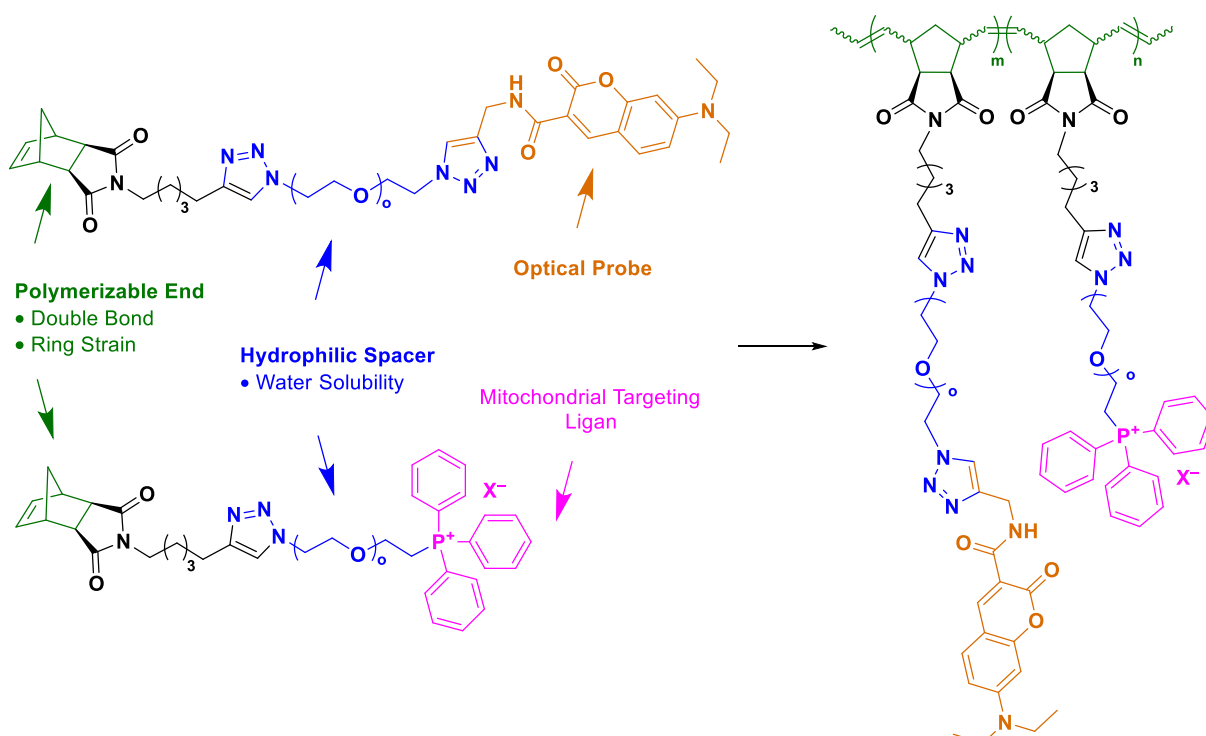
Light-Cleavable Linkers



Scheme 6: Literature examples of endogenously and exogenously stimulated cleavable linkers and the mechanism of their cleavage. Endogenous stimulation is achieved upon exposure to degradable enzymes, reactive oxygen species or reductive enzymes. Exogenous stimulation can occur upon irradiation with light.

2.2 Preliminary Design's Monomer Components

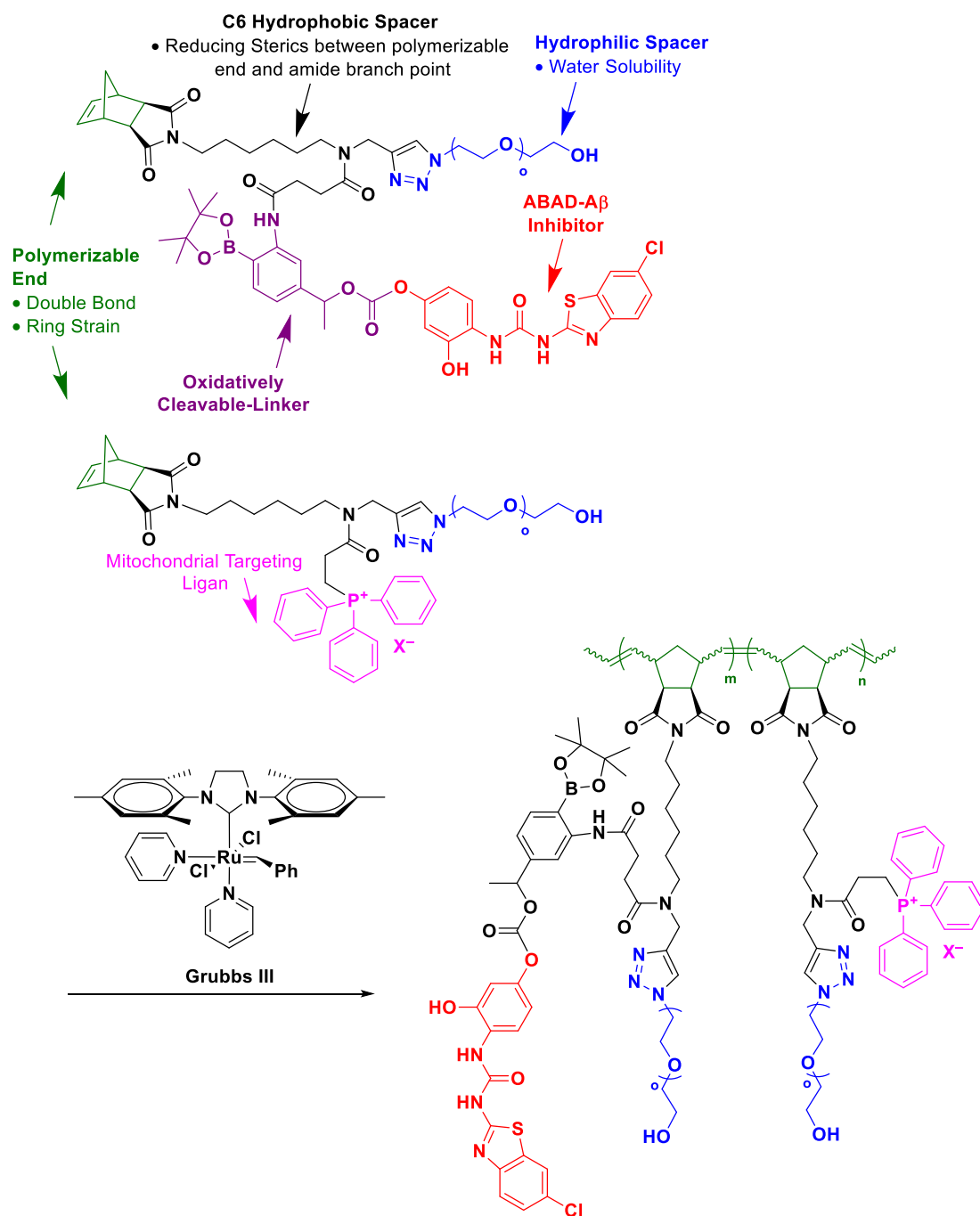
Before attempts to deliver ABAD inhibitors to the mitochondria via NPBAs are made, we needed to establish the conditions for optimal mitochondrial localization of NPBAs. For this purpose, we aimed to prepare fluorescent NPBAs via ROMP that can be used for mitochondrial targeting, scheme 7. The monomers used for the preparation of the NPBAs design via ROMP feature the same structural elements mentioned earlier, the polymerizable end, the hydrophilic linker and a mitochondrial targeting ligand, with the added fluorescent tag to visualize the mitochondrial accumulation of the NPBAs in in vitro experiments using fluorescence microscopy.



Scheme 7: Illustration of preliminary design of NPBAs that will be used to establish mitochondrial localization optimal conditions. The monomers used for the preparation of the brush architectures feature a polymerizable end, hydrophilic linker, a mitochondrial targeting ligand and a fluorescent tag.

It is important to mention that, because this project is at its early stages, the pharmacokinetic and dynamic aspects of ABAD-A β interaction inhibitors' delivery is not yet under investigation. We aspire to drive our research in this area towards *in vivo* experiments where the pharmacokinetic and dynamic profiles of ABAD-A β interaction inhibitors' delivery via NPBAs can be studied. *In vivo* experiments will help us understand how exposed the mitochondrial targeting and ABAD-A β interaction inhibitor entities need to be to access systems with a balanced pharmacokinetic and dynamic profiles. The structure of the NPBAs can be tailored by incorporating the mitochondrial targeting and ABAD-A β interaction inhibitor entities at the core of ROMP monomers as oppose to their terminus. Elongating the hydrophilic spacer will additionally aid in shielding the mitochondrial targeting and ABAD-A β

interaction inhibitor entities to enhance the pharmacokinetic and potentially the effectiveness of NPBAs as drug delivery vectors.



Scheme 8: Illustration of core-functionalized NPBAs that can be used for the mitochondrial-targeted delivery of ABAD-inhibitors. The monomers used for the preparation of the brush architectures feature a tertiary amine that constitute a branching point that links the side chain, the cleavable ABAD-A β interaction inhibitor or mitochondrial targeting ligand, to the rest of the monomer molecule. The C6-hydrophobic spacer reduces the steric between the side chain and the polymerizable group allowing ROMP to proceed smoothly to obtain narrowly-dispersed NPBAs.

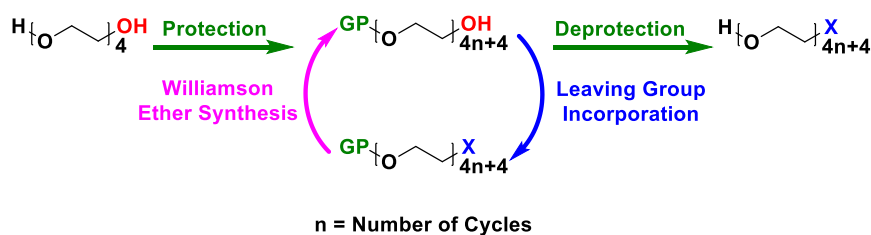
3 Synthesis of Heterotelechelic Oligoethylene Glycol Chains

To design pegylated NPs that can serve multiple purposes, i.e., cellular or subcellular targeting, drug delivery and imaging, heterotelechelic ethylene glycol oligomers are needed. Heterotelechelic oligoethylene glycol, OEG, chains oligomers with asymmetrically derivatized end groups that can enable the oligomer chain to undergo further transformations. (34) Heterotelechelic oligomers are of greater synthetic utility than their symmetric analogues because they provide the opportunity for the selective and specific transformation of their terminal functional groups. (34) In this chapter, we describe the synthesis of asymmetric OEG chains of different lengths which was adapted from a literature procedure. (82) The synthetic method is reproducible, scalable and chromatography-free.

3.1 Results and Discussion

Asymmetrically activated PEG oligomers with narrow molecular weight distribution, \mathcal{D} , which are ideally close to one for synthetic oligomers, and number average molecular weights, M_n , from 500 Da and above are commercially available but with high costs. (34) Asymmetric activation of unmodified OEG by mono-derivatization have proved to be quite challenging as the outcome of such transformation is a mixture of mono-, unmodified and di-substituted OEG chains that were chromatographically inseparable.

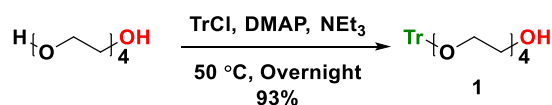
As the need for multigram quantities of monodisperse and heterobifunctional derivatives of OEG had emerged, we were prompted to explore the tetraethylene glycol oligomerization protocol developed by Wawro. *et.al.* (82) The general scheme of this synthesis begins with mono-protection of TEG, the longest oligomer of ethylene glycol commercially available at a reasonably high purity and low price. (82) This was followed by iterative functionalization with a leaving group and Williamson ether synthesis which were repeated until the desired chain length was obtained. (82) Functionalization with a leaving group followed by deprotection constituted the final steps towards asymmetric oligomers with two derivatizable ends one of which is significantly more reactive than the other. (82)



Scheme 9: General oligomerization protocol of TEG. The protocol begins with mono-protection followed by conversion of hydroxyl group into a leaving group. The product is oligomerized by iterative ether synthesis and functionalization with a leaving group. This cycle is repeated until desired OEG chain length is achieved. functionalization with a leaving group followed by deprotection constitute the final steps towards the desired oligomer. Scheme adapted from Ref. (82)

3.1.1 Mono-Protection

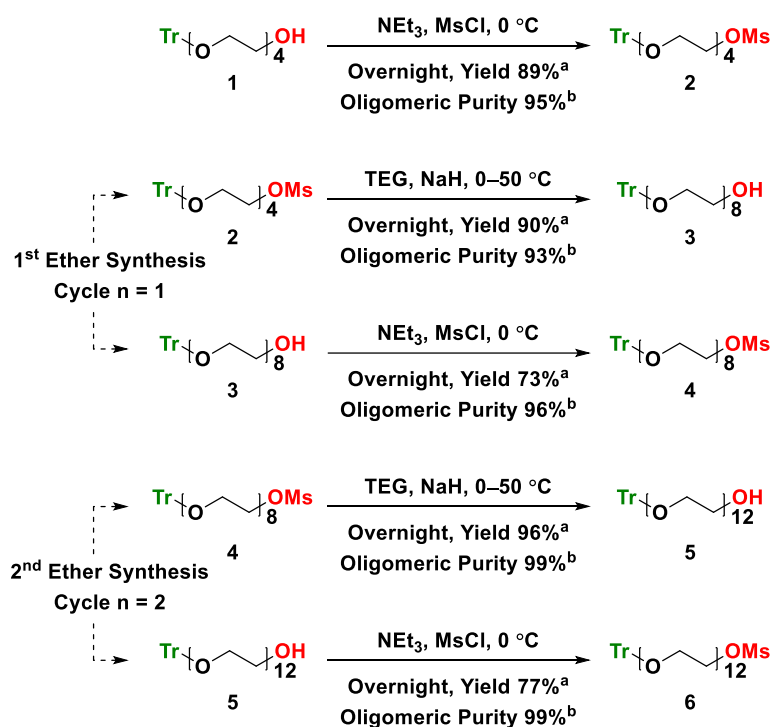
The mono-protection serves two purposes. It enables the asymmetric derivatization of TEG and promotes the chromatography-free isolation of the resulting product by liquid-liquid extraction. The pronounced hydrophobic properties in combination with the ease of its deprotection for which mild acidic conditions are required, trityl group was chosen as the protecting group. Mono-protection with trityl group was achieved by using an excess of TEG which was easily removed by aqueous wash and back extraction of $\text{Tr}(\text{EO})_4\text{H}$ with Et_2O .



Scheme 10: Mono-protection of TEG with a trityl-group mediated by NEt_3 and DMAP.

3.1.2 Williamson Ether Synthesis

The Williamson ether synthesis elongates the hydrophilic chain length of the oligomer. To achieve this, a leaving group needs to be introduced into the oligomer's structure. The incorporation of a leaving group serves additional goals, scheme 11. Not only it promotes the synthesis of ethereal linkages, but also aids in the liquid-liquid extraction of the product by increasing its solubility in organic solvents. Additionally, it serves as a derivatizable end expanding the utility of the asymmetric oligomer. As for the choice of the leaving group, tosyl and mesyl groups were both investigated. Tosylation by treatment with TsCl in the presence of NaOH in a biphasic system of THF and water triggered ethereal bond cleavage to afford a mixture of ethylene oxide oligomers which were inseparable by normal or reversed phase chromatography. In contrast, mesylation mediated by NEt_3 was well-tolerated delivering the desired mesylated product. The mesylation was carried out at 0°C until all oligomeric starting material was consumed and excess MsCl was removed by vacuum distillation.



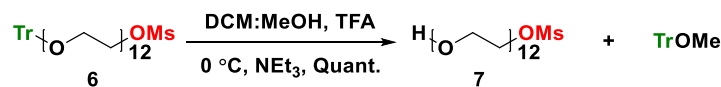
Scheme 11: The Williamson ether synthesis, using NaH, and mesylation, in the presence of NEt_3 , steps exploited for the oligomerization of TEG. The cycle is repeated until the desired chain length is obtained. ^a Isolate yield. ^b Oligomeric purity estimated by MALDI.

With regards to the Williamson ether synthesis step itself, TEG was used in excess to suppress the formation of double ether synthesis products, $\text{Tr}(\text{EO})_{8n+8}\text{Tr}$. Excess TEG can be removed by aqueous work up and the oligomerization products can be isolated via liquid-liquid extraction using organic solvents. Complete removal of TEG is crucial as its presence in the subsequent mesylation step yields mono- and di-mesylated TEG by-products which are difficult to remove by liquid-liquid extraction or chromatographic purification. EtOAc is more efficient as extraction solvent, however, it is of great importance for any traces of EtOAc to be removed before any Williamson ether synthesis is carried out as its presence results in the formation of the acetate-protected derivatives, $\text{Tr}(\text{EO})_{4n+4}\text{C}(\text{O})$ where n is the number of Williamson ethery synthesis cycles. This by-product is inseparable from oligomerization product by normal or reversed phase chromatography.

3.1.3 Deprotection

The deprotection of trityl group can be achieved by treatment with a Lewis acid such as InBr_3 or a Bronsted acid such as TFA in the presence of MeOH as a triphenyl methyl cation scavenger, scheme 12. Trifluoroacetic acid deprotection yields $(\text{EO})_{4n+4}\text{Ms}$ contaminated with TFA-protected $(\text{EO})_{4n+4}\text{Ms}$ which can be observed by NMR and mass spectrometry. Treatment with NEt_3 in the presence of MeOH deprotects the trifluoroacetate group and liberates the desired $(\text{EO})_{4n+4}\text{Ms}$

oligomers. The deprotection by-product, methoxytriphenylmethane, can be removed by the repetitive washing of the crude oil with hexane.



Scheme 12: Deprotection of trityl group by treatment of TFA in the presence of MeOH as a triphenyl methyl cation scavenger.

3.1.4 Purification

Generation of PEG-based side products is inevitable; however, it can be minimized. Thus, general precautionary measures need to be taken before attempting to oligomerize TEG via the route mentioned above. Distillation of MsCl to remove any HCl generated due to its hydrolysis upon storage is advisable to prevent premature deprotection of trityl group. The fragility of oligomer ethylene oxide chain increases with increasing lengths. Therefore, the temperature during Williamson synthesis needs to be maintained at 50 °C to minimize production of elimination products.

The products of every step were subjected to purification with activated charcoal. Attempts to purify the oligomers by normal phase chromatography resulted in spontaneous trityl-group deprotection triggered by the acidity of the silica gel and the presence of MeOH as a co-eluting solvent. Flash chromatography employing reversed phase silica resulted in poor separation of the desired product from any PEG-based contaminants. Thus, the most reproducible and practical method of purification of PEG-based oligomers available to date is liquid-liquid extraction.

3.1.5 Molecular Weight Distribution Analysis

Narrow molecular weight distribution of the oligomeric hydrophilic chains ensures the reproducibility of any synthetic procedures that follow as well as the reproducibility of any biological studied carried out using the final polymeric architectures. The monodispersity analysis aids in the optimization of the oligomerization process and helps in the accurate determination of the yield and purity of oligomers. We attempted to determine the oligomeric purity of each sample using UV-VIS-coupled HPLC chromatography fitted with a reverse-phase octadecyl- or phenyl-hexyl-modified silica column. We used a gradient flow of 0.1% TFA:MeOH or 0.1% TFA:MeCN as the elution solvent at 40 °C to reduce back pressure. Unfortunately, this technique suffered from poor separation of the oligomer from elimination by-products, $\text{Tr}(\text{EO})_{4n+3}\text{H}$ where n is the number of Williamson ethery synthesis cycles, under the employed conditions.

Mass-spectrometry, MS, based techniques provide information about molecular weight of sample components. (82) However, they suffer from absolute quantification inaccuracies due to competitive ionization events of sample components. (82) Thus, MS-based methods can only provide relative quantification of sample components. (82) Electrospray and matrix-assisted laser desorption ionization modes, ESI and MALDI respectively, were both explored. MALDI was more useful as less sample associated peaks were generated due to the absence of a multiply-ionized products making spectra less complicated to analyze. The estimated oligomeric purity is reported for each oligomer in the experimental section.

3.1.6 Summary

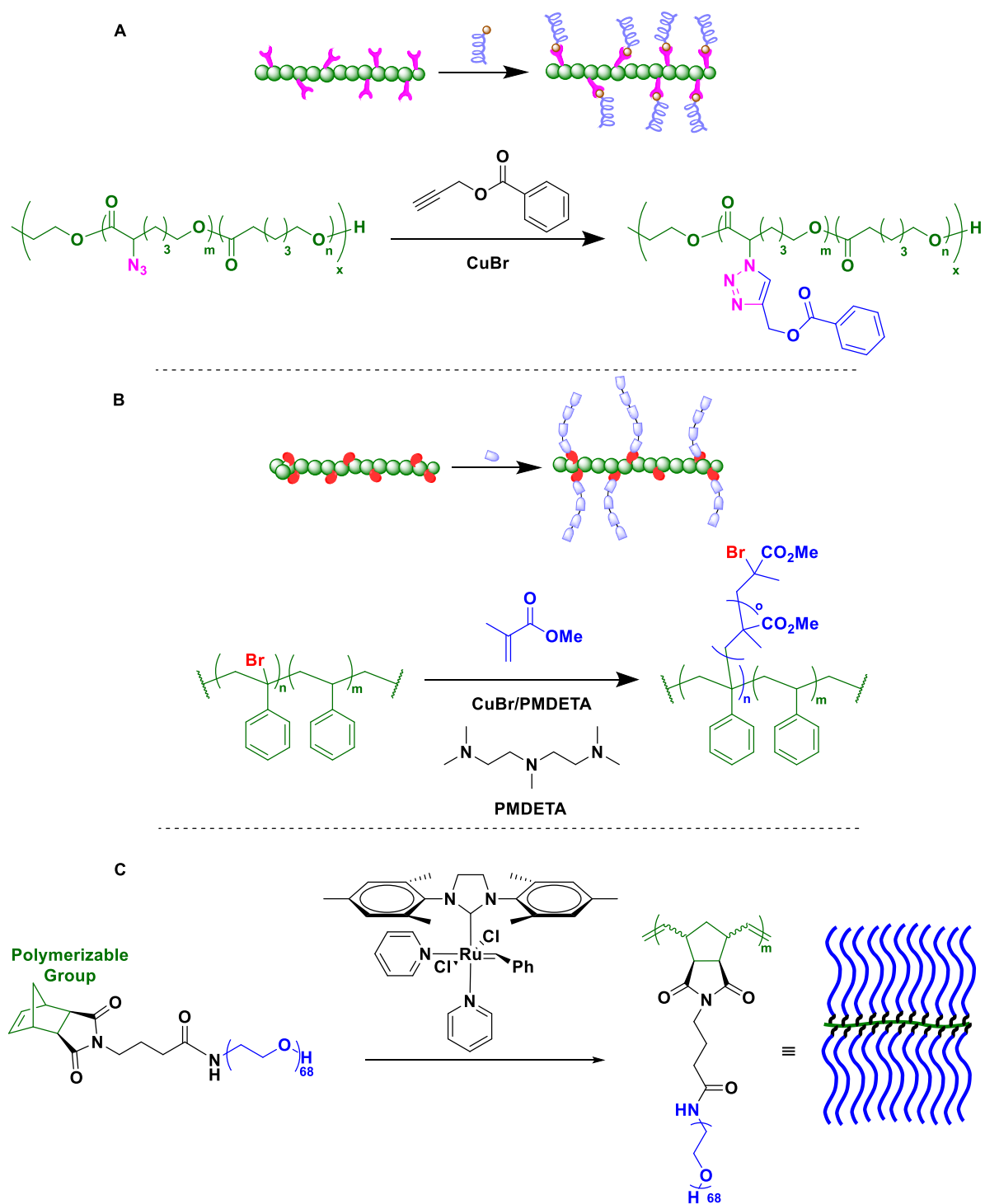
Ethylene glycol oligomers were prepared by iterative oligomerization of the commercially tetraethylene glycol according to a literature procedure. (82) The procedure proved to be reproducible, scalable and generated the desired oligomer at an estimated oligomeric purity more than 95%. Due to competitive cationization between components of the scrutinized sample, some mass spectrometry signals and others may be augmented. Therefore, mass spectrometry is more reliable and accurate when coupled to an orthogonal characterization technique. More effort needs to be dedicated towards optimization chromatographic separation conditions employed by high resolution chromatographic techniques. This includes elution solvent systems, column chromatography packing material and detection method. Some suggestions in regards of elution solvent system would be to use a gradient of water:MeOH or water:MeCN solvent system with addition of 1-5 M ammonium acetate to reduce complexation of oligomers and therefore enhance separation of oligomers.

4 Ring Opening Metathesis Polymerization: Route to Homo- & Co-polymers

In this section, the synthesis and characterization of first-generation ROMP monomers is described. The experimental outcome, presented in this section, gave rise to a monomer design that is synthetically accessible on a multigram scale. The monomer's design, which features a polymerizable group, hydrophilic spacer and optical probe or mitochondrial targeting ligand, can be amended to access monomers of different hydrophilic spacers' lengths. The monomers were subjected to homo-ROMP to establish the conditions under which ROMP is living and examine their propensity for block-polymerization. All monomers can undergo block ROMP generating homo-polymers, henceforward referred to as first-generation homo-polymers, with moderate to satisfactory molecular weight distribution. The synthesis and characterization of these homo-polymers is described. The first-generation homo-polymers were unable to overcome the first biological barrier in drug delivery that is water solubility. Consequently, co-polymerization of the monomers and investigation of their biocompatibility as well as their mitochondrial targeting capacity was not attempted.

4.1 Introduction

Graft polymers are a family of polymeric architecture, to which bottle-brush polymers belong (7). They consist of a linear polymeric backbone to which side polymeric chains are tethered. (83) Graft polymers can be prepared by one of three methods; graft onto, graft from or graft through methods. (84) (7) (83) In graft onto methods, a polymer chain with multiple functional groups is coupled to several linear polymer chains of a different composition and a terminal functional group using a suitable coupling reaction. (84) In grafting from methods, the side chains are grown from initiation sites distributed on the polymeric linear backbone. (83) In comparison, grafting through is achieved when a macromonomer, with a polymerizable functional group, is polymerized using an initiator. (7) Examples of the three approaches to graft polymer synthesis are shown in scheme 13.



Scheme 13: illustration of grafting onto (A), grafting from (B) and grafting through (C) methods used in the synthesis of graft polymers. (A) Functionalization of azide-functionalized Poly(ϵ -caprolactone) with propargyl benzoate via Cu-catalyzed 1,3-dipolar cycloaddition. (B) Grafting of poly-methacrylate pendant arms from initiation sites present in the structure of polystyrene using atom transfer radical polymerization technique. The tertiary bromide groups act as the initiation site in the polymerization process catalyzed by CuBr/PMDETA system. (C) Polyethylene glycol macromonomers can be polymerized into graft nanoparticles using Grubbs III initiator via ring opening metathesis polymerization. Schemes adapted from Ref. (84), (83) and (27) respectively.

Ring opening metathesis polymerization, ROMP, initiated by Grubbs third generation ruthenium-benzylidene catalyst has gained a wide popularity in the synthesis of graft-through nanoscopic brush architectures. (27) (7) ROMP mediated by Grubbs III has been regarded as a powerful tool for the synthesis of polymeric architectures, figure 18, with a good control over number average molecular weight, M_n , and molecular weight distribution, D . (85) (86)

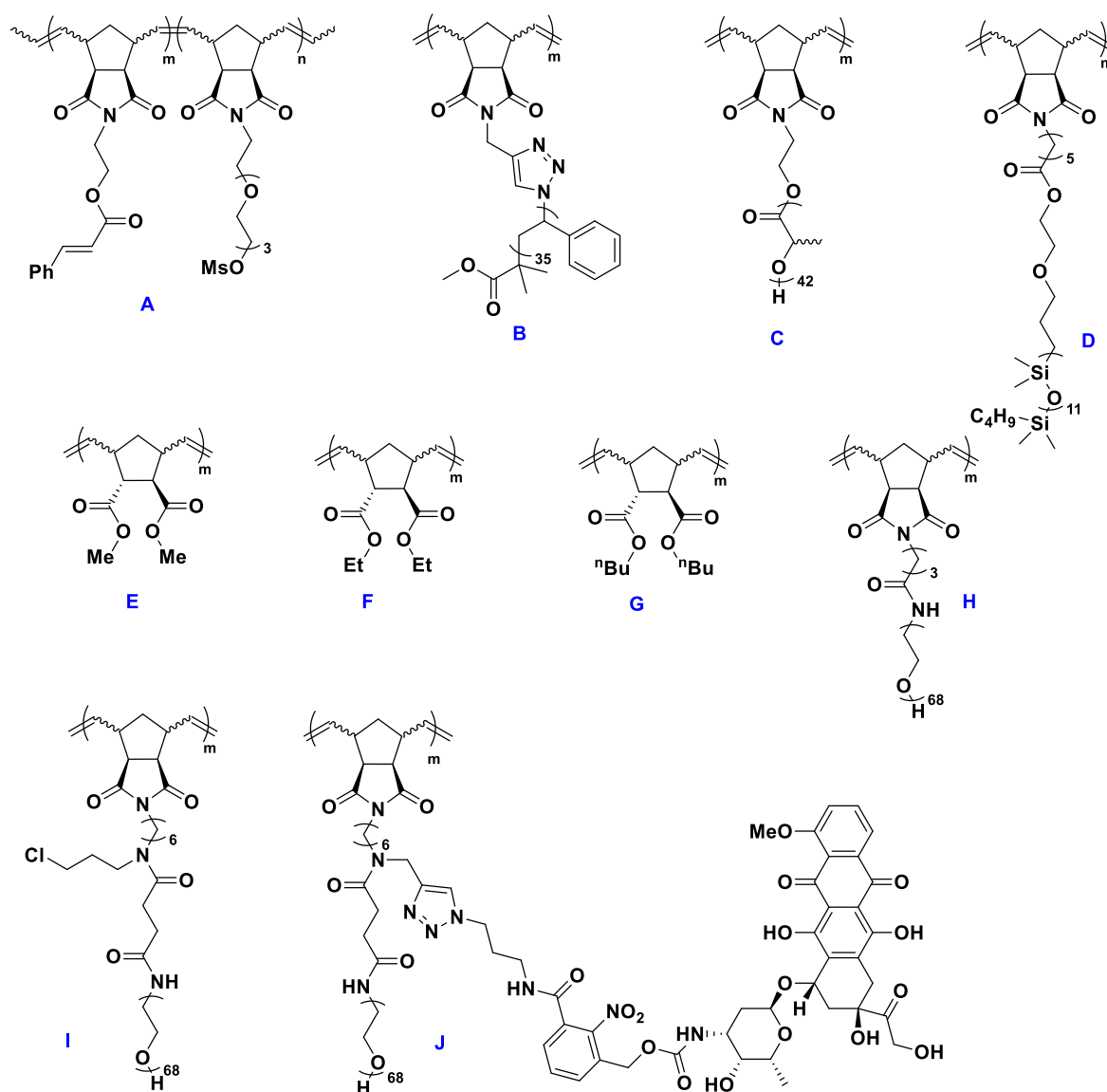


Figure 18: Structure of graft polymers synthesized via the graft-through approach using ring-opening metathesis polymerization initiated by Grubbs III catalyst. The close match between the theoretical and observed M_n and the D values ideally ranging 1.0-1.2, listed in table 1, is a testament to the good control of GIII-mediated ROMP over the polymerization process. Figures taken from Refs. (87) (91) (92) (93) (27)

Good control over M_n and \mathcal{D} is marked by the close match between the predictable and observed M_n and \mathcal{D} values ideally ranging 1.0-1.2 as shown in table 1. (85) The mild conditions under which the polymerization operates (27) (7), short reaction times (87) along with the compatibility with an array of functional groups have allowed ROMP to find many applications in biomedical sciences (88), hybrid organic-inorganic material framework (89), bio-imaging (90) and many more fields.

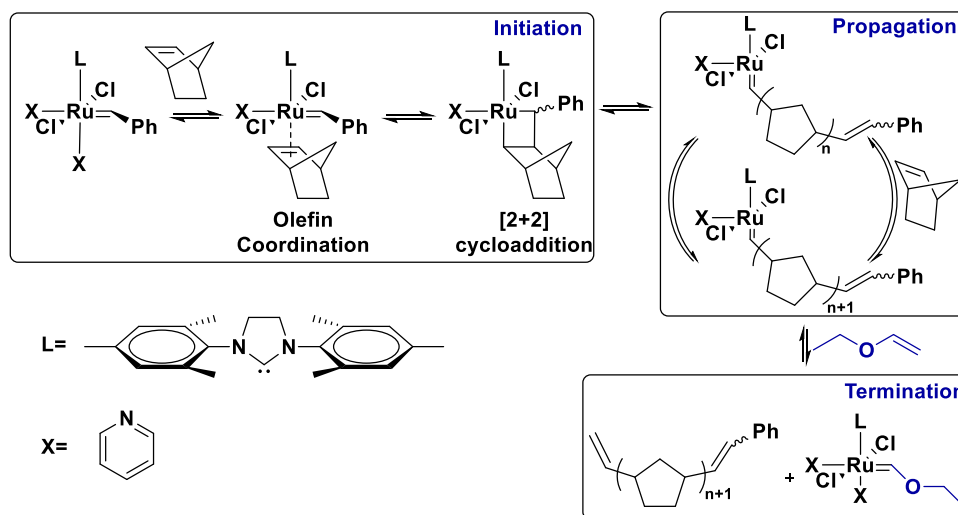
<i>polymer</i>	<i>m</i>	<i>n</i>	M_n (Theo.)	M_n (Obs.)	\mathcal{D}	Ref.
<i>A</i>	50	150	140400	133200	1.01	(87)
<i>B</i>	100	-	399000	375000	1.06	(91)
<i>C</i>	100	-	323000	319000	1.01	
<i>D</i>	100	-	128000	131000	1.02	
<i>E</i>	100	-	21000	21700	1.02	
<i>F</i>	100	-	23800	24200	1.02	
<i>G</i>	100	-	29400	29600	1.02	
<i>H</i>	10	-	32500	33200	1.07	(92) (93)
<i>I</i>	10	-	33000	34100	1.11	(7)
<i>I</i>	70	-	231000	238000	1.14	
<i>I</i>	100	-	330000	343000	1.06	
<i>J</i>	10	-	41121	33700	1.07	(27)
<i>J</i>	100	-	411210	352000	1.04	

Table 1: Theoretical and observed values of M_n and corresponding \mathcal{D} values of the structures in figure 18 as determined by GPC. The close match between the theoretical and observed M_n and the \mathcal{D} values ideally ranging 1.0-1.2 is a testament to the good control of GIII-mediated ROMP over the polymerization process. M_n and the \mathcal{D} values were determined using GPC coupled to a MALLS and RID detectors without the use of calibration curves.

4.1.1 Mechanism of Ring-Opening Metathesis Polymerization

The mechanism of ROMP proceeds with initiation of the pre-catalyst via coordination with a monomer generating a metallacyclobutane intermediate in a [2+2] cycloaddition step, scheme 14. (85) (86) The resulting metallacyclobutane undergoes cycloreversion to give the new initiation carbene complex. (85) (86) This new carbene complex enters a propagation cycle during which the rest of the monomer

molecules are consecutively inserted, via iterative [2+2] cycloaddition and reversion steps. (85) (86) After complete consumption of monomer, the propagation can be deliberately terminated by addition of a terminating reagent such as ethyl vinyl ether. (85) (86) The terminating reagent undergoes a [2+2] cycloaddition and reversion cleaving the polymer chain off and liberating the catalyst in its metathesis less active form, [Ru]=CHOR. (85) (86) (94)

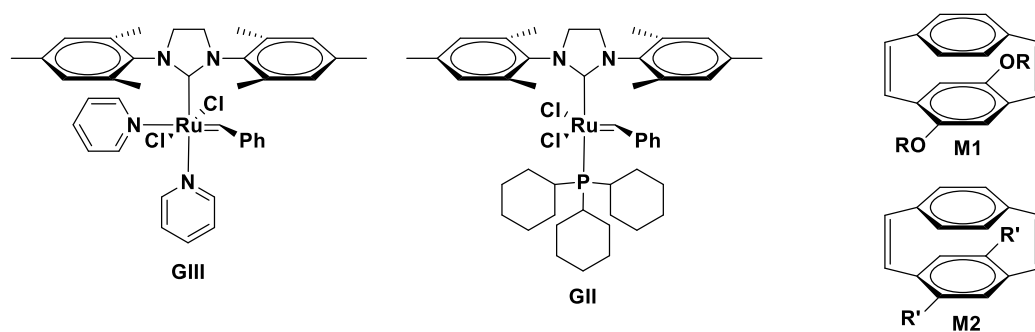


Scheme 14: Illustration of the mechanism of ROMP showing the three stages of the polymerization process including initiation via [2+2] cycloaddition and reversion, propagation and termination reactions. Figure adapted from Ref. (85)

The control of ROMP mediated by third generation Grubbs catalyst over M_n and D of the resulting polymeric architectures is attributed to the catalyst's fast initiation kinetics. (95) (96) (97) (98) The fast initiation kinetics result in an increase in the ratio of rate constant of initiation to rate constant of propagation designated by k_i/k_p , scheme 15. (99) (100) (101) This phenomenon offers fast and quantitative activation of initiator molecules and simultaneous, thus, uniform growth of propagating polymer chains. (102) (99) This attribute can suppress spontaneous termination via intramolecular "backbiting" or intermolecular "chain transfer" cross metathesis reactions that may happen during the propagation step when initiation kinetics are slow. (85) (100) Intramolecular cross-metathesis, known as backbiting, occurs when the carbene reacts with a backbone olefin in the same propagating chain generating a new propagating chain and macrocyclic structures, scheme 15. (85) (86) (103) In contrast, intermolecular cross metathesis, known as chain transfer, occurs when the carbene reacts with a backbone olefin in another propagating chain generating a dinuclear propagating chain and a linear polymer chain of higher molecular weight than predicted, scheme 15. (86) Polymerization with suppressed undesired termination cascades, intra- or intermolecular, is described as a living polymerization. (85) (86) (100) The characteristics of a living polymerization are; first order kinetics with respect to monomer consumption, narrow molecular weight distribution marked by polydispersity values, D , ideally ranging 1.0-1.2 and predictable number average molecular weights, M_n , and degree

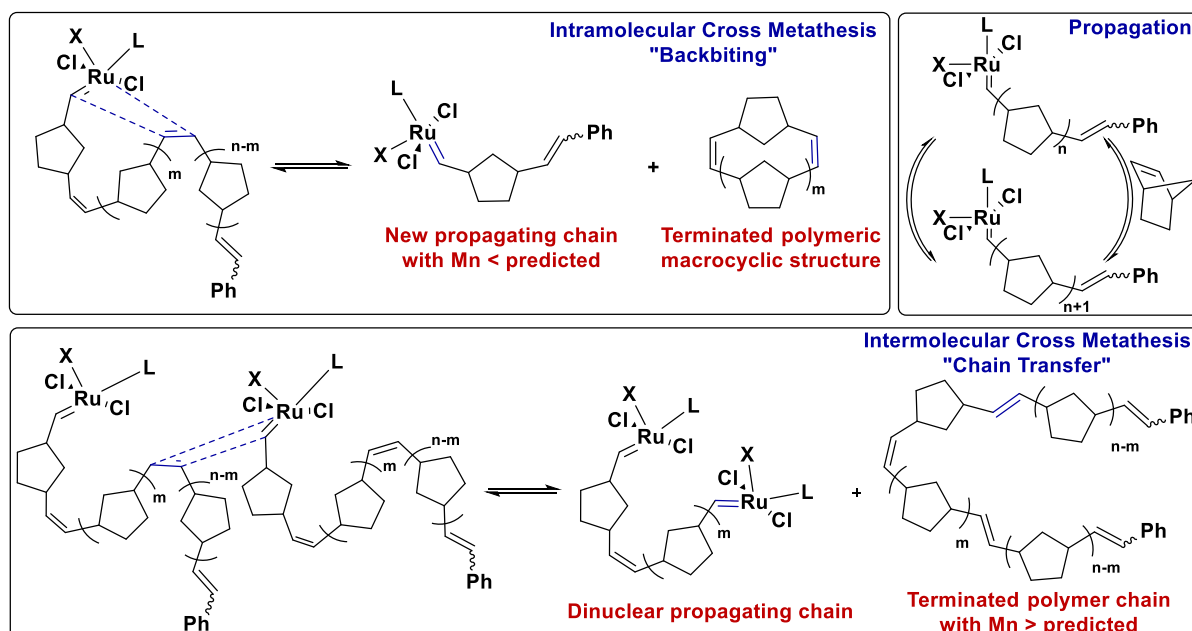
of polymerization, DP , which are linearly dependent on monomer to initiator ratio. (85) (86) (100) To ensure that polymerization is operating under living conditions, the monomer structure needs to be carefully designed.

A



M	I	T(°C)	k_i (min ⁻¹)	k_p (min ⁻¹)	k_i/k_p	Mn(kg mol ⁻¹)	PDI
M1	G2	25	0.0043	0.0003542	12.14	4.46	1.58
M1	G3	25	0.0763	0.0013995	54.52	6.09	1.38
M2	G2	25	0.0079	0.0232353	0.34	7.38	1.77
M2	G3	25	0.0984	0.0061308	16.05	5.25	1.43

B



Scheme 15: (A) Structure of cyclophanedienes M1, R = 2-ethylhexyl, and M2, R' = n-octyl, and ruthenium carbene complexes; Grubbs II and Grubbs III. The figure depicts the effect of the initiation kinetics, and ultimately k_i/k_p ratio, of the catalyst on the livingness of the ROMP process as indicated by the \mathcal{D} values. Figure adapted from Ref. (99). (B) Illustration of the intramolecular “backbiting” intermolecular “chain transfer” cross-metathesis cascades that can result in pre-mature termination of the propagation step. This can generate polymeric products with unpredictable M_n and broad M_n distribution. Figure adapted from Ref. (85)

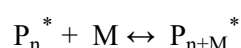
4.1.2 Monomer Design Rationale

In this section, the basic structural elements in monomer design that can promote ROMP under living conditions are reviewed. This includes elements that concern the polymerizable functional group, the

cyclic olefin, where ROMP effectively takes place and any decorative functional groups that can facilitate the modification of the resulting polymeric via orthogonal chemistries.

4.1.2.1 Ring Strain of Polymerizable Group

ROMP is a thermodynamically driven process (49) and, therefore, the thermodynamic equilibrium of the reversible propagation step can be set between three participants; monomer, reactant propagating chain and propagating chain after the addition of that monomer designated with M, P_n^* and P_{n+1}^* respectively where the asterisk symbolizes the active center. (104) (105) (106)



In an ideal case where all monomer is converted into polymer chain and therefore active species is the same (49) (104), the standard Gibbs energy of polymerization can be expressed as (104) (105) (106):

$$\Delta G_P^0 = \Delta H_P^0 - T\Delta S_P^0 = -RT \ln \frac{[P_{n+1}^*]}{[P_n^*][M]} \quad \text{equation 1}$$

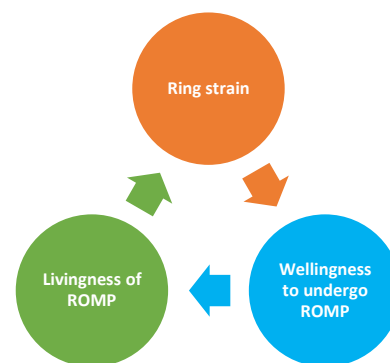
And rearranged into:

$$\Delta G_P^0 = \Delta H_P^0 - T\Delta S_P^0 = -RT \ln \frac{1}{[M]} \quad \text{equation 2}$$

$$\Delta G_P^0 = \Delta H_P^0 - T\Delta S_P^0 = RT \ln [M] \quad \text{equation 3}$$

Where ΔG_P^0 , ΔH_P^0 , ΔS_P^0 , and $[M]$ are the free energy, enthalpy and entropy terms and monomer concentration at standard-state conditions. (49) (104) (105) (106) As the polymerization occurs, the number of free monomers decreases. This results in a decrease in the entropic term $T\Delta S_P^0$ which can be compensated for by an increase in ΔG_P^0 . This, however, makes the polymerization less spontaneous and shifts the equilibrium back to the monomeric form. (105) So the equilibrium can continue to progress towards the polymeric form and the polymerization to be spontaneous, signified by a negative ΔG_P^0 , the decrease in the entropic term, $T\Delta S_P^0$, must be compensated for by a decrease in the enthalpic term. (49) (104) (105) (106) This, in the context of ROMP, is manifested by the release of strain energy that accompanies the polymerization process which has been established as its driving force. (49) Ring strain of cyclic olefins is defined as the difference in energy between products and reactants. (49)

The correlation between ring strain of cyclic olefins, their ability to overcome the ring/chain equilibrium and the livingness of the polymerization process has been studied. (49) It was shown that ROMP of cyclic olefins with the highest ring strain is the fastest to overcome the ring/chain equilibrium and the most living in nature, table 2. (49) (100) Both attributes were portrayed by highest substrate conversion, shortest reaction times and the narrowest \bar{D} values, table 2.



(49) (100)


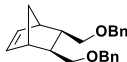

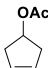
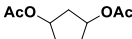
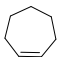
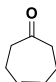
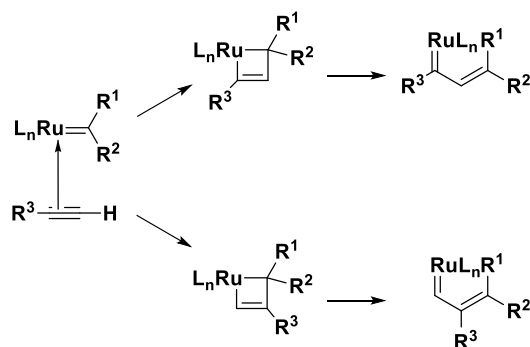
Monomer	Ring Strain kcal/mol	M/I	Yield. (%) ^c	Time hr	Mn (Theo.) ^l	Mn (Obs.) ^m	\bar{D}	Ref.
	27.2 ^a	200	93 ^d	0.5	18900	22000 ^m	1.10	(100) (107)
	N.A.	200	92 ^e	0.5	67000	60900 ^m	1.04	(100)
	6.84 ^a	500	41 ^f	24	34060	12200 ⁿ	1.5	(49)
			67 ^g			13300 ⁿ	1.3	(107)
	4.47 ^b	500	65 ^h	24	63078	28000 ⁿ	1.5	(49)
	2.29 ^b	250	0 ⁱ	0.5	46048	-	-	(49)
	6.7 ^a		84 ^j			35600 ⁿ	1.5	(49)
	6.84 ^b	250	88 ^g	24	24043	40500 ⁿ	1.6	(107)
	7.44 ^b	214	88 ^k	24	23573	66800 ⁿ	1.2	(49)

Table 2:^(a)Taken from Ref. (107). ^(b)Taken from Ref. (49). N.A. Not available. M/I designates the ratio of monomer to catalyst. ^(c)Isolated yield obtained by precipitation in MeOH. A solution of monomer (0.9 M) in CH₂Cl₂ was added to Grubbs III catalyst solution in CH₂Cl₂ (1.1 mM) at ^(d)-20 °C or room ^(e)temperature. A solution of Grubbs III catalyst in CH₂Cl₂ (0.05 M) was added to a solution of monomer in CH₂Cl₂ (^(f)3, ^(g)5, ^(h)8, ⁽ⁱ⁾6.1, ^(j)2 or ^(k)9.8 M) at room temperature. ^(l)Obtained by calculating the product of M/I and molecular weight of monomer and assuming quantitative conversion. ^(m)Determined using GPC; samples were run in CH₂Cl₂ and Mn were assigned relative to a standard curve calculated using polystyrene standards. ⁽ⁿ⁾Determined using GPC coupled to a MALLS and RID detectors; samples were run in THF and Mn were assigned without the use of calibration curves.

4.1.2.2 Functional Groups for Lateral Modifications

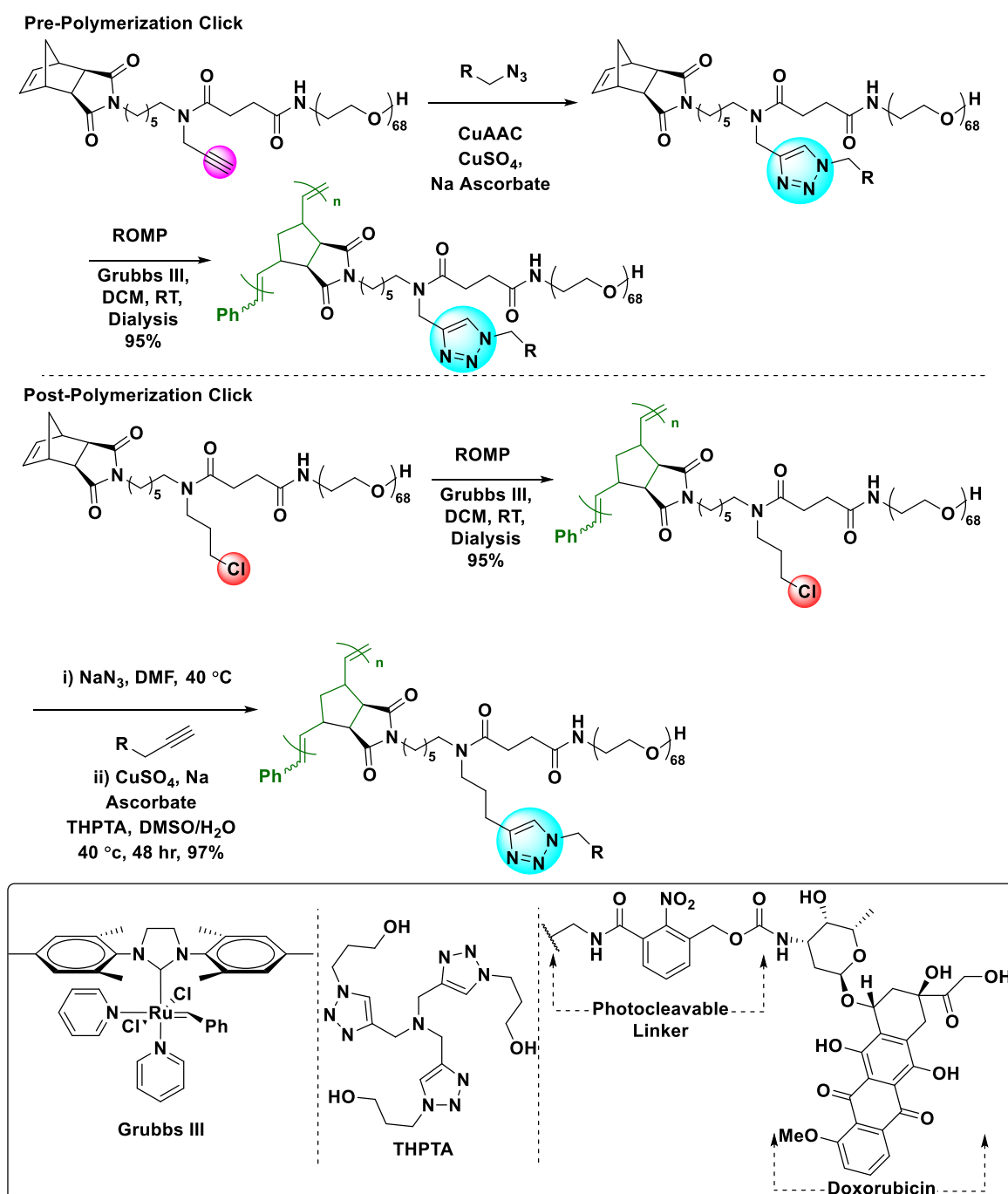
The modification of polymeric architectures has been widely used to confer the properties necessary to achieve the purposes for which these polymeric architectures were designed. (108) This requires the integration of functional groups into the polymeric structure that can allow these modifications to occur via orthogonal chemistries. (108) The fast initiating Grubbs III catalyst is compatible with a wide range of functional groups. (7) (85) (108) Nonetheless, ruthenium benzylidene complexes, such as Grubbs catalysts, were reported to interact with alkyne via enyne metathesis cascade producing 1,3-dienes, scheme 16. (108) (109)



Scheme 16: The mechanism of interaction of ruthenium carbene complexes with alkynes via enyne metathesis cascade producing 1,3-dienes. Scheme adapted from Ref. (109)

Catalyst deactivation in ROMP in the presence of azide-bearing precursors was also reported, however, no mechanistic insight into the deactivation pathway was proposed. (108) (110) Both alkynes and azides are precursors for one of the most exploited and high yielding coupling chemistries that is copper-catalyzed alkyne azide cycloaddition, CuAAC, often referred to as click reaction. (27) (7) (108) Click reaction operates under mild reaction conditions and is substrate specific which makes it tolerant to a wide range of functional groups. (108) (111) To prevent cross reactivity that may jeopardize the living nature of the polymerization, the Cu-catalyzed cycloaddition can be performed prior to ROMP since the triazole ring was shown to be compatible with the ruthenium catalyst, scheme 17. (27) (108) Alternatively, either of these functional groups can be introduced in a post-polymerization step by incorporating their precursors into the polymeric structure instead, scheme 17. (7) (108) A substitution reaction on an azide precursor such as a chloride or bromide after ROMP using sodium azide can be employed to introduce azide group/groups into the polymeric structure. (7) Both approaches have advantages and limitations. Drug loading via click chemistry prior to ROMP generates larger monomers the ring-opening polymerization of which is less feasible as the polymerizable group is less accessible to the polymerization catalyst in solution. This concept is manifested by the longer reaction times and lower yields in comparison to the approach employing the reversed sequence of transformations. (27) (7) In contrast, drug loading in a post-ROMP step, in comparison to the opposite approach, is hampered by the congestion of the of the space near the linear core of the polymeric brushes where the click

chemistry takes place, hence, the longer reaction times and the use of tris-hydroxypropyl-triazolylmethylamine, THPTA, as an accelerating ligand. (27) (7)



Scheme 17: (A) Doxorubicin loading of polyethylene glycol graft polymers via CuAAC in a pre-polymerization step to avoid cross reactivity between the alkyne group (pink) with the ruthenium benzylidene Grubbs III catalyst. This literature precedent shows the compatibility of triazole ring (blue) with the ruthenium catalyst. (B) Doxorubicin loading of polyethylene glycol graft polymers via CuAAC in a post-polymerization step to avoid cross reactivity between the azide group (green) with the ruthenium benzylidene Grubbs III catalyst. This literature precedent shows the compatibility of chloride group (red) with the ruthenium catalyst. Schemes adapted from Refs. (27) and (7) respectively.

4.1.2.3 Additional Structural Requirements

As the aim of this project is to prepare polymeric nanoparticles, NPs, that can be used for targeting and imaging of the mitochondria. In order to validate mitochondrial uptake, ROMP monomers need to feature additional structural elements. In addition to the polymerizable group, these elements include a hydrophilic spacer to confer water solubility, a mitochondrial targeting ligand and an optical probe to enable the visualization of these NPs within the mitochondria all of which are fused together via ROMP compatible linkers, such as triazole or amide linkers.

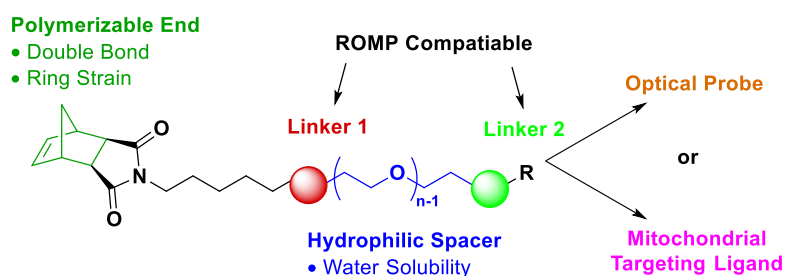


Figure 19: Structural requirements of monomers used for ROM polymer synthesis. The monomers feature a polymerizable end, hydrophilic spacer to confer water solubility, a mitochondrial targeting ligand and an optical probe to enable the visualization of these NPs within the mitochondria.

Factors that dictate the choice of these additional structural elements include; efficiency at fulfilling their intended purpose, biocompatibility and commercial or synthetic accessibility. (27) (7) Moreover, precise incorporation of these elements in the final polymeric architectures ensures reproducibility of the experimental outcome. (27) (7) Therefore, compatibility with the employed polymerization technique is an additional factor that determines the choice of these elements. (27) (7) In this section, a brief review of efficiency, biocompatibility, synthetic accessibility and ROMP compatibility of the optical probe and mitochondrial targeting ligand we chose for this project.

4.1.2.3.1 Triphenylphosphonium Salts as Mitochondrial Targeting Ligands; Mitochondrial Uptake Properties, Biocompatibility, Synthetic Accessibility and ROMP Compatibility

Mitochondria's vital importance as an organelle arises from it being the host of the aerobic cellular respiration. (12) (13) (14) In mitochondria, energy is produced and stored in the form of adenosine triphosphate, ATP, through a process termed oxidative phosphorylation using an enzyme termed ATP synthase. (12) (13) (14) This process uses nicotinamide adenine dinucleotide NAD and flavin adenine dinucleotide FAD in their reduced forms, NADH and FADH₂ respectively, the by-products of fatty acid and citric acid oxidation pathways as precursors for the synthesis of ATP, figure 20. (12) (13) (14) ATP is consumed to power other metabolic pathways by converting it into adenosine diphosphate ADP or adenosine monophosphate AMP and inorganic phosphate releasing that stored energy. (12) (13) (14)

Mitochondrial structure consists of a phospholipid bilayer-permeable outer mitochondrial membrane, OMM, inter membrane space, IMS, a phospholipid bilayer-inner mitochondrial membrane, IMM, with restricted permeability and matrix, figure 20. (12) (13) (14) The IMM is characterized with a negative potential, $\Delta\Psi_m$ of $-160 \sim -180$ mV, generated as a result of the hydrogen ions concentration gradient created by the electron transport chain to power the oxidative phosphorylation process that leads to production of ATP, figure 20. (12) (13) (14)

As previously highlighted, ABAD was shown to exacerbate A β toxicity by accentuating A β -mediated ROS production marking an event that was shown to have many ramifications among which increased release cytochrome c into the cytosol. (62) Release of cytochrome c from mitochondrial inner membrane space into the cytosol interrupts the ATP synthesis pathway jeopardizing mitochondrial function and ultimately viability. (62) The localization of ABAD-A β complex within the mitochondria of cortical brain regions observed in both AD patients and AD mouse models established mitochondria as a promising therapeutic subcellular target in the treatment of Alzheimer's disease. (62)

Some targeting approaches for the transfer of bioactive molecules across the inner mitochondrial membrane, into the matrix, exploit its negative potential. (12) (13) (14) Targeting ligands are coupled to bioactive molecule to facilitate their accumulation in the mitochondrial matrix via electrostatic interaction as a response to the negative potential. These ligands can fall in one of two major categories; small molecules or peptide mimics. (12) (13) (14)

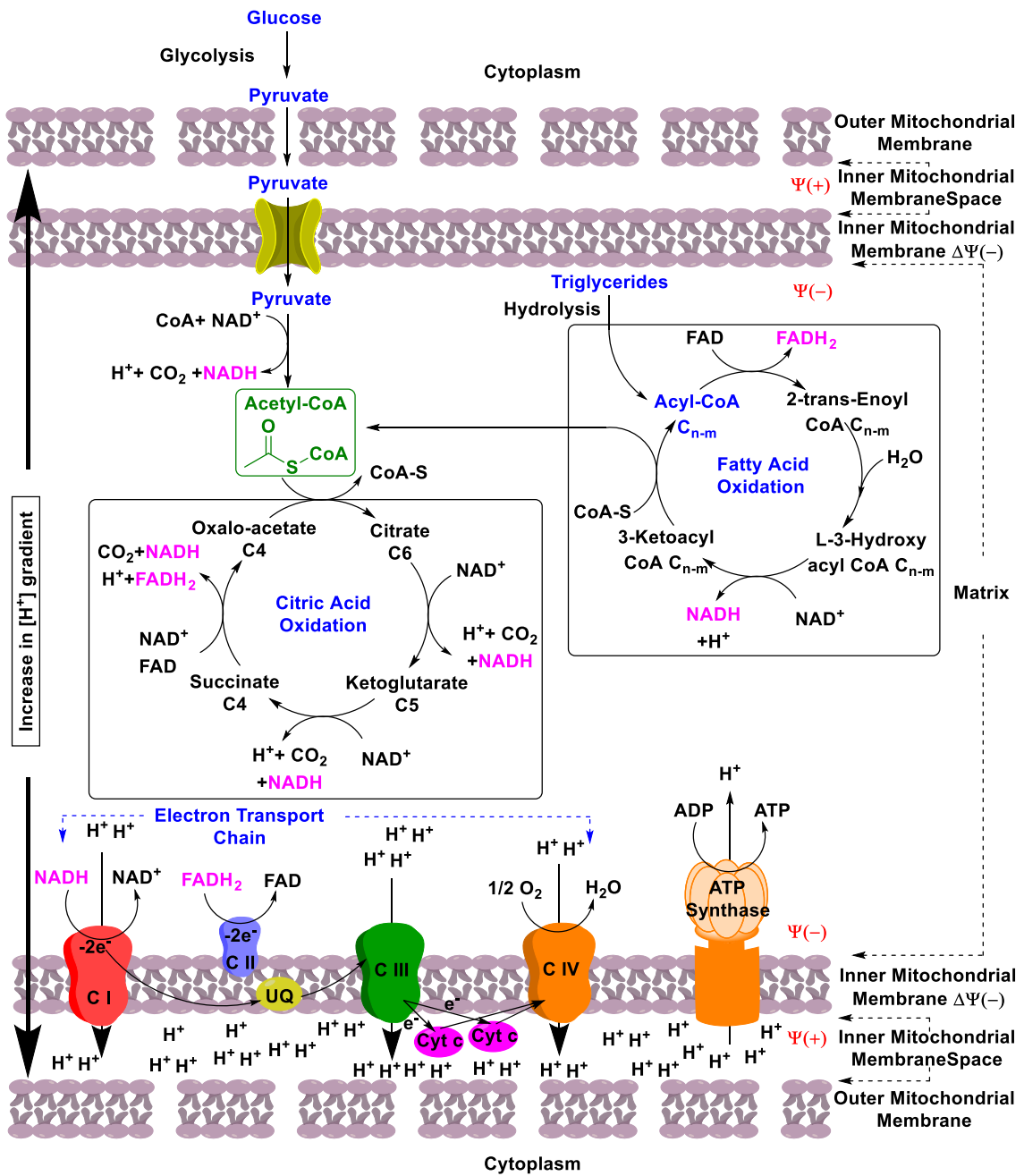


Figure 20: Mitochondria's vital importance as the host of the aerobic cellular respiration. The figure shows a brief illustration of the energy production, in the form of ATP, pathways. Glucose and triglycerides are metabolized into acetyl-CoA, and ultimately CO₂, through citric and fatty acid oxidation pathways, respectively, generating NADH and FADH₂ as by-product. These by-products are used as the fuel of the oxidative phosphorylation that leads to ATP synthesis. NADH and FADH₂ are oxidized back to NAD⁺ and FAD via complex I and II, respectively, which are constituents of the electron transport chain. The resulting electrons are transferred from CI and II to CIII via a lipid-soluble mobile carrier termed ubiquinone, UQ, via a series of redox reactions. The electrons then transferred from CII to CIV via cytochrome c, Cyt c, a water-soluble electron carrier located within the intermembrane space. At CIV, the electrons are used to reduce O₂ and form water. These series of redox reactions carried out by the electron transport chain are coupled to production of an electrochemical [H⁺] gradient across the inner membrane as a result of consumption of H⁺ during the redox reactions or their efflux by CI, III and IV. This electrochemical gradient is what drives the ATP synthesis by ATP synthase. Figure adapted from Ref. (12)

These targeting ligands, belonging to either category, feature a cationic moiety that can engage in an electrostatic interaction with the mitochondrial matrix and a hydrophobic moiety that can increase the solubility of the system and facilitate its passive diffusion through the mitochondrial lipid-bilayer membrane, figure 21. (12) (13) (14) The large hydrophobic surface granted by aromatic groups was shown to accelerate the transport of cationic molecules across the lipid-bilayer membrane. (112) (113) (114) This acceleration was attributed to the favorable increase of the entropic term as described by the Arrhenius equation: (112) (113) (114)

$$k = Ae^{-\frac{\Delta G}{RT}} \quad \text{equation 4}$$

Where k is the rate constant, A is the Arrhenius factor, R is the gas constant, T is temperature in Kelvin and ΔG is the Gibbs free energy defined as

$$\Delta G = \Delta H - T\Delta S \quad \text{equation 5}$$

Where ΔH and ΔS are the enthalpic and entropic terms respectively. The entropic gain was associated with increase of the water molecules generated from the rearrangement of the mitochondrial self-assembled lipid-bilayer as the cationic molecule with the large hydrophobic surface diffuses through it. (112) (113) (114).

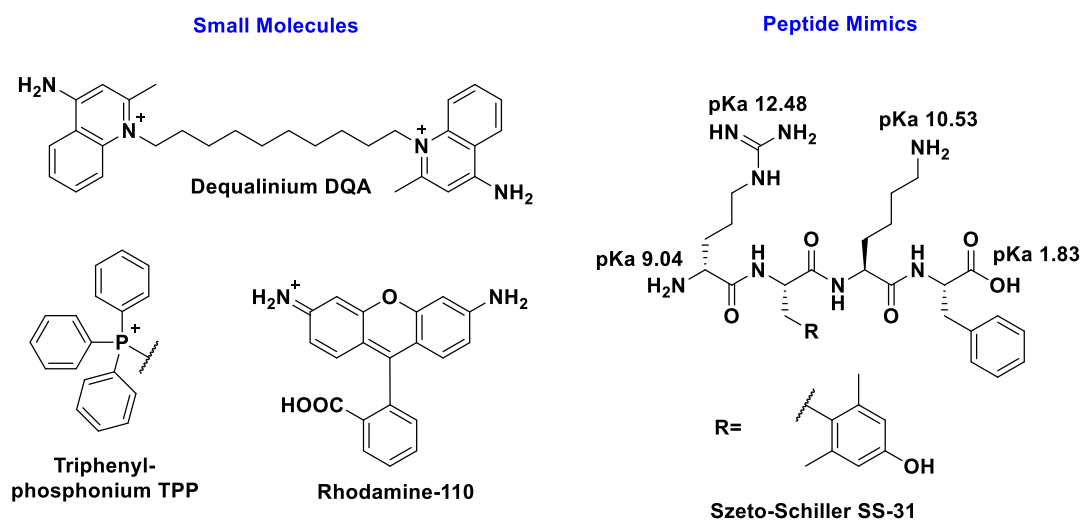
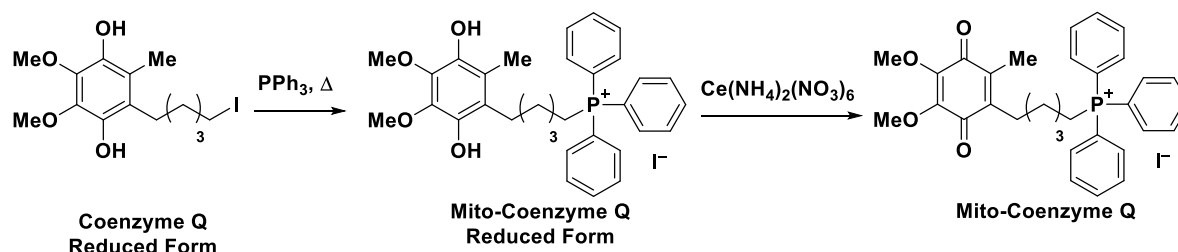


Figure 21: Examples of the two categories of synthetic mitochondrial targeting ligands; small molecules (left) and peptide mimics (right). Both feature cationic center(s) pre- or at physiological conditions and hydrophobic surfaces associated with the aromatic rings. The pKa values attached to structure of the peptide mimic SS-31, correlating with each amino acid independently, can predict the over-all electrostatic nature of the peptide that can evoke mitochondrial uptake in response to the matrix negative potential. Figure adapted from Ref. (13)

Conjugation of the anti-oxidant coenzyme Q, in its reduced form, to triphenylphosphonium TPP cationic ligand, followed by oxidation to afford the anti-oxidant, was shown to enhance its mitochondrial uptake, thus, its efficiency in preventing mitochondrial hydrogen peroxide-induced

oxidative damage by increasing its mitochondrial uptake in comparison to untargeted equivalents. (115) The aforementioned triphenylphosphonium-coupled anti-oxidants were accessed from alkyl-halides via substitution reactions using PPh₃ as the nucleophile, scheme 18. (115) (116) The synthetic accessibility of triphenylphosphonium ligands TPP, have gained these cationic species a wide popularity as tools for exploring mitochondrial uptake.



Scheme 18: Preparation of triphenylphosphonium salts from alkyl-bromide via substitution reaction using PPh₃. Scheme adapted from Ref. (116)

Despite their wide-spread application as mitochondrial targeting ligands, the mechanism by which triphenylphosphonium-coupled bioactive material induce their cytotoxic effect is still unclear. Several reports associated extensive mitochondrial uptake of TPP-coupled therapeutics, at concentrations above 10 μM , with depolarization of IMM and impairment of mitochondrial respiration and ATP synthesis. (117) (118) (119) Additional *in vitro* studies lent support to these findings by showcasing mitochondrial Ca²⁺ overload as a result of treatment with TPP-coupled therapeutics due to inhibition of Ca²⁺ efflux from mitochondrial matrix causing mitochondrial swelling and ultimately dysfunction. (119) The validity of these finding is yet to be established considering the role the coupled therapeutic material may have had in the reported cytotoxic effect.

Ruthenium-catalyzed metathesis in general and ROMP in particular of TPP cationic ligands-bearing monomers is, to our knowledge, unprecedented. Therefore, cross-reactivity in this context is yet to be established. This aspect is explored in this and the following chapter.

4.1.2.3.2 Coumarin Derivatives as Optical Probes; Optical Properties, Biocompatibility, Synthetic Accessibility and ROMP Compatibility

Coumarin derivatives have found many applications in fluorescence microscopy as fluorescent tags (120) and fluorescent chemosensors. (121) Coumarin and its derivatives are UV excitable and blue fluorescent dyes. (120) (121) Coumarin derivatives were shown to exhibit a stronger fluorescence signal, when excited in the UV-Vis region, in comparison to other UV-Vis excitable dyes such as fluorescein or rhodamine, figure 22. (122)

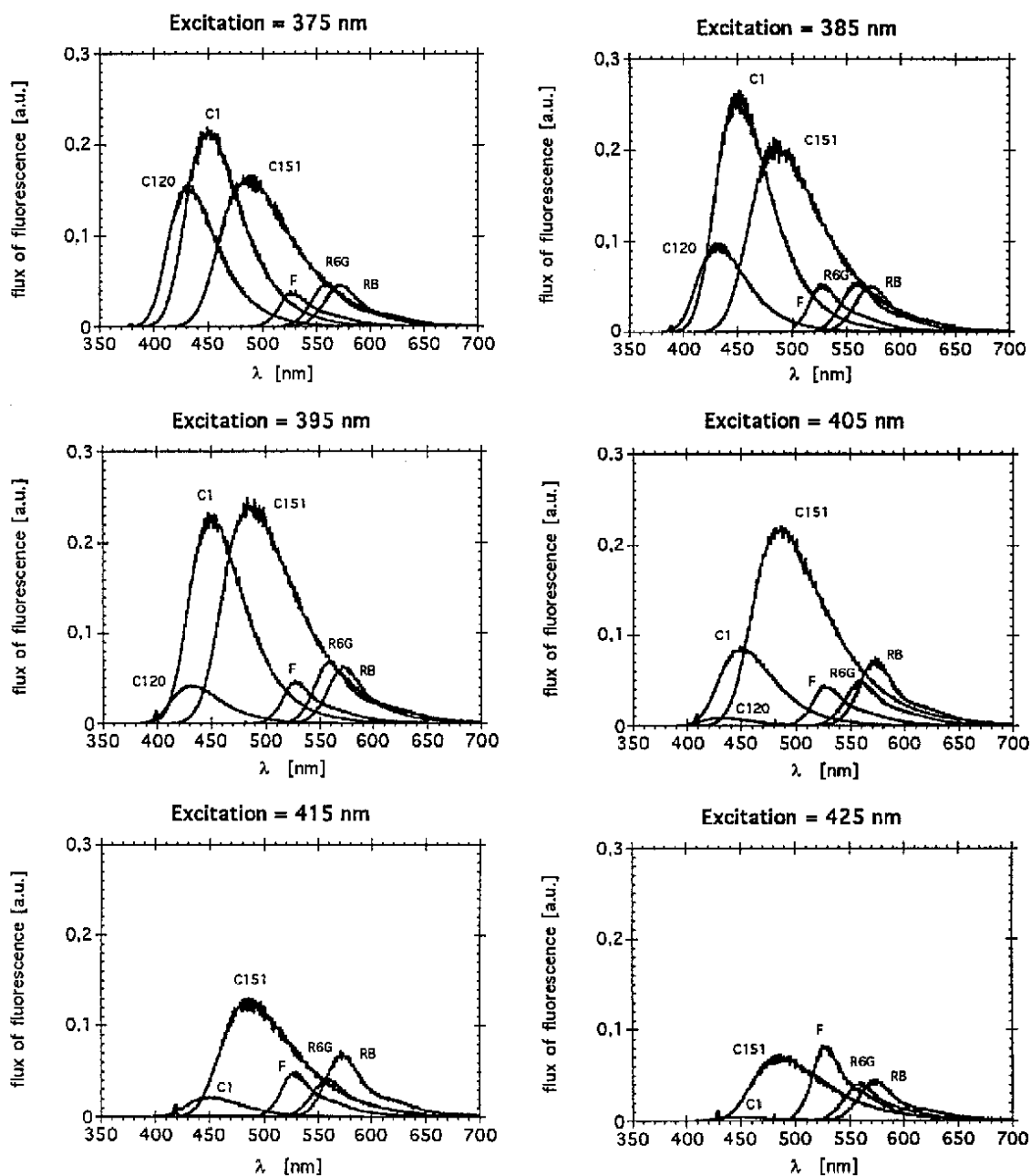


Figure 22: Fluorescence intensity of C, coumarin; F, fluorescein; R, rhodamine solutions in ethanol (10^{-5} M) at different excitation wavelengths. The fluorescence spectra show the high fluorescence intensity of coumarin derivatives at short UV wavelengths in comparison to other UV-Vis excitable dyes. Figure copied from Ref. (122) Structure of dye is presented in figure 23

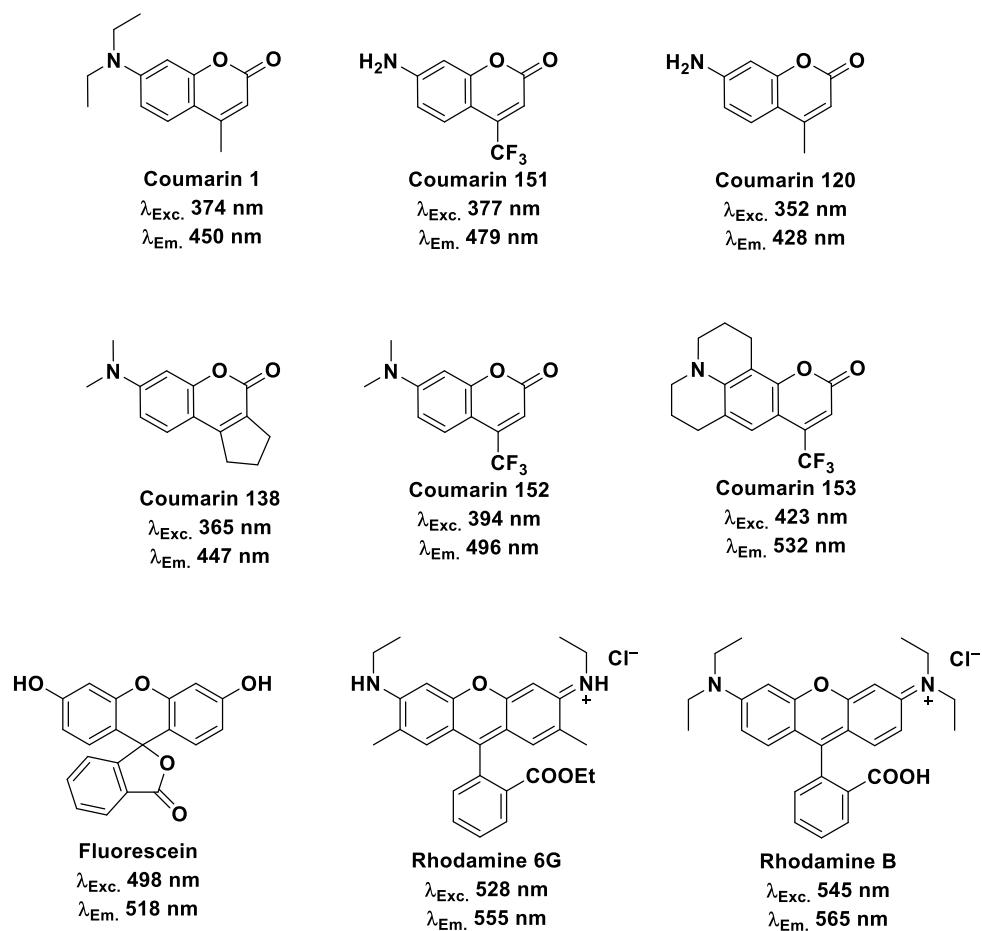
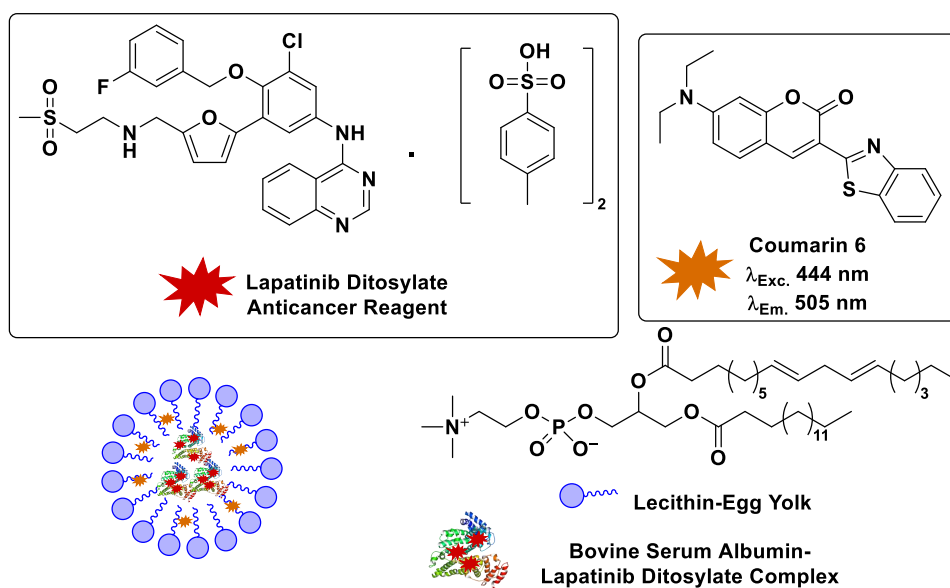


Figure 23: Structure of C, coumarin; F, fluorescein; R, rhodamine dyes the fluorescence of which was presented in figure 22 and their corresponding excitation and emission wavelengths taken from Ref. (122)

The higher propensity of photon absorption, often referred to as absorption cross-section, of diethylamino coumarin derivatives at short UV wavelengths, such as 350-377 nm, facilitated their use in combination with other stains such as nuclear, e.g. 4',6-diamidino-2-phenylindole or DAPI, and lysosomal stains based on 4,4-Difluoro-4-bora-3a,4a-diaza-*s*-indacene, e.g. LysoTracker™ Red DND-99, in cellular localization studies, figure 24. (123)

A. Composition of LTNPs



B. Confocal Microscopy Images of U87 Cells

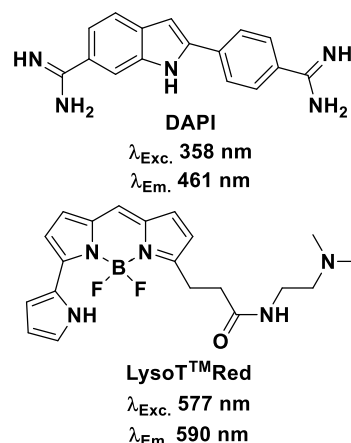
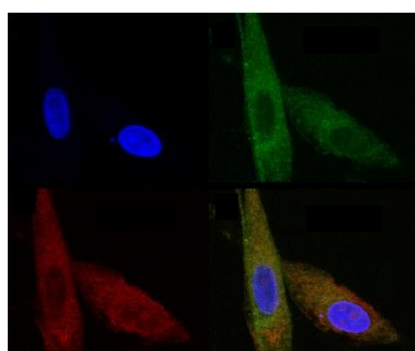


Figure 24: (A) Composition of a lapatinib-incorporated lipoprotein-like nanoparticles system (LTNPs). The composition consists of a bovine serum albumin-lapatinib complex core and stabilized by a liposomal shell of lecithin within which coumarin-6 is dispersed. (B) Confocal images of U87, human glioblastoma astrocytoma, after incubation with coumarin-6 loaded LTNPs, green channel, and staining of nuclei, blue channel, and lysosomes, red channel, with DAPI and LysoTracker™ Red DND-99 respectively showing the localization of the NPs within the lysosomes. Figure adapted from Ref. (123)

Coumarin and its derivatives are also NIR excitable blue fluorescent dyes using two-photon microscopy. (122) In conventional fluorescence microscopy, the fluorescent molecule is brought to its excited state S_1 by absorbing one photon of an appropriate wavelength, figure 25. (124) (125) This event is followed by a non-radiative relaxation of the excited molecule to the lowest vibrational substate of the excited state and a subsequent radiative decay to the ground state, S_0 . (124) (125) In contrast, in a two-photon microscopy, the fluorescent molecule reaches its excited state by simultaneously absorbing two photons each of approximately half the energy and twice the wavelength of the single photon absorbed in conventional fluorescence microscopy, figure 25. (124) (125)

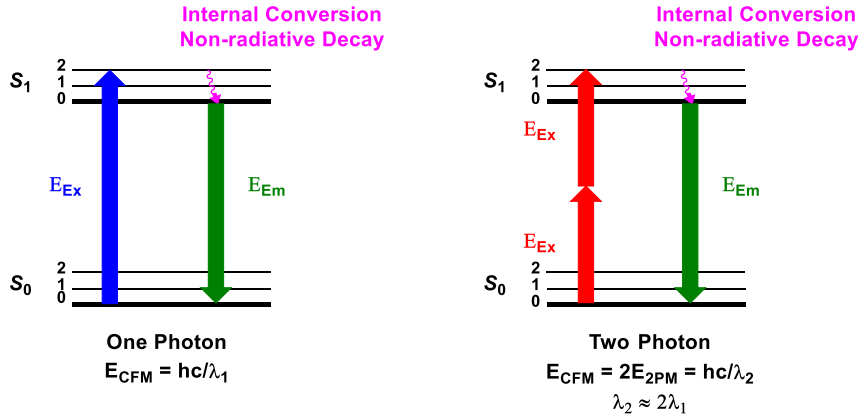


Figure 25: Jablonski diagram depicting the fluorescence process that occurs in a conventional one-photon microscopy (left) and two-photon microscopy (right). The two-photon excitation requires the simultaneous action of two photons each half the energy and double the wavelength of that needed in a one-photon process to excite the fluorophore to the same excited state. Adapted from Ref. (124) (125)

The optical consequence of two-photon induced fluorescence is the confinement of the fluorescence region to a smaller volume than that of one-photon fluorescence microscopy, figure 26. (124) (125) The fluorescence distribution in the focal region of an objective lens, with a numerical aperture $NA = \sin \alpha$, is described by (126) (127):

$$I(u, v) = \left| 2 \int_0^1 J_0(v\rho) e^{-iu\rho^2/2} \rho d\rho \right|^2 \quad \text{equation 6}$$

Where u is the axial coordinate in the focal region and is a function of λ as described by (126) (127):

$$u = \frac{8\pi z \sin^2(\alpha/2)}{\lambda} \quad \text{equation 7}$$

The fluorescence distribution, I , increases as the focal point is approached marked by decrease in the value of z , and ultimately u , term. (124) (125) The significance of this decrease is more pronounced in the case of two-photon microscopy since the wavelengths used to excite the fluorophore molecules are twice the length as those used in conventional fluorescence microscopy. (124) (125) In practical terms, the confinement to a smaller volume results in a reduction in out of focus fluorescence, figure 26. (124) (125) This not only enhances the resolution of the image but also minimizes out of focus photobleaching of the fluorophore molecules and photochemically-induced toxicity of the live specimen. (124) (125)

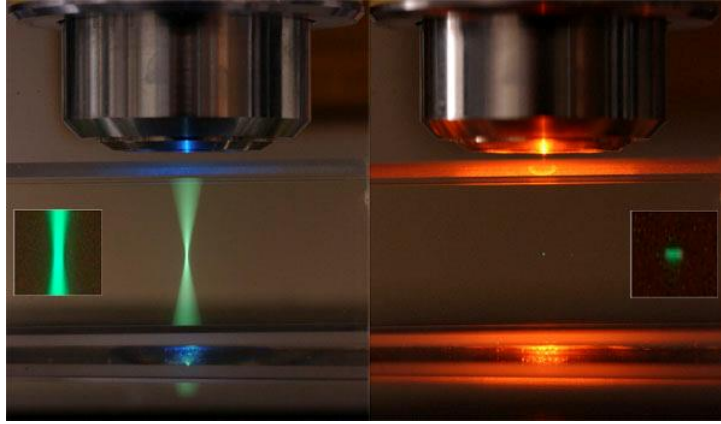


Figure 26: One-photon (left) and two-photon (right) induced fluorescence of a dilute fluorescein solution in a quartz cuvette showing the confinement of the illumination space to a smaller volume in the case of two-photon fluorescence the ramification of which is the protection of the fluorophore molecules and specimen beyond and below the focus against photobleaching and photocytotoxicity. Figure adapted from Ref. (165)

This simultaneous action of two photons on the same fluorophore at the same excitation event can be achieved when a high flux of photons is applied. (125) (128) (129) Practically, this can be met by using a stream of laser pulses with a pulse duration τ_p and repetition rate f_p of about 100 fs and 80 MHz respectively, figure 27. (122) (124) (125). The efficiency of the two-photon excitation process is highly dependable on parameters that include the near infrared, NIR, excitation wavelength and NIR absorption cross section of the dye as well as the average laser power as described by (124) (129):

$$I_f \approx \delta_2 P^2 \left[\pi \frac{(NA)^2}{hc\lambda} \right]^2 \quad \text{equation 8}$$

Where I_f is the fluorescence intensity, δ_2 is the molecular cross-section of the excitable dye, P is the laser power, NA is the numerical aperture of the objective lens, h is Planck's constant, c is the speed of light and λ is the excitation wavelength. (124) These parameters can be tuned to ensure optimal fluorescence output for best image resolution yet minimize thermally induced specimen damage which is the result of prolonged exposure to high intensity light. (128) (129) (130)

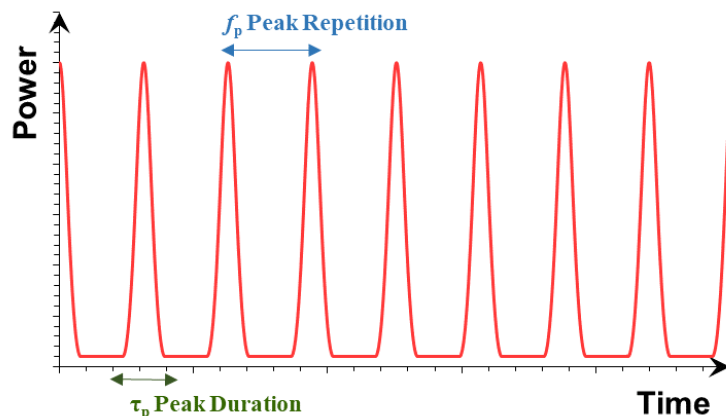
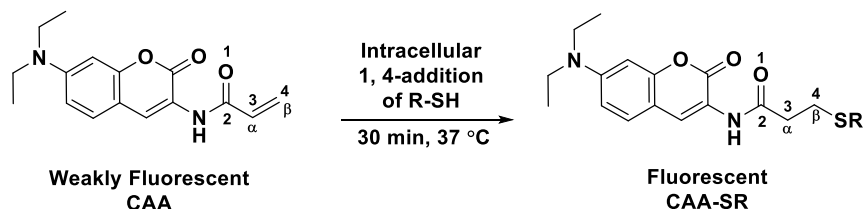


Figure 27: A train of laser pulses of a pulse duration of τ_p and repetition frequency of f_p designed to generate a flux of photons to allow for a simultaneous action of two photons on the same fluorophore at the same excitation event. Figure adapted from Ref. (124).

The quadratic dependence of the fluorescence output in a two-photon excitation event on excitation laser power represented by equation 8 was shown to be a hallmark behavior of two-photon fluorescent dyes. This was experimentally validated for several dyes, among which are coumarin derivatives, by plotting the logarithms of consecutive values of beam power against the logarithms of the corresponding fluorescence intensity of fluorophore solution of a known concentration the slope of which was two. (124) (125)

Coumarin derivatives were shown to display low cytotoxic effect at concentrations below 25 μM . The mitochondrial viability of RAW264.7 cells, a macrophage cell-line, against a weakly fluorescent acrylamide bearing coumarin derivative, CAA, was assessed using a 3-(4,5-dimethylthiazol-2-yl)-2,5-diphenyltetrazolium bromide cell viability assay, known as MTT assay. (131) In this study, CAA was used as a chemosensor for the detection of thiols such as cysteine, Cys, homocysteine, Hcy, and glutathione, GSH, scheme 19.



Scheme 19: The fluorescence switch of CAA, weakly fluorescent, chemosensor upon Michael-type addition of biothiols to the α,β -unsaturated carbonyl terminus. Figure adapted from Ref. (131)

The detection is accomplished by a fluorescence turn-on response occurring as the weakly fluorescent CAA undergoes a 1,4-addition of the biothiol to its α,β -unsaturated carbonyl terminus. The cellular viability was estimated to be greater than 80% after incubation with CAA for 24 h at concentrations ranging from 0-25 μM , figure 28. (131)

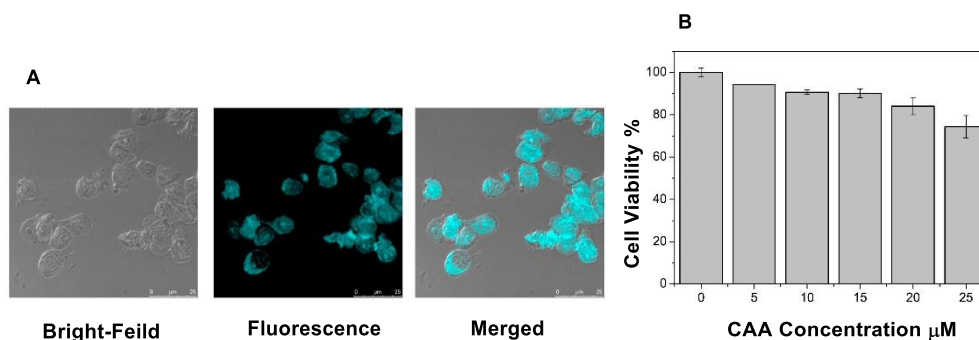


Figure 28: (A) Confocal fluorescence images of RAW 264.7 cells, shown in the bright-field channel to the left, after incubation with CAA (10 μM), shown in the blue fluorescent channel in the middle, for 30 min at 37 $^{\circ}\text{C}$. Both channels were merged as shown in the image to the right to validate cellular uptake of CAA. (B) Cellular viability chart of RAW 264.7 cells after incubation with CAA at concentrations ranging from 0 to 25 μM at 37 $^{\circ}\text{C}$ for 24 hrs. Figures adapted from Ref. (131)

The ease of their synthesis remains coumarin derivatives' most attractive feature. They can be prepared from commercially available material such as salicylaldehydes and Meldrum's acid via Knoevenagel condensation. (132) (133)

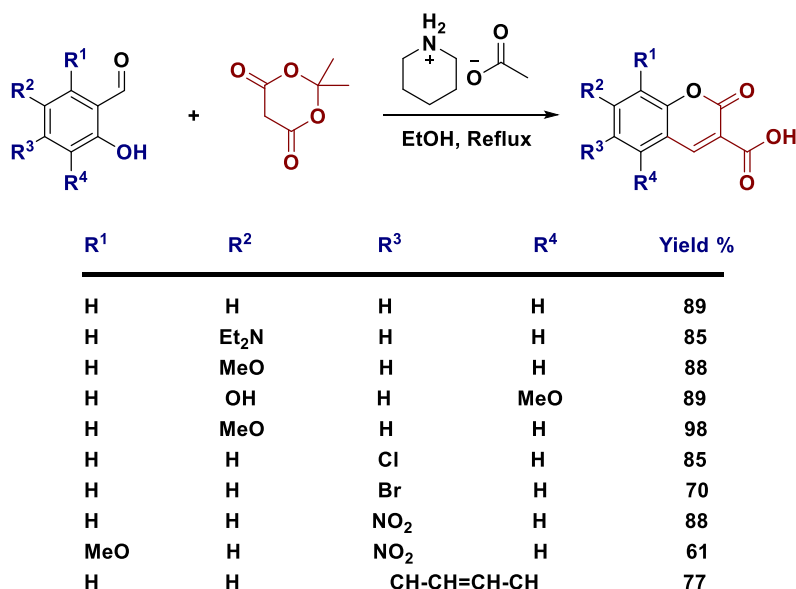


Figure 29: Synthetic accessibility of a range of coumarin derivatives by Knoevenagel condensation of salicylaldehydes and Meldrum's acid. Figure adapted from Ref. (132)

The functional group tolerance of ruthenium metathesis complexes being widely acknowledged. (7) (85) (86) (102) (108) (134) Substrates bearing functional groups ranging from alcohols (7), aldehydes (85), ketones (85) and amides (27) (7) were shown to undergo ROMP initiated by ruthenium metathesis complexes with no appreciable interference or cross-reactivity, figure 18. Even olefins in conjugated systems such the fluorescent cyanine 5 were reported as ROMP compatible substrates, figure 9. (51)

4.2 Synthesis and Characterization of First-Generation Homopolymers

In this section, the synthesis of our first-generation monomers that feature the structural elements discussed above is described. Tetra-ethylene glycol-based hydrophilic spacers were integrated into the monomer structure to confer water solubility on the resulting polymers, figure 30. The monomers were subjected to homo-ROMP to examine their propensity for block-polymerization and establish the ROMP conditions under which the polymerization is living.

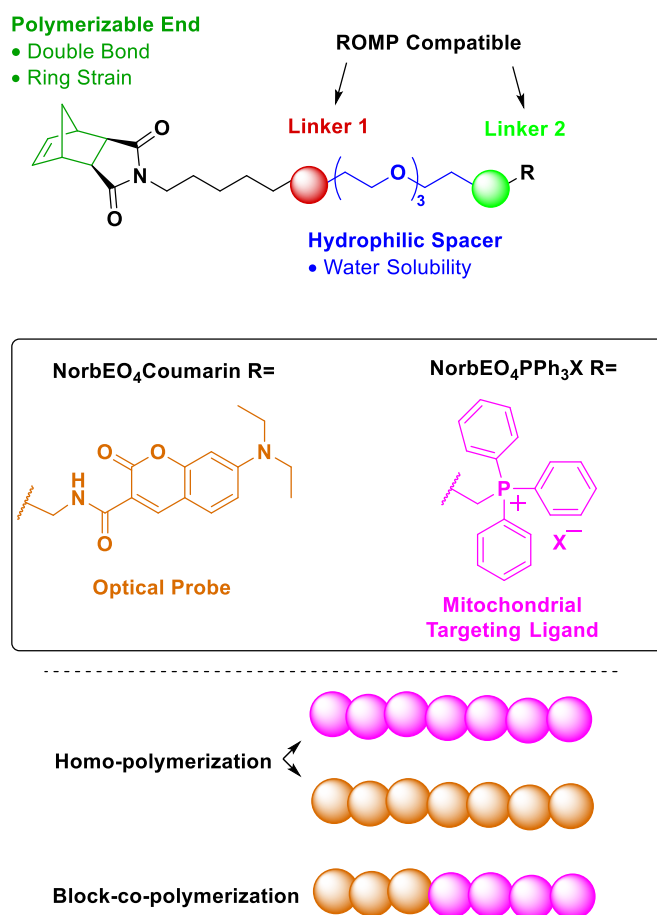
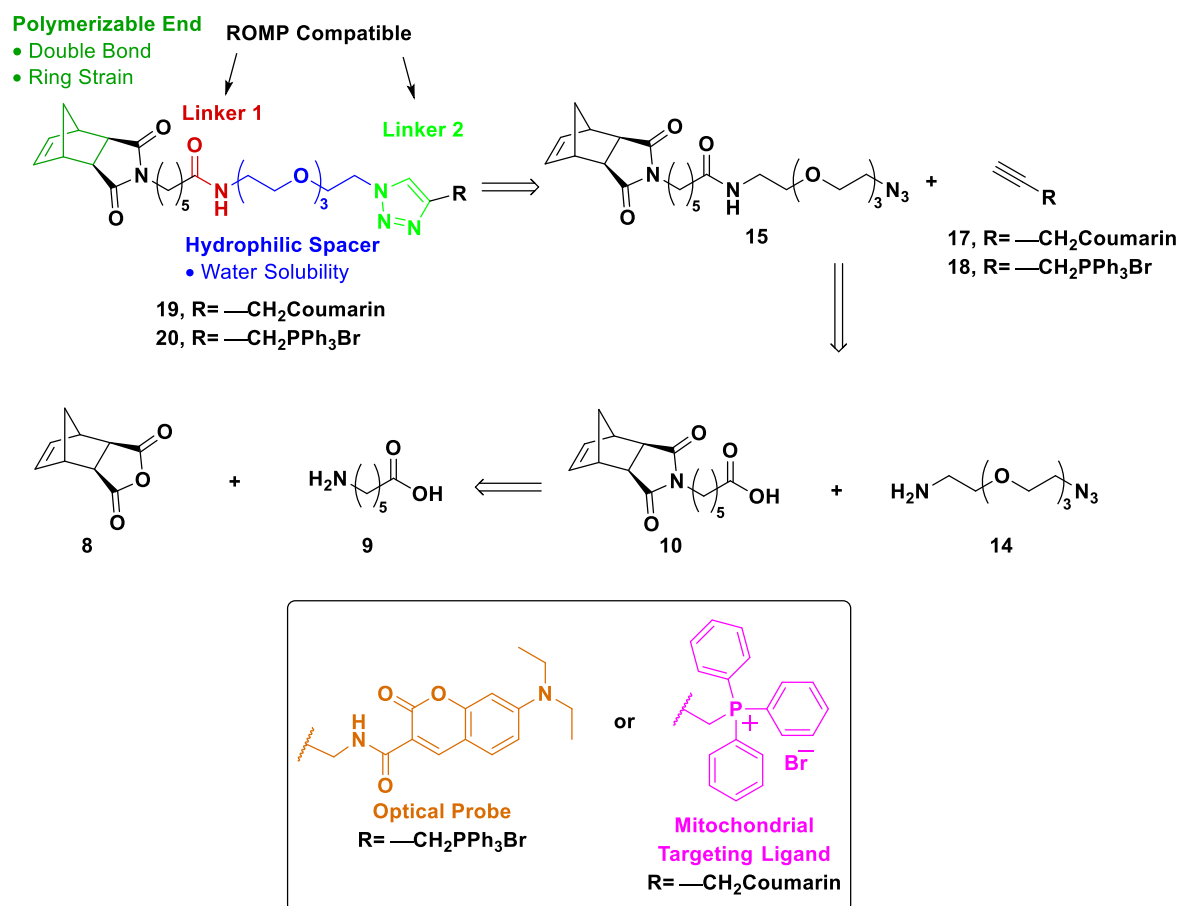


Figure 30: (Top) Brief illustration of general the structure of both monomers, fluorescent and mitochondrial targeting featuring the elements discussed in the previous section. Monomer's structure features a polymerizable end, hydrophobic spacer, TEG-based hydrophilic segment and a terminal group that is either fluorescent, to make up NorbEO₄Coumarin, or mitochondrial targeting, to access NorbEO₄PPh₃I. (Bottom) The monomers were subject to homo-polymerization to establish the conditions under which the polymerization of these monomers is living.

4.2.1 Monomer Synthesis

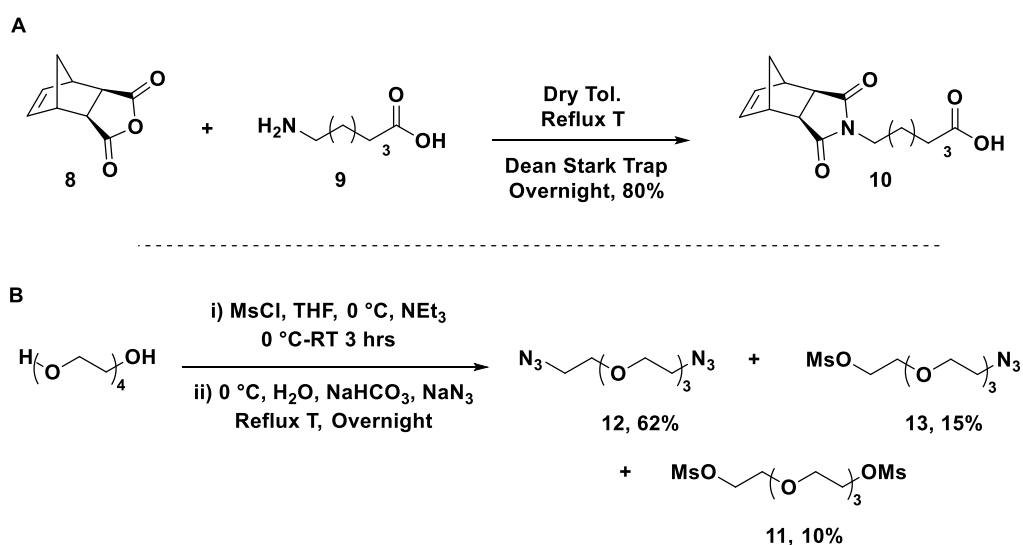
Our initial synthesis plan to access both monomers, the one bearing 7-(diethylamino)coumarin-3-carboxylic acid as the optical probe, NorbEO₄Coumarin, and the one bearing triphenyl phosphonium bromide as the mitochondrial targeting ligand, NorbEO₄PPh₃Br, is depicted in scheme 20.



Scheme 20: First synthesis plan to access both the fluorescent monomer bearing 7-(diethylamino)coumarin-3-carboxylic acid as the optical probe and the mitochondrial targeting monomer bearing triphenyl phosphonium ligand as the subcellular targeting moiety.

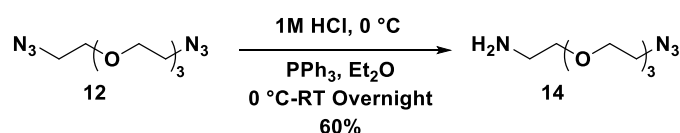
CuAAC between terminal azide **15** and terminal alkyne **17** or **18** and would furnish monomers NorbEO₄Coumarin or NorbEO₄PPh₃Br respectively. The terminal azide **15** could be accessed from azidoethyl-triethyleneoxide amine **14** and *N*-(hexanoic acid)norbornene dicarboximide **10** under amide coupling conditions. *N*-(Hexanoic acid)-norbornene dicarboximide **10** can be prepared via condensation of hexanoic acid **9** and norbornene dicarboxylic anhydride **8**. Using intermediate **15** as the common precursor for the synthesis of monomers **19** and **20** was envisioned to simplify their synthesis by minimizing the number of synthesis steps and reaction intermediates and reducing the time needed for their multigram scale production.

The condensation of hexanoic acid **9** and cis-5-norbornene-exo-dicarboxylic anhydride **8** furnished the desired *N*-(hexanoic acid)-norbornene dicarboximide **10** in 80% yield, scheme 21. *N*-(Hexanoic acid)-norbornene dicarboximide's amide coupling partner, azidoethyl-triethyleneoxide amine **14**, was prepared by desymmetrization of tetraethylene glycol, TEG, according to Schwabacher. *et. al*'s protocol. (135) (136) In a one-pot reaction, TEG was di-mesylated by treatment with mesyl chloride in the presence of a base then converted to the di-azide derivative **12** using sodium azide. The transformation generated a mixture of chromatographically separable mono- and di-azide derivatives along with residual starting di-mesylated precursor, scheme 21.



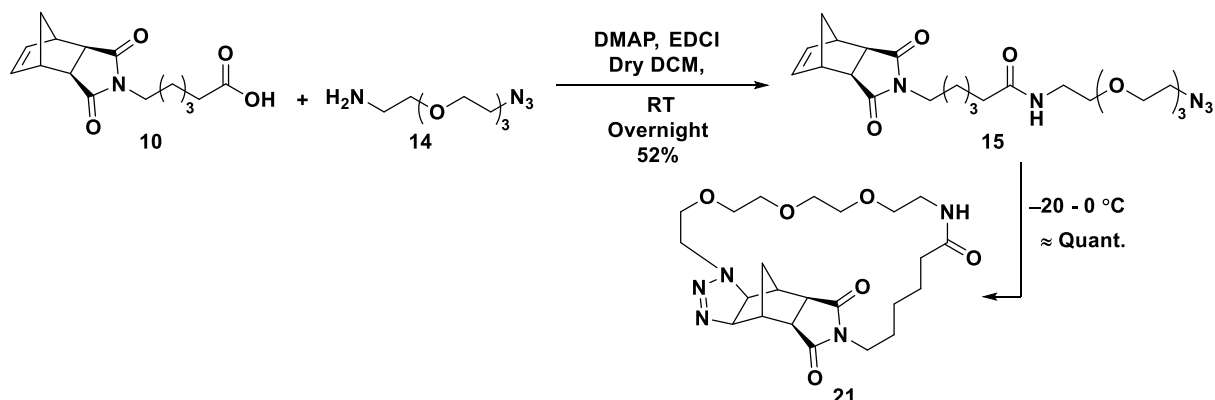
Scheme 21: (A) Condensation of hexanoic acid and norbornene dicarboxylic anhydride into *N*-(hexanoic acid)-norbornene dicarboximide. (B) Dimesylation of tetraethylene glycol TEG and subsequent mesylate-azide exchange using sodium azide

The di-azide **12** was partially reduced by treatment with triphenyl phosphine in a vigorously stirred solvent system comprising of Et₂O and dilute, 1 M, aqueous hydrochloric acid. The resulting amino-azide derivative **14** spontaneously partitioned into the aqueous phase due to its protonation which minimized its over reduction into the di-amino side product, scheme 22.



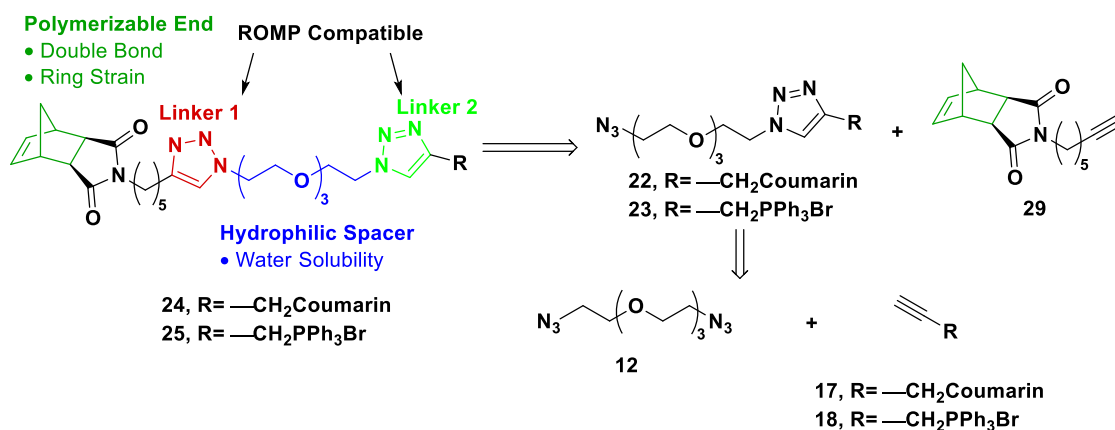
Scheme 22: Desymmetrization of azidoethyl-triethyleneoxide azide by reduction with PPh₃ in aqueous 1M HCl.

The amide coupling of *N*-(hexanoic acid)-norbornene dicarboximide **10** and azidoethyl-triethyleneoxide amine **14** in the presence of 4-dimethylaminopyridine, DMAP, and 1-ethyl-3-(3-dimethylaminopropyl)- carbodiimide, EDCI, successfully produced the desired terminal azide **15**. Unfortunately, intermediate **15** was not stable and underwent intramolecular cycloaddition of the azide group to the strained alkene which was confirmed by the disappearance of the olefinic ¹H NMR signal and the azide IR stretch, scheme 23.



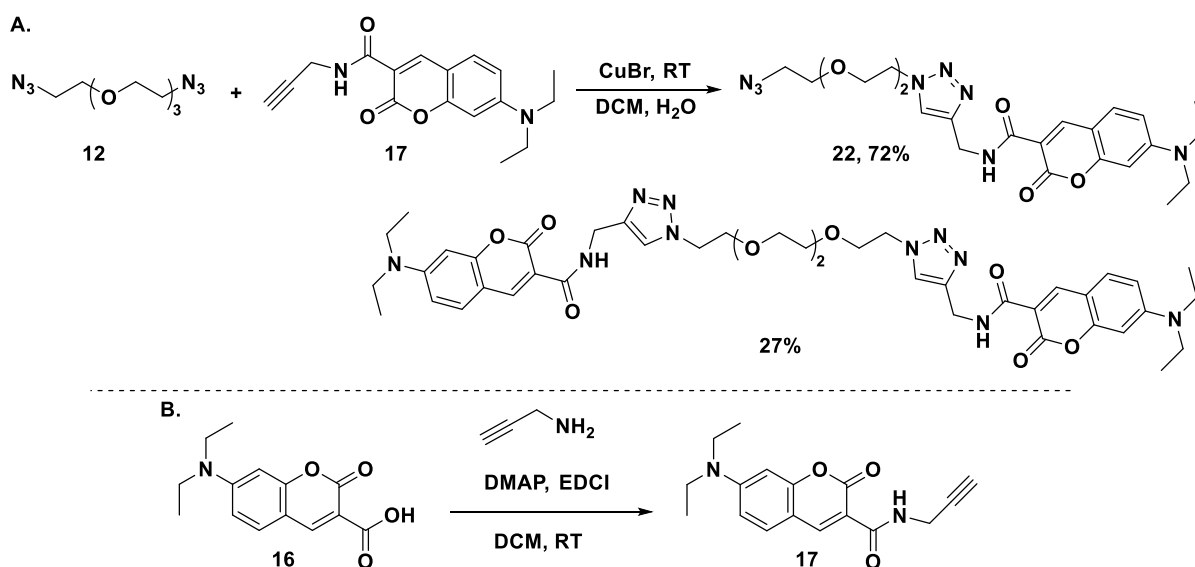
Scheme 23: Amide coupling of *N*-(hexanoic acid)-norbornene dicarboximide and azidoethyl-triethyleneoxide amine in the presence of DMAP and EDCI. Intermediate **15** underwent intramolecular cycloaddition into **21** observed even upon storage of **15** at -20 °C showcasing the high affinity of the azide and the strained alkene.

To overcome this limitation, instead of using azidoethyl-triethyleneoxide amine **14** as the hydrophilic spacer, its azidoethyl-triethyleneoxide azide precursor **12** and TEG desymmetrization intermediate was used, scheme 21. The choice of the intermediate was based on the ease and high yield of its synthesis. The synthesis scheme of both monomers was amended to reverse the sequence of incorporation of the polymerizable group and fluorescent molecule or cationic ligand noted in to avoid any intramolecular cycloaddition between the strained olefin and the terminal azide, scheme 24.



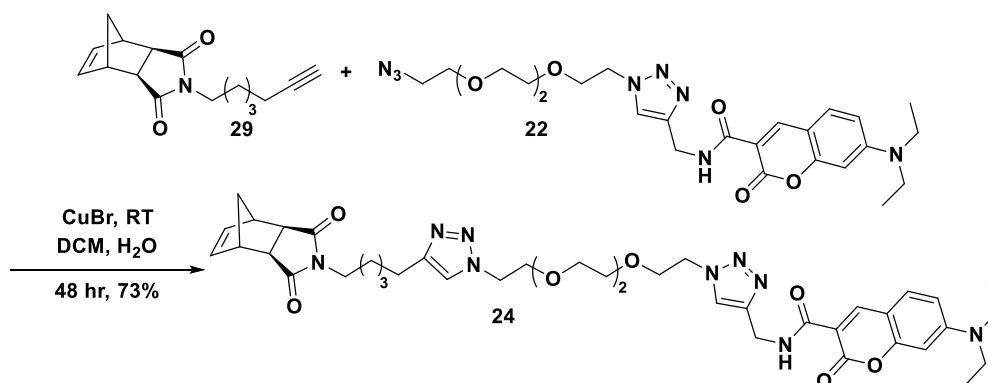
Scheme 24: Amended synthesis plan to access both the fluorescent monomer bearing 7-(diethylamino)coumarin-3-carboxylic acid as the optical probe and the mitochondrial targeting monomer bearing triphenyl phosphonium ligand as the subcellular targeting moiety. The sequence of incorporation of the polymerizable group and fluorescent molecule or cationic ligand was reversed to prevent intra-molecular CuAAC of the terminal azide to the strained alkene.

The di-azide spacer **12** was coupled to **17** via CuAAC to afford the terminal azide **22** in 72 % yield. The di-azide spacer was added in excess to minimize the formation of the di-coupling side-product, scheme 25. The desired terminal azide **22** and the di-coupling side-product were separable by means of normal phase chromatography.



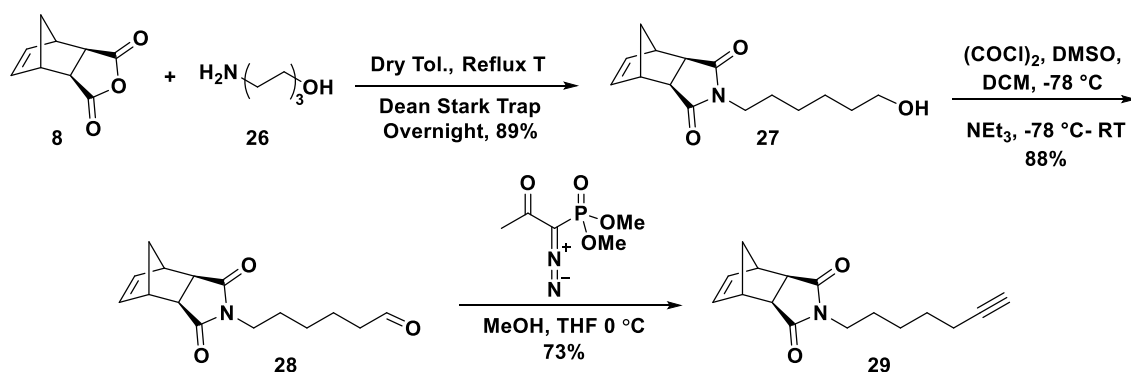
Scheme 25: (A) Copper-catalyzed alkyne-azide cycloaddition of 7-(diethylamino)coumarin-3-carboxylic propargylamide and azidoethyl-triethyleneoxide azide. (B) Amide coupling of 7-(diethylamino)coumarin-3-carboxylic acid and propargyl amine in the presence of EDCI and DMAP.

The aforementioned 7-(diethylamino)coumarin-3-carboxylic propargylamide **17** was prepared via amide coupling of propargyl amine and 7-(diethylamino)coumarin-3-carboxylic acid **16** in the presence of EDCI and catalytic amounts of DMAP, scheme 25. The terminal azide **22** was coupled to *exo*-N-(6-heptyn-1-yl)-norbornene dicarboximide **36** via CuAAC to introduce polymerizable group constituting the final step in the synthesis of the first-generation fluorescent ROMP monomer **24**, henceforth referred to as NorbEO₄Coumarin, scheme 26.



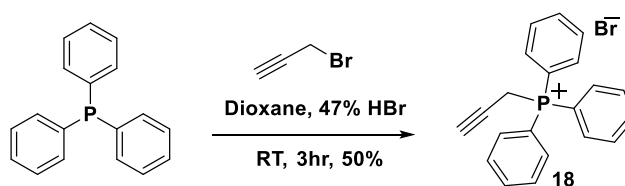
Scheme 26: CuAAC of the terminal azide **22** to *exo*-N-(6-heptyn-1-yl)-norbornene dicarboximide as the final step in the synthesis of the first-generation fluorescent ROMP monomer **24** or NorbEO₄Coumarin.

The *exo-N*-(6-heptyn-1-yl)-norbornene dicarboximide **29** was prepared from the product of condensation of *cis*-5-norbornene-*exo*-dicarboxylic anhydride **8** and 6-amino-1-hexanol **26**, *exo-N*-(6-hexan-1-ol)-norbornene dicarboximide **27**, by oxidation under Swern oxidation conditions followed by Seyferth–Gilbert homologation using Ohira-Bestman reagent, scheme 27.



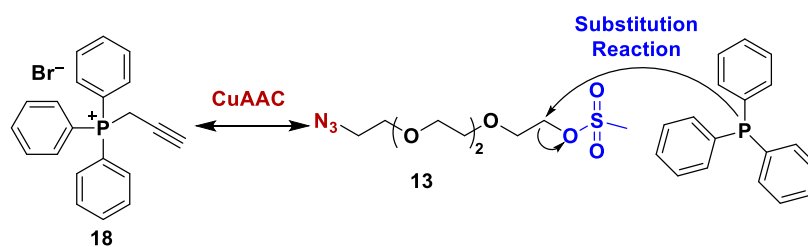
Scheme 27: Synthesis of *exo-N*-(6-heptyn-1-yl)-norbornene dicarboximide **29** from *exo-N*-(6-hexan-1-ol)-norbornene dicarboximide **27** by Swern oxidation followed by a Seyferth–Gilbert homologation.

At this point, we realized that utilizing the same di- azide linker **12** for the synthesis of the mitochondrial targeting monomer **25** may be fraught with complications. The complications may arise from the difficulty in separating the mono- and di-coupling products of **12** and **18** which was prepared from propargyl bromide by nucleophilic substitution using PPh₃ according to Schweizer, *et. al.*'s protocol depicted in scheme 28. (137) The stability of the phosphorus center in phosphonium salts under chromatographic separation conditions was a major concern.



Scheme 28: Synthesis of propargyltriphenylphosphonium bromide
Figure adapted from Ref. (137)

For these reasons, we switched to using azidoethyl-diethylene oxide-ethyl mesylate **13** the by-product of the desymmetrization of TEG, scheme 29. This asymmetric linker can facilitate the incorporation of the mitochondrial ligand via either the CuAAC to propargyltriphenylphosphonium bromide **18** utilizing its azide terminus or a substitution of the mesylate group with triphenylphosphonium using triphenylphosphine as the nucleophile.



Scheme 29: The flexibility of the incorporation of the mitochondrial targeting triphenylphosphonium ligand using the asymmetric azidoethyl-diethylene oxide-ethyl mesylate as the hydrophilic spacer

Because the synthesis of this linker via the one-pot di-mesylation and subsequent mesylate-azide exchange route described in scheme 21 is low yielding we switched our attention to its synthesis via the asymmetric activation of TEG method described by Bouzide, *et. al.* (**138**) Following this method, TEG was treated with nearly stoichiometric amounts of silver oxide, as the base, and tosyl chloride in the presence of catalytic amounts of potassium iodide. The monotosylation of TEG under these conditions occurs in a higher yield than when conventional monotosylation conditions, such as stoichiometric amounts of TsCl and a base like NaOH, NaH or NEt_3 were employed. This increase in selectivity of the monotosylation process was attributed to the intramolecular hydrogen-bonding augmented by chelation of TEG to of Ag_2O , figure 31. (**138**) This intramolecular H-bonding is believed to activate one of the hydroxyl groups by making it more acidic and therefore more engaged in the tosylation process. (**138**)

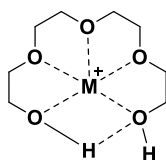
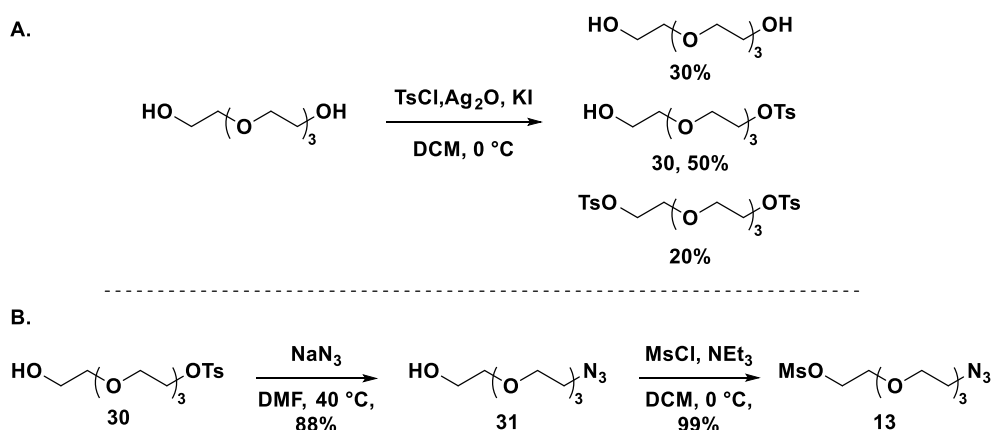


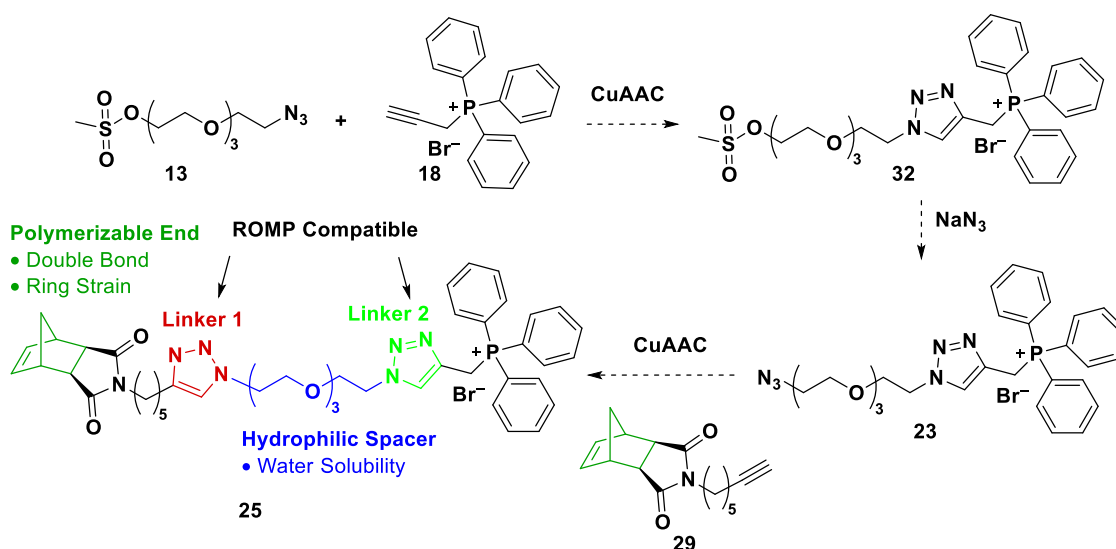
Figure 31: Chelation of TEG to of Ag_2O resulting in augmentation of intramolecular hydrogen-bonding activating one of the hydroxyl groups making more susceptible to tosylation. Figure adapted from Ref. (**138**)

The reaction generated a mixture of mono- and di-tosylated TEG as well as traces of non-reacted TEG which, because of their length, were successfully separated by means of normal-phase chromatography. The absence of the side product was confirmed by ^1H NMR in deuterated DMSO, (**138**). The triplet at δ 4.58 (t, $J = 5.5$ Hz, 1H, 1) that corresponds to hydroxyl proton does not shift or broaden with variation of the concentration therefore was used to integrate the signals of the entire spectrum. This transformation was followed by a tosylate-azide exchange and a subsequent mesylation to afford the desired asymmetric spacer **13**, scheme 30.



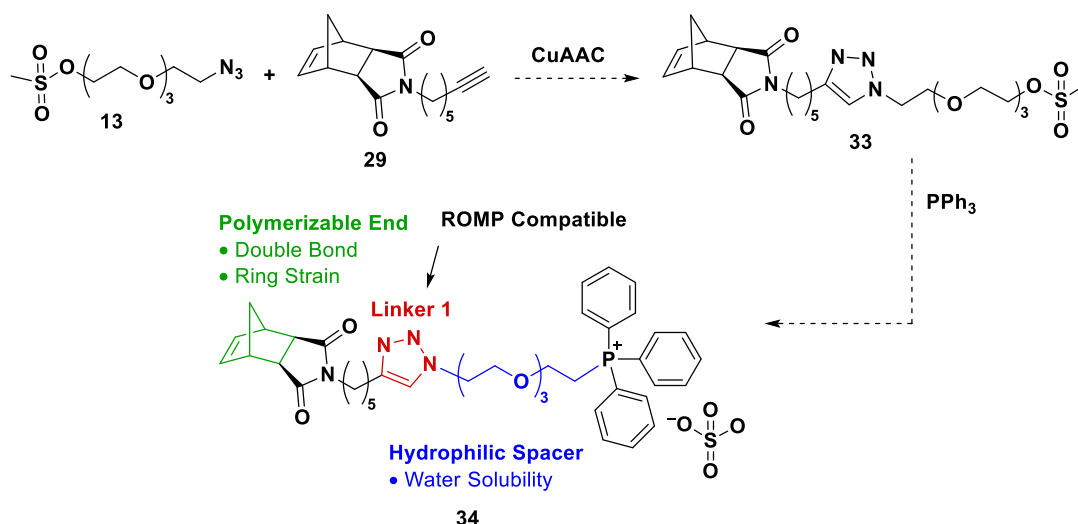
Scheme 30: (A) The asymmetric activation of TEG using Ag_2O , as the base, and tosyl chloride in the presence of catalytic amounts of potassium iodide. The transformation generates a mixture of un-reacted TEG and its mono- and di-tosylated derivatives which were chromatographically separable. (B) the subsequent transformation of the mono-tosylated TEG into the asymmetric azidoethyl-diethylene oxide-ethyl mesylate spacer.

The cationic triphenylphosphonium ligand can be introduced using propargyltriphenylphosphine bromide **18** in which case it can be followed by a mesylate-azide exchange and a subsequent CuAAC to *exo*-*N*-(6-heptyn-1-yl)-norbornene dicarboximide **29**, scheme 31.



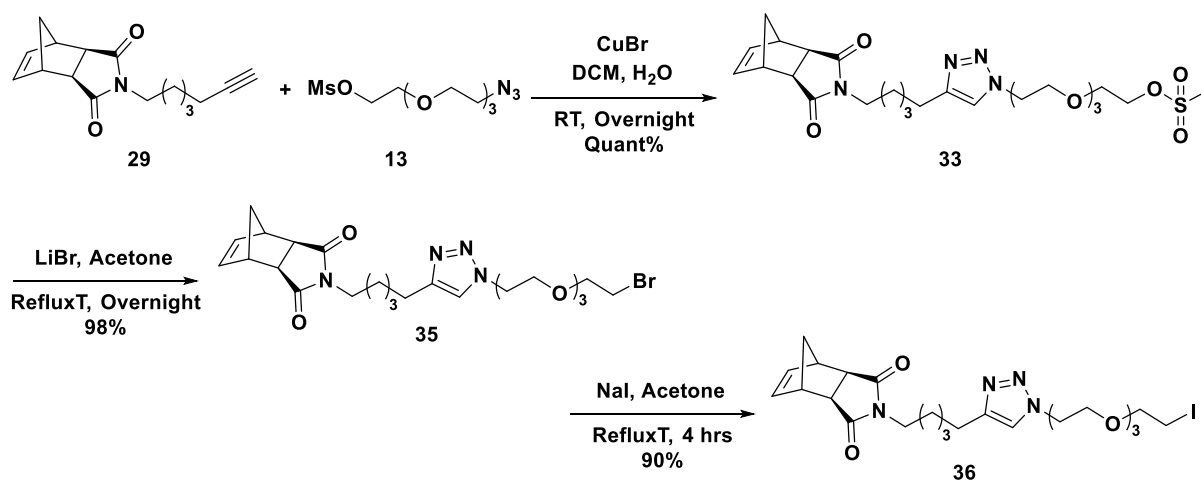
Scheme 31: Introduction of triphenylphosphonium mitochondrial targeting ligand via coupling of azidoethyl-diethylene oxide-ethyl mesylate to propargyltriphenylphosphine bromide followed by a mesylate-azide exchange and a subsequent CuAAC to *exo*-*N*-(6-heptyn-1-yl)-norbornene dicarboximide **29** to introduce the polymerizable end.

Because we were unable to predict the compatibility of triphenylphosphonium salts with nucleophilic substitution reactions employing hard nucleophiles such as azide anions, we decided to incorporate the cationic triphenylphosphonium ligand at the last stage of monomer synthesis via substitution of the mesylate group using PPh_3 as the nucleophile, scheme 32.



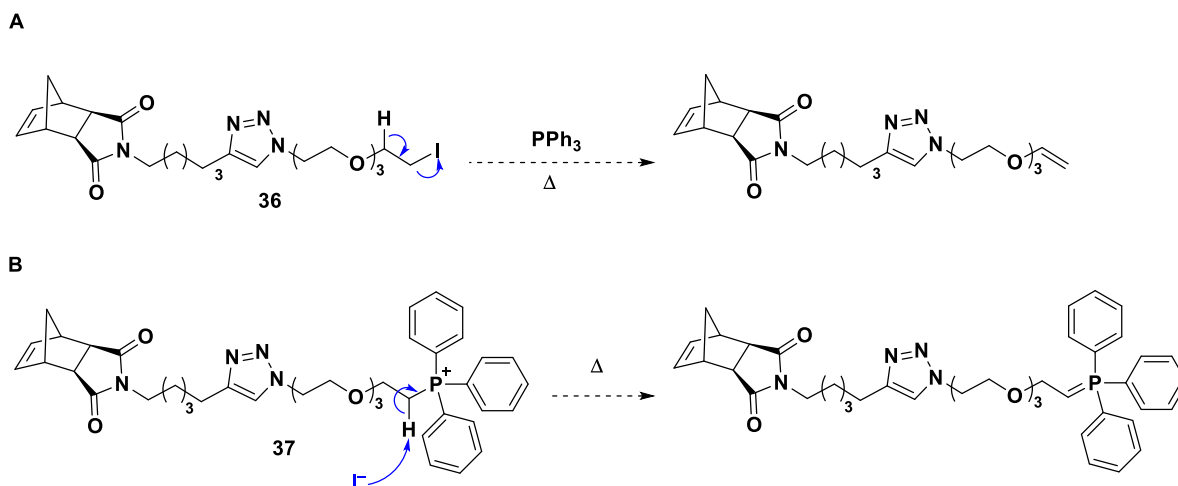
Scheme 32: Introduction of triphenylphosphonium mitochondrial targeting ligand via substitution of the mesylate using PPh_3 after a CuAAC to *exo-N*-(6-heptyn-1-yl)-norbornene dicarboximide prevent any unpredictable cross reactivity or decomposition of the phosphonium salt.

This monomer design was effectively accessed by coupling azidoethyl-diethylene oxide-ethyl mesylate 20 to *exo-N*-(6-heptyn-1-yl)-norbornene dicarboximide **29** via CuAAC to produce the terminal mesylate **33**, scheme 33. This was followed by a mesylate-bromide exchange and a subsequent bromide-iodide exchange to deliver the alkyl-iodide **36**. The iodide-mesylate substitution was attempted on the account of iodide being a better leaving group than mesylate. (**139**) Mesylate can be directly substituted with iodide, however, the step wise substitution of alkyl-mesylate **33** into alkyl-bromide **35** then alkyl-iodide **36** gave better yields, scheme 33. A final substitution reaction using PPh_3 as the nucleophile decorated the monomer with the mitochondrial targeting triphenylphosphonium iodide ligand *exo-N*-(6-pentyl-1)-norbornene dicarboximide triazole-ethyl-diethylene oxide-ethyl-triphenylphosphonium iodide **37**, henceforth referred to as NorbEO₄PPh₃I. We found that conditions of this substitution step need to drive substrate conversion to completion due to the lack of separation techniques, to our knowledge, that can isolate the phosphonium iodide product **37** from unreacted alkyl-iodide **36** under conditions that can maintain the stability of the phosphonium center in **37**. Gradient reversed-phase chromatographic purification of the triphenyl phosphonium salt employing solvent systems such as 0.1% TFA:H₂O:MeCN or 1M NH₄OAc:H₂O:MeCN resulted in its decomposition into a mixture of phosphorus-based products, detected by ³¹P NMR, that we were unable to identify. The only purification scheme we were able to perform whilst maintaining the stability of the phosphonium center is by sonicating the crude oil under ambient conditions in Et₂O to remove excess PPh_3 .



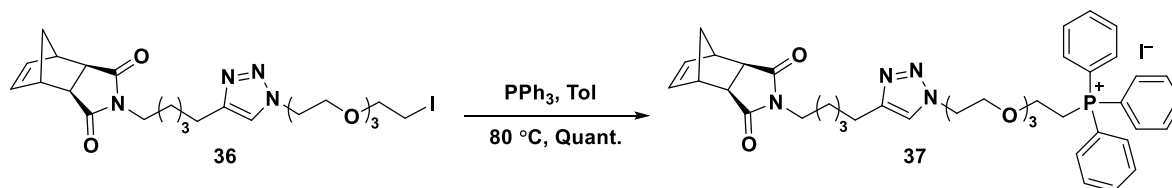
Scheme 33: Synthesis of terminal alkyl-mesylate **33** via CuAAC of exo-*N*-(6-heptyn-1-yl)-norbornene dicarboximide **29** to azidoethyl-diethylene oxide-ethyl mesylate **13**. This transformation was followed by a step-wise mesylate-halide substitution of alkyl-mesylate into alkyl-bromide then alkyl-iodide to facilitate the subsequent and final derivitization step to access the mitochondrial targeting ligand.

Because the substitution was thermodynamically driven, elimination reactions could be anticipated. Thermal decomposition of alkyl iodide **36** into terminal olefin is one of the background elimination reactions that can occur, scheme 34. (139) Additionally, thermal decomposition of the phosphonium salt **37** into the corresponding ylide as a result of the nucleophilic attack of the counterion halide on the methylene group preceding the phosphonium center is another background elimination reaction that may jeopardize the purity of the product, scheme 34. (140)



Scheme 34: Thermodynamically driven elimination of HI from alkyl-iodide **36** (A) or alkyl-phosphonium iodide **37** (B) as potential background reactions anticipated in the synthesis of alkyl-phosphonium iodide **37**.

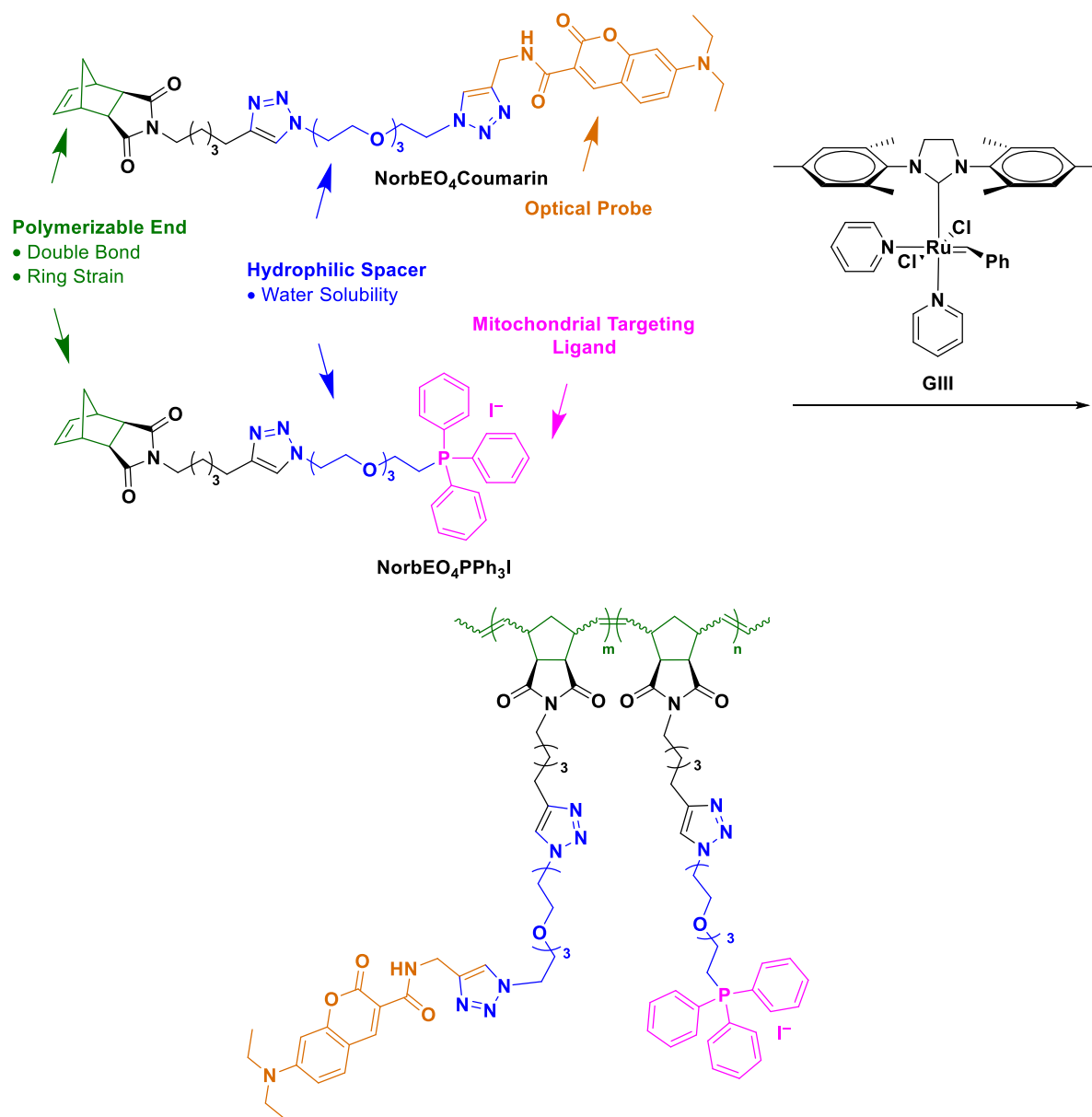
We found that warming up an excess of neat PPh_3 , 50 equivalents, to its melting point, $80\text{ }^\circ\text{C}$, at which the reaction's temperature was maintained at all times followed by dropwise addition of a solution of the alkyl-iodide **36** in dry and degassed toluene drives substrate conversion to completion and suppresses thermodynamically driven elimination reactions. Use of toluene aided in transferring the alkyl-iodide **36** precursor and maintaining the internal reaction temperature at $80\text{ }^\circ\text{C}$. Degassing the toluene prevented the oxidation of PPh_3 into $\text{PPh}_3(\text{O})$ making the isolation of the desired product go significantly smoother. These reaction conditions combined maximum substrate conversion and product stability, scheme 35.



Scheme 35: The optimal conditions in the substitution reaction that furnishes the desired alkyl-triphenylphosphonium iodide **37** using PPh_3 as the nucleophile. The conditions combined maximum substrate conversion and product and substrate stability. Excess PPh_3 can be recycled by dissolution in Et_2O followed by chromatographic purification.

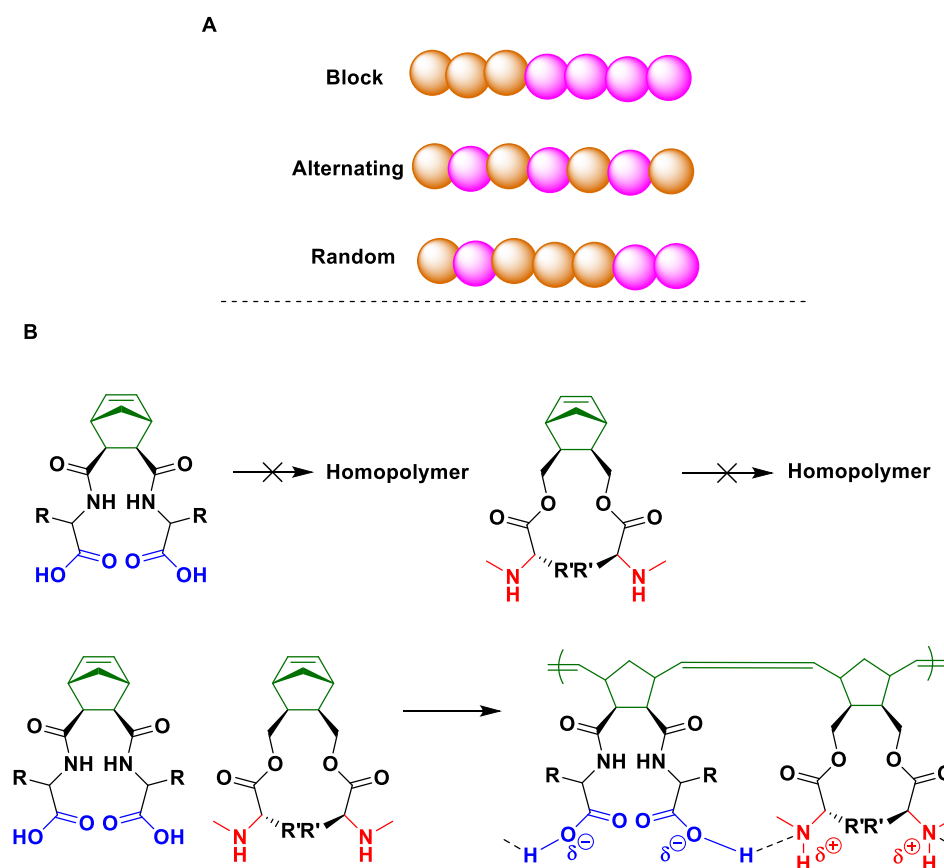
4.2.2 Homopolymers Synthesis and Characterization

As the aim of this project to prepare co-polymeric NPs that can target the mitochondria and be used for imaging to validate mitochondrial uptake, both monomers need to be precisely incorporated into the polymeric architecture, scheme 36. ROMP is a versatile tool in terms of how the monomers can be incorporated. ROMP can be used to generate block, alternating and random polymers, scheme 37.



Scheme 36: General design of co-polymers bearing hydrophilic segment, optical probe and mitochondrial targeting ligand synthesized from their corresponding monomers by ROMP mediated by Grubbs III catalyst.

The structure of polymerizable end of *N*-norbornene dicarboximide in the design depicted in scheme 36 lacks the functional groups that can induce alternation in the polymerization process as shown in scheme 37. Since variation in the ratio of each monomer will produce brush NPs with different properties, the precise incorporation of each monomer is essential for establishing water solubility, optical activity, cellular and subcellular uptake as well as viability profiles, we envisioned that block polymerization is the most precise approach to generating sequence-controlled brush polymers.



Scheme 37: (A) Modes of polymerization using ROMP technique. The figure depicts two monomers of different structure indicated, by the two colors orange and pink, copolymerized in block, alternating or random fashion. (B) Alternate ROMP of aminoacid derived monomers having carboxylic and amino groups initiated by Grubbs III catalyst. The alternation in monomer insertion in the propagating polymer chain was driven by the acid-base interaction between the penultimate unit in the propagating chain and the incoming monomer. Scheme is adapted from Ref. (172)

To predict the ability of our monomers to undergo block polymerization, we investigated the kinetics of their homo-polymerization and evaluated the quality of the resulting polymeric architectures using ^1H NMR and GPC. We assumed that before and after the point of crossing over from one monomer sequence to another in a block-*co*-polymerization reaction, the homo-polymerization behavior of each monomer in its corresponding block is comparable to that observed during homo-polymerization of each monomer separately, figure 32. In practical terms, this means that the *co*-polymerization process should feature a living nature during the homo-polymerization of each monomer in its corresponding

sequence. As inspired by all the literature precedent, the livingness of ROMP is marked by the first order dependence of the polymerization rate on monomer concentration, the close match between predicted and observed M_n and narrow molecular weight distribution. (27) (7) (91)

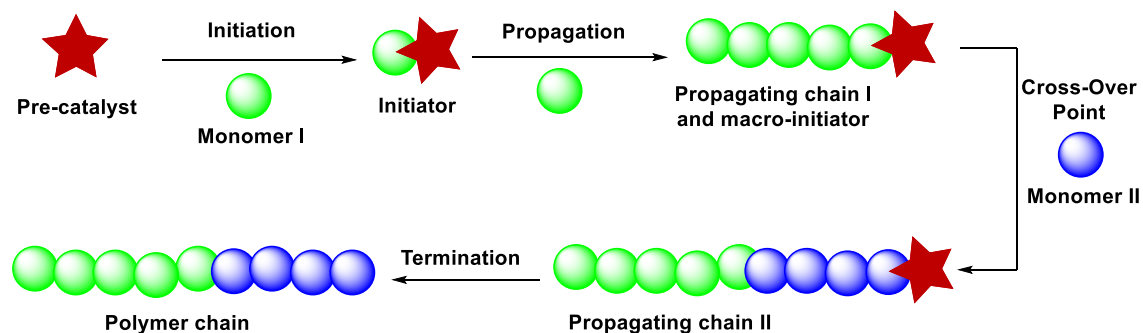


Figure 32: Illustration of stages of block polymerization of two structurally different monomers (green and blue) initiated by a pre-catalyst (red). The discussion in this section relates to the behavior of homo-polymerization of each monomer in its designated sequence before and after the cross-over point in a copolymerization reaction.

Homo-ROMP of our first-generation monomers, scheme 36, was initiated by GIII and conducted at constant initial monomer concentration of 0.1-0.05 M in DMF. Homo-polymerization of more dilute monomer solution struggled to reach complete consumption of monomer. More concentrated monomer solutions were practically difficult to prepare as the corresponding solvent volumes were not sufficient to homogeneously dissolve the monomer samples. Solvent effect was not explored as the polymerization was hampered by coagulation observed when THF or chloroform were the solvent of choice.

4.2.2.1 Homo-Polymerization ¹H NMR Kinetics

Polymerization rate dependence on monomer concentration for the homo-polymerization of NorbEO₄Coumarin and NorbEO₄PPh₃I at 10, 20, 30 and 40 equivalents with respect to GIII catalyst was determined using ¹H NMR. This was achieved by monitoring the lapse of olefinic signal of the polymerizable N-norbornene dicarboximide end over time as described in the experimental section in detail. The ¹H NMR kinetics of the homo-polymerization of NorbEO₄Coumarin exhibited a deviation from the pseudo-first order kinetic profile associated with living ROMP. Pseudo-first order ROMP obeys the pseudo-first order rate law described by:

$$-\frac{\partial[M]}{\partial t} = k_{obs}[M]_t ;$$
$$k_{obs} = k_{homo}[G]_0$$

Where $-\partial[M]/\partial t$, k_{obs} , $[M]_0$, and $[M]_t$ designates the rate of monomer consumption over time, observed rate constant, initial monomer concentration and monomer concentration at the corresponding time point respectively. k_{homo} is the rate constant of homopolymerization and $[G]_0$ is the catalyst's initial concentration.

Second-order kinetic profile is more fitted for describing NorbEO₄Coumarin homopolymerization behavior which could be an indication of background secondary metathesis events, figure 33. The homo-polymerization of NorbEO₄Coumarin was conducted at an initial $[M]_0$ of 0.10 M because its homo-polymerization at $[M]_0 = 0.05$ M exhibited polymerization kinetics that significantly deviated from that of pseudo-first order. In contrast, the homopolymerization of NorbEO₄PPh₃I showed a first-order dependence of homo-polymerization rate on monomer concentration as illustrated by the line plots of time versus the logarithmic values of $[M]_0/[M]_t$, figure 34.

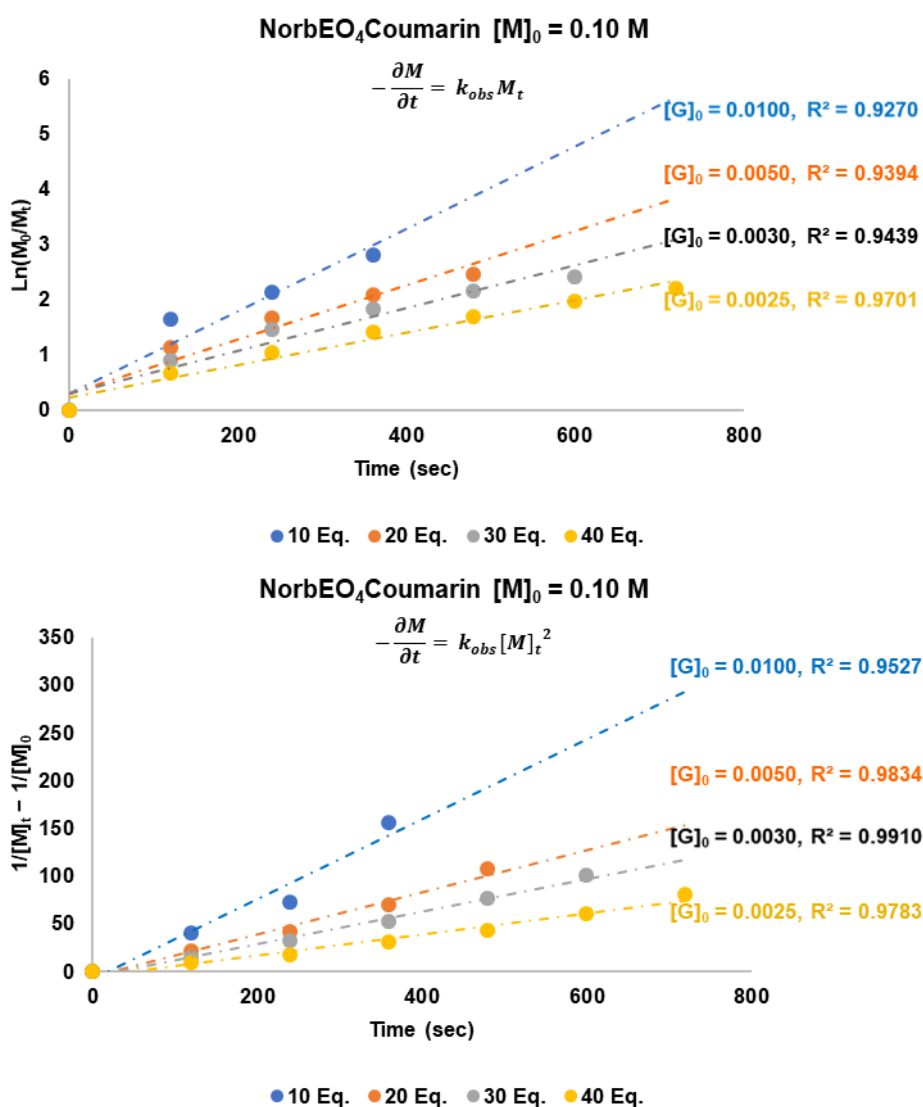


Figure 33: Line plots of $\ln([M]_0/[M]_t)$, top, and $1/[M]_t - 1/[M]_0$, bottom, versus time, showing that second-order kinetic profile is more fitted for describing the homopolymerization behavior of NorbEO₄Coumarin. The homo-polymerization of a solution of NorbEO₄Coumarin with an initial concentration of 0.10 M, reached after addition of catalyst solution, was initiated by Grubbs III catalyst in DMF at 298 K. The homo-polymerization was carried out at monomer to initiator ratio of 10 (blue), 20 (orange), 30 (grey) and 40 (yellow) equivalents. The line plots show the second-order dependence of homo-polymerization rate on $[M]$ as described by the second-order rate equation:

$$-\frac{\partial [M]}{\partial t} = k_{obs}[M]_t^2$$

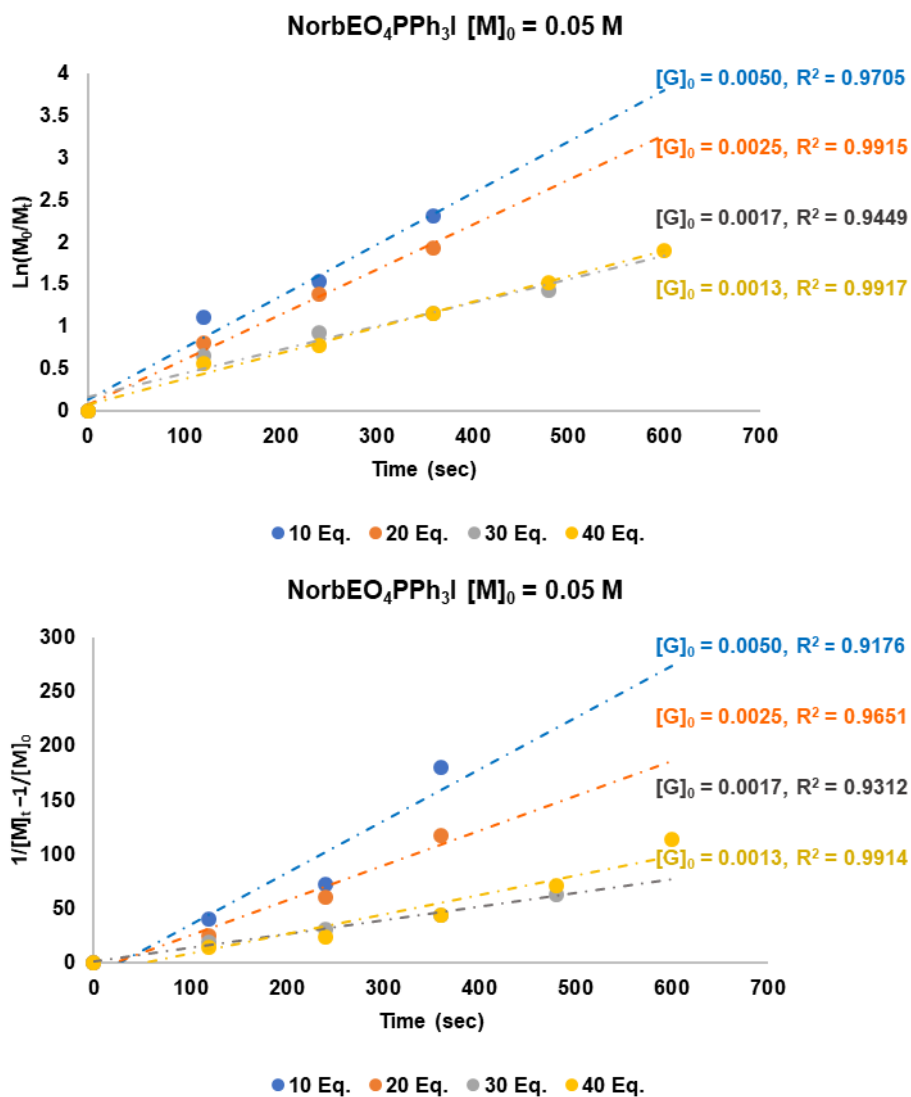


Figure 34: Line plots of $\ln([M]_0/[M]_t)$, top, and $1/[M]_t - 1/[M]_0$, bottom, versus time, showing that pseudo-first order kinetic profile is more fitted for describing the homopolymerization behavior of NorbEO₄PPh₃I. The homo-polymerization of a solution of NorbEO₄PPh₃I with an initial concentration of 0.05 M, reached after addition of catalyst solution, was initiated by Grubbs III catalyst in DMF at 298 K. The homo-polymerization was carried out at monomer to initiator ratio of 10 (blue), 20 (orange), 30 (grey) and 40 (yellow) equivalents. The line plots show the pseudo-first order dependence of homo-polymerization rate on $[M]$ as described by the second-order rate equation:

$$-\frac{\partial[M]}{\partial t} = k_{\text{obs}}[M]_t$$

4.2.2.2 Evaluation of Propagating Homo-Polymer Chains of First-Generation Monomers

GPC was used to determine the M_n and \bar{D} of the final polymeric products of the homo-polymerization reaction described above, after quenching with ethyl vinyl ether (EVE), in attempt to further assess the living nature of the homo-polymerization process. GPC traces, appendix 1, and analysis, presented in table 3, show a deviation of M_n from theoretical values that was consistent across all polymerization experiments.

Monomer	[M] ₀	M/I ^a	k_{Obs}^b 10 ⁻³ s ⁻¹	M ^c conv.%	$Mn_{Theo.}^d$ kDa	$Mn_{Obs.}^e$ kDa	DP ^f	$\bar{D}_{Obs.}^e$
NorbEO₄Coumarin	0.10 M	10	7.4	94	8.1	5.2	6	1.10
		20	4.9	91	16	11	13	1.15
		30	3.9	91	24	17	21	1.34*
		40	2.9	89	33	20	25	1.20*
NorbEO₄PPh₃I	0.05 M	10	6.4	90	8.5	5.3	6	1.12
		20	5.3	86	17	10	12	1.13
		30	2.8	80	25	13	15	1.13
		40	3.0	85	34	17	21	1.16

Table 3: ^(a)Monomer to initiator ratio also referred to as number of equivalents of monomer with respect to initiator. ^(b)Observed rate of homo-polymerization determined by ¹H NMR as described in the previous section. ^(c)Determined by ¹H NMR as described in the experiments section. ^(d)Estimated by calculating the product of M/I and M_w of monomer. ^(e) Determined using GPC; samples were run in LiBr in DMF (0.2 M) and M_n were assigned relative to a standard curve calculated using polyethylene glycol standards. ^(f)Calculated by dividing the M_n values over M_w of corresponding monomer. Results show the deviation of $Mn_{Obs.}$ From $Mn_{Theo.}$. * \bar{D} values higher than ideal value which could be an indicative of secondary-metathesis events. (85)

GPC results of the homo-polymers show a linear dependency of Mn_{Obs} on M/I, figure 35. \bar{D} values of most homo-polymer samples remain below 1.2, except the two marked by an asterisk, Ideally, \bar{D} values need to be as close as possible to 1.0 for a polymerization to be considered living. (85) (91)

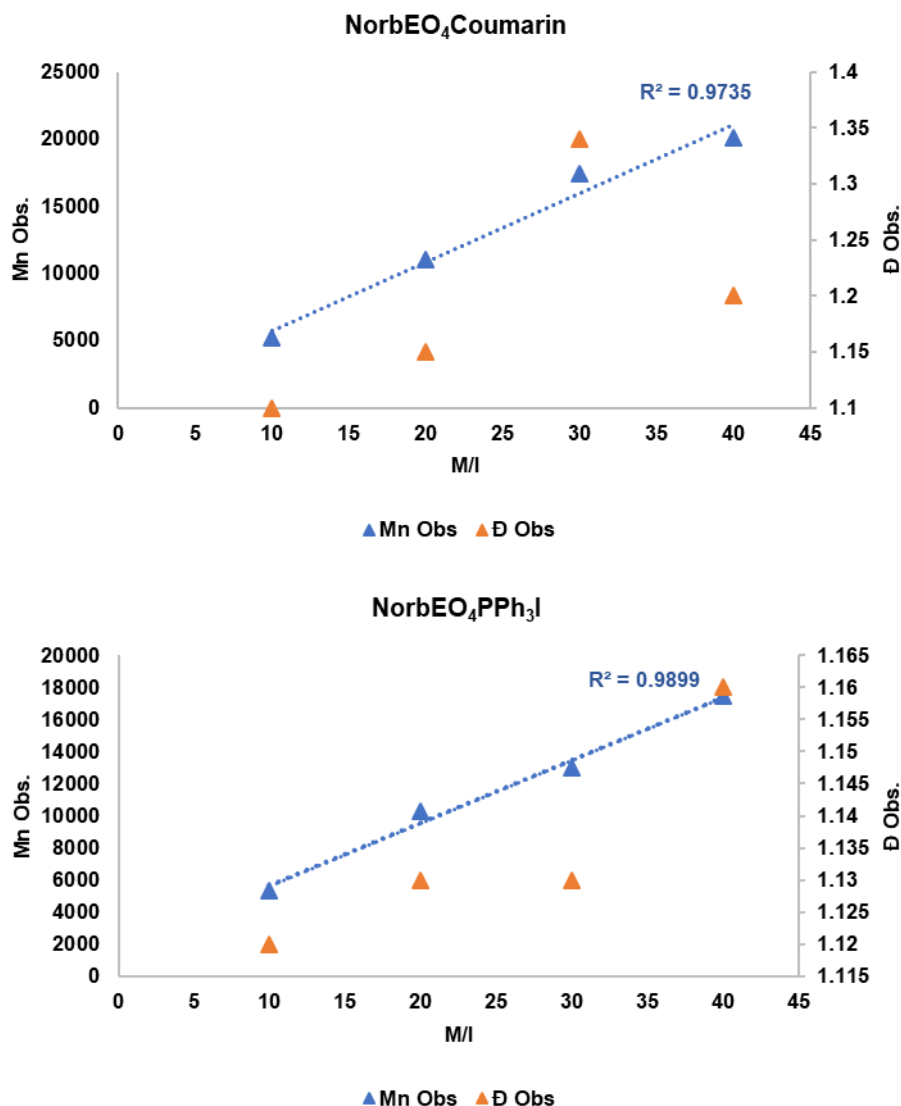


Figure 35: Linear dependence of observed number average molecular weight, M_n , of homo-polymer samples of both NorbEO₄Coumarin and NorbEO₄PPh₃I on monomer to initiator ratio, M/I , a feature of living polymerization. (85) Dispersity indices remain below 1.2 for most homo-polymer samples. Ideally, \bar{D} values need to be as close as possible to 1.0 for a polymerization to be considered living. (85) (91)

GPC analysis of the ¹H NMR samples, after quenching and preparation as described in experimental section, allowed for the estimated evaluation of progression of the M_n and \bar{D} during the propagation stage of the homo-polymerization process. GPC traces show the anticipated increase of M_n of the propagating chain over time due to iterative insertion of monomer molecules. Further analysis of these traces shows a broadening of the peak, of a factor of 1.01-1.05, corresponding to the propagating species overtime, figure 36, and table 4. This could be an indicative of secondary metathesis events.

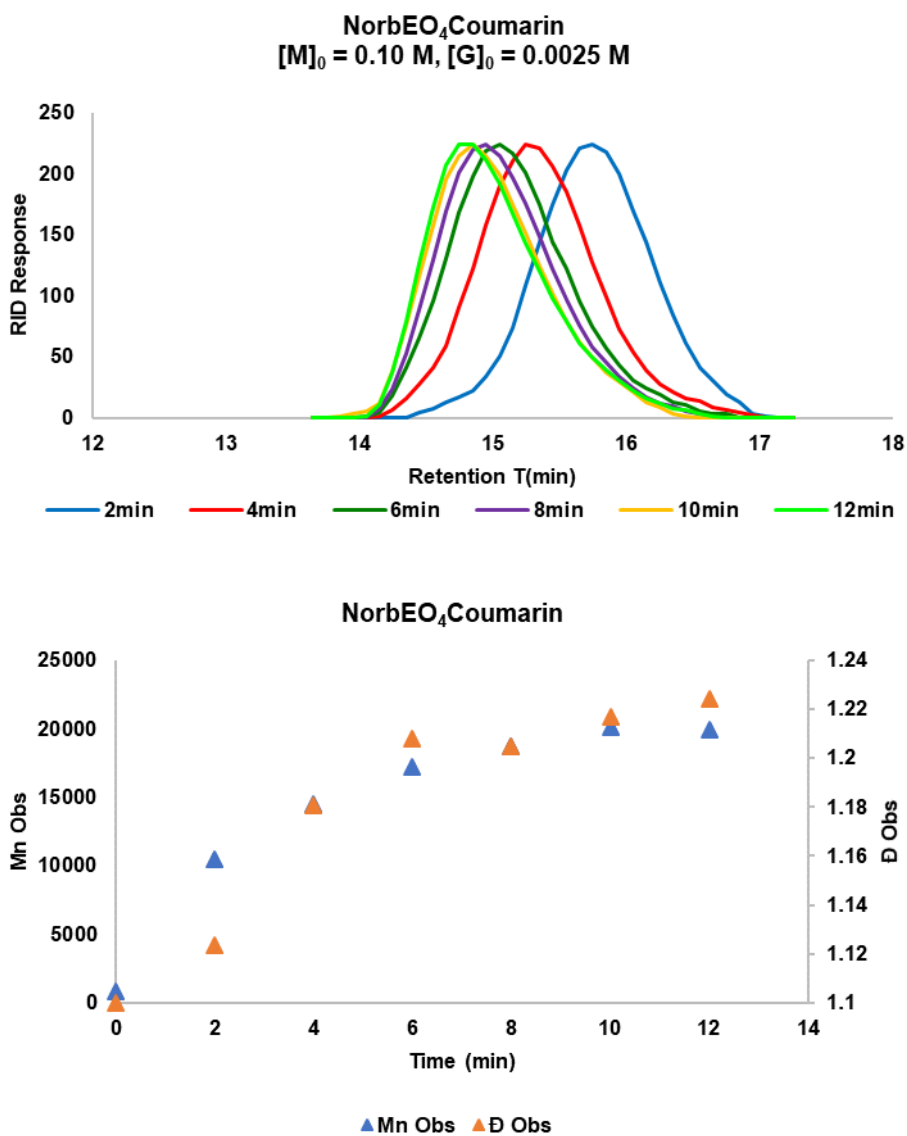


Figure 36: (Top) GPC traces of ¹H NMR samples of the homo-polymerization aliquots withdrawn from the reaction mixture at 2 min intervals. The GPC samples were prepared by quenching of the ¹H NMR sample with EVE, evaporation and redissolution in DMF. The traces were acquired at 30 °C using LiBr in DMF (0.2 M) as the eluting solvent with a flow-rate of 0.8 mL/min. (Bottom) Further analysis of the GPC traces reveal the anticipated increase in Mn over time as a result of insertion of monomer molecules into the growing polymer chain (blue triangles). The analysis also reveals the increase in *D* marked by broadening of the product peak of a factor of 1.01-1.5 overtime.

Monomer	Time (min)	Mn _{Obs.} kDa	Đ _{Obs.}	Broad. F.
NorbEO₄Coumarin	0	8.1	1.10	1
	2	11	1.12	1.02
	4	14	1.18	1.05
	6	17	1.21	1.02
	8	17	1.20	1.0
	10	20	1.22	1.01
	12	20	1.22	1.01

Table 4: Mn and Đ values of the ¹H NMR kinetic study samples obtained by GPC after quenching with EVE, evaporation and redissolution in DMF. Mn values of the propagating chain increased over time as a result of insertion of monomer molecules into the growing polymer chain so as the Đ values by a factor of 1.01-1.05 overtime.

4.2.3 Biocompatibility of First-Generation Ring-Opening Metathesis Homopolymers

The aim of establishing the biocompatibility profile of the first-generation of homo-polymers is to determine the ratio of fluorescent to mitochondrial targeting monomers to be incorporated into the structure of first-generation copolymers that can maintain a minimal cytotoxic effect. The biocompatibility assays screen the cellular viability of a chosen cell line against a range of concentrations of NPs' solution. The concentration range selected for this purpose was 0-100 μM. Unfortunately, no water solubility was observed at this range of concentrations. Therefore, the biocompatibility examination of this generation of homo-polymers was aborted. An attempt to solve water solubility issues was made and is discussed in the next chapter.

4.2.4 Summary

Synthesis plan was designed and to prepare first generation monomers. The monomers successfully underwent ROM homo-polymerization generating corresponding brush polymers with moderately broad molecular weight distribution. The homo-polymers lack of water solubility prevented us from going further towards assessing their biocompatibility.

5 Revised Synthesis of Homo- and *Co*-polymers via Ring Opening Metathesis Polymerization

Polymerization

In this section, the synthesis of our second-generation ROMP monomers that feature the same basic structural elements as first-generation monomers except for the longer hydrophilic segment is described, figure 37. The tetra-ethylene glycol-based spacer was replaced with a dodeca-ethylene glycol-based one to enhance water solubility of the corresponding polymeric products. The monomers were subjected to homo-ROMP to further validate conditions under which ROMP is living and examine their propensity for block-polymerization. Homopolymers show an overall enhanced water solubility, yet water solubility of NorbEO₁₂Coumarin-derived homo-polymers remains limited. Consequently, only biocompatibility of NorbEO₁₂PPh₃I-derived homo-polymers was examined and *co*-polymers were synthesized with higher ratio of NorbEO₁₂PPh₃I to NorbEO₁₂Coumarin. NPs are showing a promising cellular uptake, yet no mitochondrial uptake under the employed conditions is detected.

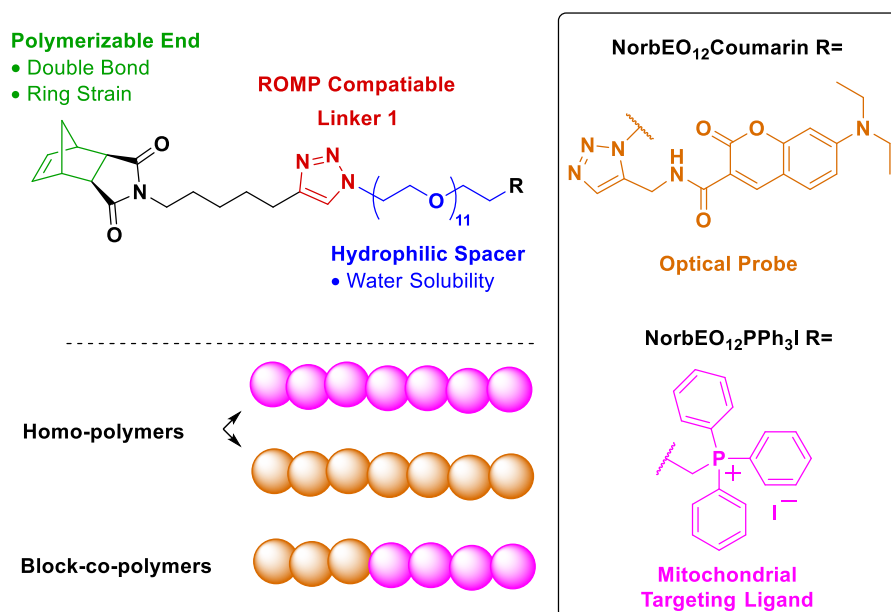
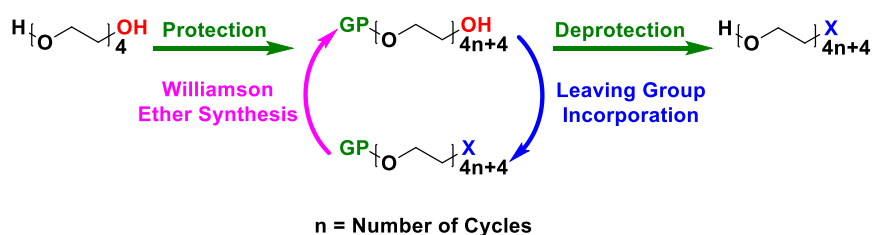


Figure 37: (Top) Brief illustration of general the structure of both monomers, fluorescent and mitochondrial targeting featuring the same structural elements as the first-generation monomers. Monomer's structure features a polymerizable end, hydrophobic spacer, DodecaEG-based hydrophilic segment and a terminal group that is either fluorescent, to make up NorbEO₁₂Coumarin, or mitochondrial targeting, to access NorbEO₁₂PPh₃I. (Bottom) The monomers were subject to both homo-polymerization, to validate the conditions under which the polymerization of these monomers is living, and co-polymerization to synthesize fluorescent and mitochondrial targeting co-polymers.

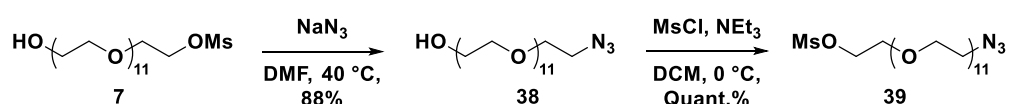
5.1 Revised Monomer Synthesis

Since the homo-polymers prepared from first-generation monomers were unable to overcome the first biological barrier in drug delivery, that is water solubility, we revised our monomer design to feature a three-fold longer hydrophilic spacer DodecaEG. The synthesis of the asymmetric spacer, hydroxy-undeca-ethylene oxide-ethyl mesylate **7**, was described in detail in the second chapter. Briefly, the synthesis proceeded by mono-protection of tetra-ethylene glycol with a trityl group and a subsequent mesylation and Williamson ether-synthesis steps, scheme 38.



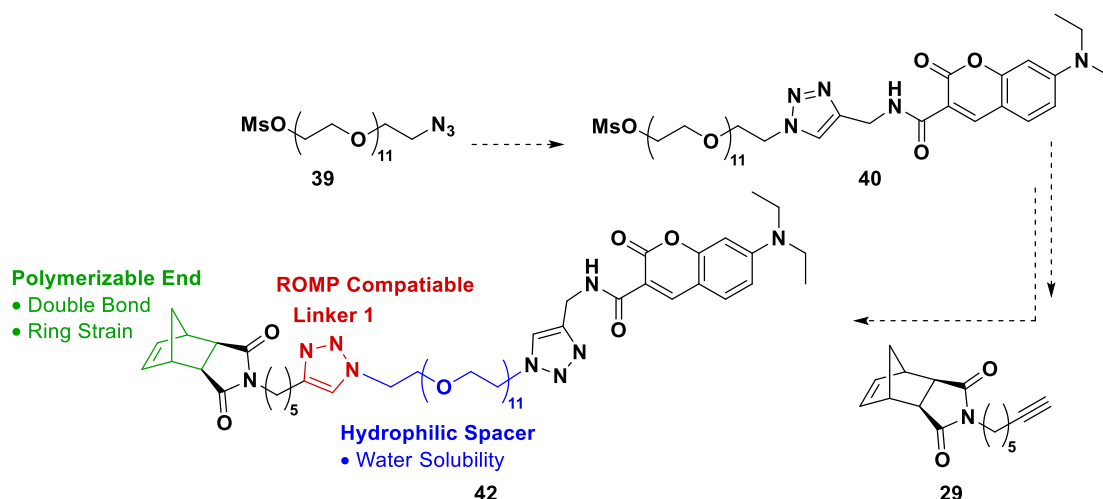
Scheme 38: Illustration of the general synthesis scheme of hydroxy-undeca-ethylene oxide-ethyl mesylate spacer used as a building block in the synthesis of second-generation monomers.

The mesylation followed by ether synthesis cycle was repeated twice to achieve the three-fold elongation of the ethylene glycol-based linker featured in first-generation monomers. A final mesylation and a subsequent deprotection of the trityl- group constituted the final steps towards the synthesis of hydroxy-undeca-ethylene oxide-ethyl mesylate **7** used in the synthesis of our second-generation monomers. This transformation was followed by a tosylate-azide exchange and a subsequent mesylation to afford the bifunctional azido-undecaethylene oxide-ethyl mesylate **39**, scheme 39.



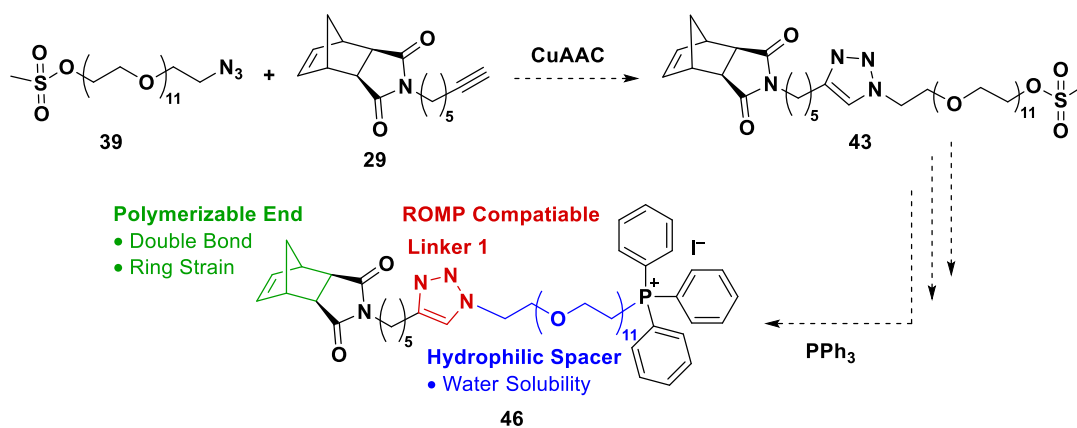
Scheme 39: The transformation of hydroxy-undeca-ethylene oxide-ethyl mesylate into the asymmetric bifunctional azido-undecaethylene oxide-ethyl mesylate spacer

The synthetic plan of the second-generation monomers was inspired from first-generation monomer's synthesis results. The bifunctional azido-undecaethylene oxide-ethyl mesylate spacer **39** was envisioned to be useful for the synthesis of both, the fluorescent NorbEO₁₂Coumarin and mitochondrial targeting NorbEO₁₂PPh₃I monomers, if the sequence of coupling of the structural elements of both was chosen carefully. We envisioned that CuAAC of azido-undecaethylene oxide-ethyl mesylate **39** to 7-(diethylamino)coumarin-3-carboxylic propargylamide **17**, followed by mesylate-azide exchange and, lastly, CuAAC to *exo-N*-(6-heptyn-1-yl)-norbornene dicarboximide would prevent intramolecular cycloaddition, if the sequence was in reverse, and furnish the fluorescent **42**, or NorbEO₁₂Coumarin, product, scheme 40.



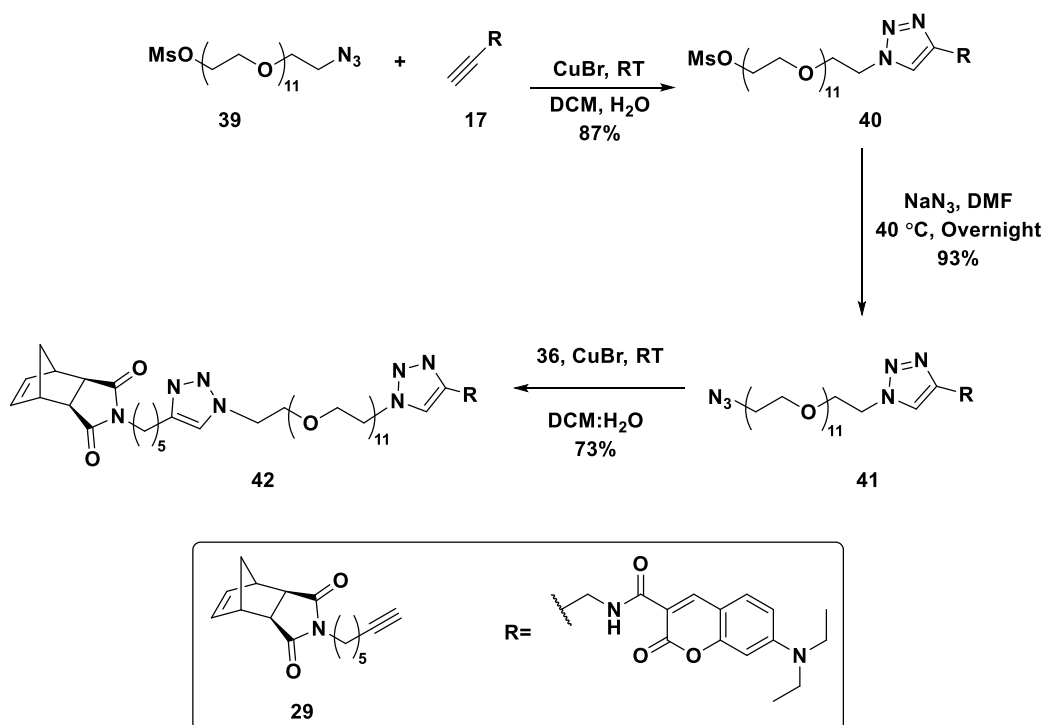
Scheme 40: The planned sequence of incorporating the fluorescent component, via coupling of hydrophilic spacer **39** to 7-(diethylamino)coumarin-3-carboxylic propargylamide **17** followed by coupling of the resulting product (not shown) to *exo-N*-(6-heptyn-1-yl)-norbornene dicarboximide **29** to synthesize the fluorescent **42**, or NorbEO₁₂Coumarin.

As for **46**, or NorbEO₁₂PPh₃I, monomer, CuAAC of azido-undecaethylene oxide-ethyl mesylate **39** to *exo-N*-(6-heptyn-1-yl)-norbornene dicarboximide followed by a direct or step-wise mesylate-iodide exchange and, lastly, a nucleophilic substitution using PPh₃ would generate the desired the mitochondrial targeting monomer, scheme 41.



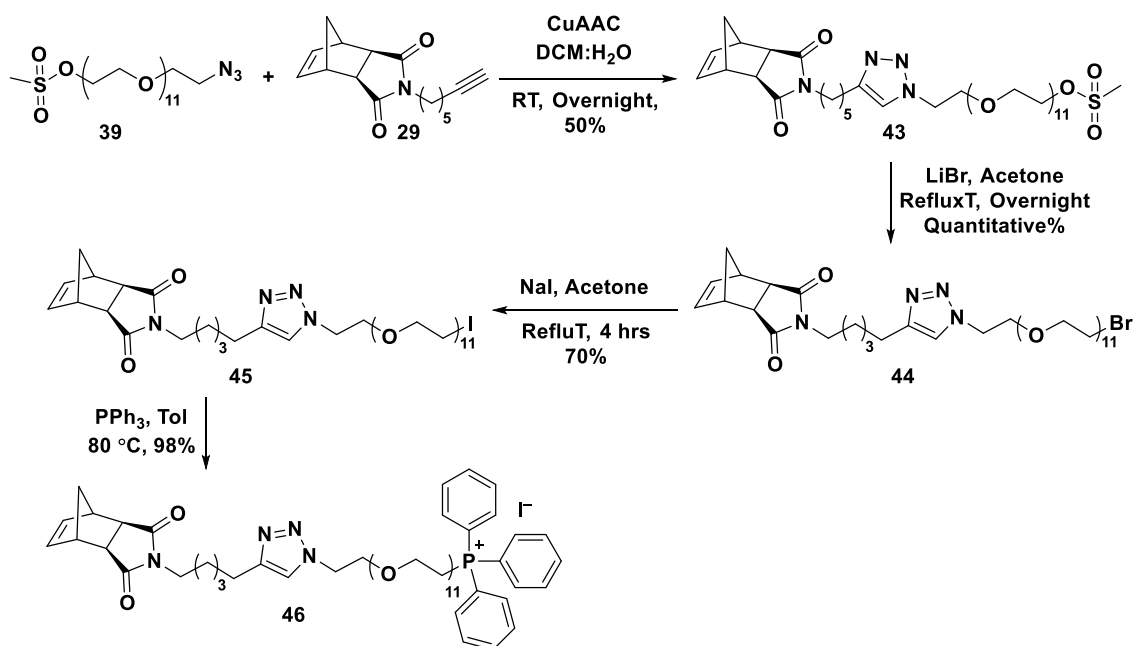
Scheme 41: The planned sequence of incorporating the fluorescent component, via coupling of hydrophilic spacer **46** to *exo-N*-(6-heptyn-1-yl)-norbornene dicarboximide **29** followed by mesylate-iodide (product not shown) and a final nucleophilic substitution using PPh₃ to synthesize the **46**, or NorbEO₁₂PPh₃I.

Indeed, CuAAC of azido-undecaethylene oxide-ethyl mesylate **39** to 7-(diethylamino)coumarin-3-carboxylic propargylamide **17** successfully generated the alkyl-mesylate **40**. A subsequent mesylate-azide exchange yielded the terminal alkyl-azide **41**, scheme 42. A CuAAC step between the aforementioned terminal azide and *exo-N*-(6-heptyn-1-yl)-norbornene dicarboximide produced our second-generation fluorescent ROMP monomer **42**, henceforward referred to as NorbEO₁₂Coumarin.



Scheme 42: CuAAC of alkyl-mesylate **39** to coumarin derivative **17** to furnish alkyl-mesylate **40** followed by mesylate-azide exchange using NaN_3 then another CuAAC of resulting terminal-azide **41** to *exo-N*-(6-heptyn-1-yl)-norbornene dicarboximide **29** to furnish **42** or NorbEO₁₂Coumarin.

On the other hand, the synthesis of the mitochondrial targeting monomer proceeded with a CuAAC of the same hydrophilic linker, azido-undecaethylene oxide-ethyl mesylate **39**, to *exo-N*-(6-heptyn-1-yl)-norbornene dicarboximide **29** producing alkyl-mesylate **43**, scheme 43. This transformation was followed by a mesylate-bromide exchange and a subsequent bromide-iodide exchange to deliver the alkyl-iodide **45**. As rationalized in the previous section, the iodide-mesylate substitution was attempted on the account of iodide being a better leaving group than mesylate and the step wise substitution of alkyl-mesylate **43** into alkyl-bromide **44** then alkyl-iodide **45** gave better yields. A final substitution reaction using PPh_3 as the nucleophile decorated the monomer with the mitochondrial targeting triphenylphosphonium iodide ligand **46**, henceforth referred to as NorbEO₁₂PPh₃I.



Scheme 43: Synthesis of alkyl-mesylate **43** via CuAAC of exo-*N*-(6-heptyn-1-yl)-norbornene dicarboximide **29** to azidoethyl-decaethylene oxide-ethyl mesylate **39** followed by a Step-wise mesylate-halide substitution to facilitate the subsequent and final substitution step using PPh₃ to access the mitochondrial targeting **46** or NorbEO₁₂PPh₃I.

5.2 Homo- and Co-Polymers Synthesis and Characterization

The homo-polymerization behavior of second-generation monomers was assessed similarly to the homo-polymerization of first-generation monomers to further validate the living polymerization conditions and propensity of monomers for block-*co*-polymerization.

5.2.1 Homo-Polymerization ¹H NMR Kinetics

Polymerization rate dependence on monomer concentration for the homo-polymerization of NorbEO₁₂Coumarin and NorbEO₁₂PPh₃I at 20, 30, 40, 50 and 60 equivalents with respect to GIII catalyst was determined using ¹H NMR. This was achieved by monitoring the lapse of olefinic signal of the polymerizable *N*-norbornene dicarboximide end over time as described in the experimental section in detail. The ¹H NMR kinetics of the homo-polymerization of NorbEO₁₂Coumarin and NorbEO₁₂PPh₃I exhibited a pseudo-first order dependence of homo-polymerization rate on monomer concentration as depicted in figure 38.

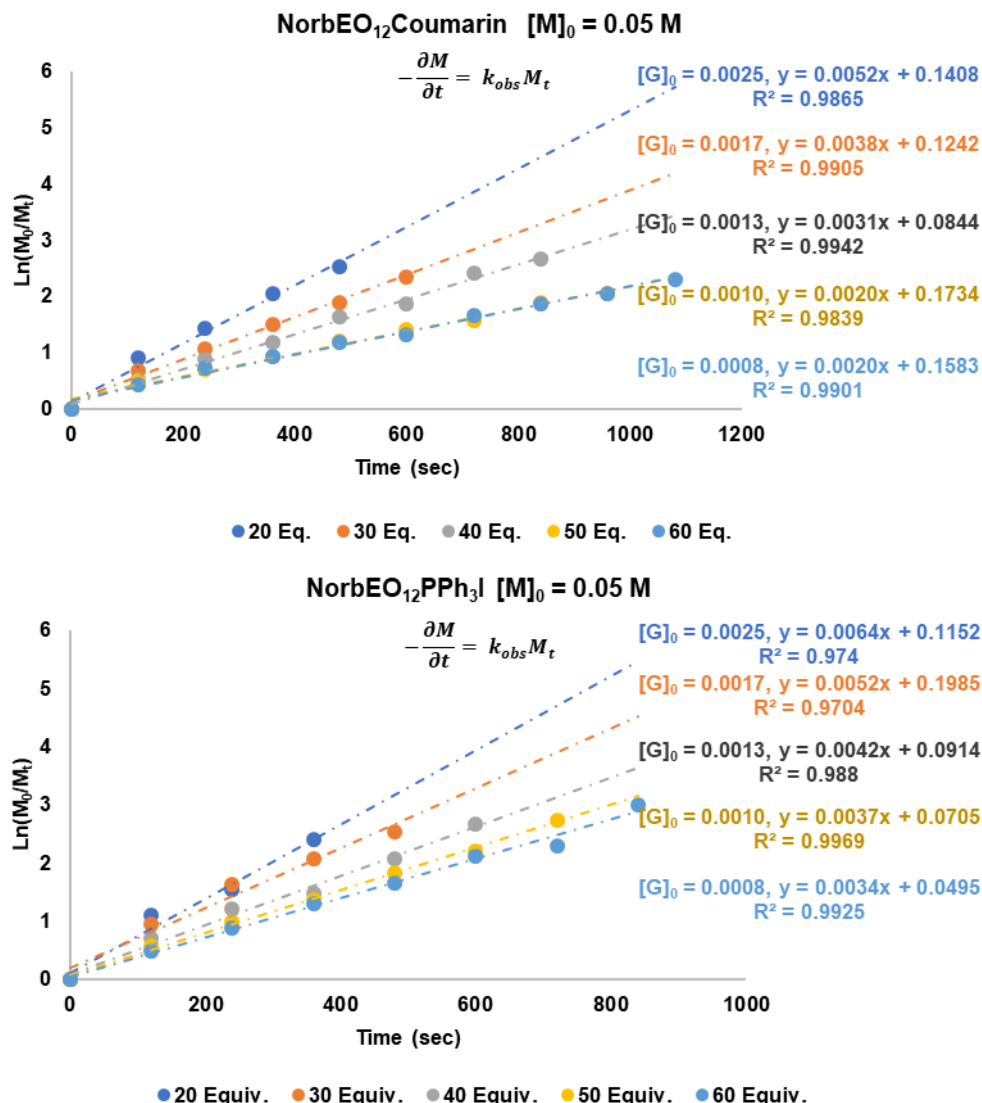


Figure 38: : Line plots of $\ln([M]_0/[M]_t)$ versus time, showing first-order kinetics for the homo-polymerization of NorbEO₁₂Coumarin (top) and NorbEO₁₂PPh₃I (bottom) solution with an initial concentration of 0.05 M. The homo-polymerization was initiated by Grubbs III catalyst in DMF at 298 K. The homo-polymerization was carried out at monomer to initiator ratio of 20 (blue), 30 (orange), 40 (grey), 50 (yellow) and 60 (cyan) equivalents. The line plots show the first order dependence of homo-polymerization rate on [M] as per the first-order rate equation:

$$-\frac{\partial [M]}{\partial t} = k_{obs}[M]_t$$

In comparison to first-generation homo-polymers' kinetic profile, these results suggest that end groups, coumarin and triphenyl phosphonium, may influence the homo-polymerization kinetics and elongation of the hydrophilic spacer reduces the extent of this influence. The values of the observed rate constant of homo-polymerization listed in table 5 show an effect of end-group interactions on the rate of polymerization. The interaction between coumarin molecules decreases the rate of the homo-polymerization of NorbEO₁₂Coumarin by a factor of ≈ 1.4 , for values in **bold**, compared to rate of

homo-polymerization of NorbEO₁₂PPh₃I. A comparison of the rate of homo-polymerization of second-generation monomer, NorbEO₁₂PPh₃I, to that of first generation, NorbEO₄PPh₃I, shows that the rate of homo-polymerization scales up by a factor of ≈ 1.3 , for underlined values, with increasing length of hydrophilic spacer.

M/I ^a	[G] ₀	NorbEO ₄ PPh ₃ I		NorbEO ₁₂ Coumarin		NorbEO ₁₂ PPh ₃ I	
		DP ^b	$k_{Obs}^c \cdot 10^{-3} s^{-1}$	DP ^b	$k_{Obs}^c \cdot 10^{-3} s^{-1}$	DP ^b	$k_{Obs}^c \cdot 10^{-3} s^{-1}$
10	0.005	6	6.4	-	-	-	-
20	0.0025	<u>12</u>	<u>5.3</u>	13	5.2	<u>12</u>	<u>6.4</u>
30	0.0017	15	2.8	17	3.8	17	5.2
40	0.0013	<u>21</u>	<u>3.0</u>	21	3.1	<u>21</u>	<u>4.2</u>
50	0.0010	-	-	28	2.0	25	3.7
60	0.0008	-	-	28	2.0	22	3.4

Table 5: ^(a)Monomer to initiator ratio, **M/I**, also referred to as number of equivalents of monomer with respect to initiator. ^(b)Calculated by dividing the Mn values, determined by **GPC**, over Mw of the corresponding monomer. ^(c) Observed rate of homo-polymerization determined by ¹H NMR as described in the experimental section.

These results proved useful from a practical point of view when the *co*-polymerization of the two monomers, NorbEO₁₂Coumarin and NorbEO₁₂PPh₃I, was attempted. ROMP must always be monitored and terminated as soon as a maximum conversion of monomer is reached to minimize secondary metathesis cascades. (85) Thus, knowledge of the homo-polymerization rate of a monomer at a known initial concentration and M/I defines the time window within which the polymerization is expected to reach maximum conversion of monomer. (85) The kinetics of the homo-polymerization of NorbEO₄Coumarin was not included in the analysis of the effect of end-group interactions on the homo-polymerization kinetics as it was conducted at different concentration, 0.1 M.

5.2.2 Evaluation of Propagating Homo-Polymer Chains of Second-Generation Monomers

GPC was used to determine the M_n and \mathcal{D} of the final polymeric products of the homo-polymerization reaction described above, after quenching with EVE, in attempt to further assess the living nature of the homo-polymerization process. GPC traces, appendix 2, and analysis, presented in table 6, show the deviation of M_n from theoretical values described in the previous chapter. Nonetheless, the GPC results of the homo-polymers show a linear dependency of $M_{n,Obs.}$ on M/I , figure 39. \mathcal{D} values of most homo-polymer samples remain below 1.2, except the three marked by an asterisk. Ideally, \mathcal{D} values need to be as close as possible to 1.0 for a polymerization to be considered living. (85) (91) No improvement in the molecular weight distribution, symbolized by \mathcal{D} , that was anticipated for second-generation homo-polymers was observed in comparison to first-generation homo-polymers. This invites the question of whether our approach of assigning molecular weight, M_n , and molecular weight distribution, \mathcal{D} , of branched polymeric architectures relative to a calibration curve of linear polymeric standards is an accurate one.

Monomer	$[M]_0$	M/I^a	conv.% ^b	$M_{n,Theo}$ kDa ^c	$M_{n,Obs.}$ kDa ^d	DP^e	$\mathcal{D}_{Obs.}^f$
NorbEO₁₂Coumarin	0.05 M	20	82	23	15	13	1.20*
		30	81	35	20	17	1.20*
		40	86	46	24	21	1.20*
		50	87	58	33	28	1.16
		60	82	70	32	28	1.17
NorbEO₁₂PPh₃I	0.05 M	20	98	24	14	12	1.14
		30	92	36	21	17	1.18
		40	93	48	25	21	1.18
		50	95	60	30	25	1.18
		60	95	72	29	22	1.17

Table 6: ^(a)Monomer to initiator ratio also referred to as number of equivalents of monomer with respect to initiator. ^(b)Determined by ¹H NMR as described in the experimental section. ^(c)Estimated by calculating the product of M/I and M_w of monomer. ^(d) Determined using GPC; samples were run in LiBr in DMF (0.2 M) and M_n were assigned relative to a standard curve calculated using polyethylene glycol standards. ^(e)Calculated by dividing the M_n values over M_w of corresponding monomer. Results show the deviation of $M_{n,Obs.}$ From $M_{n,Theo.}$. * \mathcal{D} values higher than ideal value which could be an indicative of secondary-metathesis events. (85)

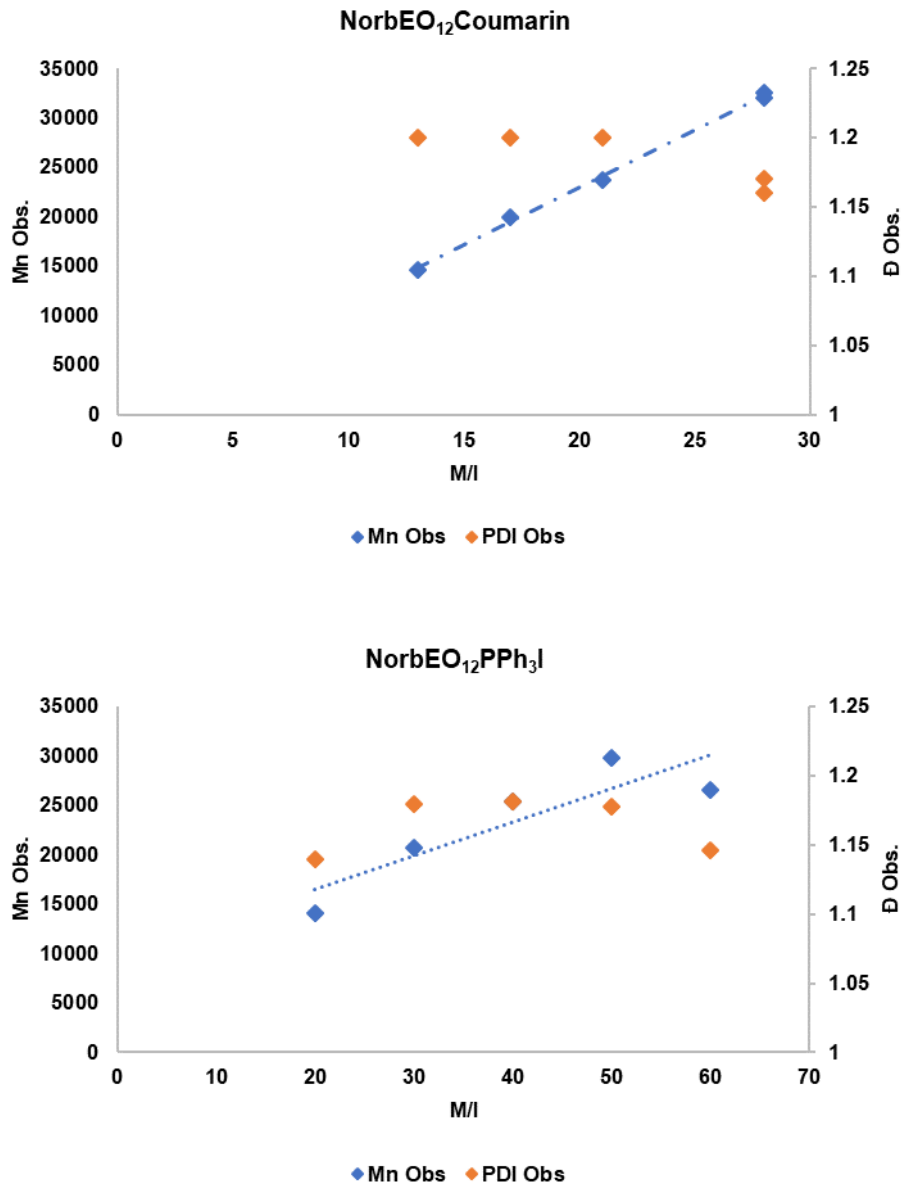


Figure 39: : Linear dependence of number average molecular weight, M_n , of homo-polymer samples of both NorbEO₁₂Coumarin and NorbEO₁₂PPh₃I on degree of polymerization, DP, a feature of living polymerization. (85) Dispersity indices remain below 1.2 for most homo-polymer samples. Ideally, \bar{D} values need to be as close as possible to 1.0 for a polymerization to be considered living. (85) (91)

GPC analysis of the ^1H NMR samples, after quenching and preparation as described in experimental section, allowed for the estimated evaluation of progression of the M_n and \bar{D} during the propagation stage of the homo-polymerization process. GPC traces of homo-polymerization of 60 equiv. of NorbEO₁₂PPh₃I, figure 40, or NorbEO₁₂Coumarin, appendix 3 **Error! Reference source not found.**, show the anticipated increase of M_n of the propagating chain during propagation cycle due to iterative insertion of monomer molecules. Molecular weight distribution of the NorbEO₁₂PPh₃I- and NorbEO₁₂Coumarin-derived propagating polymer chain broadens by a factor of 1.01-1.03 and 1.01-1.06 respectively as shown in table 7 and appendix 4.

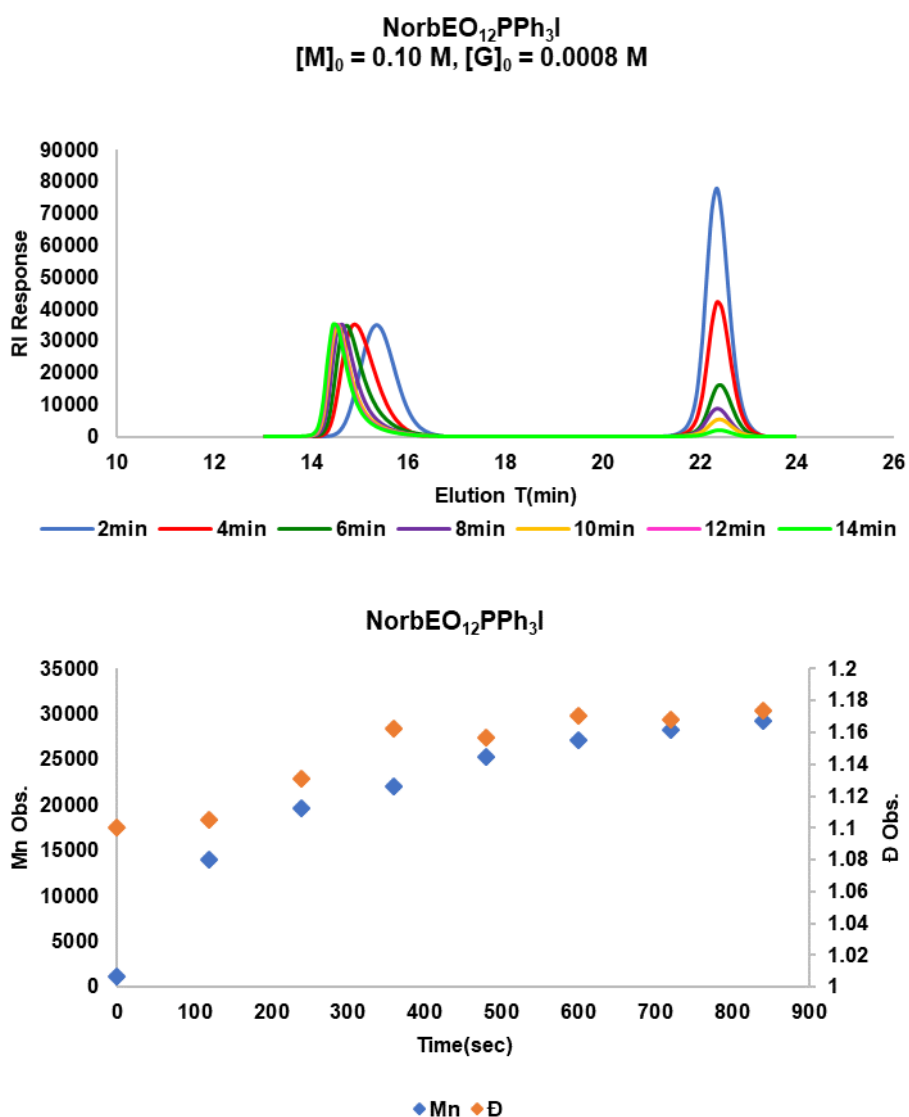


Figure 40: (Top) GPC traces of ^1H NMR samples of the homo-polymerization of 60 equiv. of NorbEO₁₂PPh₃I reaction mixture at 2 min (160 sec) intervals. The GPC samples were prepared by quenching of the ^1H NMR sample with EVE, evaporation and redissolution in DMF. The traces were acquired at 30 °C using LiBr in DMF (0.2 M) as the eluting solvent with a flow-rate of 0.8 mL/min. (Bottom) Further analysis of the GPC traces reveal the anticipated increase in M_n over time as a result of insertion of monomer molecules into the growing polymer chain (blue diamonds). The analysis also reveals the increase in \bar{D} marked by broadening of the product peak of a factor of 1.01-1.03 overtime.

Monomer	Time (min)	$Mn_{Obs.}$ kDa	$\bar{D}_{Obs.}$	Broad. F.
NorbEO₁₂PPh₃I	0	1.2	1.10	1.00
	2	14	1.11	1.01
	4	20	1.13	1.02
	6	22	1.16	1.03
	8	25	1.16	1.00
	10	27	1.17	1.01
	12	28	1.17	1.00
	14	29	1.17	1.00

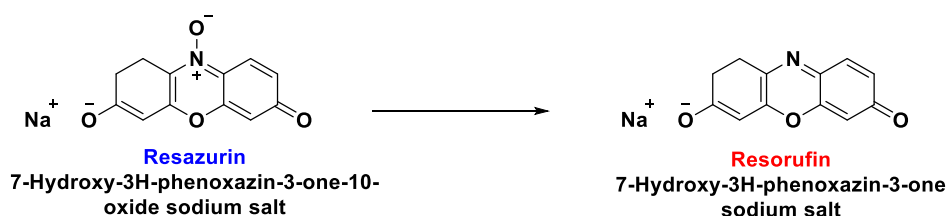
Table 7: Mn and \bar{D} values of the 1H NMR kinetic study samples obtained by GPC after quenching with EVE, evaporation and redissolution in DMF. Mn values of the propagating chain increased over time as a result of insertion of monomer molecules into the growing polymer chain so as the \bar{D} values by a factor of 1.01-1.03 overtime.

The conclusion drawn from the first-order kinetic, linear dependency of number-average molecular weight Mn on monomer to initiator ratio M/I and narrow molecular weight distribution \bar{D} determined by 1H NMR and GPC respectively is that our second-generation monomers can undergo living ROMP under the conditions, described in detail in experimental, with moderate secondary metathesis. An orthogonal characterization technique is needed to further validate the occurrence of secondary metathesis cascades and quantify their extent.

5.3 Biocompatibility of Second-Generation Ring-Opening Metathesis Homopolymers

The viability of human embryonic kidney cells, HEK 293, was screened against NorbEO₁₂PPh₃I-derived homo-polymers, of degree of polymerization ranging from 12-25, in at micromolar concentrations from 0-100 μM . The cellular viability was determined using alamarBlue® assay as described in the experimental section in detail. AlamarBlue® is a colorimetric cell viability assay that quantitatively assesses the reducing power of cells as an indication of their health. (**141**) Upon cellular uptake, the non-toxic, cell permeable and non-fluorescent alamarBlue® reagent, resazurin, is reduced to its highly-fluorescent product resorufin derivative, scheme 44. (**141**) The fluorescence outcome is a

measure of cell health variation as a result of chemical compound-mediated cytotoxicity. (141) The cellular viability scales up with decreasing concentration for all NorbEO₁₂PPh₃I-derived homo-polymers. NorbEO₁₂PPh₃I-derived homo-polymers of a degree of polymerization of 12 showed superior biocompatibility at concentrations from 6-100 μM, figure 41. The poor water solubility of NorbEO₁₂PPh₃I-derived homo-polymers limited to formation of inhomogeneous suspensions which precluded us from investigation their cytotoxic effect.



Scheme 44: Illustration of the colorimetric chemical reactions utilized by the cell viability assay alamarBlue®. In alamarBlue®, the indicator is converted from its non-fluorescent form to its fluorescent derivative resorufin. The latter, detected using a fluorescence reader, quantifies the reducing power of the cell as a measure of its health.

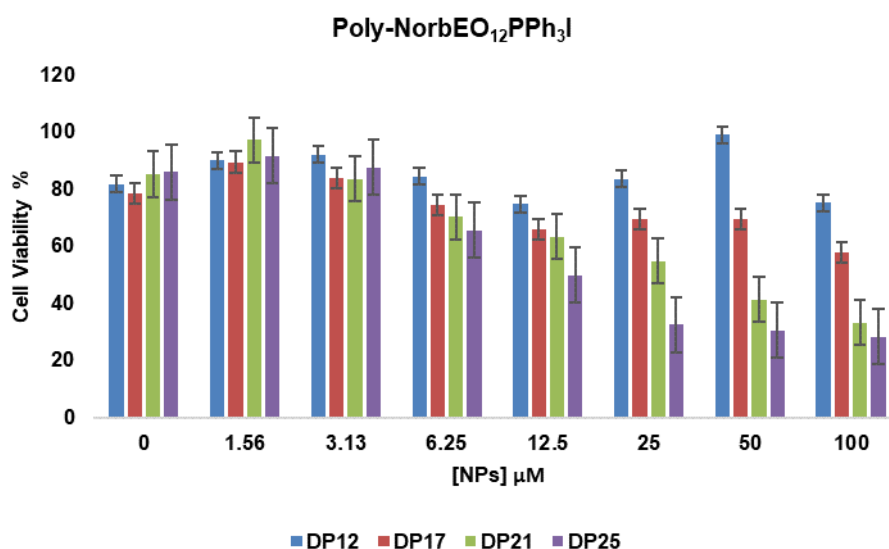


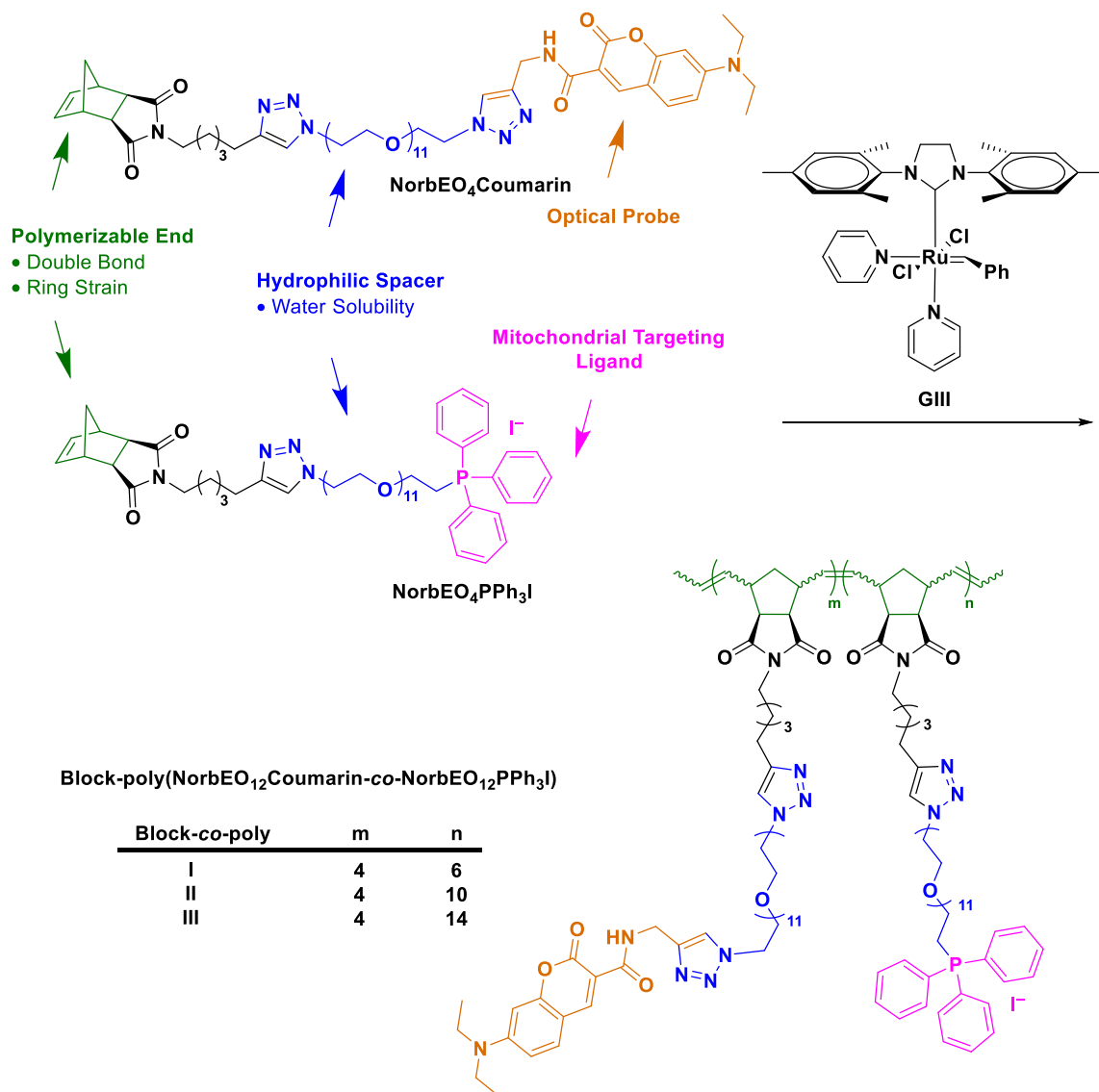
Figure 41: Cellular viability chart of HEK 293 cells after incubation with NorbEO₁₂PPh₃I-derived homo-polymers at concentrations ranging from 0 to 100 μM at 37 °C for 3 hrs. Cellular viability scales up with decreasing concentration for all samples with NorbEO₁₂PPh₃I-derived homo-polymers of a degree of polymerization of 12 showing superior biocompatibility. The viability of cells was assessed using alamarBlue® assay,

5.4 Summary

Second generation monomers were successfully prepared by a synthetic scheme adapted from that of first-generation monomers. The monomers successfully underwent ROM homo-polymerization generating corresponding brush polymers with moderate to good molecular weight distribution. The homo-polymers show an enhanced water solubility compared to first-generation analogous. Yet, the water solubility of coumarin homo-polymers remains limited. Therefore, only the biocompatibility of NorbEO₁₂PPh₃I-derived homo-polymers was assessed. Their biocompatibility scales down with increasing concentrations and M_n .

6 Synthesis and Characterization of First-Generation Co-polymers

Having established that NorbEO₁₂PPh₃I-derived homo-polymers display superior water solubility, we proceeded towards the synthesis of NorbEO₁₂PPh₃I and NorbEO₁₂Coumarin block-co-polymers, henceforth referred to as first-generation block-co-polymers. The two monomers were co-polymerized with greater number of equivalents of NorbEO₁₂PPh₃I with respect to NorbEO₁₂Coumarin, scheme 45.



Scheme 45: General design of co-polymers bearing dodeca-ethylene glycol as the hydrophilic segment, 7-(diethylamino)coumarin-3-carboxylic amide as the optical probe and triphenylphosphonium iodide as the mitochondrial targeting ligand. The block-co-polymers, poly(NorbEO₁₂Coumarin-co-NorbEO₁₂PPh₃I), were synthesized from their corresponding monomers, at a coumarin:PPh₃I ratio of 4:6, 4:10 and 4:14, by ROMP mediated by Grubbs III catalyst.

The block-*co*-polymers, poly(NorbEO₁₂Coumarin-*co*-NorbEO₁₂PPh₃I), were synthesized from their corresponding monomers, at a coumarin:PPh₃I ratio of 4:6, 4:10 and 4:14, by ROMP. The *co*-polymerization was initiated at room temperature by Grubbs III and conducted at a constant initial monomer concentration. The catalyst solution was added to the first monomer's solution, NorbEO₁₂Coumarin (0.05 M), to prepare the first block and the polymerization was monitored by ¹H NMR. When ≈ 90% monomer conversion was reached, the solution of the second monomer, NorbEO₁₂PPh₃I (0.1 M which is diluted to 0.05M upon addition), was added in one portion to prepare the second block and polymerization is monitored by ¹H NMR. When ≈ 90% monomer conversion was reached, the polymerization was terminated by excess addition of a terminating reagent such as ethyl vinyl ether EVE. The GPC traces of the final polymeric products from which the number average molecular weights of the block-*co*-polymers, poly(NorbEO₁₂Coumarin-*co*-NorbEO₁₂PPh₃I), and molecular weight distribution \mathcal{D} , table 8, were determined are presented in figure 42.

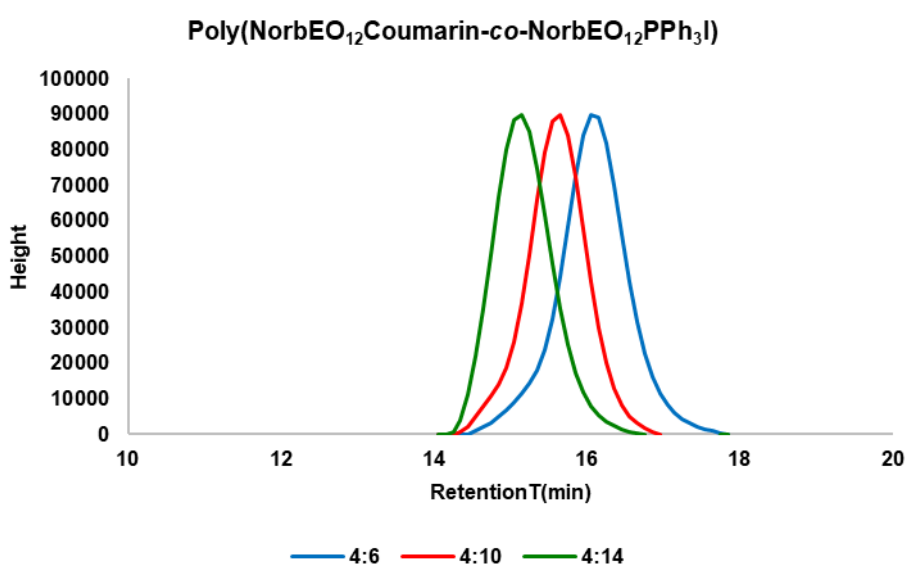


Figure 42: GPC traces of block-*co*-polymers, poly(NorbEO₁₂Coumarin-*co*-NorbEO₁₂PPh₃I), I, II and III. Traces were acquired using LiBr in DMF (0.05 M) as the eluting solvent. Composition of *co*-polymers I, II and III, their corresponding M_n and \mathcal{D} are shown in table 8.

Co-poly	Tot. M/I ^a	M ₁ /I ^b	M ₂ /I ^b	M _n ^{Theo.} (kDa) ^c	M _n ^{Obs.} (kDa) ^d	\mathcal{D} ^{Obs.} ^e
I	10	4	6	12	9	1.13
II	14	4	10	17	12	1.14
III	18	4	14	21	17	1.14

Table 8: ^(a)Total monomer to initiator ratio Tot. M/I refer to the total number of equivalents of monomer with respect to initiator. ^(b) Monomer to initiator ratio M₁/I and M₂/I refer to the number of equivalents of NorbEO₁₂Coumarin and NorbEO₁₂PPh₃I with respect to initiator respectively. ^(c)Defined as the sum of the products of number of equivalents and molecular weight calculated for each monomer. ^(d, e) Determined using GPC; samples were run in LiBr in DMF (0.05 M) and M_n were assigned relative to a standard curve calculated using polyethylene glycol standards.

In all block-*co*-polymer samples, I, II and III, the observed ratio of NorbEO₁₂PPh₃I to NorbEO₁₂Coumarin, obtained using ¹H NMR spectroscopy as shown in figure 58, is close to the desired ratio listed in table 9. We were unable to determine the degree of polymerization of each monomer in the final block-*co*-polymer structure using quantitative ¹H NMR using calibration methods that employ internal standards. These methods, to our knowledge, require the integration of all proton signals corresponding to each block in the final block-*co*-polymer structure and referencing the area to that of the internal standard. (142) (143) This was not possible as a result of the overlap of most signals due to structural similarity between the two monomers. However, one can envision that a quantitative *in situ* ¹H NMR monitoring of consumption of the first monomer in a block-*co*-polymerization reaction can provide the DP of that monomer from which the DP of the second monomer in the final block-*co*-polymer can be derived after determining the ratio of both monomers by ¹H NMR.

Co-Polymer	M ₁ Feed ^a	M ₂ Feed ^b	Ratio _{Theo.} ^c	M ₁ DP ^d	M ₂ DP ^e	Ratio _{Obs.} ^f
I	4	6	1.5	-	-	1.66
II	4	10	2.5	-	-	2.38
III	4	14	3.5	-	-	3.85

Table 9: ^(a)Monomer feed of NorbEO₁₂Coumarin. ^(b)Monomer feed of NorbEO₁₂PPh₃I. ^(c)Theoretical ratio of both calculated by dividing monomer feed of NorbEO₁₂PPh₃I/NorbEO₁₂Coumarin. ^(d)Degree of polymerization of NorbEO₁₂Coumarin in the final polymeric architecture. ^(e)Degree of polymerization of NorbEO₁₂PPh₃I in the final polymeric architecture. ^(f)The ratio of NorbEO₁₂PPh₃I/ NorbEO₁₂Coumarin obtained by ¹H NMR as described in the experimental section.

Fluorescence spectra show that excitation and emission maxima for all three block-*co*-polymers, I, II and III, are maintained at ≈ 430 and ≈ 474 nm respectively. The two-photon fluorescence associated with coumarin derivatives is also maintained. Two-photon fluorescence of block-*co*-polymers I, II and III was generously examined by the Light Manipulation Group located in the School of Physics at the University of St Andrews. Briefly, the quadratic dependence of the fluorescence intensity on excitation laser power, which is a characteristic of two-photon fluorescent dyes, was obtained by plotting the logarithms of laser power against the logarithms of the corresponding fluorescence intensity of the block-*co*-polymers solution of a concentration of 10 μ M the slope of which was two. Experimentally, this was achieved by shining a pulsed laser beam of a known wavelength λ and an average power of ≈ 50 mW with a pulse duration τ_p and repetition rate f_p of about 100 fs and 80 MHz respectively, figure 43. Screening a number of pulsed laser beam wavelengths between 800-1000 nm identified 830 nm as the optimal two-photon excitation wavelength where the logarithmic line plot is best fit, figure 43 and appendix 5.

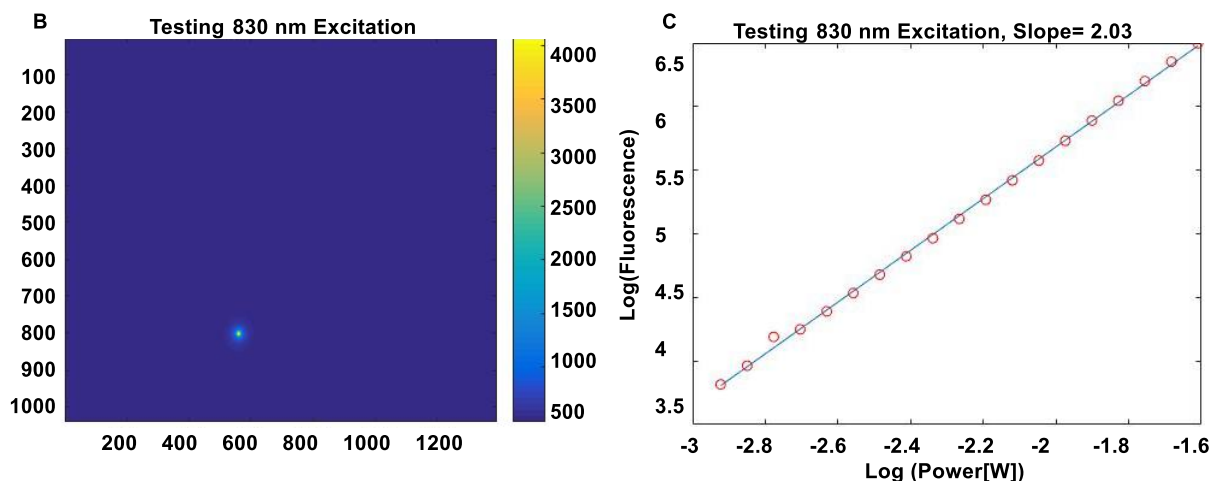
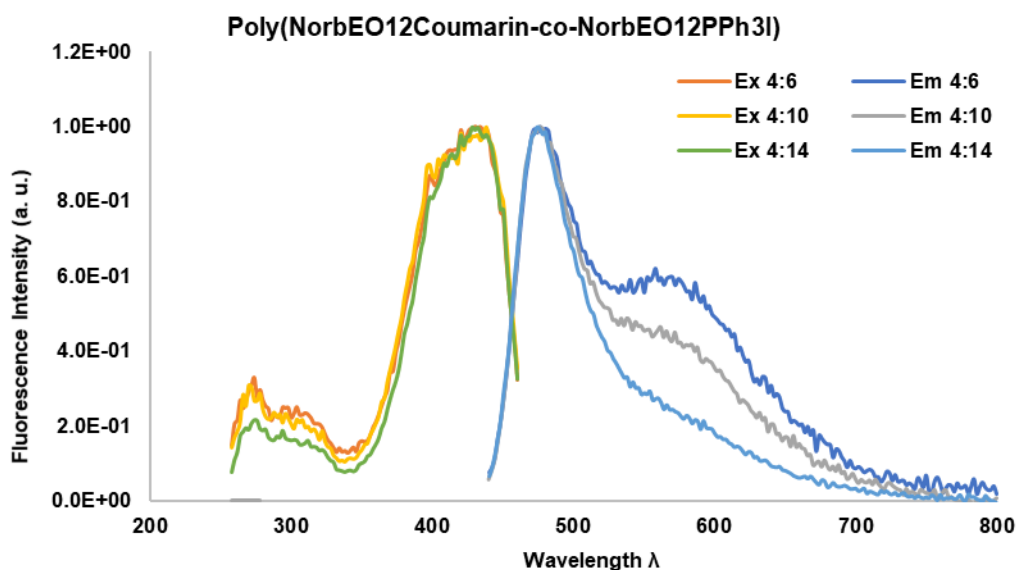


Figure 43: (A) Fluorescence spectra of block-co-polymers, I, II and III, 10 μM solution in deionized water, show that excitation and emission maxima for all three, are maintained at ≈ 430 and ≈ 474 nm respectively. (B) Two-photon induced fluorescence of block-co-polymer I, 10 μM solution in deionized water, using a Ti-shapphire laser showing the confinement of the fluorescence to a focal spot. (C) Linear plot of the logarithmic value of laser power against corresponding logarithmic values of the fluorescence output showing a line of best fit with a slope of ≈ 2.0 which validates the quadratic dependence of fluorescence intensity on excitation laser power a characteristic of two-photon fluorescent dyes. The best fitting of the line plot observed at laser power excitation wavelength of 830 nm established this wavelength as the optimal two-photon excitation λ for block-co-polymer I.

We proceeded towards assessing the biocompatibility of block-co-polymers, poly(NorbEO₁₂Coumarin-co-NorbEO₁₂PPh₃I), I, II and III. The viability of human embryonic kidney cells, HEK 293, was screened against micromolar concentrations, from 0-100 μM , of block-co-polymers I, II and III. The viability was assessed using alamarBlue® assay as described in the experimental section. The outcome of the assay over-estimated the biocompatibility of the NPs by showing cell-viability values at

concentrations 25-100 μM higher than controls. This observation, which seemed to associate with the presence of the fluorescent coumarin moiety, is, to our knowledge, unprecedented. When the biocompatibility of the non-fluorescent NorbEO₁₂PPh₃I-derived homo-polymers was assayed using alamarBlue® as described in the previous section, the cell viability scaled down to \approx 30-80% when HEK 293 cells were incubated with 100 μM solution of NorbEO₁₂PPh₃I-derived homo-polymers with a DP of 12-25, figure 44.

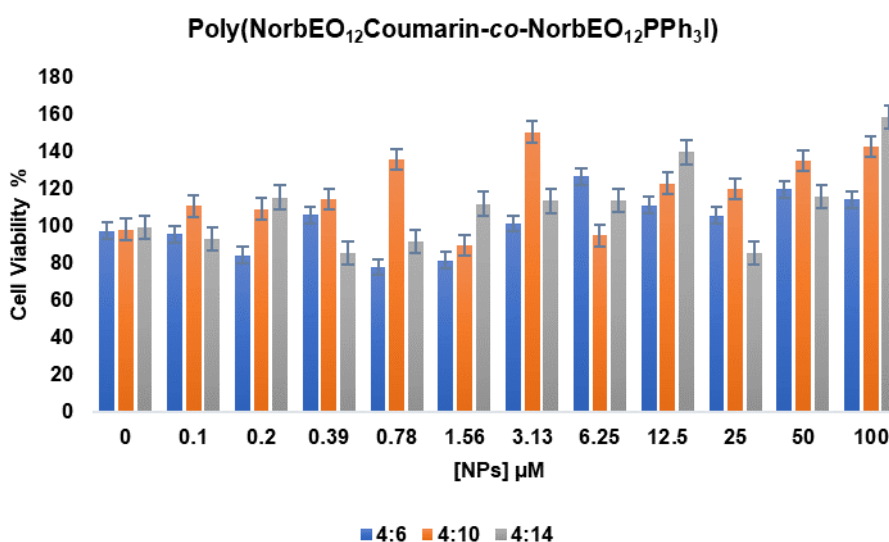
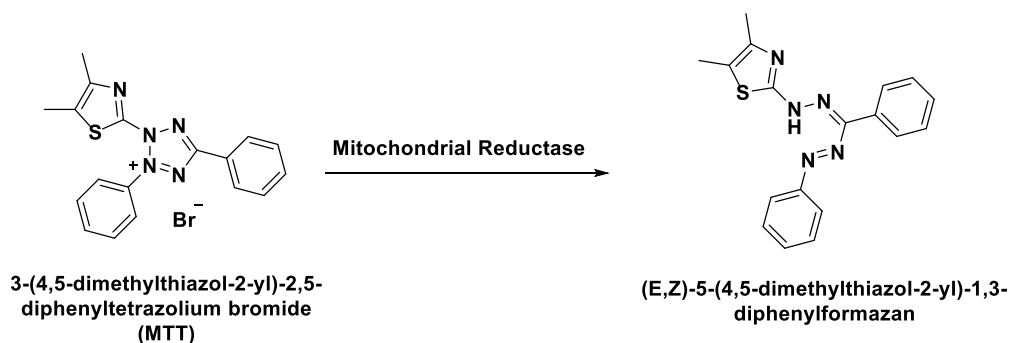


Figure 44: Cellular viability chart of **HEK 293** cells after incubation with block-co-polymers I, II and III at concentrations ranging from 0 to 100 μM at 37 °C for 3 hrs. Assay results seem to over-estimate the biocompatibility of the NPs by showing cell-viability values at concentrations 100-25 μM higher than controls. The viability of cells was assessed using **alamarBlue®** assay as described for NorbEO₁₂PPh₃I-derived homo-polymers.

A similar behavior was observed when the viability of SH-SY5Y neuroblastoma cells was screened against micromolar concentration of block-co-polymers I, II and III were assessed using MTT assay. MTT assay, MTT (3-(4,5-dimethylthiazol-2-yl)-2,5-diphenyltetrazolium bromide) assay, is also a colorimetric cell viability assay that quantitatively assesses the reducing power of cells as an indication of their health, scheme 46. (144) Upon cellular uptake, the cell permeable MTT reagent is reduced to formazan. The absorbance intensity of formazan at 570 nm is a measure of cell health variation as a result of chemical compound-mediated cytotoxicity. (144) Incubation of SH-SY5Y cells with 0-100 μM solution of block-co-polymers I, II and III for three hours prior to introducing MTT reagent induced a change in cell morphology. The change in morphology of cells that were incubated with 100-60 μM was severe and resembled the change of morphology associated with treatment of cells with a lysis buffer. Yet, this cytotoxic effect was not reflected by the assay results. The MTT assay results showed SH-SY5Y cell viability was only reduced to \approx 60-90% after incubation with polymeric NPs at 100 μM for 3 hrs, figure 45.



Scheme 46: Illustration of the colorimetric chemical reaction utilized by MTT cell viability assay. In MTT assay, the indicator is converted from its tetrazolium salt form to the corresponding formazan. The latter, detected using an absorbance reader, quantifies the reducing power of the cell as a measure of its health. The assay was performed as described in the experimental section. Figure adapted from Ref. (144)

The outcome drawn from the biocompatibility assays of block-*co*-polymers I, II and III in comparison to NorbEO₁₂PPh₃I-derived homo-polymers suggests that the presence of diethylamino-coumarin in block-*co*-polymers I, II and III ameliorates the biocompatibility of the polymeric NPs. This contradicts with what has been published on the cytotoxic effect of diethylamino-coumarin derivatives. (131) We were unable to identify the mode of interference of diethylamino-coumarin with the assay probes considering that both colorimetric assays, alamarBlue® and MTT, are standard biocompatibility tests for assessing the chemical compound-induced cytotoxic effect.

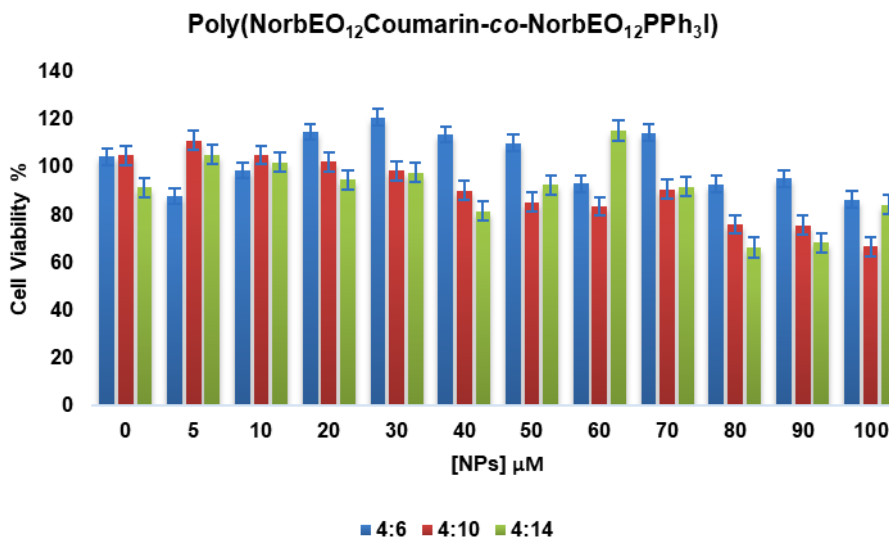


Figure 45: Cellular viability chart of SH-SY5Y cells after incubation with block-*co*-polymers I, II and III at concentrations ranging from 0 to 100 μM at 37 °C for 3 hrs. Assay results seem to over-estimate the biocompatibility of the NPs by showing that the viability of cells was only reduced down to ≈ 60-90% after incubation of cells with polymeric NPs at 100 μM for 3 hrs in comparison to controls. The viability of cells was assessed using MTT assay as described in the experimental section.

As we were not able to firmly establish the cytotoxic effect of block-*co*-polymers I, II and III at concentrations ranging 40-100 μM , we decided to assay the cellular uptake capacity of the polymeric NPs at low concentrations, 5-20 μM , using fluorescence microscopy. We envisioned that incubation of cells with NPs at a concentration as low as 5 μM at five-minute intervals, fixation followed by imaging using confocal laser scanning microscopy would be a good starting point. This approach would enable us to estimate cellular uptake capacity at different time points whilst maintaining a sufficient cellular viability. For this purpose, SH-SY5Y cells were seeded on eleven coverslips. The adherence and morphology of cells was used as markers during the entire process to assess the quality of cell culturing, manipulation and handling methods.

Prior to incubation with the NPs, cells on all coverslips were stained with a mitochondrial marker, MitoTracker™ deep red, to enable the detection of any mitochondrial localization of the NPs, figure 46. In a previous step, the cells were counter-stained with a nuclear marker, Hoechst, to mark individual cells. To this point, no cell detachment was observed but a slight change in morphology was observed only after staining with MitoTracker™ deep red. The choice of MitoTracker™ deep red as the mitochondrial stain was based on its excitation and emission maxima that are in a faraway optical region from that of the NPs, figure 47. As for Hoechst, its excitation overlaps with the excitation peak of NPs because the shortest excitation wavelength in the confocal microscope set up is 405 nm. This issue can theoretically be solved by using sequential scanning. Sequential scanning is a useful tool that can be used to detect multiple fluorophores present in the same specimen. (145) By employing sequential scanning, one can excite and filter as well as record the emission of each fluorophore separately. (145) This can improve image quality by minimizing cross-talk, or emission overlap, between the fluorophores that could be observed when fluorophores are excited and detected simultaneously. (145)

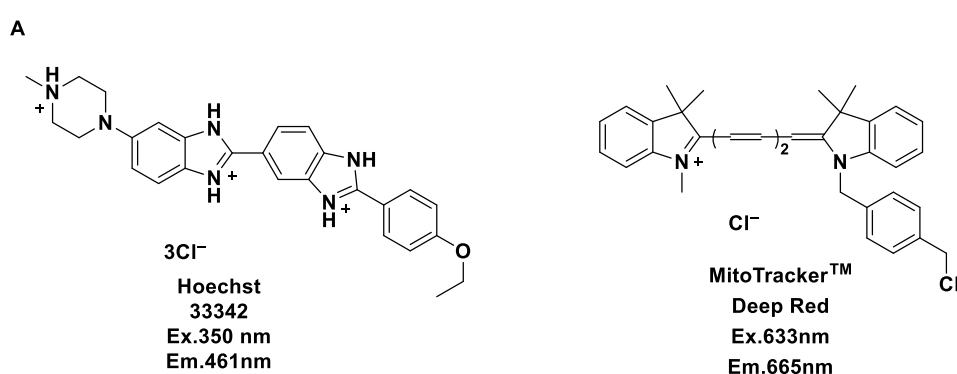
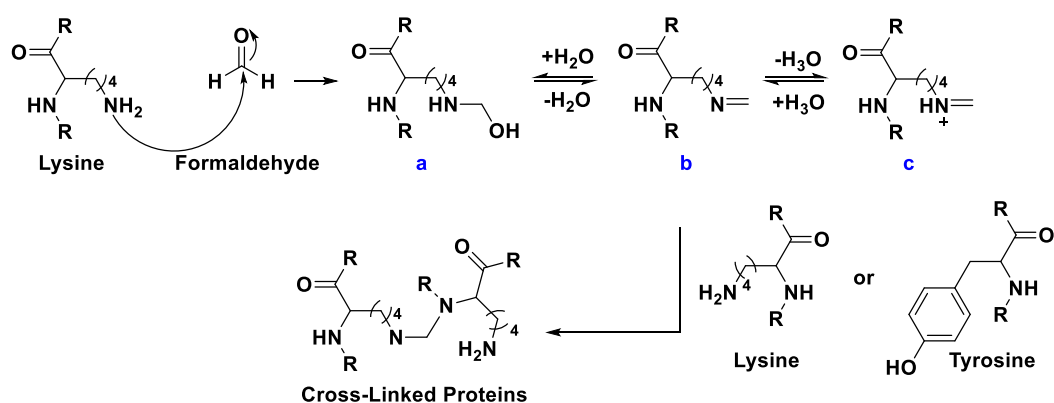


Figure 46: Structure, excitation and emission maximum wavelengths of the nuclear and mitochondrial stains used in the cellular uptake experiment. MitoTracker™ deep red was used to enable the detection of any mitochondrial localization of the NPs. Mitochondrial staining was counter-stained with a nuclear marker, Hoechst, to mark individual cells.

Ten of the cell cultures were incubated with a 5 μM solution of block-*co*-polymers I, NorbEO₁₂coumarin 4: NorbEO₁₂PPh₃I 6, from 0-50 minutes at five-minute intervals and one culture was used as a control. At this stage, cell detachment and changes in morphology were evident the extent of which increased with increased incubation times. These changes may have been caused by an environmental stress exerted on cells by the incubated NPs. Each culture was then fixed using 4% formaldehyde to promote the retention of NPs within the cells and preserve the morphology of the cells by cross-linking intracellular proteins as shown in scheme 47. (146) Samples then were mounted on slides to prepare them for imaging.



Scheme 47: The mechanism by which formaldehyde cross-links intracellular proteins and ultimately preserves the morphology of cells and facilitates the retention of NPs. Formaldehyde interacts with nucleophilic amines generating corresponding imine b which is in equilibrium with its hydrolyzed form a. Imine b is protonated to generate iminium c which undergoes addition by nucleophilic residues such as lysine or tyrosine. Scheme adapted from Ref. (146)

Using the fluorescence microscope in the confocal set up fitted with a DAPI filter, we were able to detect a punctate cyan staining in all slides except in the control slide. The distribution of the cyan staining within cells in each slide was inhomogeneous, yet, it seemed to generally increase with increased incubation times. Clustering of nuclei and a decrease of their count was also detected and its extent scales up with increased incubation times. Due to time constraints we were only able to capture images of the slide corresponding to the culture that had been incubated with block-*co*-polymers I, NorbEO₁₂coumarin 4: NorbEO₁₂PPh₃I 6, for 30 minutes using a confocal microscope, figure 48. We envisioned that by using sequential scanning we can excite Hoechst, NPs and MitoTracker™ deep red at 405, 458 and 633 nm, respectively, and filter their emission through three separate bandpass filters with wavelengths of 414 – 449 nm, 469 – 486 nm and 654–680 nm, respectively, to minimize overlap of emission between fluorophores. We managed to excite and detect Hoechst and MitoTracker™ Deep Red as shown in the blue and red channels in figure 48. Some emission of both fluorophores was detected in the green channel, the NPs channel, however, that can be reduced in future work by reducing the concentration of the staining solution of both fluorophores. The most important and unexpected

observation is that the emission of the punctate staining is detected in both the 414 – 449 nm and 469 – 486 nm channels but at a significantly greater extent in the former. The average size of the punctate staining was estimated by manually measuring the area within each fluorescent spot using ImageJ software. The punctate staining was found to be of an average area of $247 \pm 0.06 \text{ nm}^2$. The enlarged punctate staining, $2.39 \pm 0.36 \mu\text{m}^2$, visible in both 414 – 449 nm and 469 – 486 nm might, white triangles, be associated with punctate staining in its aggregated form. Because the boundaries of the punctate staining were not well-defined and clear, the area measurement may have been over-estimated. Therefore, if the punctate staining was associated with cellular up take of the NPs, area measurement reported above may not accurately reflect the actual size of the NPs. Therefore, future work needs to include NPs' size determination using more reliable techniques.

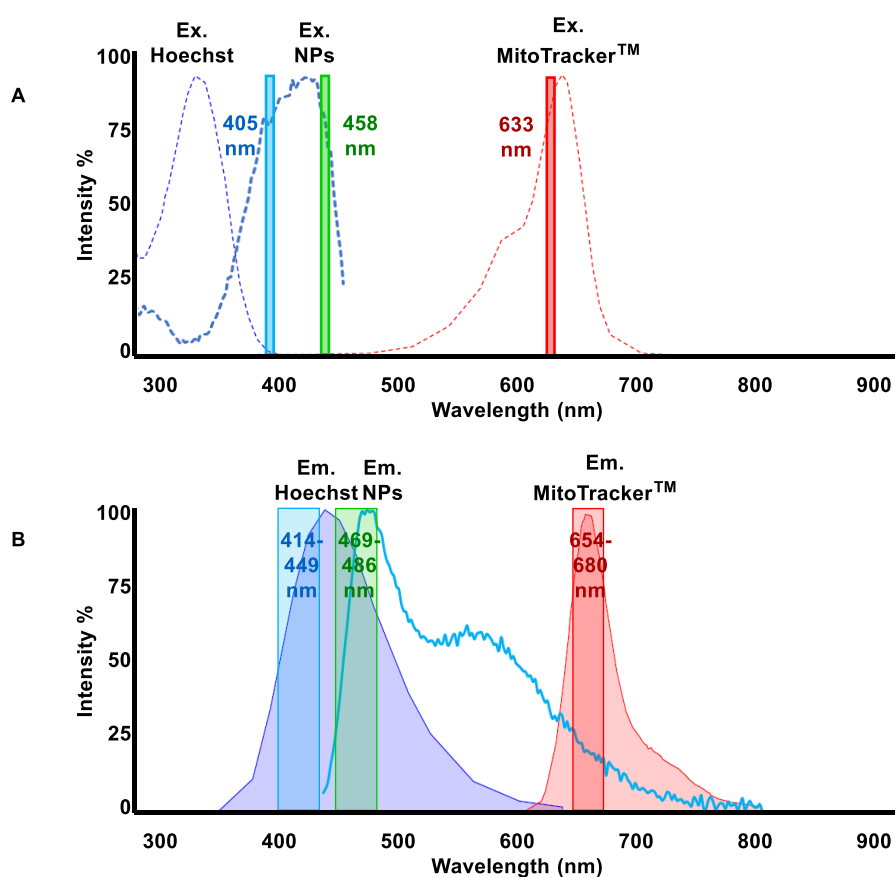


Figure 47: (A) Excitation spectra of Hoechst (purple), NPs (blue) and MitoTracker™ deep red (red) with excitation maxima of 350, 430 and 644 nm. Excitation laser lines available in the confocal microscope set up that can be used to visualize the stans and NPs are 405, 458 and 633 nm. Use of laser lines 405 and 458 nm may result in overlap between excitation of Hoechst and NPs. This issue can theoretically be resolved by sequential scanning. (C) Emission spectra of Hoechst (purple), NPs (blue) and MitoTracker™ deep red (red) with emission maxima of 461, 474 and 665. Fluorescence spectra of Hoechst and MitoTracker™ deep red were generated using fluorescence-spectra viewer tool (173) on top of which fluorescence spectrum of NPs was overlaid.

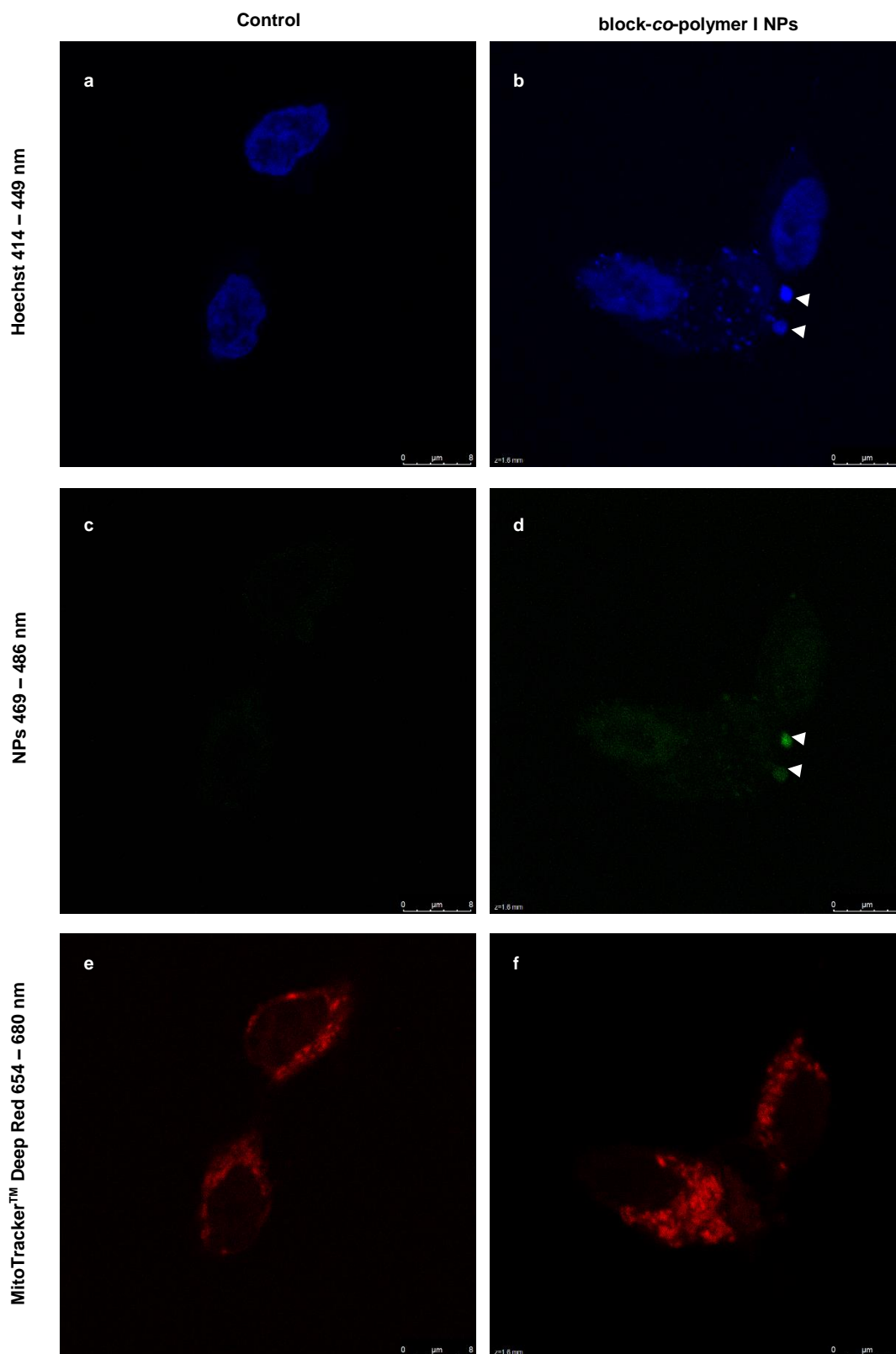


Figure 48: Confocal microscopy images of SH-SY5Y cells after 30 min incubation with block-co-polymer I, coumarin:PPh₃I of 4:6, (right column) vs. controls (left column). Cells were stained with MitoTracker™ deep red , red channels or e and f, and counter-stained with Hoechst, blue channels or a and b. The punctate staining, only detected in SH-SY5Y cells after incubation with block-co-polymer I, is better detected in the 414 – 449 nm than 469 – 486 nm shown in green of c and d. Images were captured using an oil objective with a magnification of 63× and a zoom of 3.9. The enlarged punctate staining, white triangles, visible in both blue and green channels, b and d, might be associated with punctate staining in its aggregated form.

Using the optical sectioning ability of confocal microscopy, we were able to validate the presence of the punctate stinging in all of the focal planes within the cell. Optical sectioning is one of confocal microscopy interesting features and it was introduced as a method that can allow for the imaging of a thick specimen without having to slice it into thin sections. (145) Using optical sectioning, one can capture images from the deepest to the topmost focal plane of the specimen at different time points and reconstruct these images into a 3D projection, figure 49. (145) Practically, this can be achieved by moving the specimen using the confocal microscope's motorized stage away from the objective at μm distances to capture images from deepest to topmost plane or *vice versa*. (145)

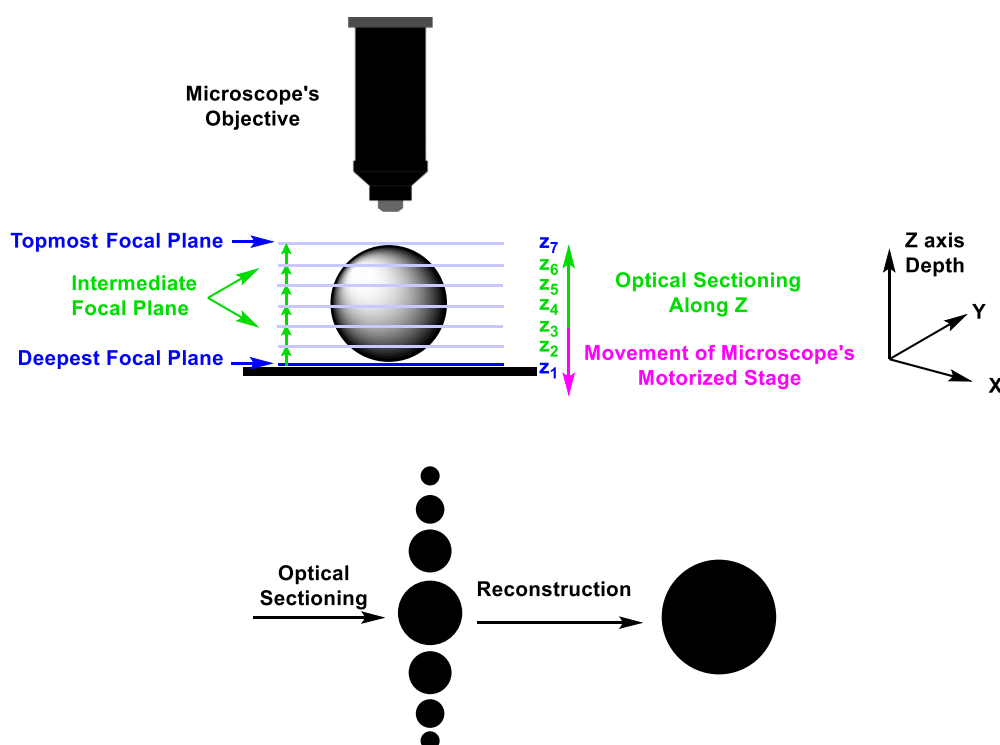


Figure 49: Illustration of how images can be created using optical sectioning feature of confocal microscopy. Using optical sectioning, one can capture images from the deepest to the topmost focal plane at different time points by moving the specimen using the confocal microscope's motorized stage away from or towards the objective at μm distances. Images can then be computationally reconstructed into a 3D projection. Optical sectioning was introduced as a method that can allow for the imaging of a thick specimen without having to slice it into thin sections. (145)

No mitochondrial localization was detected in the sample that was incubated with block-*co*-polymer I for 30 or even 50 min, figure 50. In light of this observation, the stability of the mitochondrial targeting phosphonium moiety in aqueous media during sample preparation and storage and under physiological conditions during incubation with cells need to be addressed. Using ^1H NMR, we were unable to detect any changes the structure of the block-*co*-polymers I, II and III, after storing their aqueous solutions at 4 °C for 30 days.

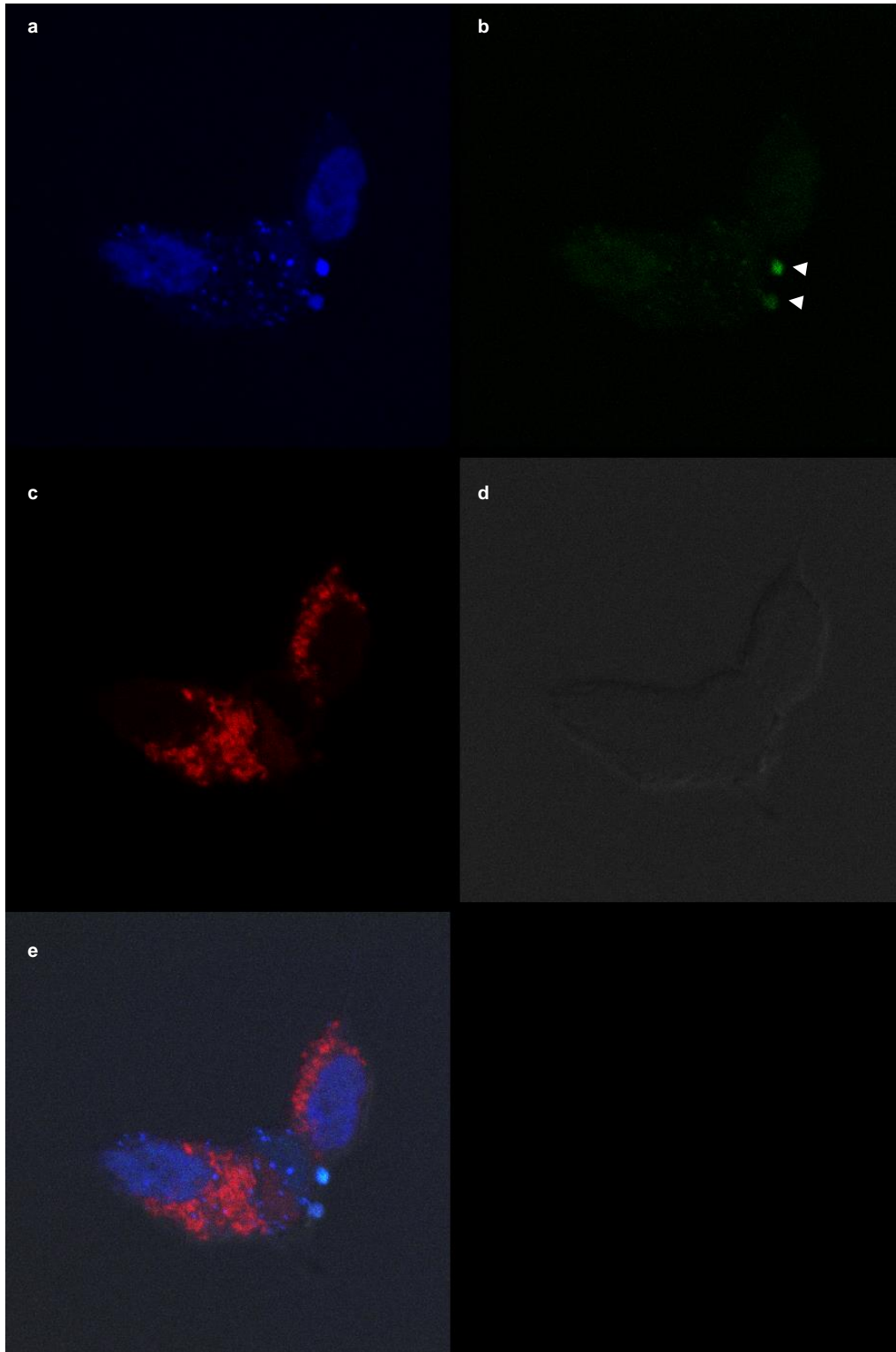


Figure 50: Confocal microscopy images of SH-SY5Y cells, bright field channel d, after 30 min incubation with block-co-polymer I, coumarin:PPh₃I of 4:6. Cells were stained with MitoTracker™ deep red , red channels or c, and counter-stained with Hoechst, blue channels a. The punctate staining, detected in both blue and green channels a and b, shows no localization into the mitochondrial, merged channels in e, Images were captured using an oil objective with a magnification of 63× and a zoom of 3.9.

Nonetheless, an orthogonal characterization technique is needed to lend support to this observation and further validate the stability of the mitochondrial targeting phosphonium center in aqueous and cell culture media. Another plausible scenario is that the 4:6 ratio of NorbEO₁₂Coumarin: NorbEO₁₂PPh₃I is not the optimal combination for mitochondrial targeting. Testing of block-*co*-polymer II and III may assist in establishing the optimal NorbEO₁₂Coumarin: NorbEO₁₂PPh₃I combination. In regards of the technical aspects of imaging.

At this point, we can draw a conclusion that the punctate staining is associated with treatment of SH-SY5Y cells with the block-*co*-polymeric NP I. However, to establish that this staining was induced by cellular up take, several aspects require further validation. The detection of block-*co*-polymeric NP I's fluorescence within the 414-449 nm instead of 469 – 486 nm range contradicts with the fluorescence spectrum recorded for block-*co*-polymeric I solution, 10 μ M, in water. This phenomenon might be attributed to the fixation protocol we employed. Treatment of cells with 4% formaldehyde may have altered the structure of the fluorescent moiety causing the fluorescence to shift towards shorter wavelengths. Measuring the fluorescence of block-*co*-polymer I, II and III in 4% formaldehyde may shed some light and assist in confirming that the fluorescent punctate staining is indeed associated with the NPs. Recording confocal images of the fluorescent NPs in a non-physiological environment, immobilized on a coverslip for example, may provide more information about their appearance that one can rely on when studying the behavior of these NPs in a physiologically-relevant environment. Additionally, size needs to be more accurately measured, using techniques such as dynamic light scattering or atomic force microscopy, to assist in the validation of cellular uptake.

6.1 Summary

Based on the water solubility profile of the second-generation homo-polymers, first-generation *co*-polymers were prepared with greater number of equivalents of NorbEO₁₂PPh₃I with respect to NorbEO₁₂Coumarin. As we were not able to firmly establish the biocompatibility of block-*co*-polymers I, II and III as the presence of the coumarin moiety seemed to interfere with the cytotoxicity assay probes. Preliminary cellular up-take studies of block-*co*-polymer I show that a promising cellular up take capacity that still needs to be validated. Yet, no mitochondrial localization of block-*co*-polymers was detected.

7 Conclusions and Future Considerations

The significance of ethylene-oxide based spacers to this project lies in the presence of two terminal functional groups that, with the appropriate chemistry, can be precisely asymmetrically activated. Asymmetric activation of two terminal groups with identical reactivity enable the spacer to be further derivatized by incorporation of multiple functional groups that can perform different tasks. We were able to access asymmetrically activated ethylene oxide-based spacers of lengths ranging from four to twelve ethylene oxide building block. This was accomplished by oligomerization of tetraethylene glycol, the longest ethylene oxide oligomer commercially available with a 99% oligomeric purity and low cost. The oligomerization was achieved by iterative mesylation and ether synthesis cycles which were repeated until the desired oligomer length was accessed. The procedure is reproducible, scalable and facilitates the isolation of the desired product by liquid extraction. Oligomeric purity of the oligomerization products was estimated by ^1H NMR and MALDI. ^1H NMR enables the estimation of the abundance of the oligomeric product in the scrutinized sample but cannot identify oligomeric impurities. In comparison, MALDI can detect the presence of oligomeric impurities and identify them. However, due to competitive ionization between sample components, MALDI's signal intensity does not quantitatively determine product's abundance in the sample. Ideally, high-resolution chromatographic techniques are employed to resolve a sample into its components which can further be assessed by other spectroscopic techniques. In this context, more efforts need to be dedicated in the future to optimizing the conditions of high-resolution chromatographic separation of our ethylene oxide oligomeric samples. Accurate determination of oligomeric purity of our hydrophilic spacers avoids discrepancies in molecular weight between monomers and final ROMP architectures.

The asymmetrically activated tetra-ethylene glycol and dodeca-ethylene glycol-based spacers were further derivatives into two generations of ROMP-suitable monomers. In addition to the polymerizable end and the hydrophilic spacer, the ROMP monomers harbored a mitochondrial targeting ligand, named NorbEO_xPPh₃, or a di-ethylamine coumarin fluorescent tag, named NorbEO_xCoumarin, to enable the visualization of the brush architecture within the mitochondria. Both generations of monomers were subjected to homo-polymerization, initiated by Grubbs III catalyst, to establish the conditions under which their ROMP is living and examine their propensity to block-ROMO. The homo-polymerization was monitored by ^1H NMR by withdrawing aliquots of the homo-polymerization mixture, diluting the aliquots in CDCl_3 and acquiring their ^1H NMR spectra to study the kinetics of monomer depletion. After completion of ^1H NMR acquisition, the samples were quenched with ethyl vinyl ether, evaporated, dissolved in DMF and submitted to GPC analysis to determine the homo-polymers M_n and \bar{D} values.

The general trend observed with homo-polymerization reactions is that end groups, coumarin and triphenyl phosphonium, slow down the homo-polymerization kinetics due to non-covalent interactions between them, presumably attractive or repulsive forces. The extent of this influence is of a greater

magnitude amongst the coumarin residues. Slowing down ROMP kinetics increases the growing polymer chain to undergo secondary metathesis events such as backbiting or chain transfer. The pseudo-first order rate of homo-polymerization kinetics can generally be increased by increasing monomer's initial concentration, $[M]_0$, and by increasing the length of the hydrophilic spacer both of which we observed to favor ROMP over secondary metathesis cascades.

Submitting the polymerization aliquots to ^1H NMR acquisition without quenching introduces errors by not accounting for monomer consumption taking place in the time frame between sample preparation and acquisition. Therefore, reaction aliquots must be quenched with ethyl vinyl ether prior to ^1H NMR acquisition. Ethyl vinyl ether can be evaporated after quenching and samples can be dissolved in CDCl_3 then submitted to ^1H NMR acquisition. This approach may be more laborious especially when multiple polymerization reactions are run sequentially in the same day. Nonetheless, it is more accurate for determining the rate of monomer consumption, detecting the occurrences of secondary metathesis reactions and establishing the overall kinetic profile.

To determine the degree of polymerization of homo-polymers using ^1H NMR, we monitored the lapse of olefinic signal of the polymerizable N-norbornene dicarboximide end at $\approx \delta$ 6.19 and integrated it relative to the aromatic signal of NorbEO_xCoum at $\approx \delta$ 6.56 ppm or aliphatic signal of NorbEO_xPPh₃I at $\approx \delta$ 4.46 ppm. A quantitative *in situ* ^1H NMR monitoring of consumption of ROMP monomers using internal standards is far more reliable for determining the degree of polymerization of homo-polymers.

Co-polymerization's ^1H NMR and GPC kinetics must be studied in the same manner as homo-polymerization reactions to ensure that the living nature of the ROMP is sustained throughout all co-polymerization stages; the homo-polymerization of the first block, cross-over point and homo-polymerization of the second block. Additionally, a quantitative *in situ* ^1H NMR monitoring of consumption of ROMP monomers using internal standards in a block-co-polymerization reaction can provide the DP of each monomer in its corresponding block from which the molecular weight of the final polymeric product can be derived and compared to the value obtained by GPC.

Assignment of number average molecular weight, M_n , weight average molecular weight, M_w , and molecular weight distribution, \mathcal{D} , of branched polymeric architectures relative to a calibration curve of linear polymeric standards using gel permeation chromatography coupled to a refractive index detector may not be an accurate approach. Linear and brush-like polymers, albeit may have equal average molecular weight, have different hydrodynamic radii and therefore have different retention times and refract the incident light differently. Because calibration curves are not corrected to account for such difference, alternate method of assignment needs to be considered. Using light scattering as an orthogonal technique is a common method for accurate determination of average molecular weight since the light-scattering detector's response is sensitive to molecular weight as described by:

$$\text{Light Scattering Output (mV)} = K_{LS} \times I_{\text{Laser}} \times M_w \times \theta \times \text{Concentration} \times \text{Inj. Vol}$$

$$K_{LS} = \frac{(2\pi n_0)^2 (dn/dc)^2}{N_A \lambda^4}$$

Where K_{LS} is a light scattering constant which depends on both the setup and sample, I_{Laser} is the intensity of the incident laser beam, M_w is molecular weight, θ is the scattering angle, n_0 is the refractive index of the pure solvent, dn/dc is the refractive index increment of the solute/solvent system, λ is the wavelength of the laser used and $N_A = 6.022 \cdot 10^{23} \text{ mol}^{-1}$ is Avogadro's number. (147)

Stability of the phosphonium center in our nanoscopic polymeric brush architectures (NPBAs) is detrimental to their mitochondrial uptake driven by mitochondrial inner negative potential. Stability of the phosphonium center in aqueous media and under cell culture and manipulations conditions, designed for assessing cellular uptake and toxicity of NPBAs, must be assessed. Measuring changes in the zeta potential value of NPBAs under storage and cell culture and manipulations conditions can help in gaining insight surrounding the propensity of the phosphonium centre to undergo charge neutralization reactions. Zeta potential is the potential at the slipping plane encircling a particle submerged in a medium, figure 51. (148) ^1H NMR can also be used to study the stability of the phosphonium center in model compounds with less noisy ^1H NMR spectra than our NPBAs such as the model compounds depicted in figure 52.

Particles' size and tendency to aggregation in the absence and presence of serum proteins needs to be assessed prior to embarking on biological studies. Knowledge surrounding particles' tendency to aggregation in the absence and presence of serum protein will help us predict their stability against aggregation upon storage and *in vitro* studies. Particles size can be determined by several techniques such as transmission electron microscope, TEM, or atomic force microscopy, AFM. However, dynamic light scattering, DLS, remains the most favorable due to the easier experimental set up and operation. Particles' propensity to aggregation can be monitored by measuring size using DLS or by measuring the zeta potential value.

Traces of transition metals, such as ruthenium, in the pharmacological products are a major concern. Ruthenium is classified as an elemental impurities of a significant safety concern and its permitted concentration should not exceed 1 ppm for drugs to be administered via parenteral routes and 10 ppm for drugs to be administered orally. (149) Therefore, future efforts need to be dedicated to quantifying ruthenium traces in our NPBAs. Inductively coupled plasma-mass spectrometry, ICP-MS, can be used to detect traces of metals in pharmacological products. ICP is a plasma generated by inductively heating a gas, such as argon, to high temperatures, > 6000 K, with an electromagnetic coil. As the sample travels through the argon plasma, it gets decomposed, atomized then ionized. The ionized species are then detected by a mass spectrometer. (150)

Rate of cellular uptake determination is very important for assessing efficiency of our NPBAs in targeting the mitochondria. Our progress in this area is a good starting point, yet significant alterations need to be made to optimize assessment of mitochondrial targeting and uptake. Life imaging of cellular uptake of NPBAs allows for monitoring of cellular and mitochondrial uptake, under conditions that mimic physiological environment, in real time. However, imaging of fixed samples prior to imaging of life specimen saves valuable time whilst optimizing experimental conditions. Changes in fluorescence profile of our fluorescent NPBAs after treatment with 4% formaldehyde upon fixation of cells requires validation.

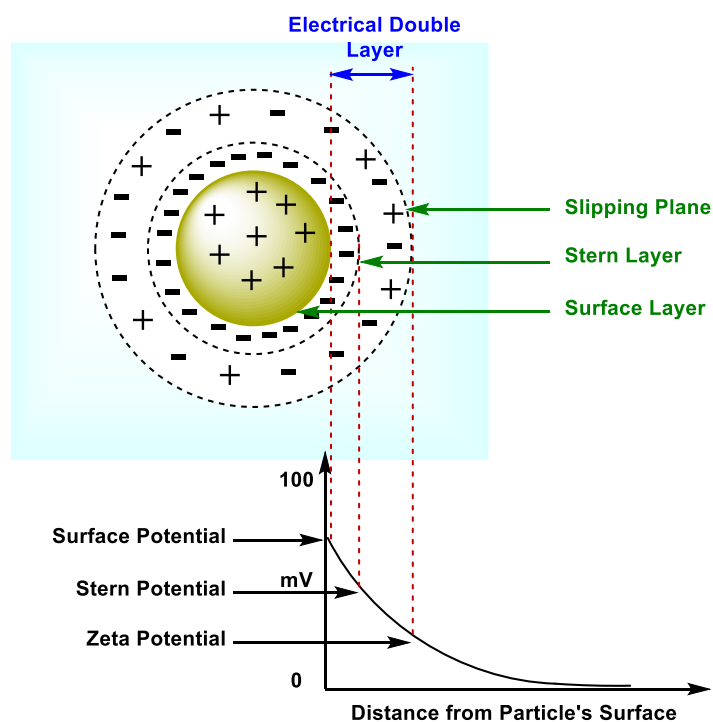


Figure 51: Zeta potential which is defined as the potential at the slipping plane encircling a particle submerged in a medium. Figure adapted from Ref. (148)

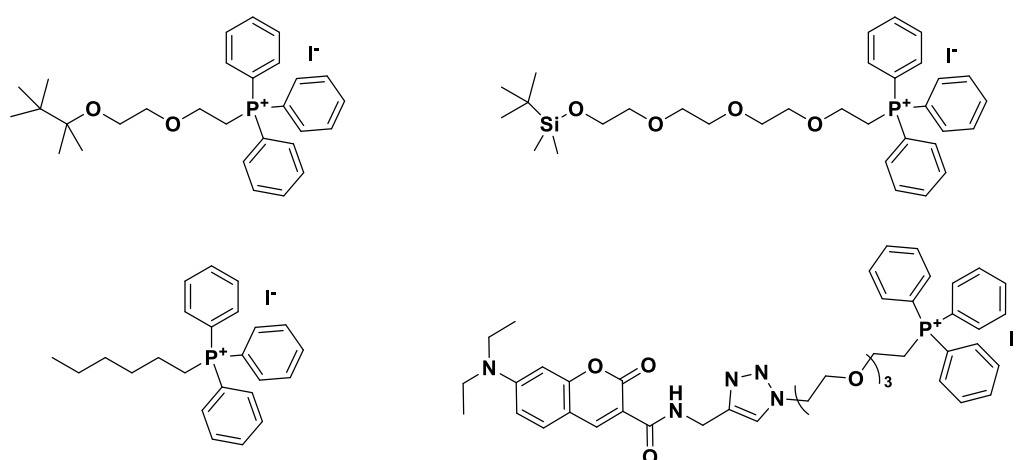


Figure 52: Model compounds that can be used to monitor the stability of the phosphonium center using ¹H NMR.

This can be achieved by acquiring the fluorescence spectra of solution of NPBAs in 4% aqueous formaldehyde. If treatment of NPBAs with 4% formaldehyde causes a shift in their fluorescence profile, other cell fixation protocols must be screened. Protocols must be examined for any potential shift they may cause to the fluorescence profile of the NPBAs. Depending on the outcome of the fixatives screening, mitochondrial stains and *co*-stains and be chosen accordingly. The mitochondrial stains and *co*-stains of choice should exhibit fluorescence profiles that don't overlap with that of the NPBAs. Cell density for cellular uptake needs to be reduced from 2.00×10^5 cells/well, if a 6-well plate is used, to allow for a homogenous uptake of NPBAs amongst cells. Because mitochondrial uptake was shown to require a mitochondrial targeting probe with not only a cationic charge but also balanced hydrophobic properties, model compounds, such as compounds depicted in figure 53, can be employed for the pursuit of the optimal structure of the mitochondrial targeting probe. The structure of NPBAs can be tailored accordingly. After treatment of stained cells with the fluorescent mitochondrial targeting probe, the probe's mitochondrial localization can be visualised using fluorescence microscopy. Fluorescence outcome of the mitochondrial probe can be quantified by measuring the brightness intensity of each pixel using a special software.

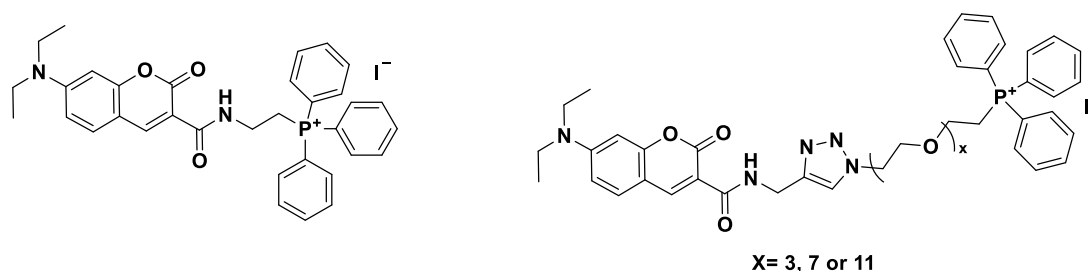


Figure 53: Model compounds can be employed for the pursuit of the optimal structure of the mitochondrial targeting probe with balanced cationic and hydrophobic properties.

Finally, our cell viability assessment could not provide information concerning the biocompatibility of our fluorescent NPBAs due to an interference of the coumarin moiety's fluorescence. Consequently, cell viability assays alternative to the colorimetric assays we employed, alamarBlue® and MTT assays, need to be considered to determine the biocompatibility of NPBAs and the maximum NPBAs' concentration we can work with whilst designing cell imaging experiments. Imaging cell viability assays that detect membrane permeability using fluorescent DNA-binding dyes are a possibly good alternative. These assays discriminate between healthy and dead cells by employing two fluorescent DNA-binding probes; one that is cell-permeant and can be taken up by both healthy and dead cells and another that is cell-impermeant and can only bind to DNA upon cell membranes in damaged. The two

probes can be visualized under a fluorescent microscope using two different filters. Fluorescence outcome can be quantified by measuring the brightness intensity of each pixel using a special software.

8 Future Work

Membrane electrochemical gradient created by the electron transport chain is a key regulator of ATP production. (151) (152) Depolarization of the membrane electrochemical gradient is believed to associate with ATP synthesis interruption leading to mitochondrial dysfunction and ultimately cell death. (151) (152) It is of great importance for future biological applications of mitochondrial targeting using triphenylphosphonium ligands to test their cytotoxic profile for any membrane electrochemical gradient depolarization effect associated with their influx into mitochondrial matrix. Heiskanen. *et. al.* monitored the depolarization of mitochondrial membrane potential in living pheochromocytoma-6 cells undergoing apoptosis induced by staurosporine. (152) The authors stained the mitochondria with tetramethylrhodamine methyl ester, a stain that is taken up by mitochondria in response to their membrane potential without covalent binding, and observed the onset of its release into the cytosol, using laser-scanning confocal microscopy, triggered by addition of staurosporine. (152)

AD affects neurons and synapses in brain regions found in cerebral cortex and hippocampus. (10) Cellular and subcellular uptake evoked by membrane potential raise questions concerning the ability of cationic triphenylphosphonium ligands to discriminate between AD-affected and non-affected cells. For this purpose, more information needs to be gathered on the anatomy of AD-affected cells, including cellular membrane and mitochondrial membrane potential, and how they compare to their AD-non-affected analogues. This hypothesis can be tested by studying cellular and subcellular uptake kinetics of our triphenylphosphonium-bearing NPBA's using primary AD-affected neurons harvested from different brain regions. Cellular membrane and mitochondria can be stained and cellular and mitochondrial uptake kinetics of our fluorescent and triphenylphosphonium-bearing NPBA's can be monitored using confocal microscopy or flow cytometry.

Cleavable linkers between the delivery vector and therapeutic material facilitate the latter's endogenously or exogenously spatial and temporal stimulated release. (78) Location of the cleavable linker relative to the side chains of NPBA's, terminal or core-adjacent, not only may bestow different pharmacokinetics and dynamics upon the overall system, but also may display different therapeutic material's release kinetics. Kinetics of therapeutic material's releases is one of the key aspects that dictate the success of the delivery vector at fulfilling its intended purpose. Initial investigations can be carried out to examine the effect of cleavable linker's location on its release kinetics, figure 54. The rate of linker cleavage can be assessed using NPBA's that can release a reporter dye which can be detected using confocal microscopy. (153) The success of this approach depends on the difference in excitation and emission wavelengths of the reporter dye in its bound and free forms. For this purpose, the reporter dye and its cleavable linker-coupled derivative have to be synthesized and their fluorescence spectra have to be compared to predict the feasibility of this approach.

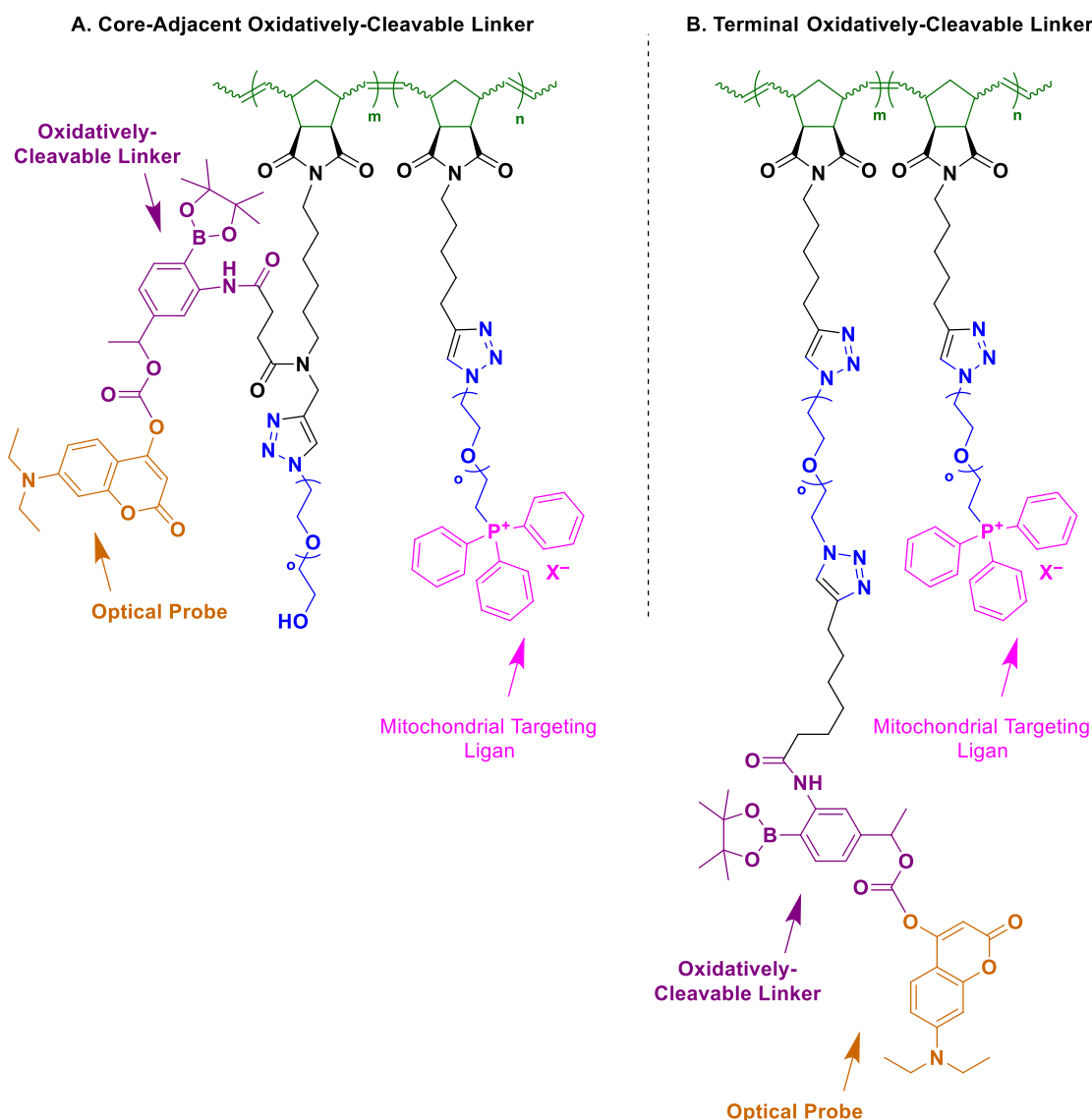
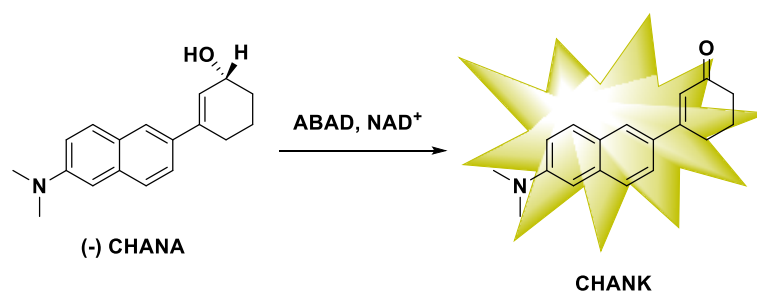


Figure 54: Structure of nanoscopic polymeric brush architectures prepared by ROMP. The NPBAs feature a mitochondrial targeting ligand and ROS-cleavable linker coupled to coumarin derivative. The coumarin-coupled ROS-cleavable linker can be incorporated at the terminus of a hydrophilic linker or as its side chain adjacent to the core of the NPBAs. The coumarin acts as a reported dye to study the kinetics of its release upon cleavage of the ROS-sensitive boronic ester linker using fluorescence microscopy.

The most prominent question remains if mitochondrial targeting and delivery of an ABAD-A β inhibitor can boost the latter's potency relative to its non-targeting form. After establishing linker cleavage and inhibitor release kinetics, the efficacy of the inhibitor can be assessed in live cells using a fluorogenic probe for detecting ABAD activity as an alcohol dehydrogenase enzyme. The outcome can be compared to the results obtained when the ABAD-A β inhibitor is used in its non-targeted form. Muirhead, *et. al.* developed a fluorogenic probe, (-)-cyclohexenyl amino naphthalene alcohol [(-)-CHANA], to measure the alcohol dehydrogenase activity of ABAD in live cells. (154) ABAD converts the non-fluorescent

[(-)-CHANA] into its strongly fluorescent ketone derivative cyclohexenyl amino naphthalene ketone, or CHANK, which can be visualized using fluorescence microscopy, scheme 48.



Scheme 48: Schematic representation of the conversion of the fluorogenic probe, (-)-cyclohexenyl amino naphthalene alcohol [(-)-CHANA], to strongly fluorescent ketone derivative cyclohexenyl amino naphthalene ketone, or CHANK, catalyzed by ABAD and its co-factor NAD^+ . The fluorescence of CHANK can be measure using confocal microscopy.

The ultimate downstream application of NPBA is the delivery of therapeutics to the brain across the blood brain barrier, BBB. The BBB protects the brain against micro-organisms and internal toxins and can account for why many of the drugs that exhibited a satisfactory therapeutic potential *in vitro* failed to accumulate in sufficient concentrations in the brain *in vivo*. (8) Pathways across the blood brain barrier include transcellular pathways, such as receptor or adsorptive-mediated transcytosis, and paracellular pathways. (8) One of the important questions we look forward to answering is if our mitochondrial targeting NPBA can be used to deliver therapeutic materials to the brain by exploiting the adsorptive mediated transcytosis pathway. Little is known about the capacity of triphenylphosphonium ligands to cross the BBB. (20) Preliminary investigations employing BBB models can be a good place to start answering such question. (155) In case of their failure to overcome the BBB, can they be used in conjunction with techniques recently developed to increase the permeability of the BBB? Researchers at Brigham and Women's Hospital developed a microbubbles-assisted focused ultrasound technology that can temporarily loosen the BBB and allow the accumulation of therapeutic material in the brain, figure 55. (156) (157) The microbubbles, under the influence of the focused ultrasound waves, vibrate and widen the tight junctions between endothelial cells allowing the passive or active paracellular transport of the therapeutic material across the BBB. (156) (157) The coupling of focused ultrasound short bursts, ~ 1–20 ms/burst applied at a low duty cycle (1–5%) for 0.5–1 min, reduces the energy needed to permeabilize the BBB, thus, prevent permanent damage to the integrity of the BBB. (156) (157)

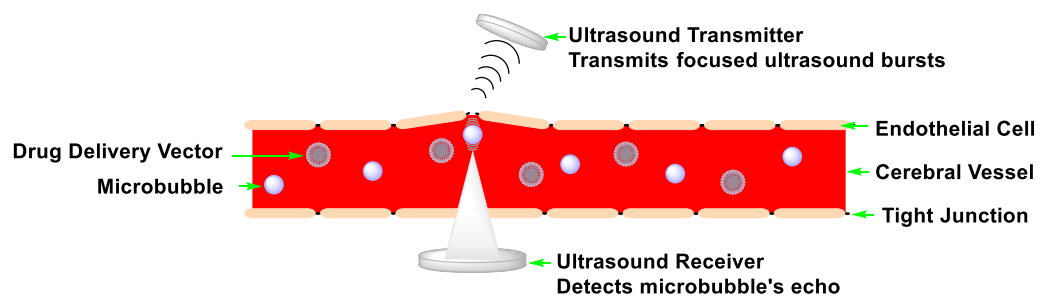


Figure 55: Schematic representation of the principle of the microbubbles-assisted focused ultrasound technology that can temporarily loosen the BBB. The microbubbles, under the influence of the focused ultrasound waves, vibrate and widen the tight junctions between endothelial cells allowing the passive or active paracellular transport of the therapeutic material across the BBB. Figure taken from Ref. (156)

9 Experimental Section

9.1 General Considerations

Toluene, Tol, dichloromethane, DCM, and tetrahydrofuran, THF, were dried by passing them through two columns of alumina, MBRAUN SPS-800 purification system. Oxalyl chloride, $(\text{COCl})_2$, and triethylamine, NEt_3 , were distilled, under argon, from and stored over calcium hydride, CaH_2 . Dimethylsulfoxide, DMSO, and dimethylformamide, DMF, were distilled, under vacuum, and stored over 4 Å molecular sieves. Methanol (MeOH) was distilled in a recycling still under argon over CaH_2 . Molecular sieves (4 Å) were activated by heating them at 200 °C under high vacuum overnight, followed by purging with argon.

9.2 Compound Characterization Techniques

Nuclear Magnetic Resonance, NMR, spectra, ^1H , ^{13}C and ^{31}P were recorded at ambient conditions and acquired on Bruker Avance III 700 and 500 spectrometers. Peak assignments were confirmed by 2D experiments. ^1H and ^{13}C chemical shifts were measured relative to TMS and referenced to the residual solvent peaks as internal standards, $\text{CDCl}_3 = 7.26$ ppm for ^1H and 77.16 ppm for ^{13}C NMR. Chemical shifts were reported in ppm, parts per million, and solvent peaks were referenced to reported literature values.

High Resolution Mass Spectrometry, HRMS, was performed by the EPSRC national mass spectrometry service (Swansea, UK). Ionization was carried out using Nano-Electrospray Ionization, NSI, and values were designated by $[\text{M}+\text{H}]^+$ or $[\text{M}+\text{NH}_4]^+$.

Fourier-Transform Infra-Red Spectroscopy, FTIR, was performed using Shimadzu IRAffinity-1 FTIR spectrometer using attenuated total reflectance, ATR, as the sampling technique. Absorption maxima are recorded in wavenumbers cm^{-1} .

Matrix Assisted Laser Desorption Ionization-Mass Spectra, MALDI-MS, were acquired using a 4800 MALDI TOF Analyser, ABSciex, equipped with a Nd:YAG 355 nm laser and calibrated using a mixture of peptides. Data was analyzed, using GPS Explorer, ABSciex, to interface with the Mascot 2.4 search engine (Matrix Science) and the MSMS data using Mascot 2.4 directly. The sample solution (0.5 μL) was applied to the MALDI target along with alpha-cyano-4- hydroxycinnamic acid matrix (0.5 μL , 10 mg/mL in 50:50 acetonitrile:0.1% TFA) and allowed to dry.

Thin Layer Chromatography, TLC, was performed using pre-coated Merck silica gel 60 (F_{254}) plates after which they were treated with phosphomolybdic acid, PMA, followed by heating as the visualization technique.

Normal Phase Liquid Chromatography, NPLC, was performed using Merck silica gel 60 (0.04 – 0.063

mm) to purify products by flash chromatography using reagent grade solvents which were used as purchased.

Gel Permeation Chromatography, GPC, was performed using two PhenoGel columns, 100 A and 500 A, 5 μ m, 300 X 7.8 mm from Phenomenex, connected in series with a refractive index detector from Shimadzu. GPC sample analysis was performed at 30 °C using LiBr in DMF as the eluent at a flow rate of 0.8 mL / min. Molecular weights were assigned by normalizing the RID response against a calibration curve that was obtained using polyethylene glycol standards.

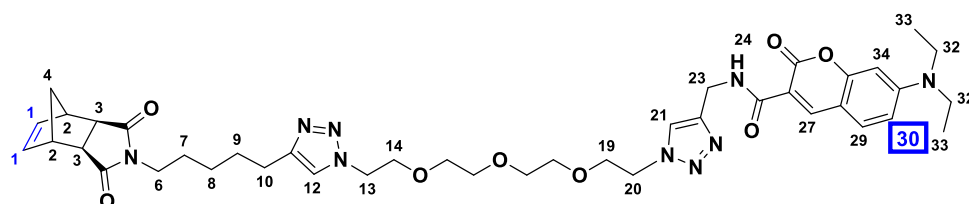
Absorbance Spectroscopy was performed using LAMBDA 950 UV/Vis spectrophotometer from PerkinElmer. Fluorescence Spectroscopy was performed to determine excitation and emission maxima of fluorescent polymer samples using Edinburgh Photonics FLS980 spectrometer employing Xenon lamp as the excitation source. Samples were dissolved in deionized water at a concentration of 10 μ M, filtered and loaded into poly-propylene cuvettes. To validate the excitation maximum, emission was fixed at 480 nm and excitation was scanned from 200 nm to 460 nm. To determine the emission maximum, excitation was fixed at 430 nm and emission was scanned from 440nm to 800 nm. Colorimetric assays were conducted using SpectraMax® M2e multi-mode microplate reader from Molecular Devices.

Two-photon induced fluorescence was examined using a titanium-sapphire laser, Chamaeleon 2, from Coherent. The pulsed laser beam was set to an average power of \approx 50 mW with a pulse duration τ_p and repetition rate f_p of about 100 fs and 80 MHz respectively. The pulsed laser beam wavelength λ was tuned across a wavelength range from 800-1000 nm to find the optimal two-photon excitation of the block-*co*-polymer sample. The block-*co*-polymer I sample was prepared by dissolution in deionized water to make up a concentration of 10 μ M, filtered and loaded into a glass dish.

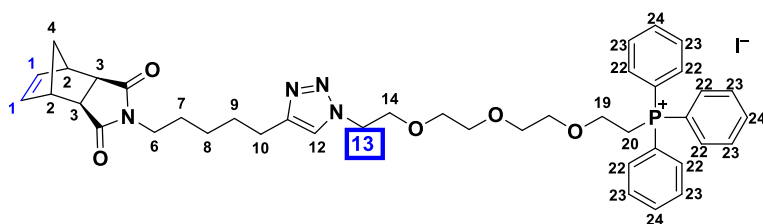
Cell imaging was performed using a confocal laser scanning microscope Leica TCS SP8. Images were captured at a magnification of 63 using a 63 \times oil objective with a numerical aperture of 1.4. Sequential scanning between frames was performed by separately exciting Hoechst, NPs, and MitoTracker™ deep red at 405, 458 and 633 nm, respectively. HyD (414 – 449 nm), PMT (469 – 486 nm) and HyD (654 – 680 nm) channels were used to detect the fluorescence of Hoechst, NPs, and MitoTracker™ deep red respectively. Images were processed using ImageJ software.

9.3 Standard Procedure for Determining the Homo-Polymerization Kinetics of First-Generation Monomers Using ^1H NMR

Polymerization and ^1H NMR sample preparation were performed under inert conditions in a glovebox as described in a literature procedure. (91) A scintillation vial (2.00 mL) was charged with the NorbEO₄Coumarin monomer (10.0-40.0 equiv., 3.36-13.4 mg, 4.13-16.5 μmol) or NorbEO₄PPh₃ monomer (10.0-40.0 equiv., 3.50-14.0 mg, 4.13-16.5 μmol) and dry and degassed DMF (21.3-145 μL to NorbEO₄Coumarin and 62.5-310 μL to NorbEO₄PPh₃) to make up a monomer solution of an initial concentration of 0.10 M for NorbEO₄Coum or 0.05 M for NorbEO₄PPh₃I samples once the catalyst solution is added. To the stirred solution, 700 rpm, at 24 °C, the homo-polymerization of each sample was initiated by addition of a solution of GIII (1.00 equiv., 0.30 mg, 0.40 μmol) in dry and degassed DMF (20.0 μL). At 2 min-interval, a sample of the reaction mixture (5.00 μL) was withdrawn, dissolved in deuterated chloroform (CDCl_3), 500 μL , transferred to an NMR tube and immediately analyzed by ^1H NMR without quenching with ethyl vinyl ether (EVE). This was due to the overlap of the EVE signal satellites with the scrutinized olefinic signal which resulted in difficulties in its quantification and, consequently, in determining monomer concentration over time.



NorbEO₄Coum



NorbEO₄PPh₃I

Polymerization rate dependence on monomer concentration was determined by ^1H NMR by monitoring the lapse of olefinic signal of the polymerizable N-norbornene dicarboximide end at $\approx \delta$ 6.19 (t, $J = 2.0$ Hz, 2H, 1) at two-minutes intervals by integrating it using the aromatic signal of NorbEO₄Coum at $\approx \delta$ 6.56 (dd, $J = 9.0, 2.5$ Hz, 1H, 30) or aliphatic signal of NorbEO₄PPh₃I at $\approx \delta$ 4.46 (t, $J = 5.2$ Hz, 2H, 13) as a reference as they don't shift or significantly broaden as a result of polymerization.

$[M]_t$ was calculated using equation:

$$[M]_t = \frac{\text{Integration} \times [M]_0}{2}$$

Where integration fitted in the equation is that of the olefinic signal in the sample aliquot withdrawn from reaction mixture at time t . 2 is the integration of the same olefinic signal of the monomer solution of initial concentration $[M]_0$ at time 0.

The homo-polymerization rate was assumed to be dependent on only the concentration of the monomer and therefore obeys the first-order rate law:

$$-\frac{\partial[M]}{\partial t} = k_{obs}t$$

Accordingly, time was plotted against the logarithmic values of $[M]_0/[M]_t$ the slope of which was identified as the polymerization rate constant k_{obs} . As described in

$$\text{Ln} \frac{[M]_0}{[M]_t} = k_{obs}t$$

9.4 Standard Procedure for Determining the Homo-Polymerization Kinetics of Second-Generation Monomers Using ^1H NMR

Homo-polymerization was performed and monitored under inert conditions in a glovebox as described for first-generation homo-polymers. A scintillation vial (2.00 mL) was charged with the NorbEO₁₂Coumarin monomer (20.0-60.0 equiv., 9.50-28.5mg, 8.25-24.8 μmol) or NorbEO₄PPh₃ monomer (20.0-60.0 equiv., 9.92-29.8 mg, 8.25-24.8 μmol) and dry and degassed DMF (145-475 μL) to make up a monomer solution of an initial concentration of 0.05 M once the catalyst solution is added. To the stirred solution, 700 rpm, at 24 °C, the homo-polymerization of each sample was initiated by addition of a solution of GIII (1.00 equiv., 0.30 mg, 0.40 μmol) in dry and degassed DMF (20.0 μL). Polymerization rate dependence on monomer concentration was determined by ^1H NMR by monitoring the lapse of olefinic signal of the polymerizable N-norbornene dicarboximide end at $\approx \delta$ 6.19 (t, $J = 2.0$ Hz, 2H, 1) at two-minute intervals by integrating it using the aromatic signal of NorbEO₁₂Coum at $\approx \delta$ 6.56 (dd, $J = 9.0, 2.5$ Hz, 1H, 49) or aliphatic signal of NorbEO₁₂PPh₃I at $\approx \delta$ 4.46 (t, $J = 5.2$ Hz, 2H, 13) as a reference. Time was plotted against the logarithmic values of $[M]_0/[M]_t$, which were calculated as described for first-generation homo-polymers, the slope of which was identified as the polymerization rate constant k_{obs} . As described in:

$$\text{Ln} \frac{[M]_0}{[M]_t} = k_{obs}t$$

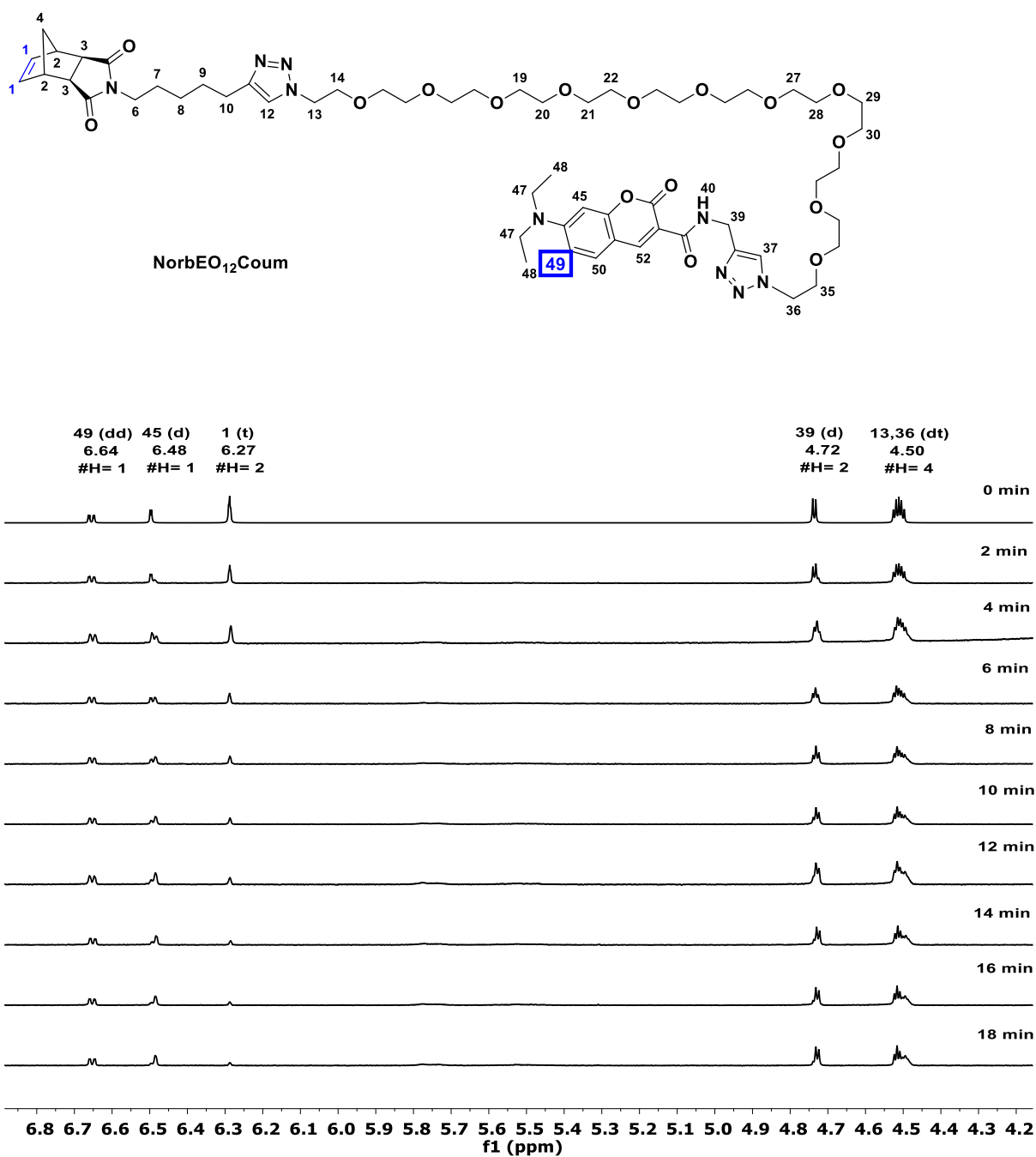


Figure 56: Lapse of olefinic signal, δ 6.27 (t, $J = 2.0$ Hz, 2H, 1), over time, 0-18 min, observed during the homo-polymerization of NorbEO₁₂Coumarin, 60 equiv. and 0.05 M, initiated by GIII catalyst, 1.0 equiv. The stacked spectra show signals δ 6.64 (dd, $J = 9.0, 2.5$ Hz, 1H, 49), 6.48 (d, $J = 2.5$ Hz, 1H, 45), 6.27 (t, $J = 2.0$ Hz, 2H, 1), 4.72 (d, $J = 5.7$ Hz, 2H, 39), 4.50 (dt, $J = 10.2, 5.2$ Hz, 4H, 13, 36), with the signal corresponding to 49 being the least to undergo broadening during polymerization which was the reason for using it as an internal reference signal. Spectra were acquired at ambient conditions using Bruker Avance III 700 MHz and CDCl₃ as the deuterated solvent.

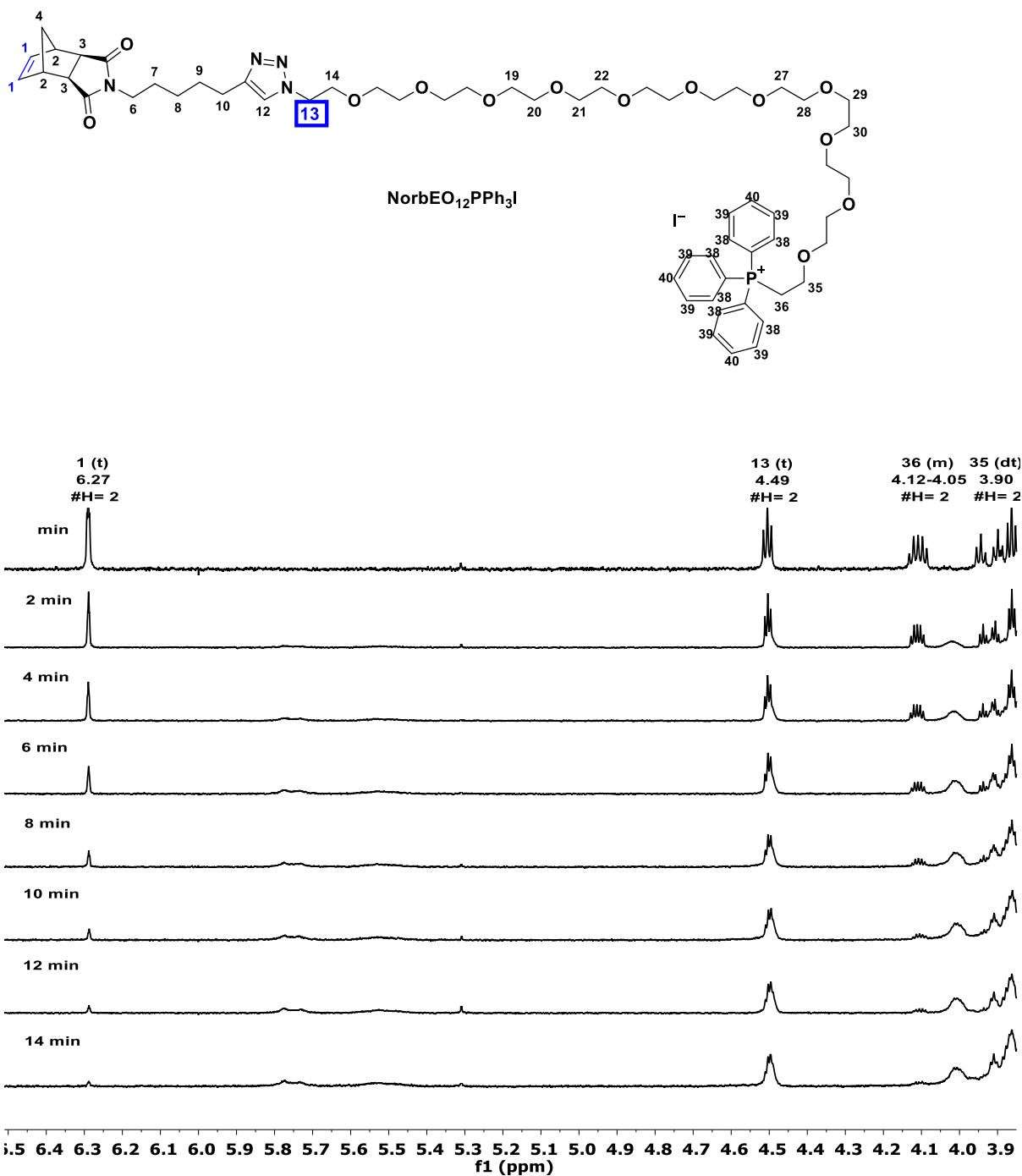


Figure 57: Lapse of olefinic signal, δ 6.27 (t, $J = 2.0$ Hz, 2H, 1), over time, 0-14 min, observed during the homo-polymerization of **NorbEO₁₂PPh₃I**, 60 equiv. and 0.05 M, initiated by **GIII** catalyst, 1.0 equiv. The stacked spectra show signals δ 6.27 (t, $J = 1.9$ Hz, 2H, 1), 4.49 (t, $J = 5.2$ Hz, 2H, 13), 4.12 – 4.05 (m, 2H, 36), 3.90 (dt, $J = 22.3, 5.8$ Hz, 2H, 35), with the signal corresponding to 13 being the least to shift during polymerization which was the reason for using it as an internal reference signal. Spectra were acquired at ambient conditions using Bruker Avance III 700 MHz and CDCl₃ as the deuterated solvent.

9.5 Standard Procedure for Evaluating the Progression of Mn and *D* of Propagating Homo-Polymer Chains of First- and Second-Generation Monomers Using GPC

Progression of Mn and molecular weight distribution, *D*, of propagating homo-polymer chains was monitored by using the aforementioned ¹H NMR samples. The samples were quenched by excessive addition of EVE, 200 μL per 500 μL NMR sample, immediately after completion of NMR acquisition, dried and dissolved in HPLC grade DMF (300 μL) after which GPC traces were acquired at 30 °C using LiBr in DMF (0.20 M) as the eluting solvent with a flow-rate of 0.8 mL/min.

9.6 Standard Homo-Polymerization Procedure of First-Generation Monomers

A scintillation vial (2.00 mL) was charged with the NorbEO₄Coumarin monomer (10.0-40.0 equiv., 3.36-13.4 mg, 4.13-16.5 μmol) or NorbEO₄PPh₃ monomer (10.0-40.0 equiv., 3.50-14.0 mg, 4.13-16.5 μmol) and dry and degassed DMF (21.3-145 μL to NorbEO₄Coumarin and 62.5-310 μL to NorbEO₄PPh₃) to make up a monomer solution of an initial concentration of 0.10 M for NorbEO₄Coum or 0.05 M for NorbEO₄PPh₃I samples once the catalyst solution is added. To the stirred solution, 700 rpm, at 24 °C, the homo-polymerization of each sample was initiated by addition of a solution of GIII (1.00 equiv., 0.30 mg, 0.40 μmol) in dry and degassed DMF (20.0 μL). When consumption of monomer reached ≈ 90%, determined using ¹H NMR as described above, excess of EVE was added (≈ 1.00 mL). The termination step was run for 15 min after which the suspension was transferred to an Eppendorf Tube®, diluted with Et₂O:Hex mixture (1:1, 0.50 mL) and centrifuged. Solvents were discarded and residual oil was repeatedly centrifuged with Et₂O to remove any residual DMF after which oil was dried under vacuum for 24 hrs to afford the desired polymer as a waxy solid.

9.7 Standard Homo-Polymerization Procedure of Second-Generation Monomers

A scintillation vial (2.00 mL) was charged with the NorbEO₁₂Coumarin monomer (20.0-60.0 equiv., 9.50-28.5mg, 8.25-24.8 μmol) or NorbEO₄PPh₃ monomer (20.0-60.0 equiv., 9.92-29.8 mg, 8.25-24.8 μmol) and dry and degassed DMF (145-475 μL) to make up a monomer solution of an initial concentration of 0.05 M once the catalyst solution is added. To the stirred solution, 700 rpm, at 24 °C, the homo-polymerization of each sample was initiated by addition of a solution of GIII (1.00 equiv., 0.30 mg, 0.40 μmol) in dry and degassed DMF (20.0 μL). When consumption of monomer reached ≈ 85-90%, determined using ¹H NMR as described above, excess of EVE was added (≈ 1.00 mL). The termination step was run for 15 min after which the suspension was transferred to an Eppendorf Tube®, diluted with Et₂O:Hex mixture (1:1, 0.50 mL) and centrifuged. Solvents were discarded and residual

oil was repeatedly centrifuged with Et₂O to remove any residual DMF after which oil was dried under vacuum for 24 hrs to afford the desired polymer as a waxy solid.

9.8 Standard Block-*Co*-Polymerization Procedure of Second-Generation Monomers

Block-*co*-polymerization was performed and monitored under inert conditions in a glovebox. A scintillation vial (2.00 mL) was charged with the NorbEO₁₂Coumarin monomer (4.00 equiv., 4.00 mg, 3.47 μmol) and dry and degassed DMF (46.0 μL) to make up a monomer solution of an initial concentration of 0.05 M once the catalyst solution is added. To the stirred solution, 700 rpm, at 24 °C, the homo-polymerization of each sample was initiated by addition of a solution of GIII (1.00 equiv., 0.60 mg, 0.80 μmol) in dry and degassed DMF (20.0 μL). Monomer consumption was followed by ¹H NMR by monitoring the lapse of olefinic signal at $\approx \delta$ 6.27 (t, $J = 2.0$ Hz, 2H, 1) at two-minute intervals by integrating it using the aromatic signal of NorbEO₁₂Coumarin at $\approx \delta$ 6.56 (dd, $J = 9.0, 2.5$ Hz, 1H, 49). When 85-90% conversion of NorbEO₁₂Coumarin was reached, a solution of NorbEO₁₂PPh₃I (6.00-14.0 equiv., 6.00-14.0 mg, 5.00-12.0 μmol) in dry and degassed DMF (33.9-167 μL) was added in one portion. The consumption was followed ¹H NMR by monitoring the lapse of olefinic signal at $\approx \delta$ 6.27 (t, $J = 2.0$ Hz, 2H, 1) at two-minutes intervals and normalizing it to the signal at $\approx \delta$ 4.46 (t, $J = 5.2$ Hz, 2H, 13). When 85-90% conversion of NorbEO₁₂PPh₃I was reached, the propagation was terminated by excess addition of EVE was added (≈ 1.00 mL). The termination step was run for 15 min after which the suspension was transferred to an Eppendorf Tube®, diluted with Et₂O:Hex mixture (1:1, 0.50 mL) and centrifuged. Solvents were discarded and residual oil was repeatedly centrifuged with Et₂O to remove any residual DMF after which oil was dried under vacuum for 24 hrs to afford the desired polymer as a waxy solid.

9.9 Determination of the Ratio of Second-Generation Monomers in the Structure of First-Generation Co-Polymers Using ^1H NMR Spectroscopy

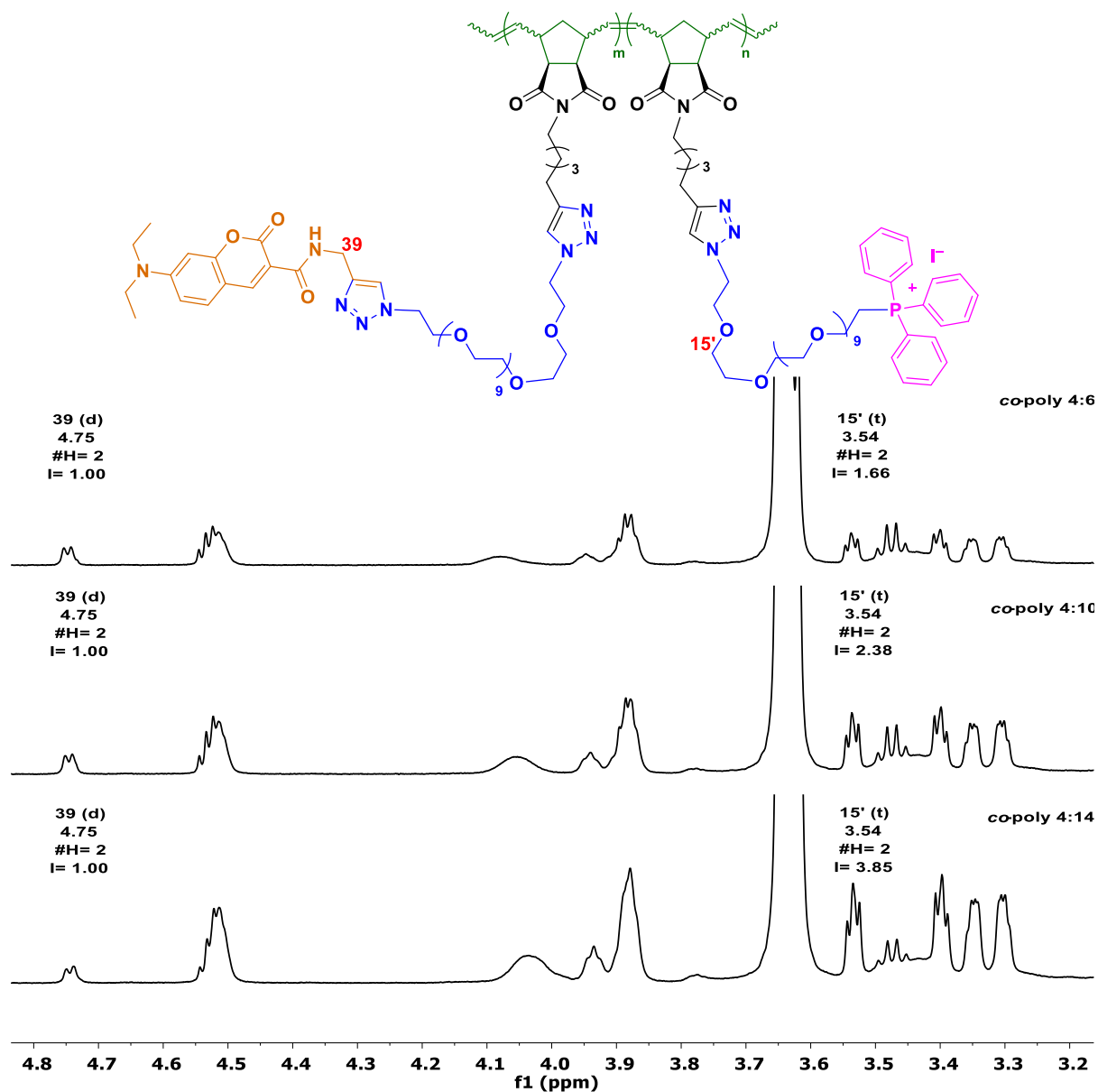


Figure 58: Stacked ^1H NMR spectra, showing only the region from δ 4.8 to δ 3.2, of the three block-co-polymers, I, II and III derived from NorbEO₁₂Coumarin and NorbEO₁₂PPh₃I at a ratio of 4:6, 4:10 and 4:14 respectively. The stacked spectra show the increase of the block-co-polymers content of the mitochondrial targeting monomer as we go from co-polymer I, II to III.

9.10 Cell Culture Methods

HEK 293 cells were cultured in Dulbecco's modified Eagle's medium, DMEM, containing glucose (25 mM), L-glutamine (4 mM), and phenol red (40 μ M). This medium was supplemented with sodium pyruvate (1 mM), 10% (v/v) heat-inactivated fetal bovine serum, FBS, and 1% penicillin streptomycin, P/S. Cells were cultivated in T75 flasks at 37 °C with 5% CO₂ at saturated humidity.

HS-SY5Y cells were cultured in Dulbecco's modified Eagle's- Ham's F-12 nutrient mixture medium, DMEM/F12, containing glucose (18 mM), L-glutamine (2.5 mM), HEPES (15 mM) and sodium pyruvate (0.5 mM). This medium was supplemented with 10% (v/v) heat-inactivated fetal bovine serum, FBS, and 1% penicillin streptomycin, P/S. Cells were cultivated in T75 flasks at 37 °C with 5% CO₂ at saturated humidity.

9.11 AlamarBlue® Cellular Viability Assay Protocol

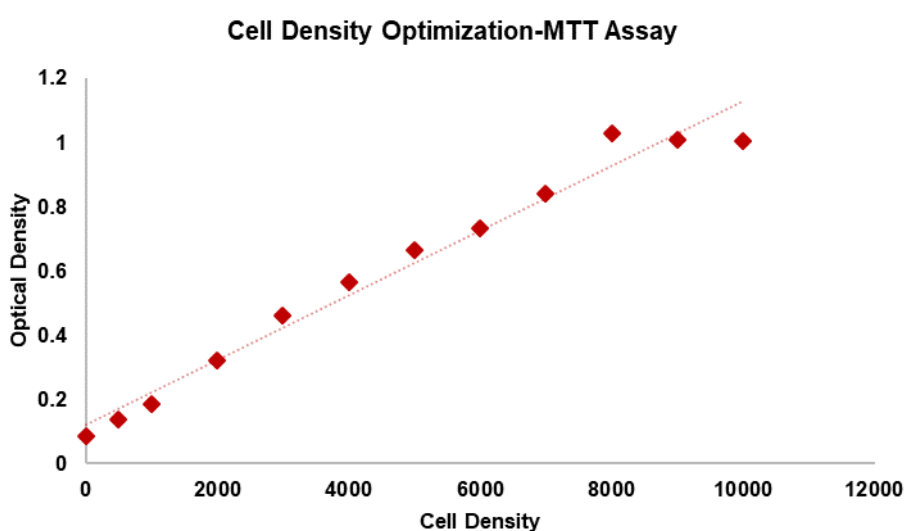
Cells were dissociated by treatment with TrypLE™, counted, resuspended in phenol-free DMEM to a 1.0×10^6 cells/mL stock, supplemented with 10% FBS and reseeded in a black, flat-bottom 96-well plate at a density of 2.0×10^4 cells per well. Cells were allowed to adhere overnight at 37 °C with 5% CO₂ after which media was removed and 100 μ L of serially diluted solutions (0-100 μ M) of NorbEO₁₂PPh₃I-derived homo-polymers (12-25 DP) in FBS-free DMEM was added. The cells were incubated with NPs for 3 hr at 37 °C with 5% CO₂ after which AlamarBlue® (10 μ L) was dispensed in each well. Cells were incubated for 3 hr at 37 °C with 5% CO₂ then fluorescence was read at excitation of 570 nm and emission of 585 nm.

9.12 MTT Cellular Viability Assay Protocol

Cells were dissociated by treatment with TrypLE™, counted, resuspended in phenol-free DMEM/F12 to a 1.0×10^6 cells/mL stock, supplemented with 10% FBS, and reseeded in a black, flat-bottom 96-well plate at a density of 5.0×10^3 cells per well. Cells were allowed to adhere overnight at 37 °C with 5% CO₂ after which media was removed and 100 μ L solutions (0-100 μ M) of block-co-polymer samples, I, II and III, diluted from a 100 μ M stock at 10 μ M intervals, in FBS-free DMEM/F12 were added. The cells were incubated with NPs for 3 hr at 37 °C with 5% CO₂ after which media from all wells is removed and a solution of MTT reagent in FBS-free DMEM/F12 (200 μ L, 4 mM) was added in each well. Cells were incubated for 3 hr at 37 °C with 5% CO₂ then media was removed from all wells. DMSO (100 μ L) was added to all wells and absorbance was read at 570 nm.

9.12.1 Cell Density Optimization for MTT Assay Protocol

Cells were dissociated by treatment with TrypLE™, counted, resuspended in phenol-free DMEM/F12 to a 1.0×10^6 cells/mL stock, supplemented with 10% FBS, and reseeded in a black, flat-bottom 96-well plate at a density of $0.0\text{--}1.0 \times 10^4$ cells per well. Cells were allowed to adhere overnight at 37 °C with 5% CO₂ after which media was removed and a solution of MTT reagent in FBS-free DMEM/F12 (200 μ L, 4 mM) was added in each well. Cells were incubated for 3 hr at 37 °C with 5% CO₂ then media was removed from all wells. DMSO (100 μ L) was added to all wells and absorbance was read at 570 nm. Absorbance was plotted against cell density. Optimal cell density is the one at which cells are distributed homogeneously on the bottom surface of the well and with an absorbance readout that falls within the detection limit of the plate reader, 0.0-2.0 OD.



9.12.1.1 Cell Staining Protocols

Cells were dissociated by treatment with TrypLE™, counted, resuspended in phenol-free DMEM/F12 to a 1.0×10^6 cells/mL stock, supplemented with 10% FBS, and reseeded on eleven coverslips, 22 mm \times 22 mm, placed in two 6-well plates at a density of 2.0×10^5 cells per well. Cells were allowed to adhere overnight at 37 °C with 5% CO₂ after which media was removed and cells were washed with a pre-warmed PBS (1 \times 3.0 mL). Cells were treated with pre-warmed Hoechst staining solution (3.0 mL, 8.12 μ M), prepared by diluting 5 μ L of a 10 mg/mL stock solution up to 10 mL using PBS, and incubated for 15 min at room temperature in the dark. Staining solution was aspirated and cells were washed with pre-warmed PBS, 3 \times 3.0 mL, and treated with a pre-warmed MitoTracker™ deep red staining solution (3.0 mL, 100 nM) prepared by diluting 1 μ L of a 1 mM stock up to 10 mL using PBS.

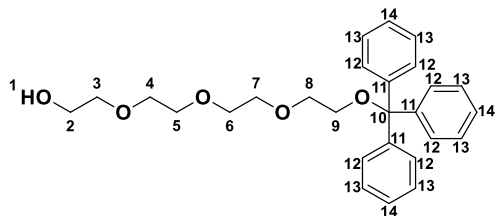
Cells were incubated for 30 min at 37 °C with 5% CO₂. Staining solution was aspirated and cells were washed with pre-warmed PBS, 3 × 3.0 mL. The adherence and morphology of cells was monitored using Leica DMI1 microscope.

9.13 Cellular Uptake Assessment Protocol

The stained cells seeded on ten coverslips were incubated with a solution of block-*co*-polymer I in PBS (2.0 mL, 5.0 μM). The incubation times for the ten samples ranged from 0-50 min at five-minutes intervals. At the end of incubation period, block-*co*-polymer I solution was aspirated and cells were washed with PBS (3 × 3.0 mL). Control and block-*co*-polymer I-incubated samples were fixed with 4% formaldehyde (2.0 mL, 15 min). Formaldehyde fixing solution was aspirated and cells were washed with PBS (3 × 3.0 mL). Coverslips were mounted on slides using mounting media.

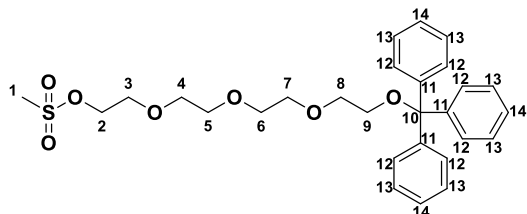
9.14 Compound Synthesis Procedures

Mono-trityl-tetraethylene glycol (**1**). Ref. (82)



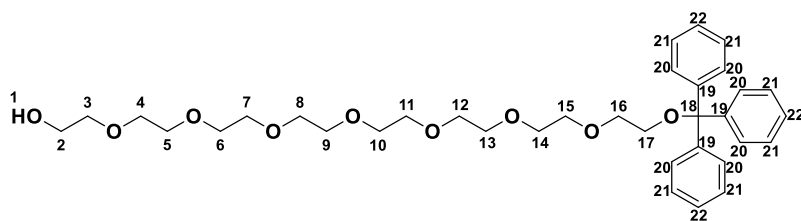
Compound was prepared according to a literature procedure. (82) Oven-dried, three-neck round-bottom flask (1.00 L), fitted with a reflux condenser, was charged with TEG (1.30 equiv., 50.0 g, 180 mmol) previously dried by azeotropic co-evaporation with dry toluene (2×50.0 ml), TryCl (1.00 equiv., 37.3 g, 139 mmol), DMAP (0.04 equiv., 0.63 g, 5.15 mmol) and dry NEt_3 (1.04 equiv., 14.6 g, 144 mmol). The reaction mixture was stirred at 50 °C overnight after which it was cooled down to RT and washed with water (400 ml) and brine (400 ml). Aqueous fractions were extracted with ether (2×400 ml) and combined organic fractions were washed with sat. NH_4Cl (50.0 ml) and brine (50.0 ml), dried over Na_2SO_4 and concentrated using a rotary evaporator to afford the desired compound as a yellow oil (56.5 g, 93% yield, Oligomeric purity 87% as estimated by MALDI). The absence of TEG was confirmed by TLC (UV 254 nm, 100% EtOAc $\text{Tr}(\text{EO})_4\text{H}$ R_f 0.64; TEG R_f 0). $^1\text{H NMR}$ (700 MHz, CDCl_3) δ 7.46 (d, $J = 7.8$ Hz, 6H, 12), 7.29 (t, $J = 7.6$ Hz, 6H, 13), 7.23 (t, $J = 7.3$ Hz, 3H, 14), 3.72 – 3.64 (m, 12H, 2, 4-8), 3.59 (t, $J = 4.6$ Hz, 2H, 3), 3.24 (t, $J = 5.2$ Hz, 2H, 9), 2.40 (t, $J = 6.4$, 1H, 1). $^{13}\text{C NMR}$ (176 MHz, CDCl_3) δ 144.2 (11), 128.8 (12), 127.9 (13), 127.1 (14), 86.7 (10), 72.6 (3), 70.9, 70.9, 70.8, 70.6 (8), 63.4 (9), 61.9 (2). Spectroscopic data agree with literature values. (82)

Mono-trityl-tetraethylene glycol mesylate (**2**).



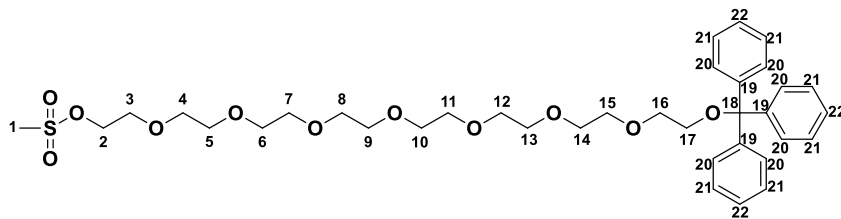
Oven-dried, one-neck round-bottom flask (250 mL) was charged with $\text{Tr}(\text{EO})_4\text{H}$ (1.04 equiv., 15.2 g, 34.9 mmol), THF (150 mL) and MsCl (1.30 equiv., 5.19 g, 45.4 mmol). Reaction mixture was cooled down to 0 °C after which NEt_3 (1.50 equiv., 5.29 g, 52.2 mmol) was added in a dropwise fashion. After the addition was complete, during which salts had formed, the reaction mixture was slowly allowed to warm up to RT. When complete consumption of $\text{Tr}(\text{EO})_4\text{H}$ was confirmed by TLC (50% EtOAc: Hexane; $R_f=0.1$ $\text{Tr}(\text{EO})_4\text{H}$, $R_f=0.37$ $\text{Tr}(\text{EO})_4\text{Ms}$), water was added to dissolve salts after which organic layer was extracted with DCM (3×100 mL), dried over Na_2SO_4 and concentrated using rotary evaporator. Excess MsCl was removed by vacuum distillation and crude was dissolved in EtOAc (150 mL). Colored impurities were adsorbed to activated charcoal. Solids were filtered over a pad of celite and EtOAc was removed using rotary evaporator to afford the title compound as a yellow oil (19.5 g, 89 % yield, Oligomeric purity 95% as estimated by MALDI). **^1H NMR** (700 MHz, CDCl_3) δ 7.46 (d, $J = 7.8$ Hz, 6H, 12), 7.30 (t, $J = 7.6$ Hz, 6H, 13), 7.23 (t, $J = 7.3$ Hz, 3H, 14), 4.36 – 4.30 (m, 2H, 2), 3.77 – 3.67 (m, 2H, 3), 3.71 – 3.63 (m, 10H, 4-8), 3.26 – 3.19 (m, 2H, 9), 2.99 (s, 3H, 1). **^{13}C NMR** (126 MHz, CDCl_3) δ 144.1 (11), 128.7 (12), 127.8 (13), 126.98 (14), 86.5 (10), 70.80, 70.7, 69.3, 69.0, 63.3, 37.7 (1). **MALDI-TOF** calcd. for $\text{C}_{28}\text{H}_{34}\text{O}_7\text{S}$ [$\text{M}+\text{Na}^+$] 537.20, found 537.28.

Mono-trityl-octaethylene glycol (**3**) Ref. (82)



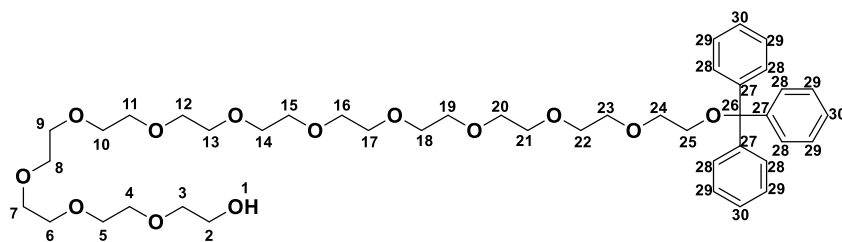
Oven-dried, three-neck round-bottom flask (250 ml), fitted with a dropping funnel and a reflux condenser, was charged with NaH (60% in mineral oil, 1.30 equiv., 1.21 g, 40.2 mmol) which was washed with dry hexane (5.00 mL). Dry THF (25.0 mL) was added and the suspension was cooled down to 0 °C. To the stirring suspension, TEG (8.00 equiv., 48.0 g, 247 mmol) previously dried by azeotropic *co*-evaporation with dry toluene (2 × 50.0 mL) was slowly added via the dropping funnel. Once the evolution of H₂ had ceased and the suspension had turned into a clear solution, the remaining TEG was added in one portion after which Tr(EO)₄Ms (1.00 equiv., 15.9 g, 30.9 mmol) in dry THF (30 mL) was added in one portion. The resulting reaction mixture was heated at 50 °C overnight. Complete consumption of Tr(EO)₄Ms was confirmed by TLC (50% EtOAc: Hexane; *R_f* = 0.37 Tr(EO)₄Ms, 100% EtOAc; *R_f* = 0.2 Tr(EO)₈H). The reaction mixture was cooled down to RT then brine (50.0 mL) was added. The organic layer was separated, washed with brine (6 × 30.0 mL) and combined aqueous fractions were extracted with Et₂O (200 mL). The absence of TEG was confirmed by TLC (100% EtOAc; *R_f* = 0). Combined organic fractions were dried over Na₂SO₄ and concentrated using a rotary evaporator to afford the desired compound as a yellow oil (17.0 g, 90% yield, Oligomeric purity 93% as estimated by MALDI). ¹H NMR (700 MHz, CDCl₃) δ 7.46 (d, *J* = 7.8 Hz, 6H, 20), 7.29 (t, *J* = 7.6 Hz, 6H, 21), 7.22 (t, *J* = 7.3 Hz, 3H, 22), 3.76 – 3.62 (m, 28H, 3-16), 3.61 – 3.58 (m, 2H, 2), 3.24 (t, *J* = 5.2 Hz, 2H, 17). ¹³C NMR (176 MHz, CDCl₃) δ 144.2 (19), 128.8 (20), 127.8 (21), 127.0 (22), 86.6 (18), 72.6, 70.9, 70.8, 70.7, 70.6, 70.5, 70.4, 63.4 (17), 61.8 (3). MALDI-TOF calcd. for C₃₅H₄₈O₉ [M+Na⁺] 635.33, found 635.10. Spectroscopic data agree with literature values. (82)

Mono-trityl-octaethylene glycol mesylate (**4**)



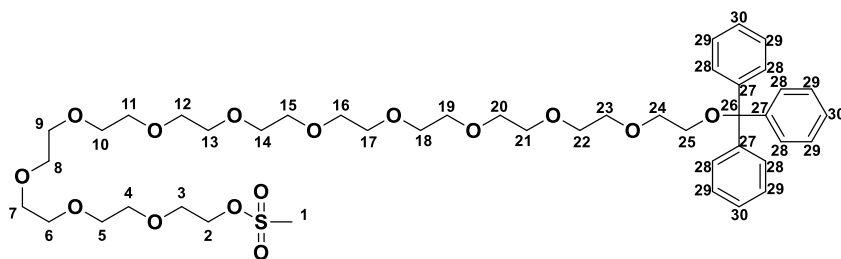
Oven-dried, one-neck round-bottom flask (250 ml) was charged with Tr(EO)₈H (1.04 equiv., 17.0 g, 27.7 mmol), THF (150 ml) and MsCl (1.30 equiv., 4.13 g, 36.1 mmol). Reaction mixture was cooled down to 0 °C after which NEt₃ (1.50 equiv., 4.36 g, 41.6 mmol) was added in a dropwise fashion. After the addition was complete, during which white salts had formed, the reaction mixture was slowly allowed to warm up to RT. When complete consumption of Tr(EO)₈H was confirmed by TLC (100% EtOAc; *R_f* = 0.2 Tr(EO)₈H, *R_f* = 0.5 Tr(EO)₈Ms), water was added to dissolve salts after which organic layer was extracted with DCM (3 × 100 mL), dried over Na₂SO₄ and concentrated using rotary evaporator. Excess MsCl was removed by vacuum distillation and crude was dissolved in EtOAc (150 mL). Colored impurities were adsorbed to activated charcoal. Solids were filtered over a pad of celite and EtOAc was removed using rotary evaporator to afford the title compound as a yellow oil (14.0 g, 73% yield, Oligomeric purity 96% as estimated by MALDI). ¹H NMR (700 MHz, CDCl₃) δ 7.48 (d, *J* = 7.8 Hz, 6H, 20), 7.32 (t, *J* = 7.6 Hz, 6H, 21), 7.25 (t, *J* = 7.3 Hz, 3H, 22), 4.44 – 4.37 (m, 2H, 2), 3.82 – 3.73 (m, 2H, 3), 3.74 – 3.61 (m, 26H, 4-16), 3.25 (t, *J* = 5.2 Hz, 2H, 17), 3.10 (s, 3H, 1). ¹³C NMR (126 MHz, CDCl₃) δ 144.1 (19), 128.7 (20), 127.8 (21), 126.9 (22), 86.5 (18), 70.80, 70.7, 70.6, 70.5, 69.3, 69.0, 63.3, 37.8 (1). **MALDI-TOF** calcd. for C₃₆H₅₀O₁₁S [M+Na⁺] 713.31, found 713.10.

Mono-trityl-dodecaethylene glycol (**5**). Ref. (82)



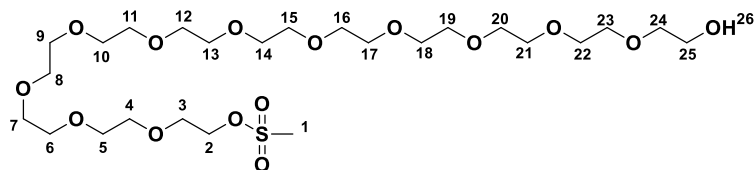
Oven-dried, three-neck round-bottom flask (250 mL), fitted with a dropping funnel and a reflux condenser, was charged with NaH (60% in mineral oil, 1.30 equiv., 1.05 g, 26.3 mmol) which was washed with dry hexane (5.00 mL). Dry THF (25.0 mL) was added and the suspension was cooled down to 0 °C. To the stirring suspension, TEG (8.00 equiv., 31.5 g, 162 mmol) previously dried by azeotropic *co*-evaporation with dry toluene (2 × 50.0 mL) was slowly added via the dropping funnel. Once the evolution of H₂ had ceased and the suspension had turned into a clear solution, the remaining TEG was added in one portion after which Tr(EO)₈Ms (1.00 equiv., 14.0 g, 20.3 mmol) in dry THF (30 mL) was added in one portion. The resulting reaction mixture was heated at 50 °C overnight. Complete consumption of Tr(EO)₈Ms was confirmed by TLC (100% EtOAc *R_f* = 0.5 Tr(EO)₈Ms, 10% MeOH:EtOAc; *R_f* = 0.3 Tr(EO)₁₂H). The reaction mixture was cooled down to RT then brine (50.0 mL) was added. The organic layer was separated, washed with brine (6 × 30.0 mL) and combined aqueous fractions were extracted with Et₂O (200 mL). The absence of TEG was confirmed by TLC (100% EtOAc; *R_f* = 0). Combined organic fractions were dried over Na₂SO₄ and concentrated using a rotary evaporator to afford the desired compound as a yellow oil (15.4 g, 96 % yield, Oligomeric purity 99% as estimated by MALDI). ¹H NMR (700 MHz, CDCl₃) δ 7.45 (d, *J* = 7.8 Hz, 6H, 28), 7.27 (t, *J* = 7.6 Hz, 6H, 29), 7.21 (t, *J* = 7.3 Hz, 3H, 30), 3.73 – 3.58 (m, 46H, 2-24), 3.22 (t, *J* = 5.2 Hz, 2H, 25). ¹³C NMR (176 MHz, CDCl₃) δ 144.2 (27), 128.7 (28), 127.8 (29), 127.0 (30), 86.5 (26), 72.5, 70.9, 70.8, 70.7, 70.6, 70.5, 70.4, 70.3, 63.4 (25), 61.8 (3). MALDI-TOF calcd. for C₄₃H₆₄O₁₃ [M+Na⁺] 811.43, found 811.20. Spectroscopic data agree with literature values. (82)

Mono-trityl-dodecaethylene glycol mesylate (**6**)



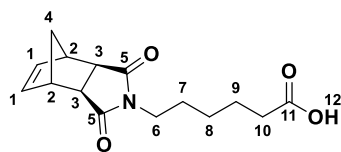
Oven-dried, one-neck round-bottom flask (250 ml) was charged with $\text{Tr}(\text{EO})_{12}\text{H}$ (1.04 equiv., 15.4 g, 19.5 mmol), THF (100 ml) and MsCl (1.30 equiv., 2.91 g, 25.4 mmol). Reaction mixture was cooled down to 0 °C after which NEt_3 (1.50 equiv., 2.90 g, 29.3 mmol) was added in a dropwise fashion. After the addition was complete, during which white salts had formed, the reaction mixture was slowly allowed to warm up to RT. When complete consumption of $\text{Tr}(\text{EO})_{12}\text{H}$ was confirmed by TLC (10% $\text{MeOH}:\text{EtOAc}$; $R_f = 0.31$; $\text{Tr}(\text{EO})_{12}\text{H}$, $R_f = 0.42$ $\text{Tr}(\text{EO})_{12}\text{Ms}$), water was added to dissolve salts after which organic layer was extracted with DCM (3×100 mL), dried over Na_2SO_4 and concentrated using rotary evaporator. Excess MsCl was removed by vacuum distillation and crude was dissolved in EtOAc (150 mL). Colored impurities were adsorbed to activated charcoal. Solids were filtered over a pad of celite and EtOAc was removed using rotary evaporator to afford the title compound as a yellow oil (13.1 g, 77% yield, Oligomeric purity 99% as estimated by MALDI). $^1\text{H NMR}$ (700 MHz, CDCl_3) δ 7.48 (d, $J = 7.8$ Hz, 6H, 28), 7.31 (t, $J = 7.6$ Hz, 6H, 29), 7.25 (t, $J = 7.3$ Hz, 3H, 30), 4.43 – 4.37 (m, 2H, 2), 3.82 – 3.76 (m, 2H, 3), 3.73 – 3.62 (m, 42H, 4-24), 3.25 (t, $J = 5.2$ Hz, 2H, 25), 3.10 (s, 3H, 1). $^{13}\text{C NMR}$ (126 MHz, CDCl_3) δ 144.1 (27), 128.4 (28), 127.9 (29), 127.2 (30), 86.52 (26), 70.8, 70.7, 70.6, 69.3, 69.0, 63.3, 37.8 (1). **MALDI-TOF** calcd. for $\text{C}_{44}\text{H}_{66}\text{O}_{15}\text{S}$ [$\text{M}+\text{Na}^+$] 889.41, found 889.30.

Mono-hydroxy dodecaethylene glycol mesylate (**7**)



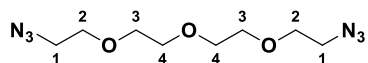
One-neck, round-bottom flask charged with Tr(EO)₁₂Ms (3.20 g, 3.69 mmol) and MeOH:DCM (7:3, 20 mL). The solution is cooled down to 0 °C after which TFA (10 mL) was added and the reaction was monitored by ¹H NMR. When the signal corresponding to the protons at the C11 position (δ 3.22 ppm, t, *J* = 5.2 Hz, 2H) disappeared, solvents were removed and the oil residue was repeatedly washed with hexane until the ¹H NMR of the oil residue showed no signs of aromatic protons. Solvents were removed after which MeOH:DCM (7:3, 20 mL) was added followed by NEt₃ (10 mL) to deprotect the trifluoroacetate group. The deprotection was monitored by ¹H NMR (δ 4.50-4.49 ppm, m, 2H, CH₂OC(O)CF₃, δ 4.39-4.37 ppm, m, 2H, CH₂OCOMs). When the deprotection reached completion, solvents were removed, crude was diluted with EtOAc (100 mL) and salts were filtered. Crude was washed with 3M HCl (20 mL), dried over Na₂SO₄ and concentrated to afford the desired compound as a light-yellow oil which was used without further purification (2.50 g, Quant. Yield). ¹H NMR (500 MHz, CDCl₃) δ 4.40 – 4.32 (m, 2H, 2), 3.77 – 3.71 (m, 2H, 3), 3.69 – 3.59 (m, 44H, 4-25), 3.38, 3.07 (s, 3H, 1). ¹³C NMR (126 MHz, CDCl₃) δ 70.8, 70.7, 70.7, 70.6, 70.6, 70.1 (24), 69.4 (3), 69.1 (2), 52.68 (25), 37.8 (1). Spectroscopic data agree with literature values. (**82**)

N-(hexanoic acid)-norbornene dicarboximide (**10**), Ref. (**158**)



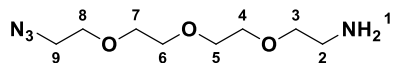
This reaction was carried out under an atmosphere of purified nitrogen using Schlenk techniques according to a literature procedure. (**158**) A three-neck, oven-dried round-bottom flask (50.0 mL) fitted with a Dean Stark trap coupled to a reflux condenser was charged with hexanoic acid (1.00 equiv., 1.00 g, 7.60 mmol), norbornene dicarboxylic anhydride (1.10 equiv., 1.30 g, 8.00 mmol) and dry toluene (50.0 mL). the resulting suspension was heated overnight at reflux temperature overnight after which it was cooled down and filtered over a plug of silica using 50% EtOAc:Hex to give the desired product as a colorless oil (1.70 g, 80%). $^1\text{H NMR}$ (700 MHz, CDCl_3) δ 6.28 (t, $J = 1.9$ Hz, 2H, 1), 3.47 (t, $J = 7.5$ Hz, 2H, 6), 3.27 (t, $J = 1.7$ Hz, 2H, 2), 2.67 (d, $J = 1.5$ Hz, 2H, 3), 2.34 (t, $J = 7.5$ Hz, 2H, 10), 1.68-1.63 (m, 2H, 9), 1.60 – 1.55 (m, 2H, 7), 1.52 (d, $J = 9.9$ Hz, 1H, 4'), 1.37 – 1.33 (m, 2H, 8), 1.22 (d, $J = 9.9$ Hz, 1H, 4). $^{13}\text{C NMR}$ (176 MHz, CDCl_3) δ 178.6 (11), 178.3 (5), 138.0 (1), 48.0 (3), 45.3 (2), 42.9 (4), 38.6 (6), 33.7 (10), 27.7 (7), 26.48 (8), 24.3 (9). Spectroscopic data agree with literature values. (**158**)

Azidoethyl-triethyleneoxide azide (**12**). Ref. (*I35*)



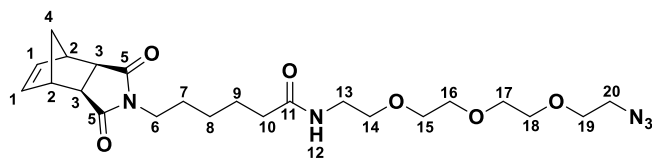
This reaction was carried out under an atmosphere of purified nitrogen using Schlenk techniques according to a literature procedure. (*I35*) To a solution of TEG (1.00 equiv., 10.0 g, 52 mmol) dried by azeotropic co-evaporation with toluene (3 × 10.0 mL) in dry THF (100 mL) MsCl (2.30 equiv., 13.0 g, 116 mmol) was added. At 0 °C, dry NEt₃ (2.20 equiv., 12.0 g, 115 mmol) was slowly added over a period of 5-10 min during which a light-yellow solid had formed. The precipitate was dissolved by addition of deionized water (30.0 mL). The biphasic system was cooled to 0 °C then NaHCO₃ (7.00 g) was added. Subsequently, NaN₃ (2.10 equiv., 7.00 g, 108 mmol) was added and the resulting reaction mixture was allowed to warm up to RT then was heated at reflux temperature overnight. The reaction mixture was cooled to room temperature then was extracted with EtOAc (4 × 100 mL). combined organic fractions were dried over Na₂SO₄ and evaporated using a rotary evaporator. Crude was purified using column chromatography using a gradient 10-50% EtOAc:Hex, 50% ETOAc:Hex *Rf* 0.6, to afford the desired di-azide product as a pale-yellow oil (7.80 g, 62%). ¹H NMR (500 MHz, CDCl₃) δ 3.74 – 3.56 (m, 12H, 2-4), 3.35 (t, *J* = 5.1 Hz, 4H, 1). ¹³C NMR (126 MHz, CDCl₃) δ 70.7 (3-4), 70.0 (2), 50.6 (1). Spectroscopic data agree with literature values. (*I35*)

Azidoethyl-triethyleneoxide amine (**14**). Ref. (**136**)

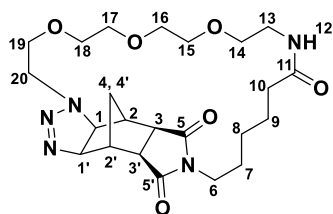


This compound was prepared according to a literature procedure. (**136**) A round-bottom flask (500 mL) was charged with Azidoethyl-triethyleneoxide azide (1.00 equiv., 8.00 g, 33.0 mmol) and a freshly prepared aqueous solution of HCL (1 M, 160 mL). At 0 °C, a solution of PPh₃ (1.20 equiv., 10.0 g, 38.0 mmol) in Et₂O (100 mL) was gradually added using a dropping funnel. After complete addition of PPh₃ solution, the dropping funnel was rinsed with additional volume of Et₂O (10.0 mL). The resulting reaction mixture was allowed to warm up to room temperature overnight. The PPh₃(O) by-product was filtered off and the aqueous layer was washed with Et₂O (3 × 150 mL). At 0 °C, the aqueous layer was basified by gradual addition of KOH (60.0 g). after the effervescence had stopped, the mixture was extracted with DCM (4 × 150 mL). combined organic fractions were dried over Na₂SO₄ and solvents were removed using rotary evaporator. Crude was purified via column chromatography, with a NEt₃-basified silica, using a gradient solvent system of 100% DCM-1%MeOH:DCM, 1%MeOH:DCM *R_f* 0.57, to give the product as a yellow oil (4.30 g, 60%). ¹H NMR (500 MHz, CDCl₃) δ 3.60 – 3.51 (m, 10H, 4-8), 3.46 (t, *J* = 5.1 Hz, 2H, 3), 3.30 (t, *J* = 5.1 Hz, 2H, 9), 3.26 (s, 2H, 1), 2.81 (t, *J* = 5.4 Hz, 2H, 2). ¹³C NMR (126 MHz, CDCl₃) δ 71.9 (3), 70.5, 70.4, 70.0, 69.9, 61.1, 50.5 (9), 41.1 (2). Spectroscopic data agree with literature values. (**136**)

N-(((azidoethyl)triethyleneoxide)hexanamide)norbornene dicarboximide (**15**)



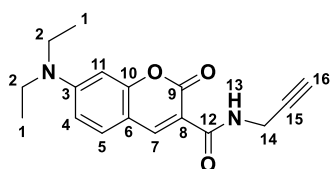
This reaction was carried out under an atmosphere of purified nitrogen using Schlenk techniques. An oven-dried, one-neck round-bottom flask (50.0 mL) was charged with *N*-(hexanoic acid)-norbornene dicarboximide (1.00 equiv., 0.80 g, 2.80 mmol), azidoethyl-triethyleneoxide amine (1.00 equiv., 0.60 g, 2.80 mmol), DMAP (0.20 equiv., 0.10 g, 0.60 mmol), EDCI (2.00 equiv., 1.10 g, 5.70 mmol) and dry DCM (20.0 mL). The reaction mixture was stirred at room temperature overnight after which DCM was removed using a rotary evaporator. Crude was purified via column chromatography using a gradient solvent system of 100% DCM-4% MeOH: DCM (4% MeOH: DCM *R_f* 0.26) to give the titled amide as a yellow oil (0.70 g, 52%). **¹H NMR** (700 MHz, CDCl₃) δ 6.28 (t, *J* = 1.9 Hz, 2H, 1), 3.71 – 3.60 (m, 10H, 15-19), 3.55 (t, *J* = 5.0 Hz, 2H, 14), 3.48 – 3.42 (m, 4H, 6, 13), 3.39 (t, *J* = 5.2 Hz, 2H, 20), 3.26 (t, *J* = 2.0 Hz, 2H, 2), 2.66 (d, *J* = 1.5 Hz, 2H, 3), 2.16 (t, *J* = 7.3 Hz, 2H, 10), 1.67 – 1.63 (m, 2H, 9), 1.58 – 1.54 (m, 2H, 7), 1.51 (d, *J* = 9.8 Hz, 1H, 4'), 1.35 – 1.30 (m, 2H, 8), 1.21 (d, *J* = 9.8 Hz, 1H, 4). **¹³C NMR** (176 MHz, CDCl₃) δ 178.2 (5), 172.8 (11), 138.0 (1), 70.9, 70.8, 70.7, 70.4, 70.2, 70.1, 50.9 (20), 48.0 (3), 45.3 (2), 42.9 (4), 39.3 (13), 38.6 (6), 36.5 (10), 27.7 (7), 26.8 (8), 25.3 (9). **HRMS** calcd. For C₂₃H₃₅N₅O₆ [M+H]⁺ 478.2666, found 478.2657. **IR** 2936, 2864 (C-H), 2099 (-N₃), 1692 (C(O)N) cm⁻¹.



¹H NMR (700 MHz, CDCl₃) δ 4.60 (d, *J* = 9.6 Hz, 1H, 1'), 3.84 – 3.76 (m, 2H, 20), 3.75 – 3.68 (m, 2H, 19), 3.66 – 3.58 (m, 9H, 1, 15-18), 3.56 – 3.51 (m, 2H, 14), 3.45 (t, *J* = 7.2 Hz, 2H, 6), 3.42 (t, *J* = 5.2

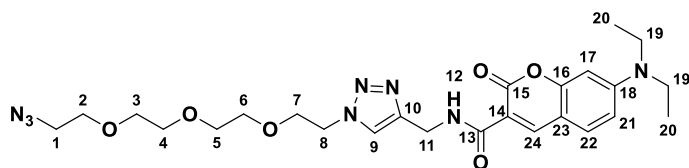
Hz, 2H, 13), 3.09 (s, 1H, 2'), 2.85 (s, 1H, 2), 2.75 (d, $J = 7.2$ Hz, 1H, 3'), 2.64 (d, $J = 7.2$ Hz, 1H, 3), 2.16 (t, $J = 7.5$ Hz, 2H, 10), 1.68 – 1.59 (m, 2H, 9), 1.60 – 1.50 (m, 2H, 7), 1.35 – 1.27 (m, 2H, 8), 1.12 (d, $J = 12.2$ Hz, 1H, 4'), 1.02 (d, $J = 12.2$ Hz, 1H, 4). $^{13}\text{C NMR}$ (176 MHz, CDCl_3) δ 177.5 (5'), 177.3 (5), 172.8 (11), 85.1 (1'), 70.7, 70.6, 70.6, 70.3, 70.0, 62.7 (1), 48.3 (20), 45.9 (3'), 45.3 (3), 44.4 (2'), 44.4 (2), 39.3 (13), 39.1 (6), 36.4 (10), 27.7 (7), 27.6 (4, 4'), 26.7 (8), 25.2 (9). **HRMS** calcd. For $\text{C}_{23}\text{H}_{35}\text{N}_3\text{O}_6$ $[\text{M}-\text{N}_2+\text{H}]^+$ 450.2604, found 450.2596. **IR** 2932, 2864 (C-H), 1690 (C(O)N) cm^{-1} .

7-(Diethylamino)coumarin-3-carboxylic propargylamide (**17**)



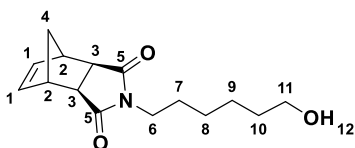
This reaction was carried out under an atmosphere of purified nitrogen using Schlenk techniques. An oven-dried, one-neck round-bottom flask (100 mL) was charged with 7-(diethylamino)coumarin-3-carboxylic acid (1.00 equiv., 0.40 g, 1.50 mmol), propargyl amine (1.00 equiv., 0.10 g, 1.50 mmol), EDCI (1.50 equiv., 0.40 g, 2.30 mmol), DMAP (0.20 equiv., 0.04 g, 0.30 mmol), and dry DCM (20.0 mL). The resulting reaction mixture was heated at reflux temperature overnight after which it was evaporated using rotary evaporator. Crude was purified by column chromatography using a gradient of 100% DCM- 10% EtOAc:DCM (100% DCM R_f 0.6) then recrystallized from DCM:Hex to afford the title compound as yellow needles (0.40 g, 90%). $^1\text{H NMR}$ (700 MHz, CDCl_3) δ 8.99 (t, $J = 5.0$ Hz, 1H, 13), 8.70 (s, 1H, 7), 7.43 (d, $J = 9.0$ Hz, 1H, 5), 6.65 (dd, $J = 9.0, 2.5$ Hz, 1H, 4), 6.50 (d, $J = 2.4$ Hz, 1H, 11), 4.23 (dd, $J = 5.4, 2.5$ Hz, 2H, 14), 3.46 (q, $J = 7.2$ Hz, 4H, 2), 2.24 (t, $J = 2.6$ Hz, 1H, 16), 1.24 (t, $J = 7.2$ Hz, 6H, 1). $^{13}\text{C NMR}$ (176 MHz, CDCl_3) δ 163.1 (12), 162.8 (9), 157.9 (10), 152.8 (3), 148.6 (7), 131.4 (5), 110.2 (4), 109.9 (8), 108.5 (6), 96.7 (11), 79.9 (15), 71.3 (16), 45.3 (2), 29.6 (14), 12.6 (1).

7-(Diethylamino)coumarin-3-carboxamide-methylene- triazole-ethyl-triethyleneoxide azide (**22**)



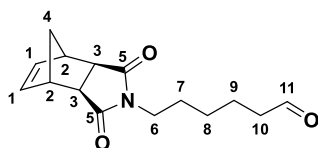
One-neck round-bottom flask (25.0 mL) was charged with azidoethyl-triethyleneoxide azide (10.0 equiv., 4.10 g, 17.0 mmol), 7-(diethylamino)coumarin-3-carboxylic propargylamide (1.00 equiv., 0.50 g, 1.70 mmol), CuBr (0.60 equiv., 0.10 g, 0.60 mmol) and DCM:H₂O (1:1, 20.0 mL). The resulting reaction mixture was stirred at room temperature overnight after which crude was washed with 50% concentrated NH₄OH in saturated NH₄Cl (3 × 50.0 mL). The combined aqueous fractions were back extracted with DCM (4 × 50.0 mL). The combined organic fractions were dried over Na₂SO₄, evaporated using rotary evaporator and purified by column chromatography using a gradient 100% EtOAc- 10% MeOH: EtOAc (10% MeOH: EtOAc *R_f* 0.53) to give the titled compound as a fluorescent yellow oil (0.70 g, 72%). **¹H NMR** (700 MHz, CDCl₃) δ 9.19 (t, *J* = 5.8 Hz, 1H, 12), 8.69 (s, 1H, 24), 7.72 (s, 1H, 9), 7.42 (d, *J* = 9.0 Hz, 1H, 22), 6.64 (dd, *J* = 9.0, 2.5 Hz, 1H, 21), 6.48 (d, *J* = 2.5 Hz, 1H, 17), 4.73 (d, *J* = 5.7 Hz, 2H, 11), 4.51 (t, *J* = 5.2 Hz, 2H, 8), 3.86 (t, *J* = 5.2 Hz, 2H, 7), 3.64 (t, *J* = 5.2 Hz, 2H, 2), 3.63 – 3.58 (m, 8H, 3-6), 3.44 (q, *J* = 7.2 Hz, 4H, 19), 3.36 (t, *J* = 5.1 Hz, 2H, 1), 1.23 (t, *J* = 7.3 Hz, 6H, 20). **¹³C NMR** (176 MHz, CDCl₃) δ 163.4 (13), 162.7 (15), 157.8 (16), 152.7 (18), 148.3 (24), 145.1 (10), 131.3 (22), 123.4 (9), 110.1 (14), 110.1 (21), 108.4 (23), 96.7 (17), 70.8 (3), 70.7 (4, 5), 70.7 (6), 70.2 (2), 69.6 (7), 50.8 (1), 50.4 (8), 45.2 (19), 35.5 (11), 12.6 (20). **HRMS** calcd. For C₂₅H₃₄N₈O₆ [M+H]⁺ 543.2674, found 543.2665. **IR** 3331 (N-H), 2870 (C-H), 2097 (-N₃), 1695 (C(O)N) cm⁻¹.

exo-*N*-(6-hexan-1-ol)-norbornene dicarboximide (**27**). Ref. (7)



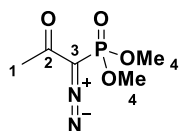
This reaction was carried out under an atmosphere of purified nitrogen using Schlenk techniques according to a literature procedure. (7) An oven-dried three-neck round bottom flask (100 mL), fitted with a Dean Stark trap and a condenser, was charged with *cis*-5-norbornene-*exo*-dicarboxylic anhydride (1.00 equiv., 2.20 g, 14.0 mmol), 6-Amino-1-hexanol (1.10 equiv., 1.80 g, 16.0 mmol) and dry toluene (50.0 mL). The reaction mixture was stirred overnight at reflux temperature under nitrogen after which it was transferred to a silica gel column and purified using a gradient of 10% EtOAc/Hexane-50% EtOAc/Hexane (50% EtOAc/Hexane *R_f* 0.3) to give the product as a colorless oil (2.80 g, 89%). **¹H NMR** (700 MHz, CDCl₃) δ 6.25 (t, *J* = 2.0 Hz, 2H, 1), 3.59 (t, *J* = 6.6 Hz, 2H, 11), 3.43 (t, *J* = 7.4 Hz, 2H, 6), 3.24 (t, *J* = 1.9 Hz, 2H, 2), 2.64 (d, *J* = 1.6 Hz, 2H, 3), 1.74 (s, 1H, 12), 1.56 – 1.50 (m, 4H, 7, 10), 1.48 (d, *J* = 9.9 Hz, 1H, 4'), 1.39 – 1.34 (m, 2H, 8), 1.32 – 1.26 (m, 2H, 9), 1.19 (d, *J* = 9.9 Hz, 1H, 4). **¹³C NMR** (176 MHz, CDCl₃) δ 178.3 (5), 137.9 (1), 62.7 (11), 47.9 (3), 45.2 (2), 42.8 (4), 38.6 (6), 32.5 (10), 27.8 (7), 26.7 (9), 25.2 (8). Spectroscopic data agree with literature values. (7)

exo-N-(6-hexan-1-yl)-norbornene dicarboximide (**28**). Ref. (7)



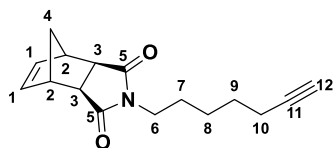
This reaction was carried out under an atmosphere of purified nitrogen using Schlenk techniques according to a literature procedure. (7) An oven-dried three-neck round bottom flask (50 mL) was charged with oxalyl chloride (1.50 equiv., 0.80 g, 6.10 mmol) and dry DCM (3.00 mL). At $-78\text{ }^{\circ}\text{C}$, a solution of dry DMSO (3.00 equiv., 1.00 g, 12.0 mmol) in dry DCM (2.00 mL) was added dropwise using a syringe over a period of 10 min. The resulting reaction mixture was stirred at $-78\text{ }^{\circ}\text{C}$ under nitrogen for 15 min after which a solution of *exo*-N-(6-hexan-1-yl)-norbornene dicarboximide (1.00 equiv., 1.00 g, 4.10 mmol) in dry DCM (25.0 mL) was added dropwise using a cannula over a period of 10 min. The resulting reaction mixture was stirred at $-78\text{ }^{\circ}\text{C}$ for 30 min. Then, NEt_3 (6.00 equiv., 2.50 g, 25.0 mmol) was added dropwise using a syringe at $-78\text{ }^{\circ}\text{C}$ over a period of 10 min after which it was allowed to warm up to room temperature during which a thick white precipitate had formed. The reaction mixture was washed twice with dilute HCl (1 M, 25.0 mL) and the aqueous layer was extracted with DCM ($3 \times 50.0\text{ mL}$). Combined organic fractions were dried over anhydrous Na_2SO_4 . Solvent was removed using rotary evaporator and crude was purified by column chromatography using a gradient of 10% EtOAc/Hexane-30% EtOAc/Hexane (30% EtOAc/Hexane R_f 0.25) to give the product as a colorless oil (0.90 g, 88%). $^1\text{H NMR}$ (700 MHz, CDCl_3) δ 9.74 (t, $J = 2.4\text{ Hz}$, 1H, 11), 6.32 (t, $J = 2.1\text{ Hz}$, 2H, 1), 3.45 (t, $J = 7.4\text{ Hz}$, 2H, 6), 3.26 (t, $J = 1.9\text{ Hz}$, 2H, 2), 2.67 (d, $J = 1.4\text{ Hz}$, 2H, 3), 2.42 (t, $J = 7.3\text{ Hz}$, 2H, 10), 1.67 – 1.61 (m, 2H, 7), 1.59 – 1.54 (m, 2H, 8), 1.51 (d, $J = 9.9\text{ Hz}$, 1H, 4'), 1.35 – 1.29 (m, 2H, 9), 1.20 (d, $J = 9.9\text{ Hz}$, 1H, 4). $^{13}\text{C NMR}$ (126 MHz, CDCl_3) δ 202.4 (18), 178.2 (5), 138.0 (1, 5), 48.0 (3), 45.3 (2), 43.7 (10), 42.9 (4), 38.5 (6), 27.7 (7), 26.5 (9), 21.6 (8). Spectroscopic data agree with literature values. (7)

Dimethyl 1-diazo-2-oxopropylphosphonate. Ref. (159)



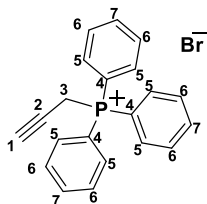
This reaction was carried out under an atmosphere of purified nitrogen using Schlenk techniques according to a literature procedure. (159) An oven-dried, one-neck round-bottom flask (500 mL) was charged with NaH (60% dispersion in mineral oil, 1.10 equiv., 2.50 g, 103 mmol) which was washed with dry hexane (3×10.0 mL) and dry THF:Tol mixture (20%, 120 mL). At 0 °C, a solution of dimethyl (2-oxopropyl)phosphonate (1.00 equiv., 16.0 g, 93.0 mmol) in dry Tol. (10.0 mL). The resulting suspension was stirred at 0-10 °C for 1 hr after which a solution of 4-acetamidobenzenesulfonyl azide (1.10 equiv., 25.0 g, 103 mmol) in dry THF (75.0 mL) was added dropwise and the resulting suspension was stirred for 2 hrs at room temperature. The yellow suspension was filtered through a celite pad and washed with Et₂O. Solvents were evaporated using a rotary evaporator and the resulting crude oil was diluted with Et₂O to precipitate excess 4-acetamidobenzenesulfonyl azide. The precipitate was filtered and Et₂O was evaporated using a rotary evaporator. The crude oil was purified by column chromatography using a gradient of 50% EtOAc:Hex-100% EtOAc (100% EtOAc *R_f* 0.4) to give the titled compound as a yellow oil (12.0 g, 79%) which was stored at 0 °C. ¹H NMR (500 MHz, CDCl₃) δ 3.81 (d, *J* = 12.0 Hz, 6H, 4), 2.23 (s, 3H, 1). ¹³C NMR (126 MHz, CDCl₃) δ 190.0, 189.9, 128.9, 119.4, 53.7, 53.6, 27.1. ³¹P NMR (202 MHz, CDCl₃) δ 14.21. Spectroscopic data agree with literature values. (159)

exo-N-(6-heptyn-1-yl)-norbornene dicarboximide (**29**)



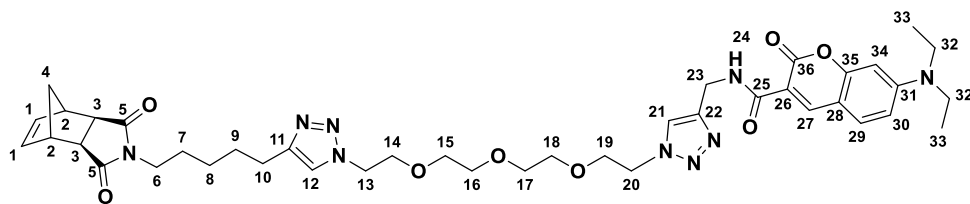
This reaction was carried out under an atmosphere of purified nitrogen using Schlenk techniques. An oven-dried, one-neck and round-bottom flask (10.0 mL) was charged with dimethyl 1-diazo-2-oxopropylphosphonate (1.20 equiv., 0.10 g, 0.50 mmol) and dry MeOH (5.00 mL). At 0 °C, K₂CO₃ (2.00 equiv., 0.10 g, 0.90 mmol) was added after which a solution of *exo*-N-(6-hexan-1-yl)-norbornene dicarboximide (1.00 equiv., 0.10 g, 0.40 mmol) in dry THF (3.00 mL) was added. The suspension was allowed to warm up to room temperature overnight under an atmosphere of nitrogen after which it was quenched with saturated NaHCO₃ (10.0 mL). The reaction was back extracted with DCM (5 × 10.0 mL) and the combined organic fractions were dried over anhydrous Na₂SO₄. Solvents were removed using a rotary evaporator and the crude product was purified by column chromatography using a gradient of 10% EtOAc:Hex-30% EtOAc:Hex (10% EtOAc:Hex *R_f* 0.3) to give the product as a yellow oil (0.10 g, 73%). **¹H NMR** (700 MHz, CDCl₃) δ 6.28 (t, *J* = 2.0 Hz, 2H, 1), 3.46 (t, *J* = 7.4 Hz, 2H, 6), 3.27 (t, *J* = 1.9 Hz, 2H, 2), 2.67 (d, *J* = 1.4 Hz, 2H, 3), 2.18 (td, *J* = 7.0, 2.7 Hz, 2H, 10), 1.92 (t, *J* = 2.6 Hz, 1H, 12), 1.59 – 1.52 (m, 4H, 14, 15), 1.50 (t, *J* = 9.9 Hz, 1H, 4'), 1.43 – 1.38 (m, 2H, 9), 1.22 (t, *J* = 9.9 Hz, 1H, 4). **¹³C NMR** (176 MHz, CDCl₃) δ 178.2 (5), 138.0 (1), 84.3 (11), 68.6 (12), 47.9 (3), 45.3 (2), 42.9 (4), 38.6 (6), 28.0 (7), 27.4 (8), 26.1 (9), 18.4 (10). **HRMS** calcd. For C₁₆H₁₉N₁O₂ [M+H]⁺ 258.1489, found 258.1490.

Propargyltriphenylphosphonium bromide (**18**). Ref. (*I37*)



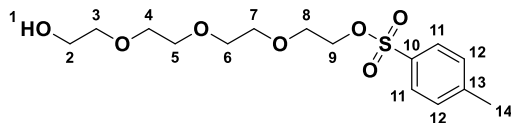
This reaction was carried out under an atmosphere of purified nitrogen using Schlenk techniques. (*I37*) A three-neck and round-bottom flask (100 mL) fitted with a dropping funnel and a reflux condenser was charged with PPh_3 (1.00 equiv., 10.0 g, 38.0 mmol) and dioxane (20.0 mL). To the resulting solution and at room temperature, HBr (48%, 5.00 mL) was added dropwise using a syringe. After the reaction mixture became homogeneous, propargyl bromide (80% solution in Tol., 1.00 equiv., 4.50 g, 38.0 mmol) was added using the dropping funnel after which the reaction mixture was stirred at room temperature for 3 hrs during which a white precipitate had formed. The white precipitate was filtered and thoroughly washed with Et_2O to give the titled compound as a white powder (7.20 g, 50%). ^1H NMR (400 MHz, Chloroform-*d*) δ 7.99 – 7.63 (m, 15H, 4-7), 5.30 (dd, $J = 15.3, 2.8$ Hz, 2H, 3), 2.26 (dt, $J = 7.0, 2.8$ Hz, 1H, 1). ^{31}P NMR (162 MHz, CDCl_3) δ 22.31. Spectroscopic data agree with literature values. (*I37*)

exo-*N*-(6-pentyl-1)-norbornene dicarboximide triazole-triethyleneoxide-triazole-ethyl-methylene-carboxamide-3-coumarin-7-diethylamine (**24**)



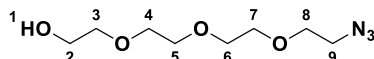
One-neck round-bottom flask (25.0 mL) was charged with *exo*-*N*-(6-heptyn-1-yl)-norbornene dicarboximide (1.00 equiv., 0.60 g, 2.40 mmol), 7-(diethylamino)coumarin-3-carboxamide-methylene- triazole-ethyl-triethyleneoxide azide (1.00 equiv., 1.30 g, 2.40 mmol), CuBr (0.60 equiv., 0.20 g, 1.30 mmol) and DCM:H₂O (1:1, 10.0 mL). The resulting reaction mixture was stirred at room temperature overnight after which crude was washed with 50% concentrated NH₄OH in saturated NH₄Cl (3 × 50.0 mL). The combined aqueous fractions were back extracted with DCM (4 × 50.0 mL). The combined organic fractions were dried over Na₂SO₄, evaporated using rotary evaporator and purified by column chromatography using a gradient 100% EtOAc- 10% MeOH: EtOAc (10% MeOH: EtOAc *R_f* 0.27) to give the titled compound as a fluorescent yellow oil (1.40 g, 73%). **¹H NMR** (700 MHz, CDCl₃) δ 9.12 (t, *J* = 5.8 Hz, 1H, 24), 8.58 (s, 1H, 27), 7.66 (s, 1H, 21), 7.38 (s, 1H, 12), 7.33 (d, *J* = 9.0 Hz, 1H, 29), 6.56 (dd, *J* = 9.0, 2.5 Hz, 1H, 30), 6.38 (d, *J* = 2.5 Hz, 1H, 34), 6.19 (t, *J* = 2.0 Hz, 2H, 1), 4.63 (d, *J* = 5.7 Hz, 2H, 23), 4.42 (dt, *J* = 16.6, 5.1 Hz, 4H, 13, 20), 3.77 (dt, *J* = 16.5, 5.2 Hz, 4H, 14, 19), 3.54 – 3.44 (m, 8H, 15-18), 3.41 – 3.30 (m, 6H, 6, 32), 3.16 (t, *J* = 1.9 Hz, 2H, 2), 2.61 – 2.56 (m, 4H, 3, 10), 1.63 – 1.54 (m, 2H, 9), 1.53 – 1.44 (m, 2H, 7), 1.40 (d, *J* = 9.9 Hz, 1H, 4'), 1.33 – 1.21 (m, 2H, 8), 1.15 (d, *J* = 7.2 Hz, 6H, 33), 1.11 (d, *J* = 9.7 Hz, 1H, 4). **¹³C NMR** (176 MHz, CDCl₃) δ 177.9 (5), 163.2 (25), 162.4 (36), 157.6 (35), 152.6 (31), 148.0 (27), 147.6 (11), 144.9 (22), 137.7 (1), 131.1 (29), 123.2 (21), 121.8 (12), 109.9 (26), 109.6 (30), 108.1 (28), 96.4 (34), 70.5 (18), 70.4 (15), 70.3 (16, 17), 69.4 (19), 69.3 (14), 50.1 (20), 49.9 (13), 47.7 (3), 45.0 (32), 45.0 (2), 42.6 (4), 38.4 (6), 35.2 (23), 28.9 (9), 27.4 (7), 26.4 (8), 25.4 (10), 12.3 (33). **HRMS** calcd. For C₄₂H₅₅N₉O₈ [M+H]⁺ 814.4246, found 814.4231.

Hydroxy-triethylene oxide-ethyl p-toluenesulfonic acid ester (**30**). Ref. (*I38*)



This reaction was carried out under an atmosphere of purified nitrogen using Schlenk techniques. (*I38*) An oven-dried, one-neck round-bottom flask (100 mL) was charged with TEG (1.00 equiv., 5.00 g, 26.0 mmol) dried by azeotropic co-evaporation with toluene (3×10.0 mL), Ag_2O (1.50 equiv., 9.00 g, 39.0 mmol), *p*-TsCl (1.10 equiv., 5.50 g, 29.0 mmol), KI (0.20 equiv., 0.90 g, 5.20 mmol) and dry DCM (30.0 mL). The resulting suspension was stirred at room temperature overnight after which Ag_2O was filtered over a pad of celite. Solvent was removed using a rotary evaporator and crude was purified by column chromatography using 100% EtOAc *Rf* 0.3 to afford the title compound as a colorless oil (5.00 g, 50%). $^1\text{H NMR}$ (500 MHz, $\text{DMSO-}d_6$) δ 7.79 (d, $J = 8.3$ Hz, 2H, 11), 7.49 (d, $J = 8.3$ Hz, 2H, 12), 4.58 (t, $J = 5.5$ Hz, 1H, 1), 4.14 – 4.07 (m, 2H, 9), 3.61 – 3.54 (m, 2H, 8), 3.51 – 3.37 (m, 12H, 2-7), 2.42 (s, 3H, 14). $^{13}\text{C NMR}$ (126 MHz, CDCl_3) δ 144.9 (10), 132.9 (13), 129.9 (11), 128.0 (12), 72.5, 70.7, 70.7, 70.5, 70.3, 69.3 (9), 68.7, 61.7 (8), 21.7 (14). Spectroscopic data agree with literature values. (*I38*)

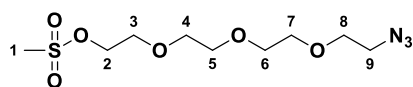
Hydroxy-triethylene oxide-ethyl azide (**31**)



This reaction was carried out under an atmosphere of purified nitrogen using Schlenk techniques. An oven-dried, one-neck round bottom flask (100 mL) was charged with hydroxy-triethylene oxide-ethyl

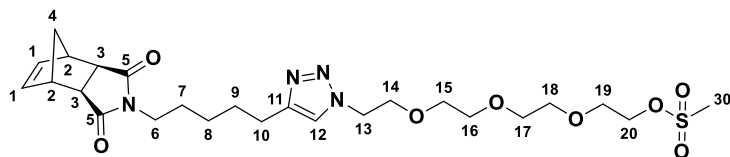
p-toluenesulfonic acid ester (1.00 equiv., 8.70 g, 25.0 mmol), NaN₃ (1.50 equiv., 2.40 g, 38.0 mmol) and dry DMF (20.0 mL). The resulting suspension was stirred at 50 °C overnight after which it was diluted with EtOAc (100 mL) and salts were filtered over a pad of celite. Solvents were removed by a rotary evaporator then vacuum distillation to afford the titled compound as a yellow oil (4.80 g, 88%). **¹H NMR** (500 MHz, CDCl₃) δ 3.68 – 3.52 (m, 11H, 3-7), 3.33 (t, *J* = 5.1 Hz, 2H, 9), 2.82 (s, 1H, 1). **¹³C NMR** (126 MHz, CDCl₃) δ 72.5 (2), 70.6, 70.6, 70.5, 70.3, 70.0, 61.6 (8), 50.6 (9). **HRMS** calcd. For C₈H₁₇N₃O₄ [M+H]⁺ 220.1219, found 220.1230.

Azidoethyl-diethylene oxide-ethyl mesylate (**13**)



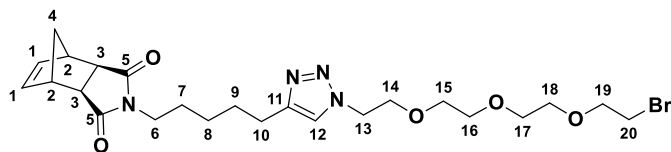
This reaction was carried out under an atmosphere of purified nitrogen using Schlenk techniques. An oven-dried, one-neck round-bottom flask (100 mL) was charged with Hydroxy-triethylene oxide-ethyl azide (1.00 equiv., 4.80 g, 22.0 mmol), MsCl (2.00 equiv., 5.00 g, 44.0 mmol) and dry THF (50.0 mL). To the stirring solution, NEt₃ (3.00 equiv., 6.70 g, 66.0 mmol) was added dropwise at 0 °C. After complete addition of NEt₃, during which a white solid had formed, the resulting suspension was allowed to warm up to room temperature overnight. Then, deionized H₂O (30.0 mL) was added to dissolve the salt and the reaction mixture was back extracted with DCM (3 × 50.0 mL). Combined organic fractions were dried over Na₂SO₄ and solvents were removed using the rotary evaporator. Crude was used in the next step without further purification as a yellow oil (6.50 g, 99%). **¹H NMR** (700 MHz, CDCl₃) δ 4.38 – 4.34 (m, 2H, 2), 3.77 – 3.72 (m, 2H, 3), 3.69 – 3.60 (m, 10H, 4-8), 3.37 (t, *J* = 5.1 Hz, 2H, 9), 3.06 (s, 3H, 1). **¹³C NMR** (176 MHz, CDCl₃) δ 70.7 (7), 70.6, 70.6 (4-6), 70.0 (8), 69.3 (3), 69.0 (2), 50.7 (9), 37.7 (1). **HRMS** calcd. For C₉H₁₉N₃O₆S [M+H]⁺ 298.0995, found 298.0102.

exo-N-(6-pentyl-1)-norbornene dicarboximide triazole-ethyl-diethylene oxide-ethyl mesylate (**33**)



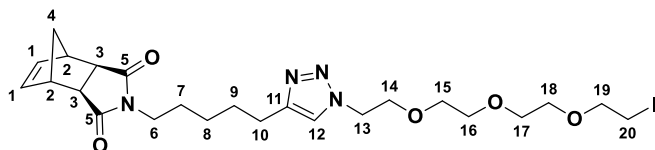
One-neck round-bottom flask (25.0 mL) was charged with *exo*-N-(6-heptyn-1-yl)-norbornene dicarboximide (1.00 equiv., 0.60 g, 2.50 mmol), Azidoethyl-diethylene oxide-ethyl mesylate (1.00 equiv., 0.70 g, 2.50 mmol), CuBr (0.60 equiv., 0.20 g, 1.50 mmol) and DCM:H₂O (1:1, 10.0 mL). The resulting reaction mixture was stirred at room temperature overnight after which crude was washed with 50% concentrated NH₄OH in saturated NH₄Cl (3 × 50.0 mL). The combined aqueous fractions were back extracted with DCM (4 × 50.0 mL). The combined organic fractions were dried over Na₂SO₄, evaporated using rotary evaporator and purified by column chromatography using a gradient 100% EtOAc- 10% MeOH: EtOAc (10% MeOH: EtOAc *R_f* 0.4) to give the titled compound as a yellow oil (1.40 g, Quant%). ¹H NMR (700 MHz, CDCl₃) δ 7.42 (s, 1H, 12), 6.27 (t, *J* = 2.0 Hz, 2H, 1), 4.49 (t, *J* = 5.3 Hz, 2H, 13), 4.38 – 4.35 (m, 2H, 20), 3.86 (t, *J* = 5.0 Hz, 2H, 14), 3.76 – 3.73 (m, 2H, 19), 3.67 – 3.58 (m, 8H, 15-18), 3.44 (t, *J* = 7.5 Hz, 2H, 6), 3.26 (t, *J* = 1.9 Hz, 2H, 2), 3.05 (s, 3H, 21), 2.69 (t, *J* = 7.7 Hz, 2H, 10), 2.66 (d, *J* = 1.5 Hz, 2H, 3), 1.71 – 1.65 (m, 2H, 9), 1.61 – 1.54 (m, 2H, 7), 1.49 (d, *J* = 9.9 Hz, 1H, 4'), 1.40 – 1.33 (m, 2H, 8), 1.20 (d, *J* = 9.9 Hz, 1H, 4). ¹³C NMR (176 MHz, CDCl₃) δ 178.2 (5), 147.9 (11), 137.9 (1), 121.9 (12), 70.8 (18), 70.7 (15), 70.6 (16, 17), 69.8 (14), 69.3 (20), 69.2 (19), 50.2 (13), 47.9 (3), 45.3 (2), 42.9 (4), 38.7 (6), 37.8 (21), 29.1 (9), 27.6 (7), 26.7 (8), 25.6 (10). IR 2936 (C=C), 2866 (C-H), 1694 (C(O)N) cm⁻¹. HRMS calcd. For C₂₅H₃₈N₄O₈S [M+H]⁺ 555.2483, found 555.2468.

exo-*N*-(6-pentyl-1)-norbornene dicarboximide triazole-ethyl-diethylene oxide-ethyl bromide (**35**)



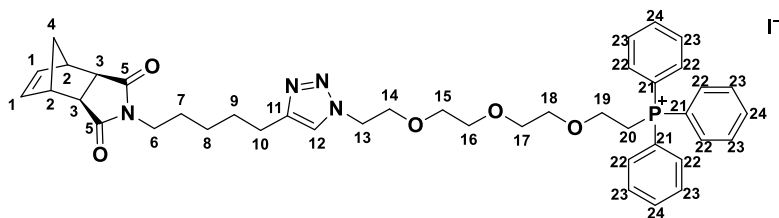
This reaction was carried out under an atmosphere of purified nitrogen using Schlenk techniques. An oven-dried, one-neck and round-bottom flask (25.0 mL) fitted with a reflux condenser was charged with *exo*-*N*-(6-pentyl-1)-norbornene dicarboximide triazole-ethyl-diethylene oxide-ethyl mesylate (1.00 equiv., 0.80 g, 1.50 mmol), LiBr (3.00 equiv., 0.40 g, 4.50 mmol) and dry acetone (10.0 mL). The resulting suspension was heated at reflux temperature overnight after which it was cooled down to room temperature, filtered and concentrated using the rotary evaporator. The resulting crude oil was purified by column chromatography using a 2% MeOH:EtOAc (10% MeOH:EtOAc *R_f* 0.6) to afford the titled compound as a light-yellow oil (0.80 g, 98%). **¹H NMR** (700 MHz, CDCl₃) δ 7.39 (s, 1H, 12), 6.21 (t, *J* = 2.0 Hz, 2H, 1), 4.43 (t, *J* = 5.2 Hz, 2H, 13), 3.80 (t, *J* = 5.0 Hz, 2H, 14), 3.73 (t, *J* = 6.2 Hz, 2H, 20), 3.61 – 3.51 (m, 8H, 15-18), 3.42 – 3.36 (m, 4H, 6-19), 3.19 (t, *J* = 1.9 Hz, 2H, 2), 2.62 (t, *J* = 7.7 Hz, 2H, 10), 2.60 (d, *J* = 1.5 Hz, 2H, 3), 1.66 – 1.58 (m, 2H, 9), 1.56 – 1.46 (m, 2H, 7), 1.43 (d, *J* = 9.9 Hz, 1H, 4'), 1.34 – 1.25 (m, 2H, 8), 1.14 (d, *J* = 9.9 Hz, 1H, 4). **¹³C NMR** (176 MHz, CDCl₃) δ 178.0 (5), 147.7 (11), 137.8 (1), 121.8 (12), 71.1 (20), 70.5 (15-18), 69.6 (14), 50.0 (13), 47.7 (3), 45.1 (2), 42.7 (4), 38.5 (6), 30.4 (19), 29.0 (9), 27.5 (7), 26.5 (8), 25.4 (10). **IR** 2938 (C=C), 2862 (C-H), 1694 (C(O)N) cm⁻¹. **HRMS** calcd. For C₂₄H₃₅N₄O₅Br [M+H]⁺ 540.1824, 541.1830, found 540.1827, 541.1827.

exo-N-(6-pentyl-1)-norbornene dicarboximide triazole-ethyl-diethylene oxide-ethyl iodide (**36**)



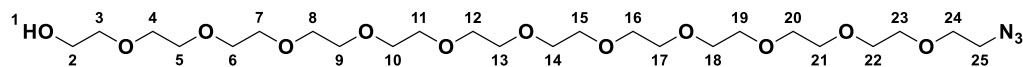
This reaction was carried out under an atmosphere of purified nitrogen using Schlenk techniques. An oven-dried, one-neck and round-bottom flask (25.0 mL) fitted with a reflux condenser was charged with *exo*-N-(6-pentyl-1)-norbornene dicarboximide triazole-ethyl-diethylene oxide-ethyl bromide (1.00 equiv., 1.00 g, 1.90 mmol), NaI (3.00 equiv., 0.90 g, 5.70 mmol) and dry acetone (10.0 mL). The resulting suspension was heated at reflux temperature for 3 hrs after which it was cooled down to room temperature, filtered and concentrated using the rotary evaporator. Crude was diluted with DCM (10.0 mL), washed with sat. Na₂S₂O₃ (15.0 mL) and dried over Na₂SO₄. The resulting crude oil was purified by column chromatography using a 2% MeOH:EtOAc (10% MeOH:EtOAc *R_f* 0.6) to afford the titled compound as a light-yellow oil (1.00 g ,90%). ¹H NMR (700 MHz, CDCl₃) δ 7.41 (s, 1H, 12), 6.23 (t, *J* = 2.0 Hz, 2H, 1), 4.46 (t, *J* = 5.2 Hz, 2H, 13), 3.83 (t, *J* = 5.0 Hz, 2H, 14), 3.70 (t, *J* = 6.8 Hz, 2H, 20), 3.63 – 3.51 (m, 8H, 15-18), 3.40 (t, *J* = 7.8 Hz, 2H, 6), 3.20 – 43.16 (m, 4H, 2, 19), 2.69 – 2.57 (m, 4H, 3, 10), 1.68 – 1.60 (m, 2H, 9), 1.57 – 1.48 (m, 2H, 7), 1.45 (d, *J* = 9.9 Hz, 1H, 4'), 1.37 – 1.25 (m, 2H, 8), 1.15 (d, *J* = 9.9 Hz, 1H, 4). ¹³C NMR (176 MHz, CDCl₃) δ 178.1 (5), 147.7 (11), 137.8 (1), 121.8 (12), 71.9 (20), 70.6 (15-18), 70.2 (19), 69.6 (14), 50.1 (13), 47.8 (3), 45.1 (2), 42.7 (4), 38.6 (6), 29.0 (9), 27.5 (7), 26.5 (8), 25.5 (10). IR 2934 (C=C), 2860 (C-H), 1694 (C(O)N) cm⁻¹. HRMS calcd. For C₂₄H₃₅N₄O₅I [M+H]⁺ 587.1711, found 587.1725.

exo-*N*-(6-pentyl-1)-norbornene dicarboximide triazole-ethyl-diethylene oxide-ethyl triphenyl-phosphonium iodide (**37**)



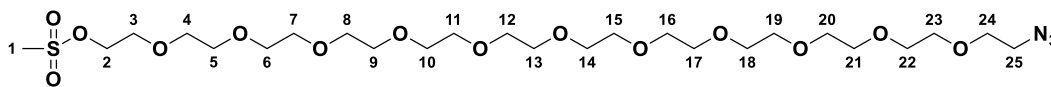
This reaction was carried out under an atmosphere of purified nitrogen using Schlenk techniques. Oven-dried three-neck round-bottom flask, fitted with a reflux condenser and a thermometer, was charged with PPh_3 (20.0 equiv., 2.70 g, 10.0 mmol). At 80 °C, a solution of *exo*-*N*-(6-pentyl-1)-norbornene dicarboximide triazole-ethyl-diethylene oxide-ethyl iodide (1.00 equiv., 0.50 g, 0.90 mmol) in dry and degassed toluene (0.20 mL) was slowly added. The reaction mixture's temperature was maintained at 80-85 °C for an hour at the end of which the complete conversion of substrate was confirmed by $^1\text{H NMR}$. The reaction mixture was allowed to cool down to room temperature during which PPh_3 had solidified. Crude was repeatedly sonicated with Et_2O to remove excess PPh_3 then dried under vacuum to give the title compound as a wax (0.70 g, Quant.). $^1\text{H NMR}$ (700 MHz, CDCl_3) δ 7.83 – 7.78 (m, 6H, 23), 7.78 – 7.73 (m, 3H, 24), 7.67 – 7.61 (m, 6H, 22), 7.43 (s, 1H, 12), 6.27 (t, $J = 2.0$ Hz, 2H, 1), 4.46 (t, $J = 5.2$ Hz, 2H, 13), 4.10 – 4.01 (m, 2H, 20), 3.91 (dt, $J = 22.2, 5.4$ Hz, 2H, 19), 3.84 (t, $J = 5.3$ Hz, 2H, 14), 3.49 (t, $J = 4.0$ Hz, 2H, 15), 3.42 (t, $J = 7.8$ Hz, 2H, 6), 3.36 3.36 (t, $J = 3.9$ Hz, 2H, 16), 3.34 – 3.31 (m, 2H, 18), 3.28 – 3.26 (m, 2H, 17), 3.24 (t, $J = 1.7$ Hz, 2H, 2), 2.69 – 2.60 (m, 4H, 3, 10), 1.68 – 1.61 (m, 2H, 9), 1.60 – 1.51 (m, 2H, 7), 1.49 (d, $J = 9.9$ Hz, 1H, 4'), 1.38 – 1.29 (m, 2H, 8), 1.18 (d, $J = 9.9$ Hz, 1H, 4). $^{13}\text{C NMR}$ (176 MHz, CDCl_3) δ 178.2 (5), 147.9 (11), 137.9 (1), 134.9 (d, $J = 2.5$ Hz, 24), 134.2 (d, $J = 11.4$ Hz, 23), 130.2 (d, $J = 12.7$ Hz, 22), 121.8 (12), 118.9 (d, $J = 86.5$ Hz, 21), 70.6 (15), 70.4 (16), 70.4 (18), 70.2 (17), 69.7 (14), 64.1 (d, $J = 6.4$ Hz, 19), 50.2 (13), 47.9 (3), 45.3 (2), 42.8 (4), 38.6 (6), 29.1 (9), 27.6 (7), 26.6 (8), 25.8 (d, $J = 53.4$ Hz, 20), 26.6 (8). $^{31}\text{P NMR}$ (121 MHz, CDCl_3) δ 25.26. **HRMS** calcd. For $\text{C}_{42}\text{H}_{50}\text{N}_4\text{O}_5\text{PI}$ $[\text{M}-\text{I}]^+$ 721.3513, found 721.3496.

Hydroxy-undecaethylene oxide-ethyl azide (**38**)



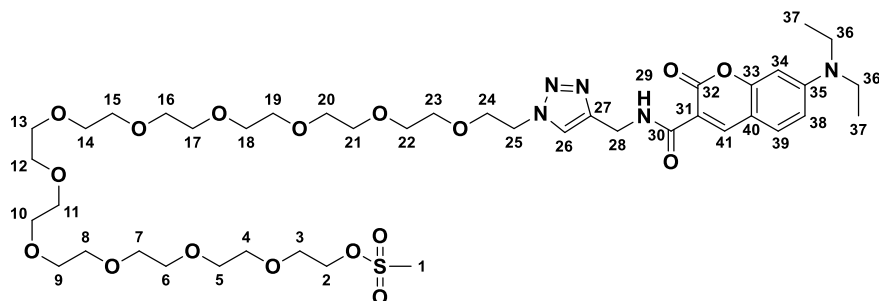
This reaction was carried out under an atmosphere of purified nitrogen using Schlenk techniques. An oven-dried, one-neck round bottom flask (100 mL) was charged with hydroxy-undecaethylene oxide-ethyl mesylate (1.00 equiv., 8.50 g, 14.0 mmol), NaN₃ (1.50 equiv., 1.30 g, 20.0 mmol) and dry DMF (20.0 mL). The resulting suspension was stirred at 50 °C overnight after which it was diluted with EtOAc (100 mL) and salts were filtered over a pad of celite. Celite pad was successively washed with DCM to retrieve the product. Solvents were removed by a rotary evaporator then vacuum distillation to afford the titled compound as a yellow oil (7.00 g, 88%). ¹H NMR (700 MHz, CDCl₃) δ 3.74 – 3.71 (m, 2H, 2), 3.69 – 3.63 (m, 42H, 4-24), 3.61 (t, *J* = 8.8 Hz, 2H, 3), 3.39 (t, *J* = 5.1 Hz, 2H, 25). ¹³C NMR (176 MHz, CDCl₃) δ 72.5 (3), 70.8, 70.8, 70.8, 70.7, 70.7, 70.6, 70.6, 70.6, 70.3, 70.2, 61.8 (2), 50.8 (25). HRMS calcd. For C₂₄H₄₉N₃O₁₂ [M+H]⁺ 572.3316, found 572.3322.

Azido-undecaethylene oxide-ethyl mesylate (**39**)



This reaction was carried out under an atmosphere of purified nitrogen using Schlenk techniques. One-neck round-bottom flask (250 ml) was charged with Hydroxy-undecaethylene oxide-ethyl azide (1.00 equiv., 4.40 g, 7.70 mmol), dry THF (100 ml) and MeCl (1.50 equiv., 1.30 g, 12.0 mmol). The reaction mixture was cooled down to 0 °C after which dry NEt₃ (1.50 equiv., 1.20 g, 12.0 mmol) was added in a dropwise fashion over a period of 5 min during which a yellow salt had formed. Suspension was allowed to warm up overnight after which deionized water (20.0 ml) was added to dissolve the salts. Aqueous fraction was separated and back extracted with DCM (3 × 150 ml). Combined organic fractions were dried over Na₂SO₄ concentrated using a rotary evaporator to give the product as a yellow oil (5.08 g, Yield: Quant.). **¹H NMR** (500 MHz, CDCl₃) δ 4.40 – 4.32 (m, 2H, 2), 3.77 – 3.71 (m, 2H, 3), 3.71 – 3.57 (m, 42H, 4-24), 3.38 (t, J = 5.1 Hz, 2H, 25), 3.07 (s, 3H, 1). **¹³C NMR** (126 MHz, CDCl₃) δ 70.8, 70.7, 70.7, 70.6, 70.6, 70.1 (24), 69.4 (3), 69.1 (2), 50.8 (25), 37.8 (1). **HRMS** calcd. For C₂₄H₄₉N₃O₁₂ [M+H]⁺ 650.3092, found 650.3110.

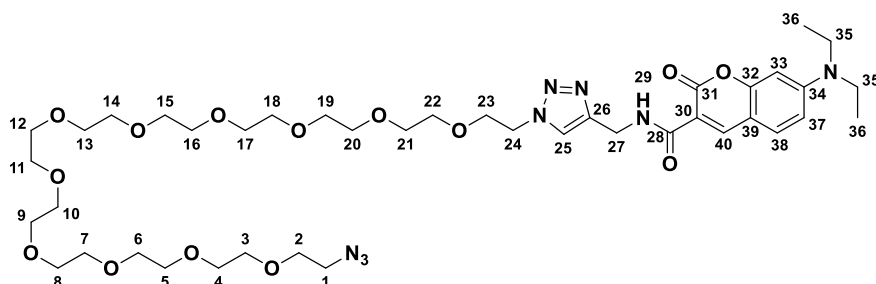
7-(diethylamino)coumarin-3-carboxamide-methylene- triazole-ethyl- decaethylene oxide-ethyl mesylate (**40**)



One-neck round-bottom flask (100 mL) was charged with azido-undecaethylene oxide-ethyl mesylate (1.00 equiv., 2.80 g, 4.30 mmol), 7-(diethylamino)coumarin-3-carboxylic propargylamide (1.00 equiv., 1.30 g, 4.30 mmol), CuBr (0.60 equiv., 0.40 g, 2.60 mmol) and DCM:H₂O (1:1, 20.0 mL). The resulting reaction mixture was stirred at room temperature overnight after which crude was washed with 50% concentrated NH₄OH in saturated NH₄Cl (3 × 50.0 mL). The combined aqueous fractions were back extracted with DCM (4 × 50.0 mL). The combined organic fractions were dried over Na₂SO₄, evaporated using rotary evaporator and purified by column chromatography using a gradient 100% EtOAc- 10% MeOH: EtOAc (10% MeOH: EtOAc *R_f* 0.2) to give the titled compound as a fluorescent yellow oil (3.60 g, 87%). ¹H NMR (500 MHz, CDCl₃) δ 9.19 (t, *J* = 5.8 Hz, 1H, 29), 8.69 (s, 1H, 41), 7.72 (s, 1H, 26), 7.42 (d, *J* = 9.0 Hz, 1H, 39), 6.64 (dd, *J* = 9.0, 2.5 Hz, 1H, 38), 6.47 (d, *J* = 2.5 Hz, 1H, 34), 4.73 (d, *J* = 5.7 Hz, 2H, 28), 4.51 (t, *J* = 5.2 Hz, 2H, 25), 4.41 – 4.33 (m, 2H, 3), 3.86 (t, *J* = 5.2 Hz, 2H, 24), 3.78 – 3.73 (m, 2H, 3), 3.69 – 3.58 (m, 40H, 4-23), 3.45 (q, *J* = 7.2 Hz, 4H, 36), 3.08 (s, 3H, 1), 1.24 (t, *J* = 7.3 Hz, 6H, 37). ¹³C NMR (126 MHz, CDCl₃) δ 163.4 (30), 162.7 (32), 157.8 (33), 152.7 (35), 148.3 (41), 145.1 (27), 131.3 (39), 123.5 (26), 110.2 (38), 110.1 (31), 108.4 (40), 96.7 (34), 70.8, 70.7, 70.6, 69.6 (23), 69.5 (2), 69.2 (3), 50.4 (25), 45.2 (36), 37.9 (1), 35.5 (28), 12.6 (37). HRMS calcd. For C₄₂H₆₉N₅O₁₇S [M+H]⁺ 948.4459, found 948.4482. IR 3335 (N-H), 2868 (C-H), 1697 (C(O)O), 1651, 1614 (C(O)NH), 1580, 1510 cm⁻¹.

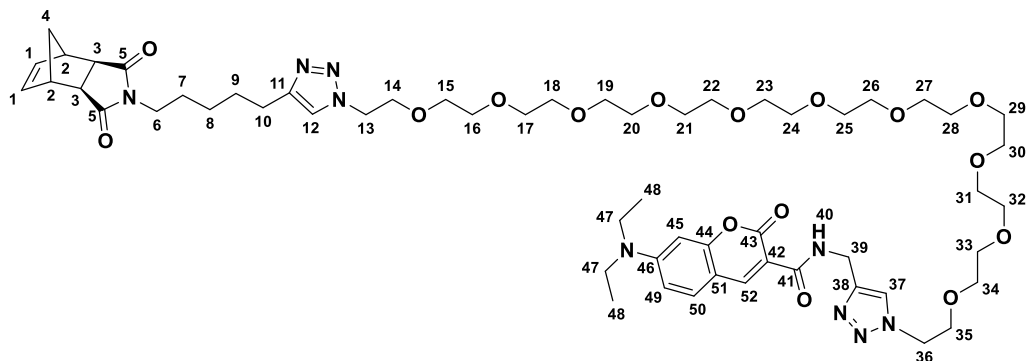
7-(diethylamino)coumarin-3-carboxamide-methylene triazole-ethyl-decaethylene oxide-ethyl azide

(41)



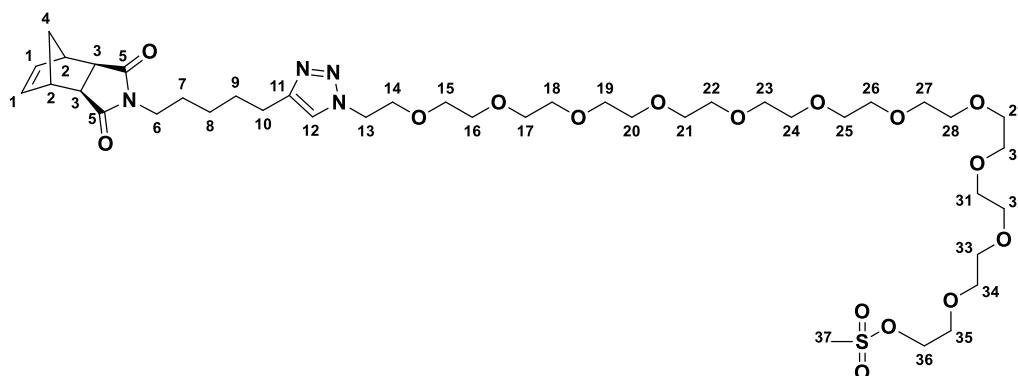
This reaction was carried out under an atmosphere of purified nitrogen using Schlenk techniques. An oven-dried, one-neck round-bottom (100 mL) fitted with a reflux condenser flask was charged with 7-(diethylamino)coumarin-3-carboxamide-methylene triazole-ethyl-decaethylene oxide-ethyl mesylate (1.00 equiv., 3.60 g, 3.80 mmol), NaN₃ (1.50 equiv., 0.40 g, 5.60 mmol) and dry DMF (15.0 mL). The resulting suspension was stirred at 50 °C overnight after which it was cooled down to room temperature. The crude was diluted by addition of EtOAc (50.0 mL) and salts were filtered over a pad of celite. The pad was successively washed with DCM to retrieve the product. Solvents were removed by a rotary evaporator then vacuum distillation to afford the titled compound as a fluorescent yellow oil (3.10 g, 93%). ¹H NMR (700 MHz, CDCl₃) δ 9.18 (t, *J* = 5.8 Hz, 1H, 29), 8.68 (s, 1H, 40), 7.71 (s, 1H, 25), 7.41 (d, *J* = 9.0 Hz, 1H, 38), 6.63 (dd, *J* = 9.0, 2.5 Hz, 1H, 37), 6.47 (d, *J* = 2.5 Hz, 1H, 33), 4.72 (d, *J* = 5.7 Hz, 2H, 27), 4.50 (t, *J* = 5.2 Hz, 2H, 24), 3.85 (t, *J* = 5.2 Hz, 2H, 23), 3.71 – 3.53 (m, 42H, 2-22), 3.44 (q, *J* = 7.2 Hz, 4H, 35), 3.38 (t, *J* = 5.1 Hz, 2H, 1), 1.22 (t, *J* = 7.3 Hz, 6H, 36). ¹³C NMR (176 MHz, CDCl₃) δ 163.4 (28), 162.6 (31), 157.8 (32), 152.7 (34), 148.3 (40), 145.1 (26), 131.3 (38), 123.4 (25), 110.1 (37), 110.1 (30), 108.4 (39), 96.7 (33), 70.8, 70.8, 70.7, 70.6, 70.2 (2), 69.6 (23), 50.8 (1), 50.4 (24), 45.2 (35), 35.5 (27), 12.5 (36). HRMS calcd. For C₄₁H₆₆N₈O₁₄ [M+H]⁺ 895.4761, found 895.4771. IR 3329 (N-H), 2866 (C-H), 2102 (-N₃), 1697 (C(O)O), 1651, 1614 (C(O)NH), 1581, 1510.

exo-*N*-(6-pentyl-1)-norbornene dicarboximide triazole-decaethylene oxide-triazole-ethyl-methylene-carboxamide-3-coumarin-7-diethylamine (**42**)



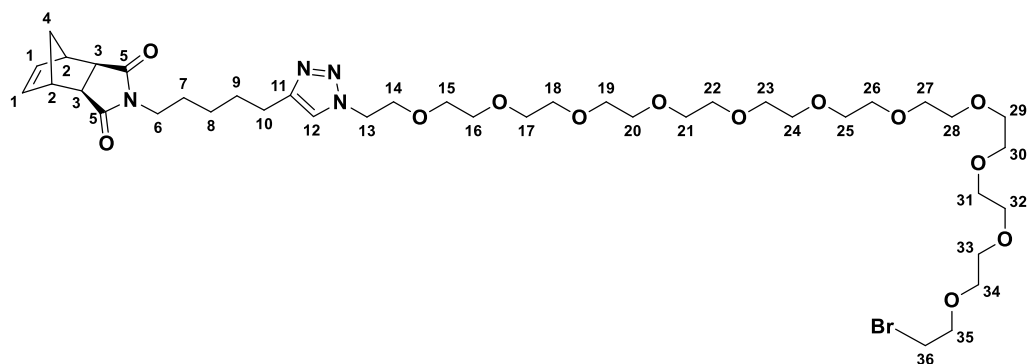
One-neck round-bottom flask (100 mL) was charged with *exo*-*N*-(6-heptyn-1-yl)-norbornene dicarboximide (1.00 equiv., 0.90 g, 3.50 mmol), 7-(diethylamino)coumarin-3-carboxamide-methylene triazole-ethyl-decaethylene oxide-ethyl azide (1.00 equiv., 3.10 g, 3.50 mmol), CuBr (0.60 equiv., 0.30 g, 2.90 mmol) and DCM:H₂O (1:1, 15.0 mL). The resulting reaction mixture was stirred at room temperature overnight after which crude was washed with 50% concentrated NH₄OH in saturated NH₄Cl (3 × 50.0 mL). The combined aqueous fractions were back extracted with DCM (4 × 50.0 mL). The combined organic fractions were dried over Na₂SO₄, evaporated using rotary evaporator give the titled compound as a fluorescent yellow oil (2.90 g, 73%). ¹H NMR (700 MHz, CDCl₃) δ 9.19 (t, *J* = 5.8 Hz, 1H, 40), 8.69 (s, 1H, 52), 7.71 (s, 1H, 37), 7.44 (s, 1H, 12), 7.42 (d, *J* = 9.0 Hz, 1H, 50), 6.64 (dd, *J* = 9.0, 2.5 Hz, 1H, 49), 6.48 (d, *J* = 2.5 Hz, 1H, 45), 6.27 (t, *J* = 2.0 Hz, 2H, 1), 4.72 (d, *J* = 5.7 Hz, 2H, 39), 4.50 (dt, *J* = 10.2, 5.2 Hz, 4H, 13, 36), 3.85 (dt, *J* = 8.7, 5.2 Hz, 4H, 14, 35), 3.63 – 3.59 (m, 40H, 15-34), 3.47 – 3.41 (m, 6H, 6, 47), 3.26 (t, *J* = 1.9 Hz, 2H, 2), 2.68 (t, *J* = 7.7 Hz, 2H, 10), 2.66 (d, *J* = 1.5 Hz, 2H, 3), 1.71 – 1.65 (m, 2H, 9), 1.61 – 1.55 (m, 2H, 7), 1.49 (d, *J* = 9.9 Hz, 1H, 4'), 1.39 – 1.33 (m, 2H, 8), 1.23 (t, *J* = 7.2 Hz, 6H, 48), 1.20 (d, *J* = 9.9 Hz, 1H, 4). ¹³C NMR (176 MHz, CDCl₃) δ 178.2 (5), 163.4 (41), 162.7 (43), 157.8 (44), 152.7 (46), 148.3 (52), 147.9 (11), 145.1 (38), 137.9 (1), 131.3 (50), 123.4 (37), 121.9 (12), 110.1 (42), 108.4 (49, 51), 96.7 (45), 70.7, 70.6, 69.8 (35), 69.6 (14), 50.4 (36), 50.2 (13), 47.9 (3), 45.3 (47), 45.2 (2), 42.9 (4), 38.7 (6), 35.5 (39), 29.1 (9), 27.7 (7), 26.7 (8), 25.6 (10), 12.6 (48). HRMS calcd. For C₅₇H₈₅N₉O₁₆ [M+H]⁺ 1152.6190, found 1152.6187.

exo-*N*-(6-pentyl-1)-norbornene dicarboximide triazole-ethyl-decaethylene oxide-ethyl mesylate (**43**)



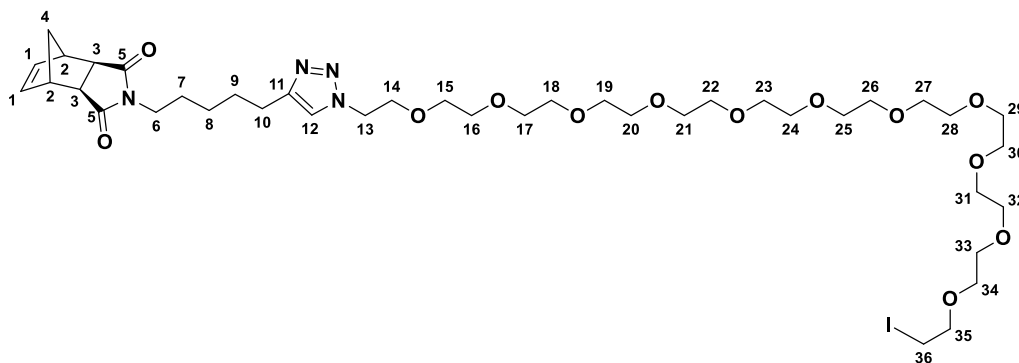
One-neck round-bottom flask (100 mL) was charged with *exo*-*N*-(6-heptyn-1-yl)-norbornene dicarboximide **36** (1.00 equiv., 2.00 g, 7.80 mmol), Azidoethyl- decaethylene oxide-ethyl mesylate (1.00 equiv., 5.10 g, 7.80 mmol), CuBr (0.60 equiv., 0.70 g, 4.70 mmol) and DCM:H₂O (1:1, 30.0 mL). The resulting reaction mixture was stirred at room temperature overnight after which crude was washed with 50% concentrated NH₄OH in saturated NH₄Cl (3 × 50.0 mL). The combined aqueous fractions were back extracted with DCM (4 × 50.0 mL). The combined organic fractions were dried over Na₂SO₄, evaporated using rotary evaporator and purified by column chromatography using a gradient 100% EtOAc- 10% MeOH: EtOAc (10% MeOH: EtOAc *R_f* 0.2) to give the titled compound as a yellow oil (3.40 g, 50%). ¹H NMR (700 MHz, CDCl₃) δ 7.44 (s, 1H, 12), 6.28 (t, *J* = 1.9 Hz, 2H, 1), 4.50 (t, *J* = 5.2 Hz, 2H, 13), 4.41 – 4.35 (m, 2H, 36), 3.85 (t, *J* = 5.2 Hz, 2H, 14), 3.78 – 3.74 (m, 2H, 35), 3.68 – 3.58 (m, 40H, 15-34), 3.45 (t, *J* = 7.6 Hz, 2H, 6), 3.26 (t, *J* = 1.9 Hz, 2H, 2), 3.08 (s, 3H, 37), 2.69 (t, *J* = 7.7 Hz, 2H, 10), 2.67 (d, *J* = 1.5 Hz, 2H, 3), 1.72 – 1.66 (m, 2H, 9), 1.61 – 1.55 (m, 2H, 7), 1.50 (d, *J* = 9.9 Hz, 1H, 4'), 1.39 – 1.34 (m, 2H, 8), 1.21 (d, *J* = 9.9 Hz, 1H, 4). ¹³C NMR (176 MHz, CDCl₃) δ 178.2 (5), 147.9 (11), 138.0 (1), 121.9 (12), 70.8, 70.7, 70.6, 69.8 (14), 69.5 (36), 69.2 (35), 50.2 (13), 47.9 (3), 45.3 (2), 42.9 (4), 38.7 (6), 37.9 (37), 29.2 (9), 27.7 (7), 26.7 (8), 25.6 (10). IR 2866.22 (C-H), 1693.50 (C(O)N) cm⁻¹. HRMS calcd. For C₄₁H₇₀N₄O₁₆S [M+H]⁺ 907.4564, found 907.4580.

exo-*N*-(6-pentyl-1)-norbornene dicarboximide triazole-ethyl-decaethylene oxide-ethyl bromide (**44**)



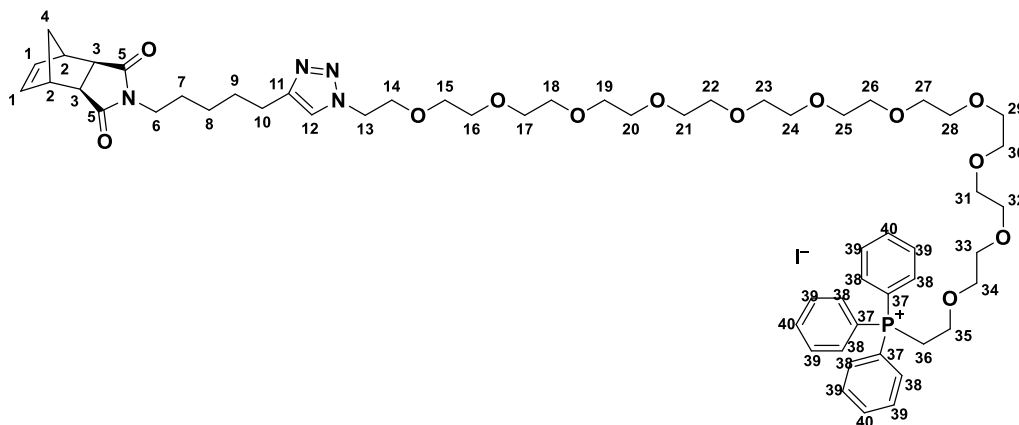
This reaction was carried out under an atmosphere of purified nitrogen using Schlenk techniques. An oven-dried, one-neck and round-bottom flask (25.0 mL) fitted with a reflux condenser was charged with *exo*-*N*-(6-pentyl-1)-norbornene dicarboximide triazole-ethyl-decaethylene oxide-ethyl mesylate **50** (1.00 equiv., 3.40 g, 3.80 mmol), LiBr (3.00 equiv., 0.90 g, 11.0 mmol) and dry acetone (20.0 mL). The resulting suspension was heated at reflux temperature overnight after which it was cooled down to room temperature, diluted by addition of EtOAc (50.0 mL), filtered and concentrated using the rotary evaporator. The resulting crude oil was purified by column chromatography using a 2% MeOH:EtOAc (10% MeOH:EtOAc *R_f* 0.25) to afford the titled compound as a light-yellow oil (3.30 g, Quant.%). **¹H NMR** (700 MHz, CDCl₃) δ 7.58 (s, 1H, 12), 6.28 (t, *J* = 1.9 Hz, 2H, 1), 4.71 (t, *J* = 5.2 Hz, 2H, 13), 3.92 (t, *J* = 5.1 Hz, 2H, 14), 3.84 (t, *J* = 6.2 Hz, 2H, 36), 3.81 – 3.65 (m, 40H, 15-34), 3.51 (t, *J* = 6.1 Hz, 2H, 35), 3.44 (t, *J* = 7.6 Hz, 2H, 6), 3.26 (t, *J* = 1.9 Hz, 2H, 2), 2.70 – 2.65 (m, 4H, 3, 10), 1.70 – 1.64 (m, 2H, 9), 1.61 – 1.54 (m, 2H, 7), 1.50 (d, *J* = 9.9 Hz, 1H, 4'), 1.40 – 1.32 (m, 2H, 8), 1.20 (d, *J* = 9.9 Hz, 1H, 4). **¹³C NMR** (176 MHz, CDCl₃) δ 178.2 (5), 147.9 (11), 137.9 (1), 122.6 (12), 71.3 (36), 70.3, 70.2, 70.1, 70.0, 69.9, 69.8, 69.7 (14), 50.2 (13), 47.9 (3), 45.3 (2), 42.9 (4), 38.7 (6), 30.7 (35), 29.0 (9), 27.6 (7), 26.7 (8), 25.5 (10). **IR** 2916 (C=C), 2874 (C-H), 1694 (C(O)N) cm⁻¹. **HRMS** calcd. For C₄₀H₆₇N₄O₁₃Br [M+H]⁺ 891.3961, 892.3993, found 891.3949, 892.3978.

exo-*N*-(6-pentyl-1)-norbornene dicarboximide triazole-ethyl-decaethylene oxide-ethyl iodide (**45**)



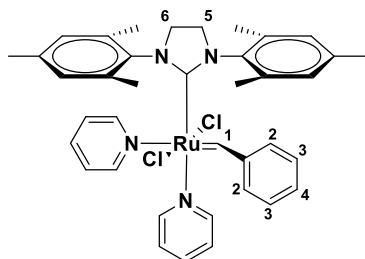
This reaction was carried out under an atmosphere of purified nitrogen using Schlenk techniques. An oven-dried, one-neck and round-bottom flask (25.0 mL) fitted with a reflux condenser was charged with *exo*-*N*-(6-pentyl-1)-norbornene dicarboximide triazole-ethyl-decaethylene oxide-ethyl bromide **51** (1.00 equiv., 1.00 g, 1.90 mmol), NaI (3.00 equiv., 0.90 g, 5.70 mmol) and dry acetone (10.0 mL). The resulting suspension was heated at reflux temperature for 3 hrs after which it was cooled down to room temperature, filtered and concentrated using the rotary evaporator. Crude was diluted with DCM (10.0 mL), washed with sat. Na₂S₂O₃ (15.0 mL) and dried over Na₂SO₄. The resulting crude oil was purified by column chromatography using a 2% MeOH:EtOAc (10% MeOH:EtOAc *R_f* 0.6) to afford the titled compound as a light-yellow oil (1.00 g, 98%). **¹H NMR** (500 MHz, CDCl₃) δ 7.45 (s, 1H, 12), 6.27 (t, *J* = 1.9 Hz, 2H, 1), 4.50 (t, *J* = 5.2 Hz, 2H, 13), 3.85 (t, *J* = 5.1 Hz, 2H, 14), 3.74 (t, *J* = 6.9 Hz, 3H, 36), 3.69 – 3.55 (m, 40H, 15-34), 3.44 (t, *J* = 7.6 Hz, 2H, 6), 3.29 – 3.21 (m, 4H, 2, 35), 2.72 – 2.62 (m, 4H, 3, 10), 1.73 – 1.62 (m, 2H, 9), 1.63 – 1.52 (m, 2H, 7), 1.50 (d, *J* = 9.9 Hz, 1H, 4'), 1.41 – 1.31 (m, 2H, 8), 1.20 (d, *J* = 9.9 Hz, 1H, 4). **¹³C NMR** (126 MHz, CDCl₃) δ 178.2 (5), 147.9 (11), 137.9 (1), 122.0 (12), 72.1 (36), 70.7, 70.6, 70.5, 70.3 (35), 69.8 (14), 50.2 (13), 47.9 (3), 45.3 (2), 42.9 (4), 38.7 (6), 29.1 (9), 27.6 (7), 26.7 (8), 25.6 (10). **IR** 2864 (C-H), 1694 (C(O)N) cm⁻¹. **HRMS** calcd. For C₄₀H₆₇N₄O₁₃I [M+H]⁺ 939.3822, found 939.3800.

exo-*N*-(6-pentyl-1)-norbornene dicarboximide triazole-ethyl-decaethylene oxide-ethyl iodide (**46**)



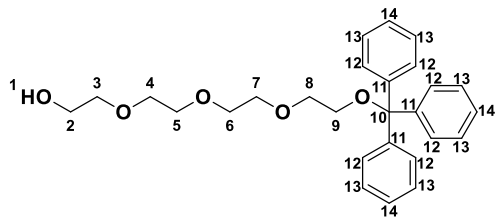
This reaction was carried out under an atmosphere of purified nitrogen using Schlenk techniques. Oven-dried three-neck round-bottom flask, fitted with a reflux condenser and a thermometer, was charged with PPh_3 (25.0 equiv., 2.8.0 g, 11.0 mmol). At 80 °C, a solution of *exo*-*N*-(6-pentyl-1)-norbornene dicarboximide triazole-ethyl-decaethylene oxide-ethyl iodide **52** (1.00 equiv., 0.40 g, 0.40 mmol) in dry and degassed toluene (0.50 mL) was slowly added. The reaction mixture's temperature was maintained at 80-85 °C for an hour at the end of which the complete conversion of substrate was confirmed by $^1\text{H NMR}$. The reaction mixture was allowed to cool down to room temperature during which PPh_3 had solidified. Crude was repeatedly sonicated with Et_2O to remove excess PPh_3 then dried under vacuum to give the title compound as a thick oil (0.40 g, Quant.). $^1\text{H NMR}$ (500 MHz, CDCl_3) δ 7.86 – 7.80 (m, 6H, 39), 7.79 – 7.74 (m, 3H, 40), 7.69 – 7.61 (m, 6H, 38), 7.44 (s, 1H, 12), 6.27 (t, $J = 1.9$ Hz, 2H, 1), 4.49 (t, $J = 5.2$ Hz, 2H, 13), 4.12 – 4.05 (m, 2H, 36), 3.90 (dt, $J = 22.3, 5.8$ Hz, 2H, 35), 3.85 (t, $J = 5.3$ Hz, 2H, 14), 3.69 – 3.55 (m, 32H, 17-32), 3.51 (t, $J = 5.0$ Hz, 2H, 15), 3.44 (t, $J = 7.6$ Hz, 2H, 6), 3.39 – 3.35 (m, 2H, 16), 3.34 – 3.31 (m, 2H, 34), 3.30 – 3.26 (m, 2H, 33), 3.25 (t, $J = 1.9$ Hz, 2H, 2), 2.72 – 2.63 (m, 4H, 3-10), 1.72 – 1.62 (m, 2H, 9), 1.62 – 1.54 (m, 2H, 7), 1.49 (d, $J = 9.9$ Hz, 1H, 4'), 1.40 – 1.31 (m, 2H, 8), 1.20 (d, $J = 9.9$ Hz, 1H, 4). $^{13}\text{C NMR}$ (126 MHz, CDCl_3) δ 178.1 (5), 147.8 (11), 137.8 (1), 134.7 (d, $J = 3.6$ Hz, 40), 134.1 (d, $J = 10.0$ Hz, 39), 130.1 (d, $J = 12.7$ Hz, 38), 121.8 (12), 118.8 (d, $J = 87.2$ Hz, 37), 70.6, 70.5, 70.4, 70.3, 69.9, 69.3 (14), 64.0 (d, $J = 7.3$ Hz, 35), 50.1 (13), 47.8 (3), 45.2 (2), 42.7 (4), 38.6 (6), 29.0 (9), 27.5 (7), 26.6 (8), 25.8 (d, $J = 52.7$ Hz, 36), 25.5 (10). $^{31}\text{P NMR}$ (202 MHz, CDCl_3) δ 25.52. **HRMS** calcd. For $\text{C}_{58}\text{H}_{82}\text{N}_4\text{O}_{13}\text{PI}$ $[\text{M}-\text{I}]^+$ 1073.5611, found 1073.5623.

[1,3-Bis(2,4,6-trimethylphenyl)-2-imidazolidinylidene]dichloro(phenylmethylene)bis(pyridine)-ruthenium(II) or Third-Generation Grubbs Catalyst. Ref. (**160**)

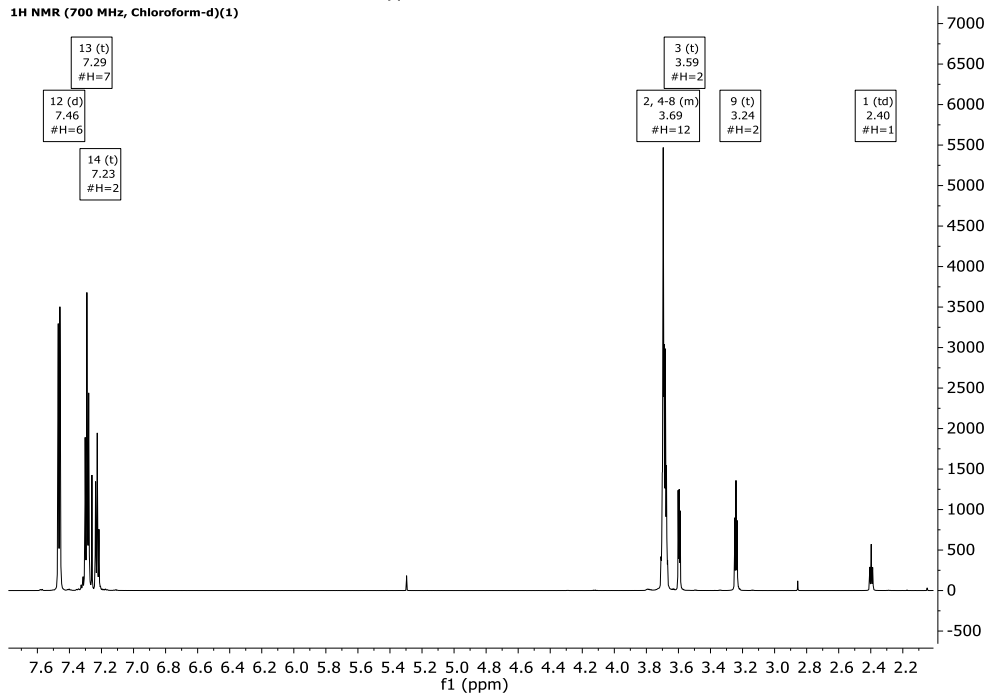


This compound was prepared under inert conditions in a glovebox as described in a literature procedure. (**160**) At 24 °C, an oven-dried, one-neck round-bottom flask (100 mL) was charged with second-generation Grubbs catalyst (0.60 g, 0.70 mmol) and dry and degassed DCM (2.00 mL). To the resulting deep red solution, excess pyridine (10.0 mL) was added and the reaction was stirred for 10 min during which the solution's color had change from deep red to deep green. Then, dry and degassed hexane (50.0 mL) was added and the resulting solution was allowed to precipitate overnight glovebox's freezer at 0 °C after which the supernatant was decanted and the green precipitate was washed with dry and degassed hexane. The precipitate was dried overnight under vacuum to afford the titled compound as a bright green powder (0.40 g, 80%). ¹H NMR (500 MHz, CDCl₃) δ 19.20 (s, 1H, CHPh), 8.62 (d, *J* = 5.3 Hz, 2H, ortho CH, pyridine), 7.82 (d, *J* = 5.9 Hz, 2H, ortho CH, pyridine), 7.67 (t, *J* = 7.4 Hz, 1H, para CH), 7.62 (d, *J* = 8.2 Hz, 2H, 2), 7.52 – 7.43 (m, 2H, para CH, pyridine, 4), 7.28 (t, *J* = 6.4 Hz, 2H, meta CH, pyridine), 7.09 – 7.05 (m, 4H, 3, mesityl), 6.98 (t, *J* = 6.8 Hz, 2H, meta CH, pyridine), 6.75 (s, 2H, mesityl), 4.21 (t, *J* = 9.2 Hz, 2H, 5), 4.04 (t, *J* = 9.2 Hz, 1H), 2.65 (s, 6H, ortho CH₃ mesityl), 2.36 (s, 3H, para CH₃ mesityl), 2.29 (s, 3H, para CH₃ mesityl), 2.23 (s, 6H, ortho CH₃ mesityl). Elemental analysis calcd. for C₃₈H₄₃Cl₂N₄Ru: C, 62.72; H, 5.96; N, 7.70. Found: C, 62.55; H, 5.93; N, 7.81. Spectroscopic data agree with literature values. (**160**)

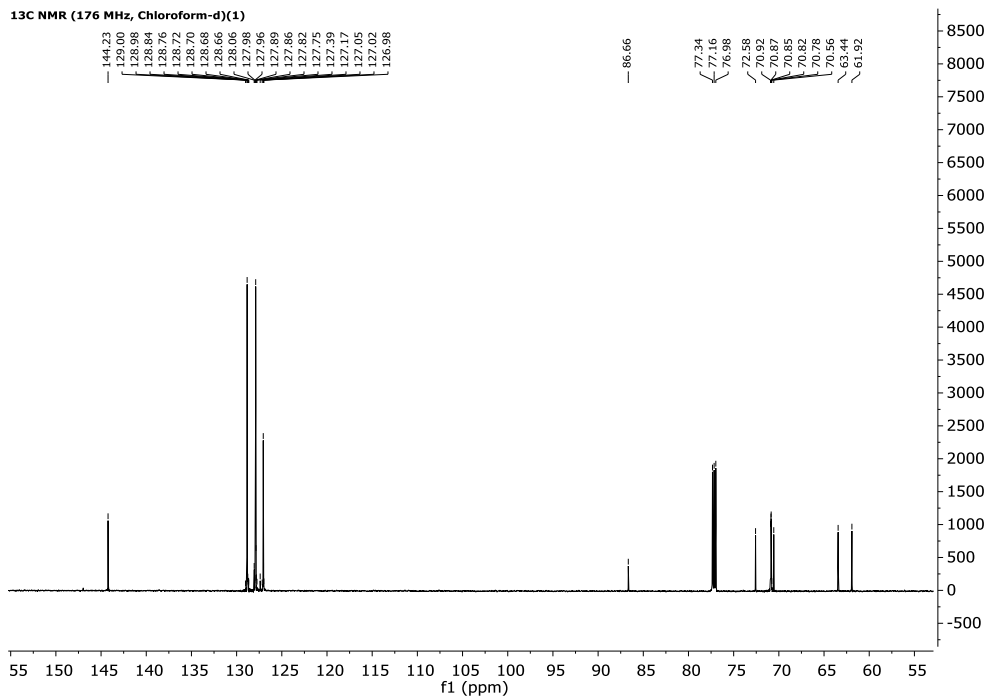
10 Spectra

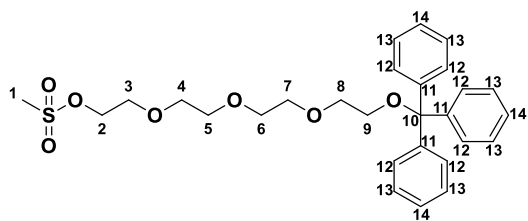


¹H NMR (700 MHz, Chloroform-d)(1)

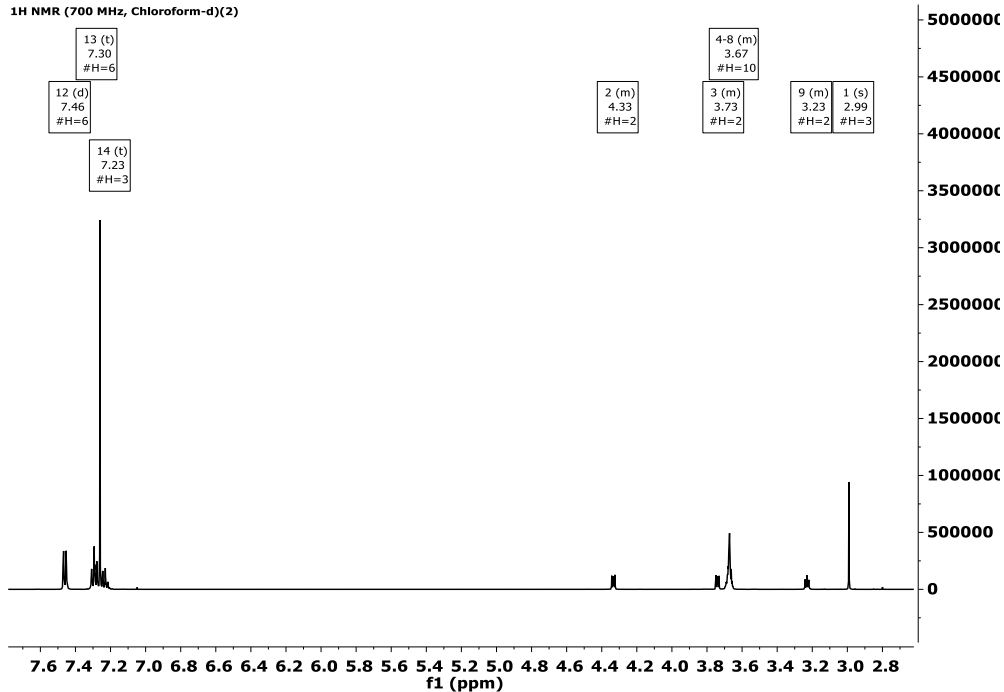


¹³C NMR (176 MHz, Chloroform-d)(1)

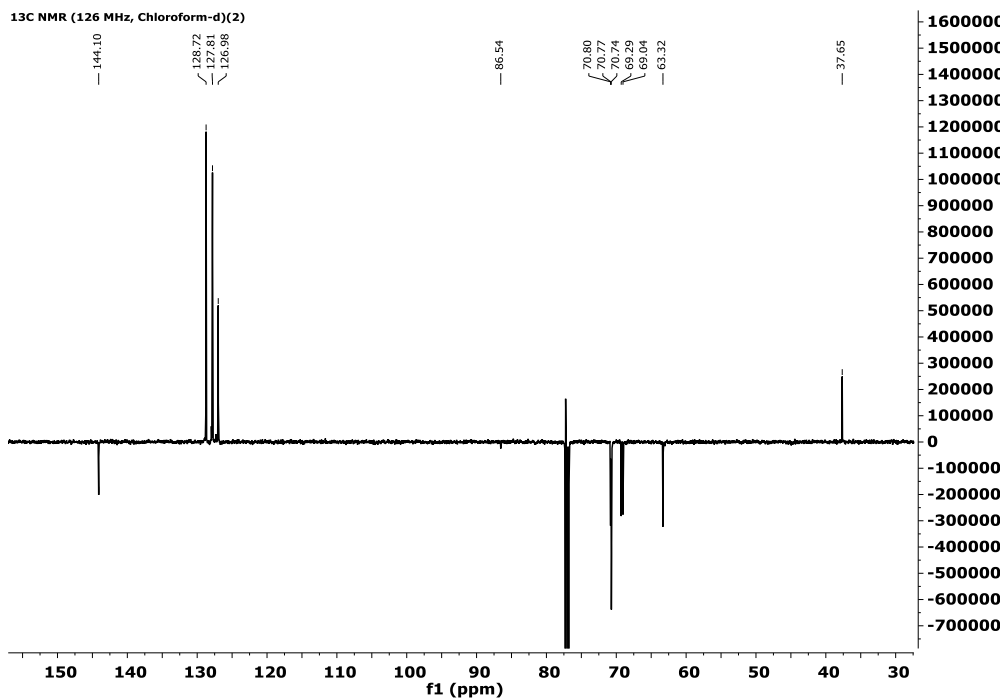


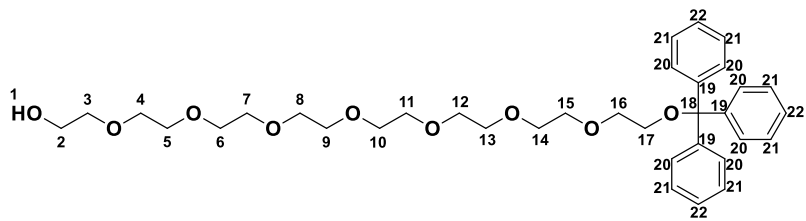


1H NMR (700 MHz, Chloroform-d)(2)

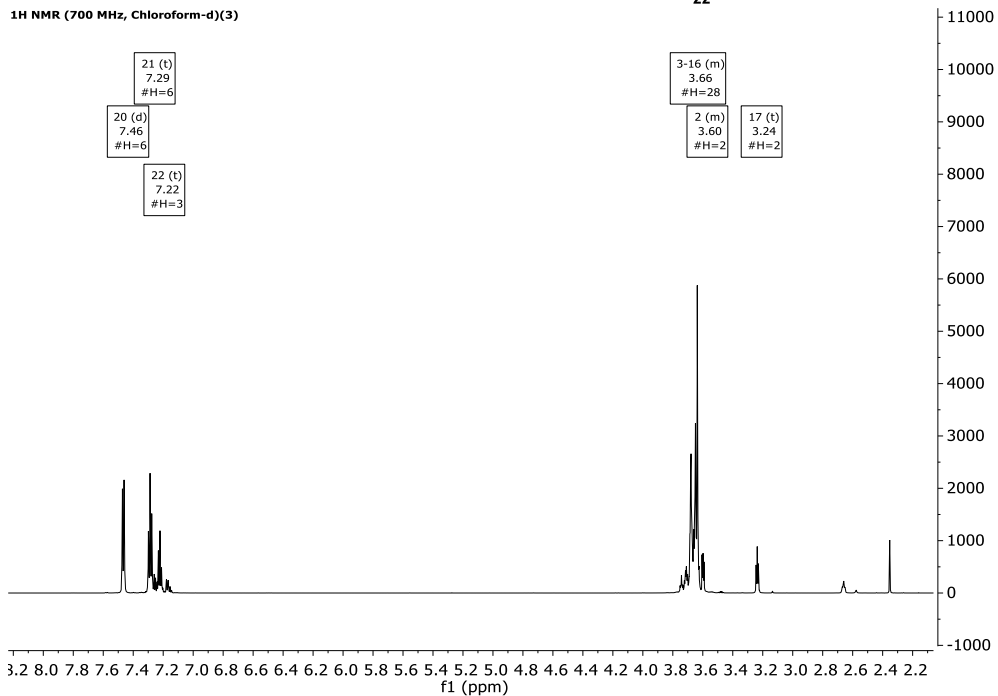


13C NMR (126 MHz, Chloroform-d)(2)

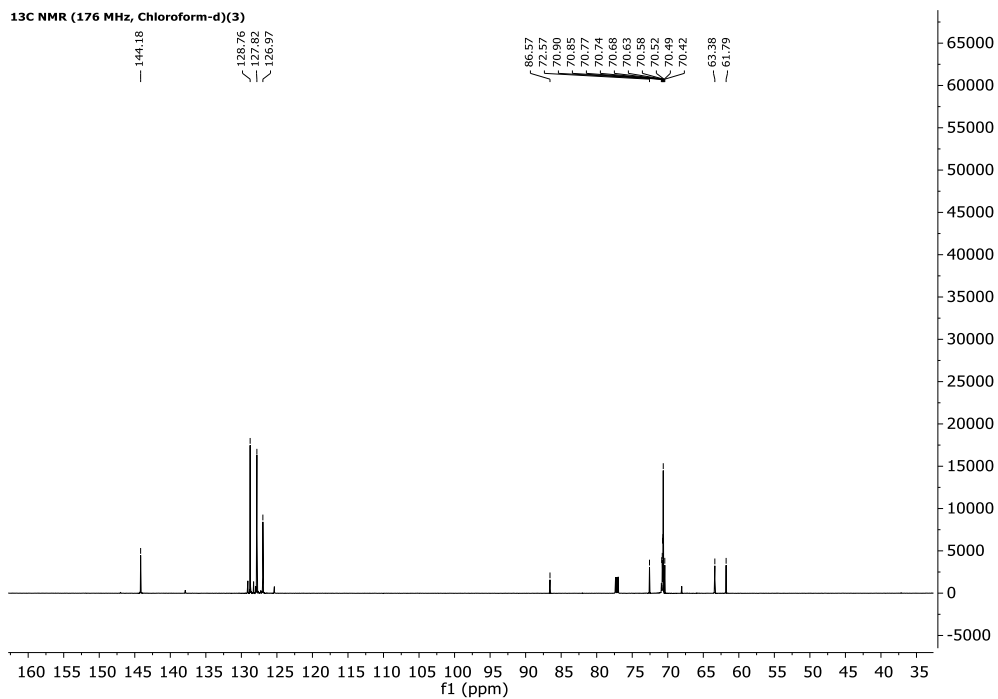


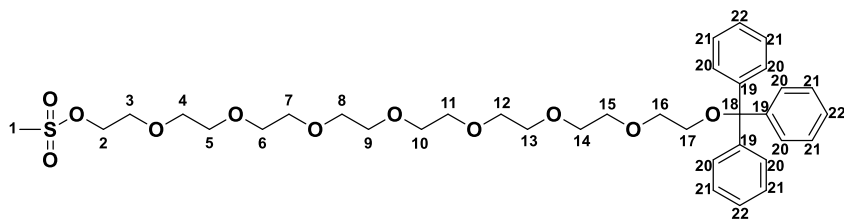


¹H NMR (700 MHz, Chloroform-d)(3)

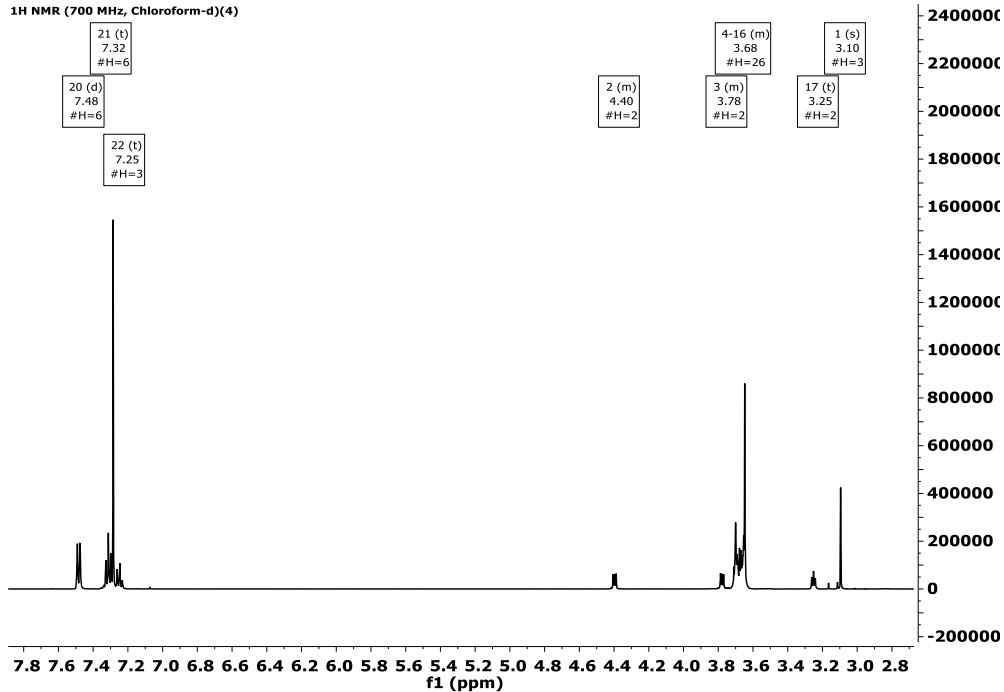


¹³C NMR (176 MHz, Chloroform-d)(3)

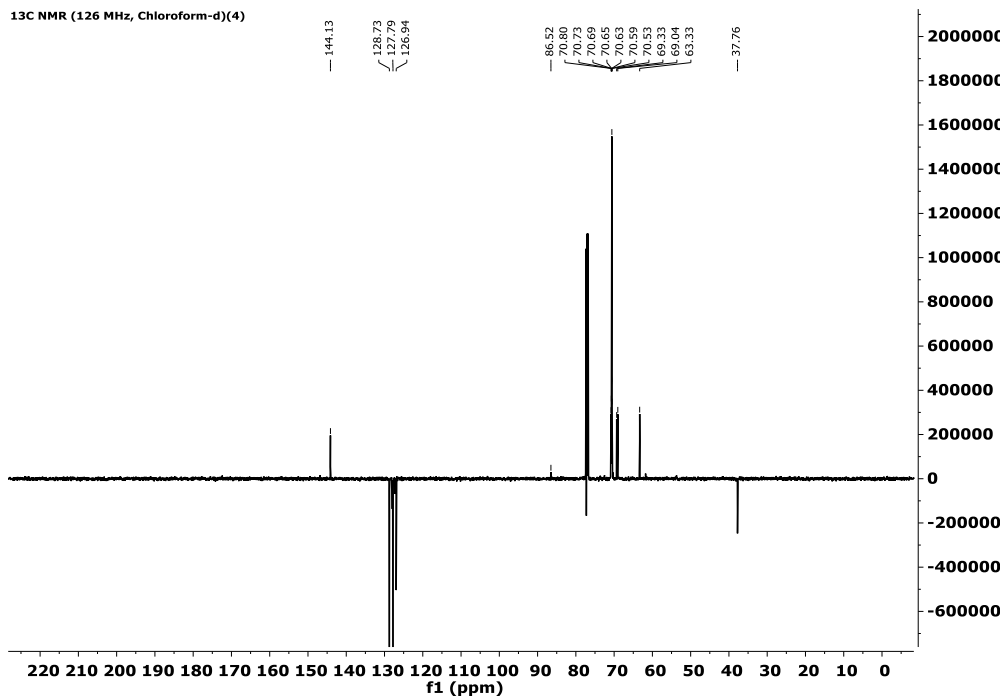


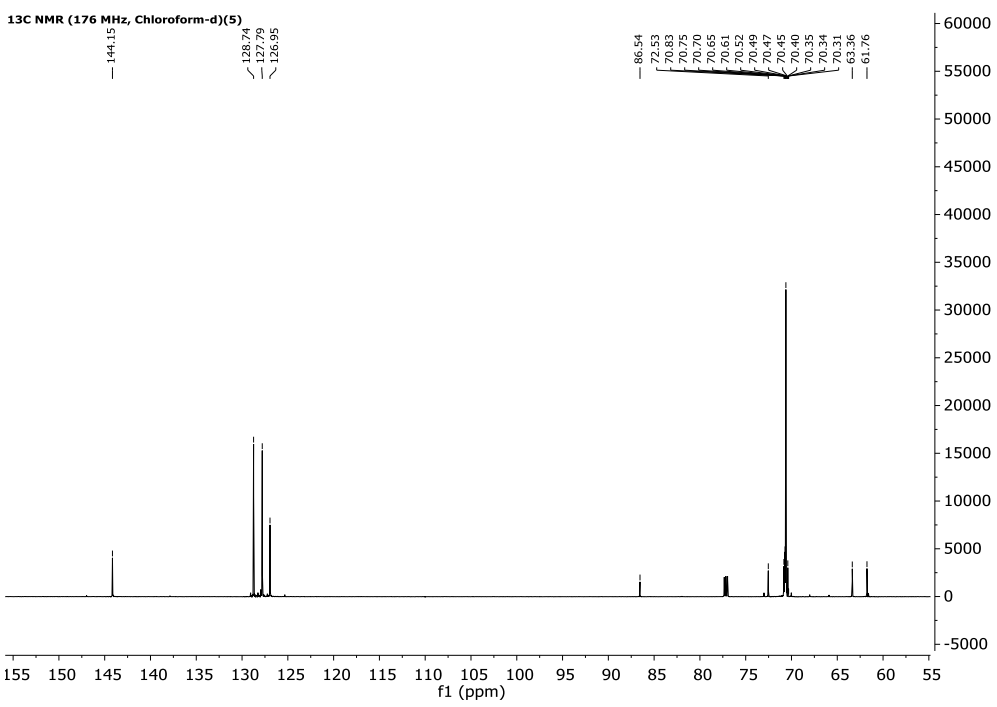
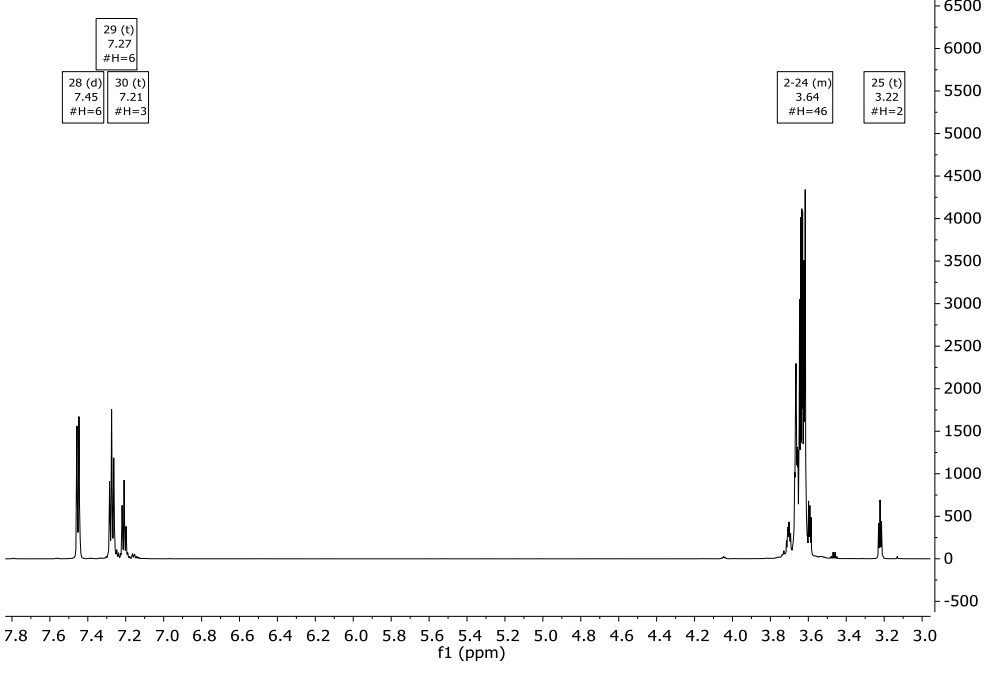
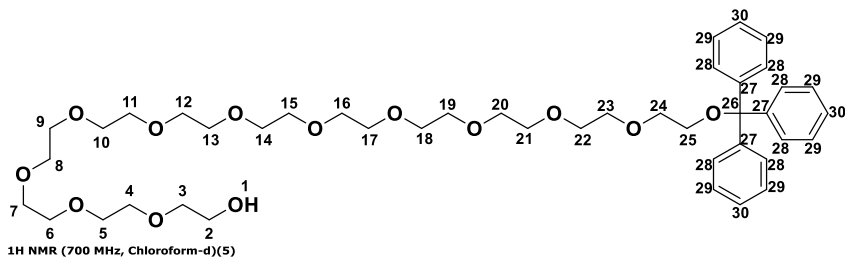


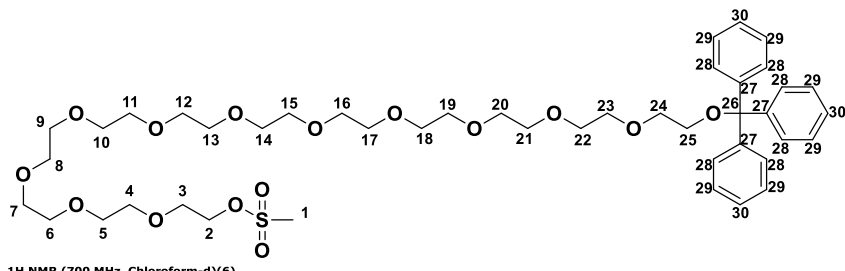
¹H NMR (700 MHz, Chloroform-d)(4)



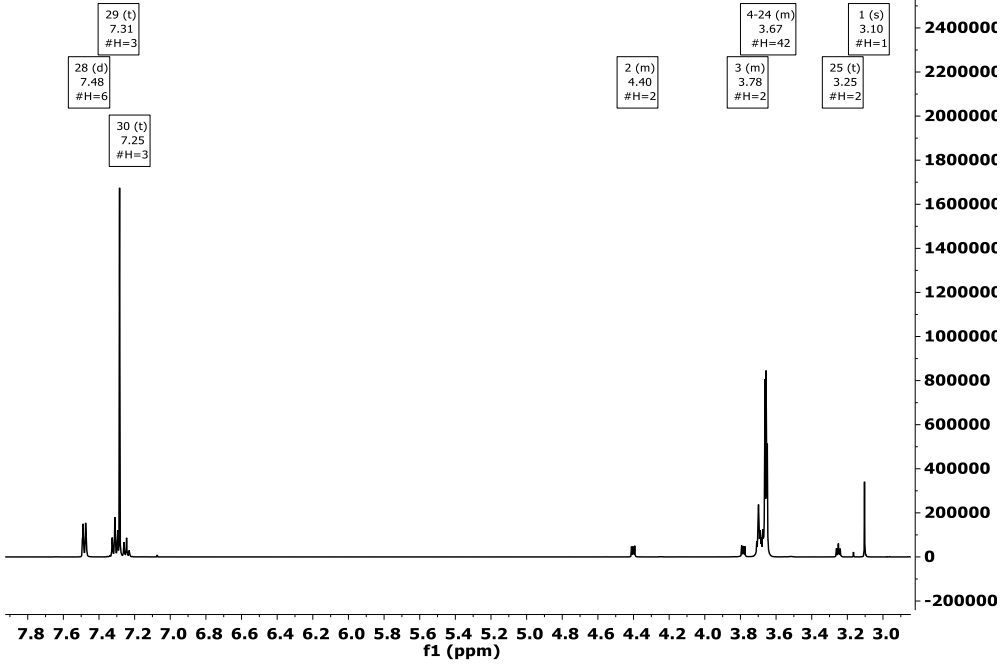
¹³C NMR (126 MHz, Chloroform-d)(4)



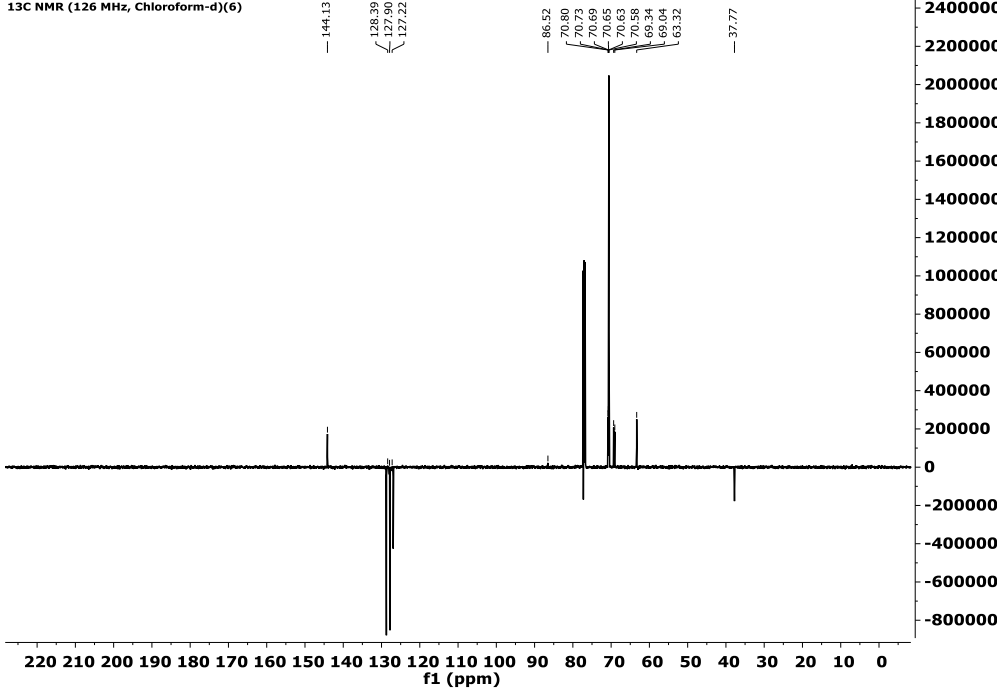


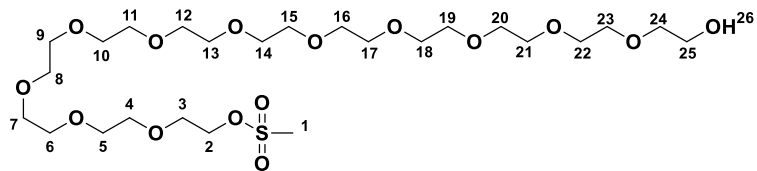


¹H NMR (700 MHz, Chloroform-d)(6)

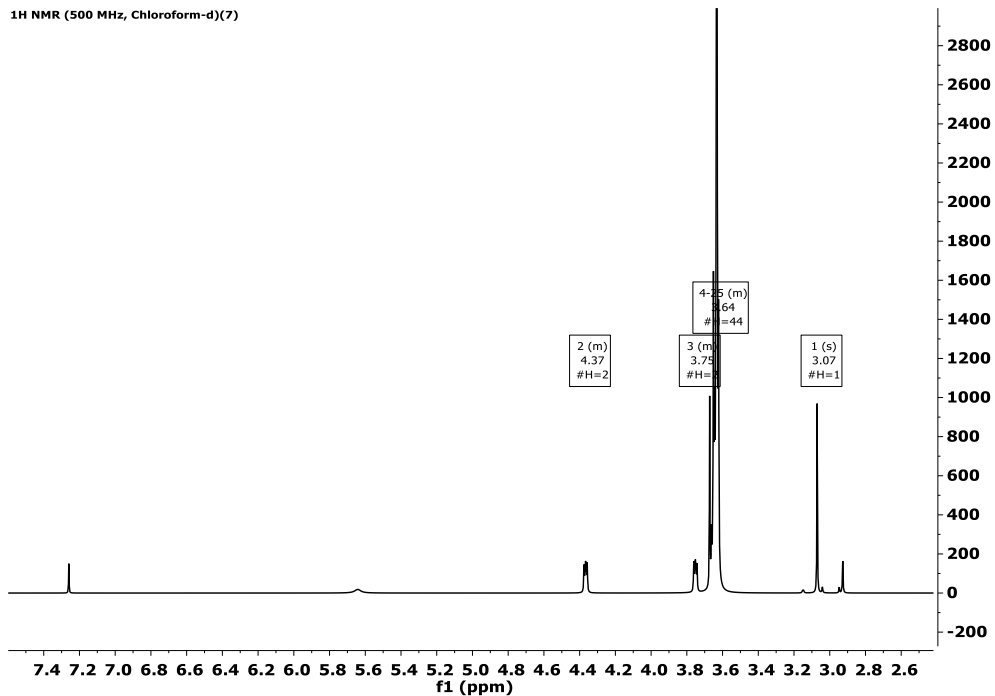


¹³C NMR (126 MHz, Chloroform-d)(6)

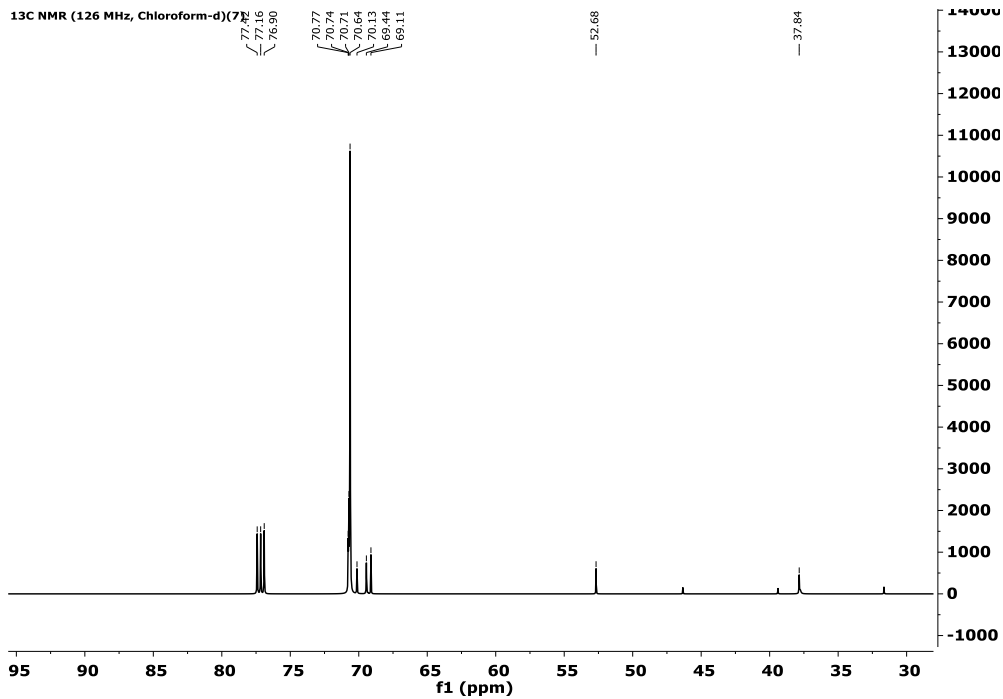


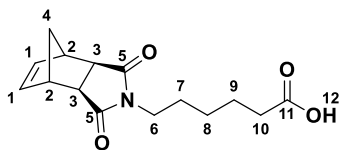


¹H NMR (500 MHz, Chloroform-d)(7)

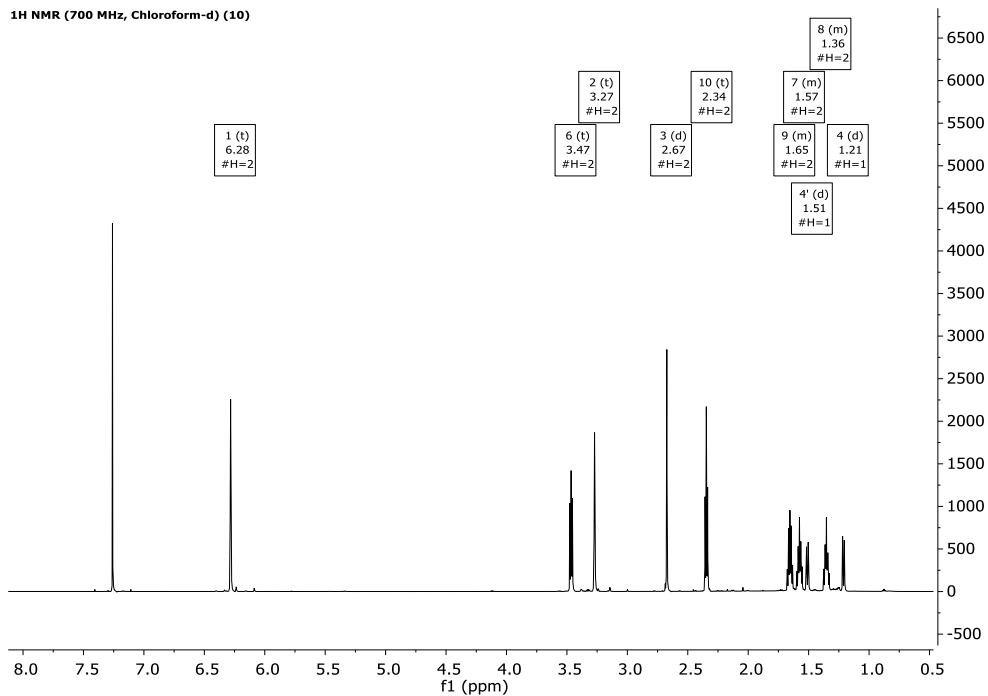


¹³C NMR (126 MHz, Chloroform-d)(7)

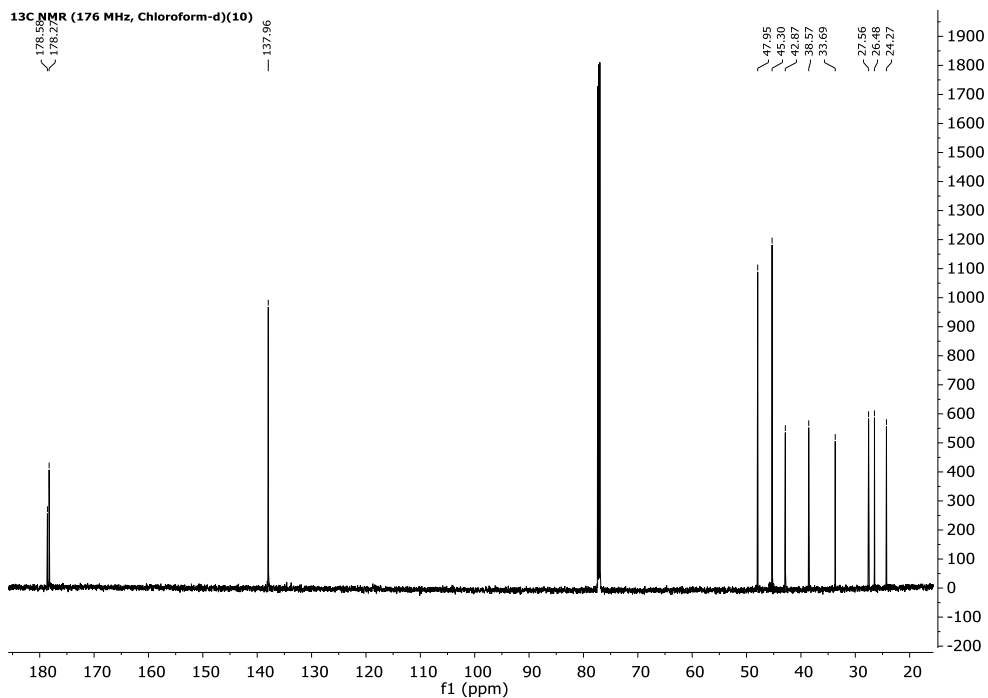


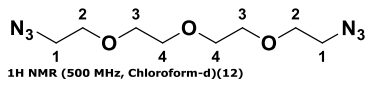


¹H NMR (700 MHz, Chloroform-d) (10)

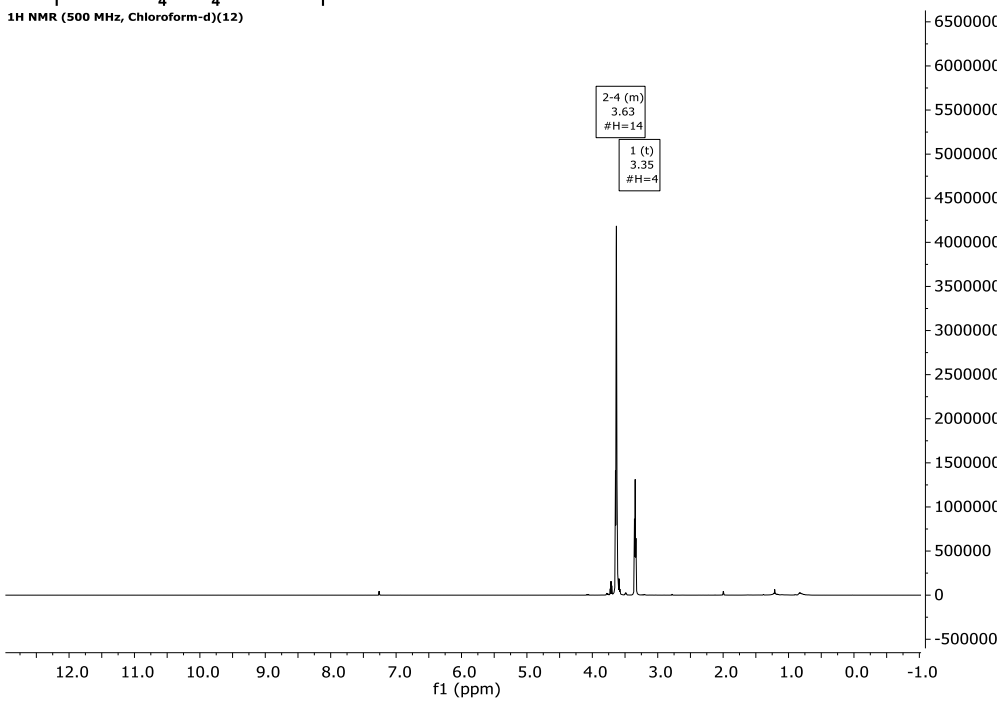


¹³C NMR (176 MHz, Chloroform-d)(10)

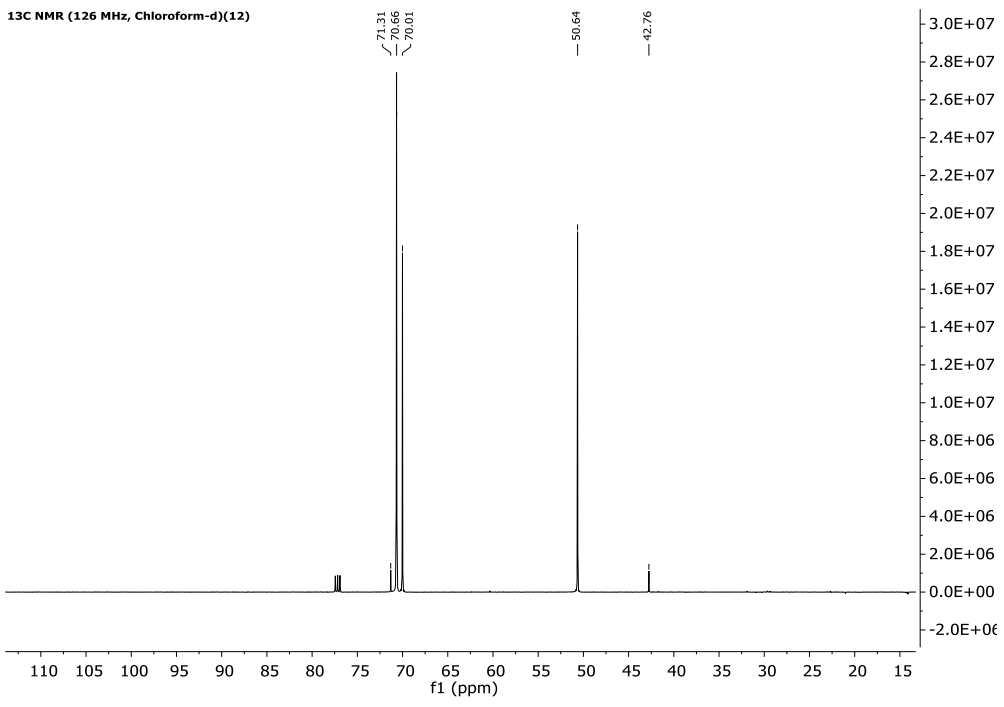


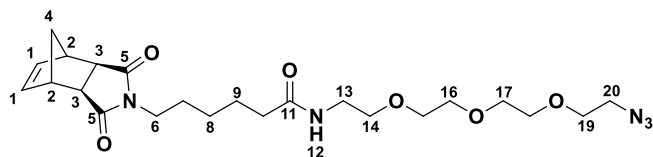


¹H NMR (500 MHz, Chloroform-d)(12)

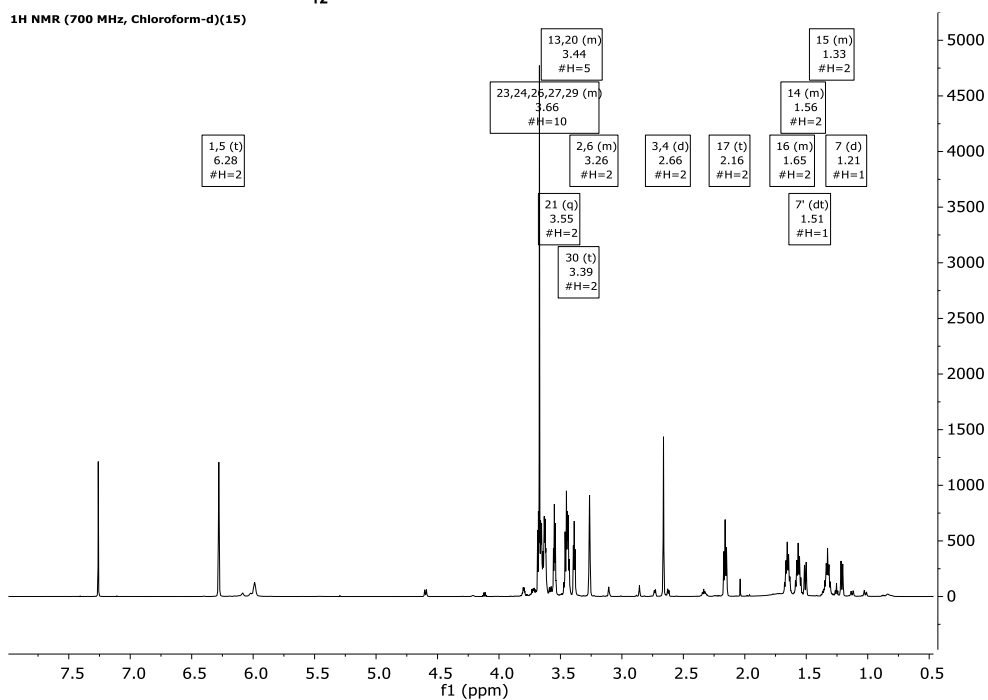


¹³C NMR (126 MHz, Chloroform-d)(12)

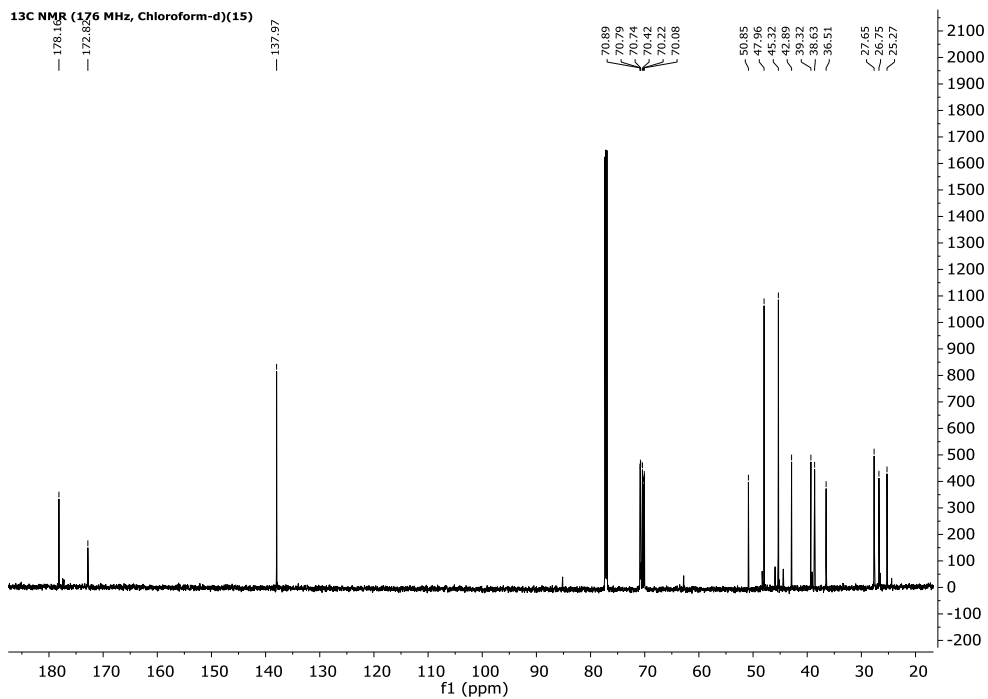


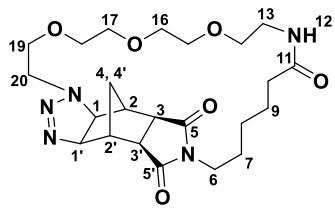


¹H NMR (700 MHz, Chloroform-d)(15)

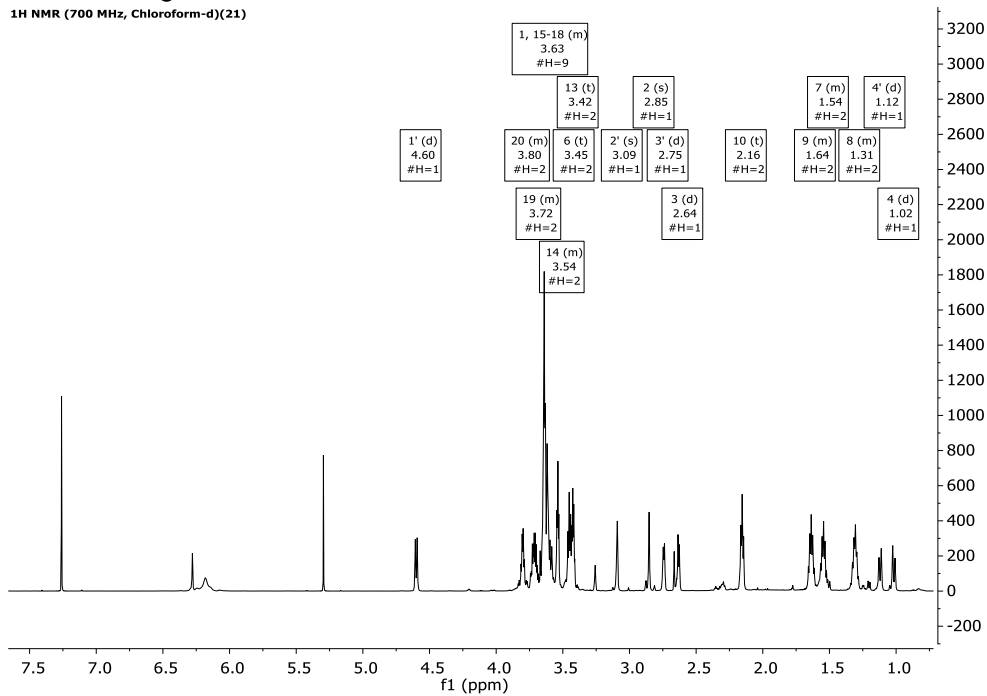


¹³C NMR (176 MHz, Chloroform-d)(15)

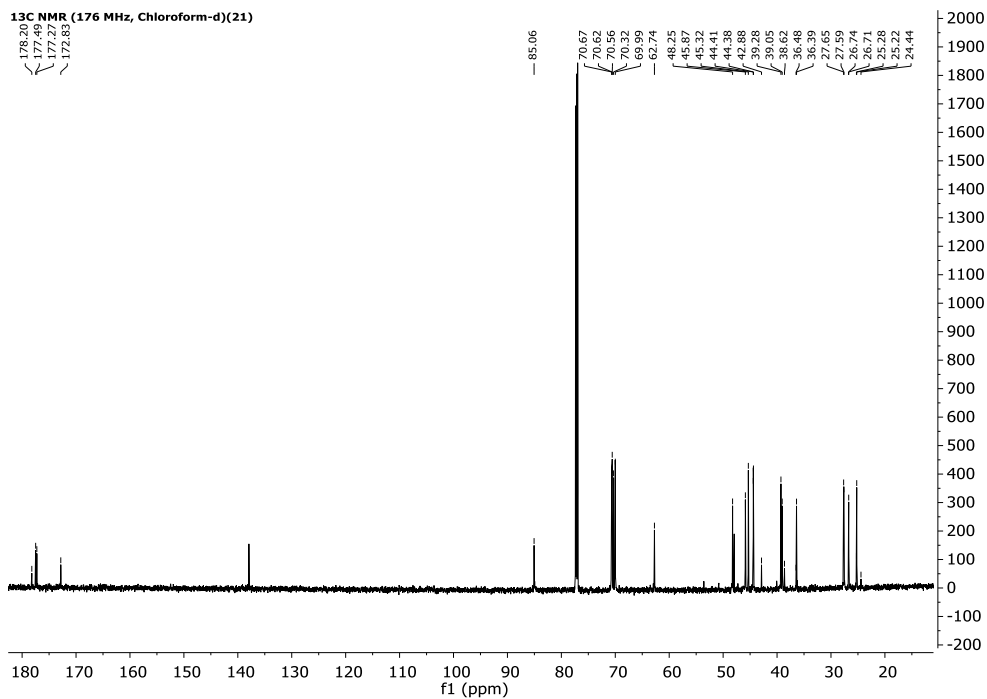


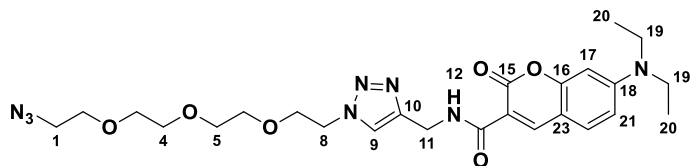


¹H NMR (700 MHz, Chloroform-d)(21)

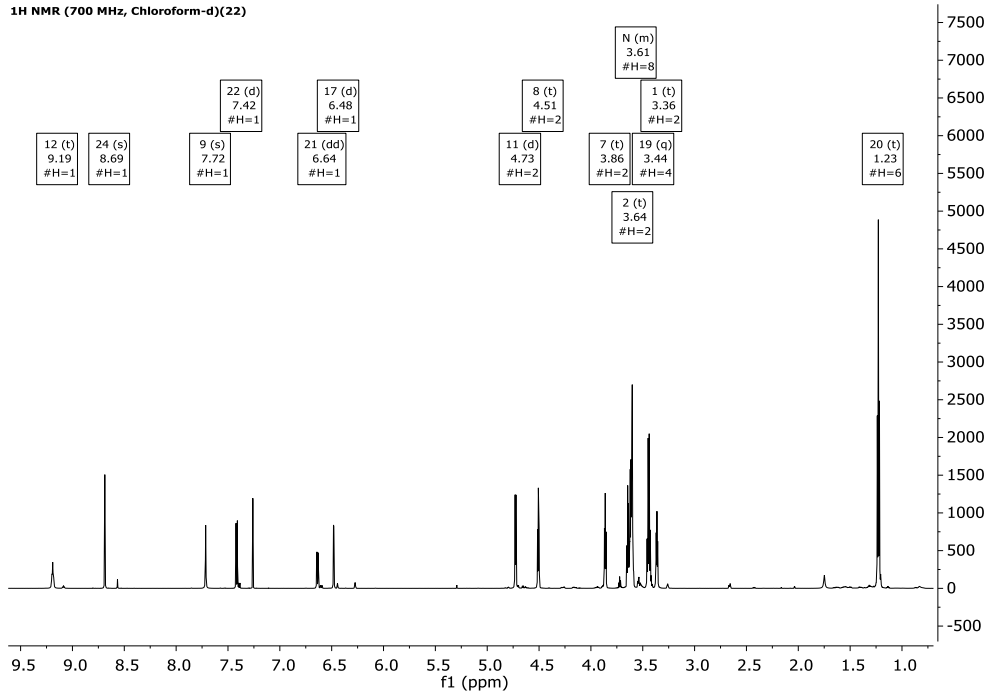


¹³C NMR (176 MHz, Chloroform-d)(21)

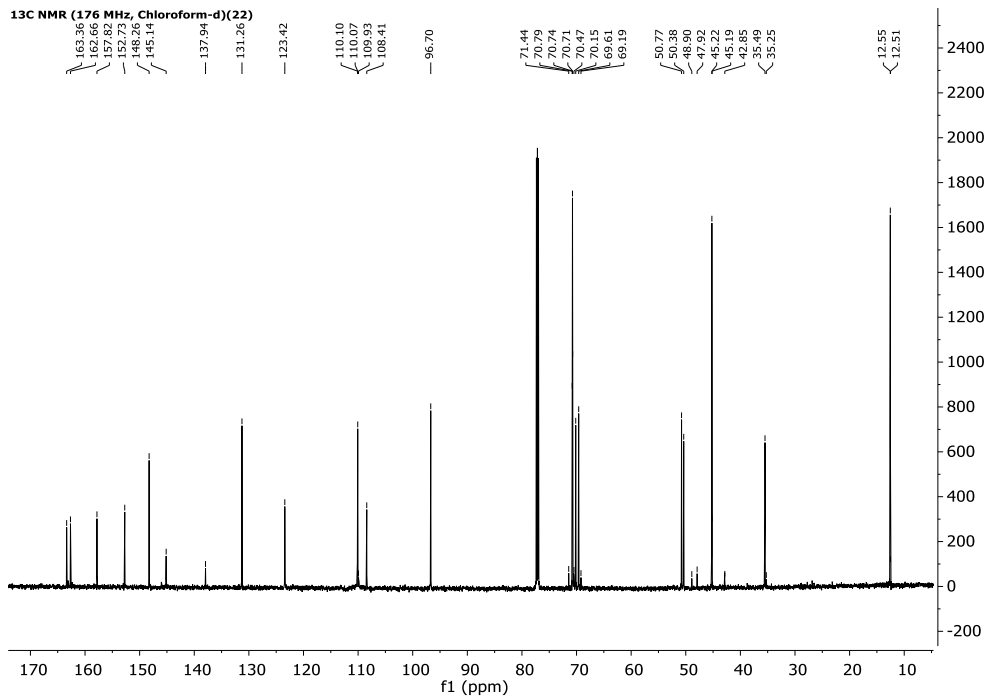


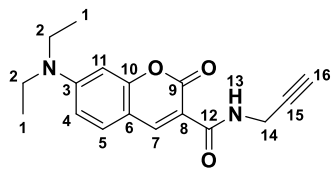


¹H NMR (700 MHz, Chloroform-d)(22)

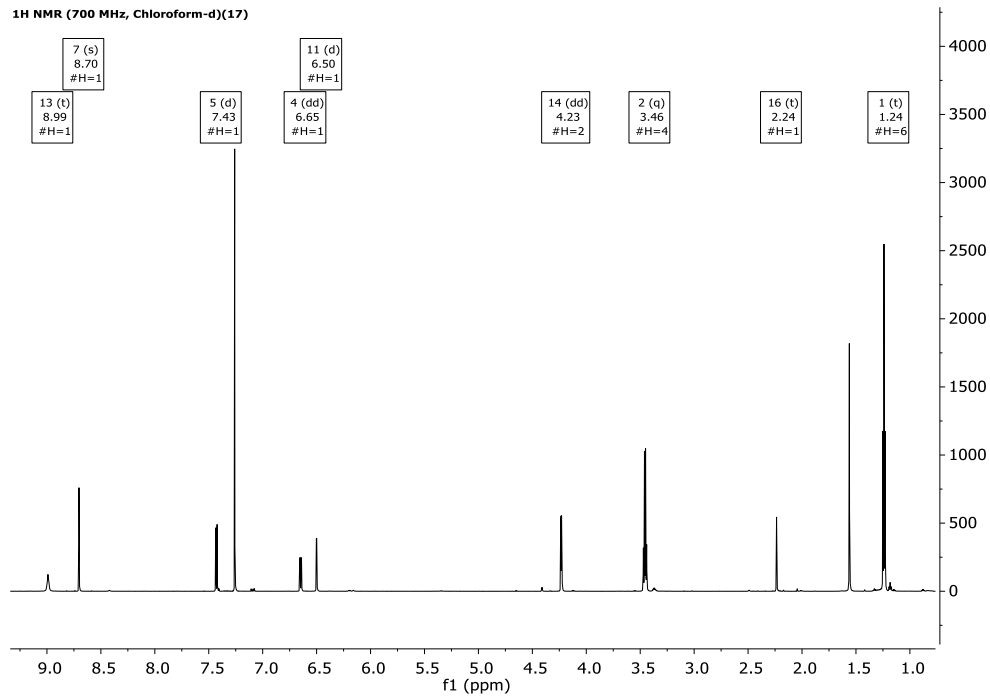


¹³C NMR (176 MHz, Chloroform-d)(22)

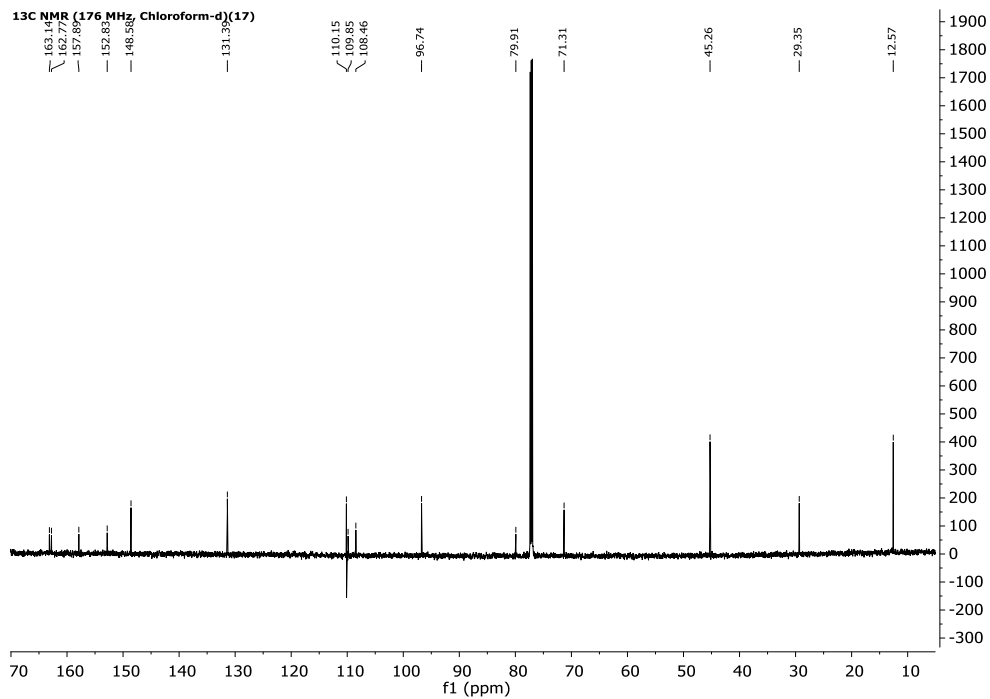


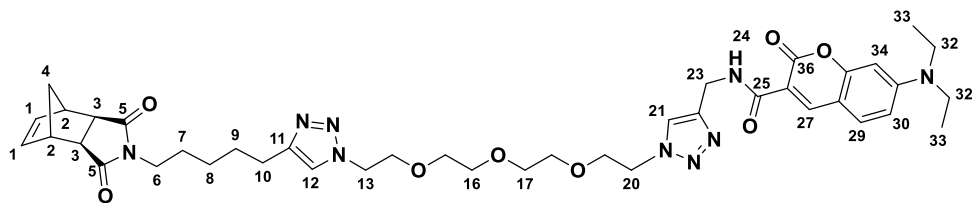


¹H NMR (700 MHz, Chloroform-d)(17)

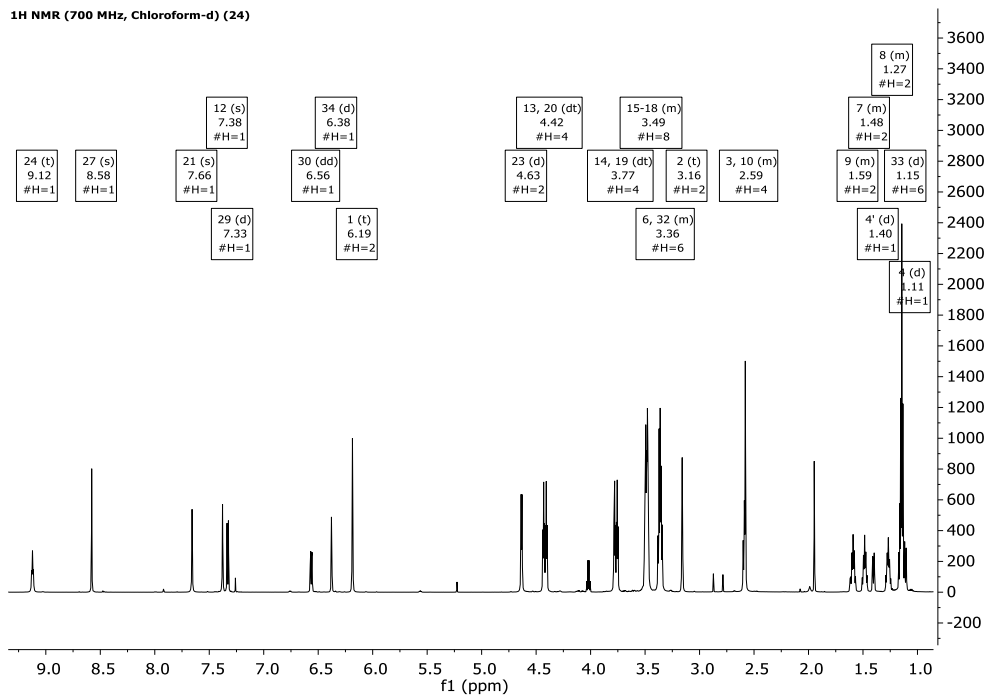


¹³C NMR (176 MHz, Chloroform-d)(17)

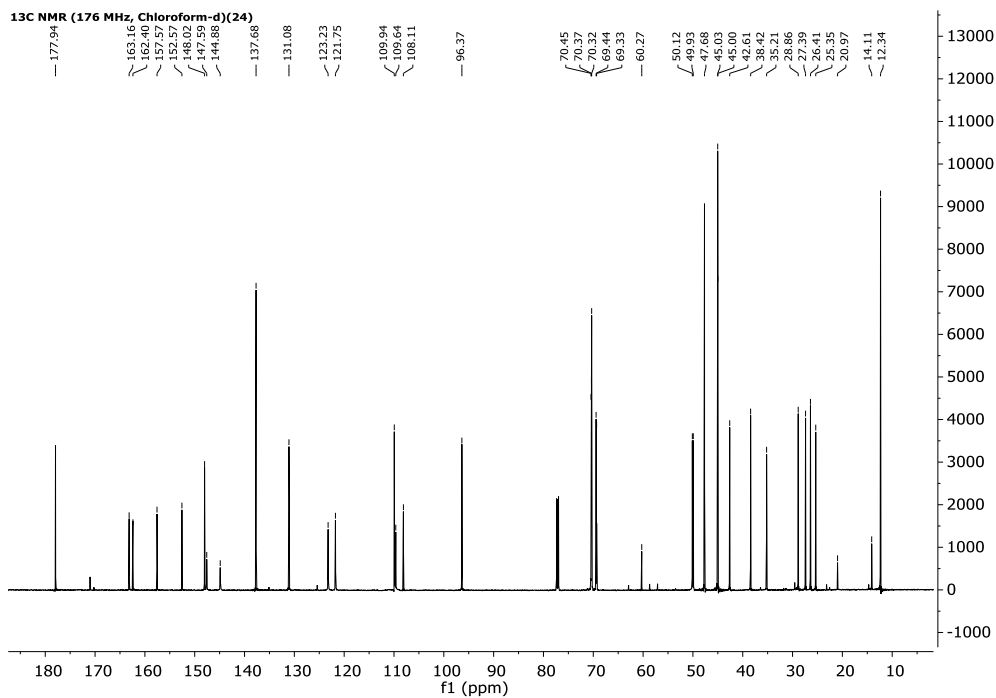


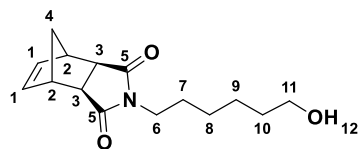


¹H NMR (700 MHz, Chloroform-d) (24)

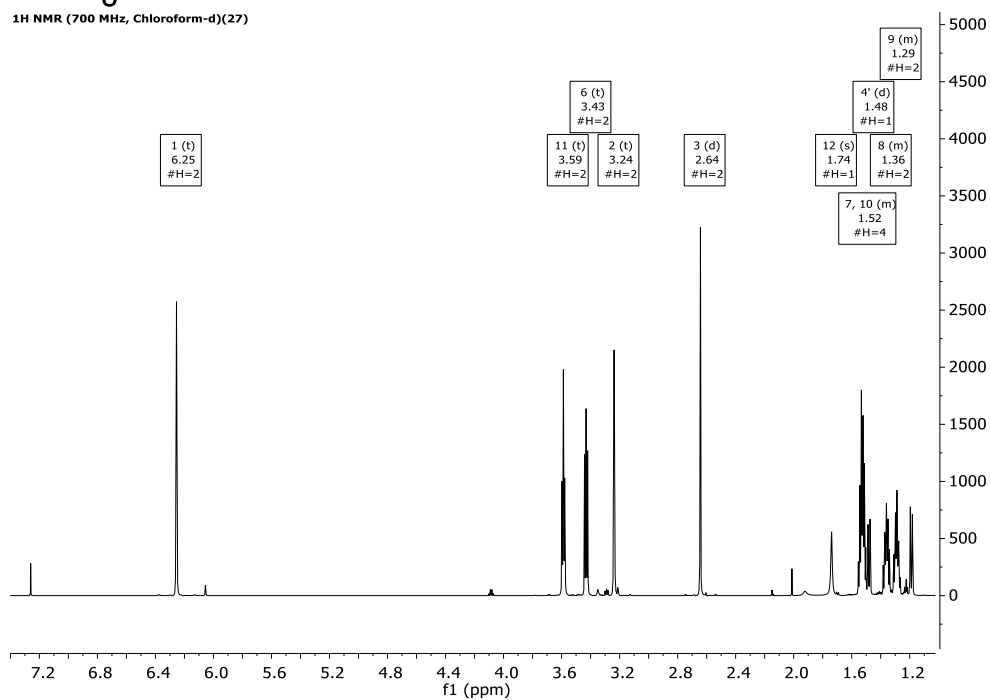


¹³C NMR (176 MHz, Chloroform-d) (24)

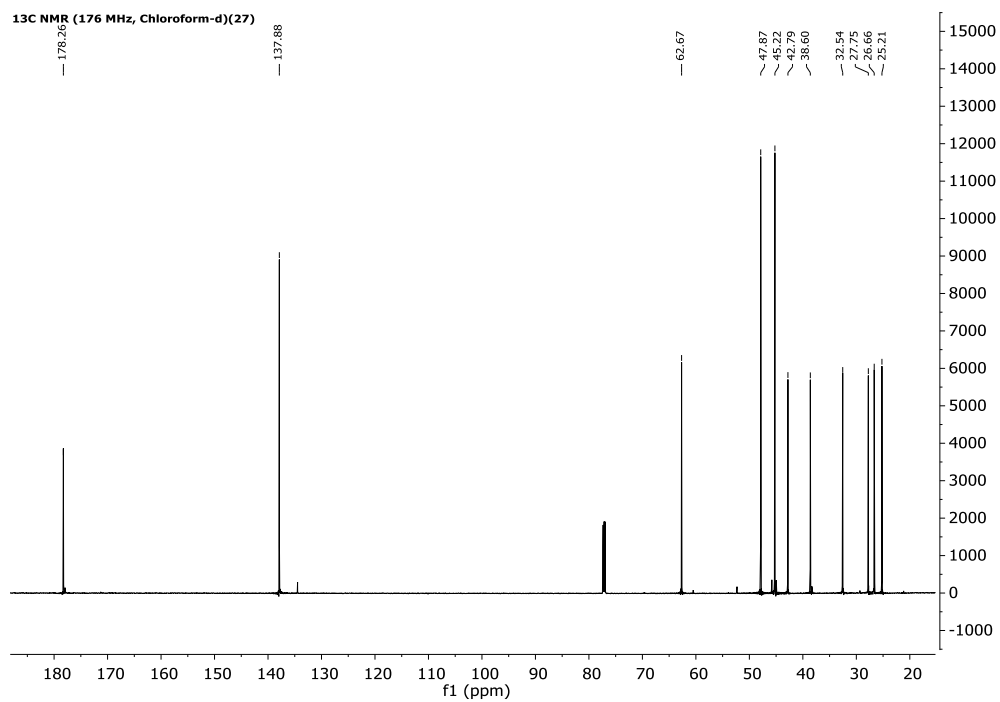


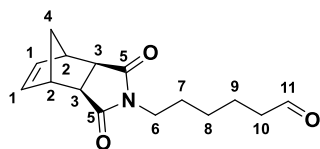


¹H NMR (700 MHz, Chloroform-d)(27)

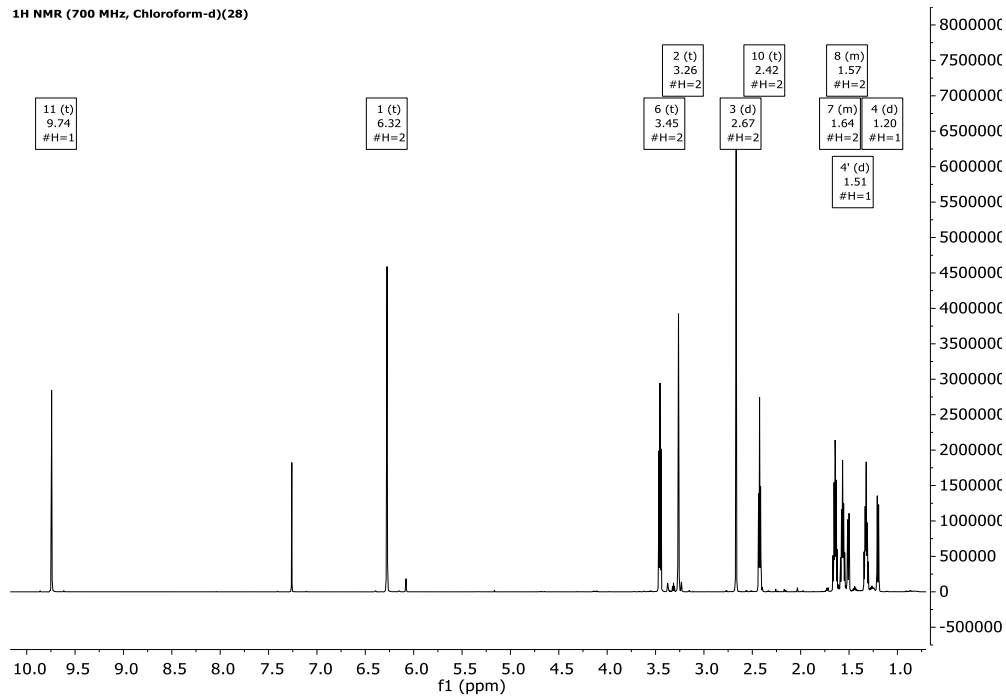


¹³C NMR (176 MHz, Chloroform-d)(27)

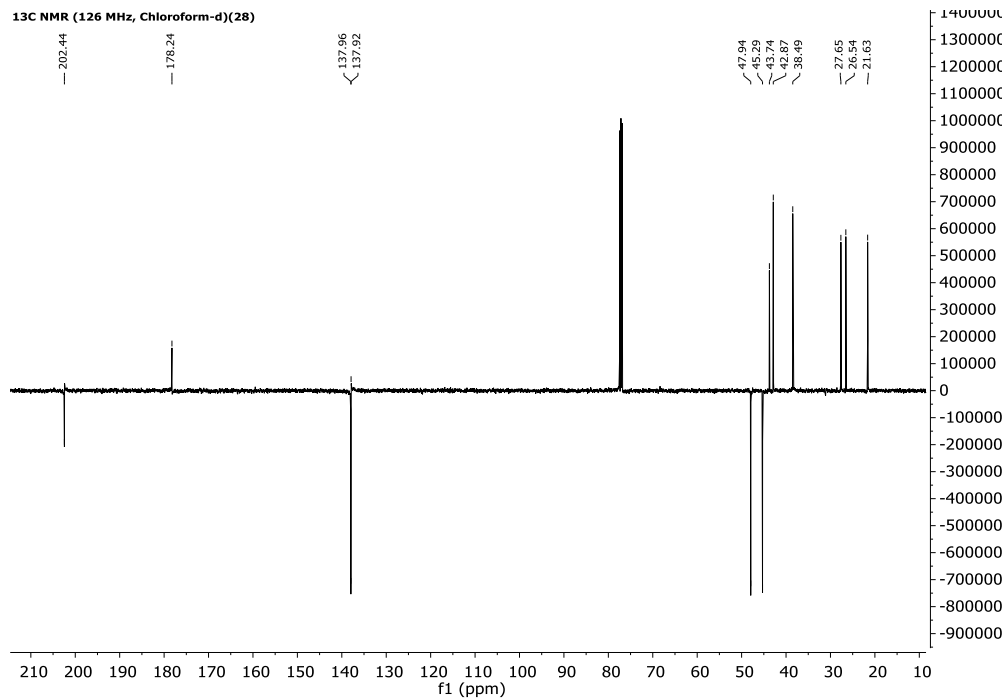


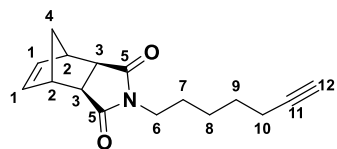


¹H NMR (700 MHz, Chloroform-d)(28)

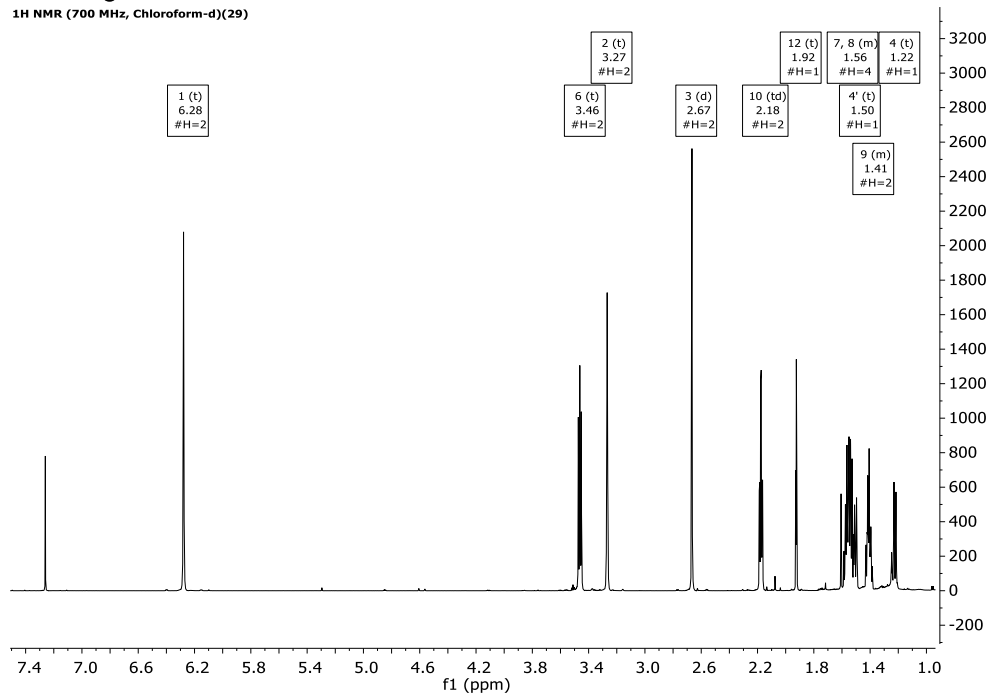


¹³C NMR (126 MHz, Chloroform-d)(28)

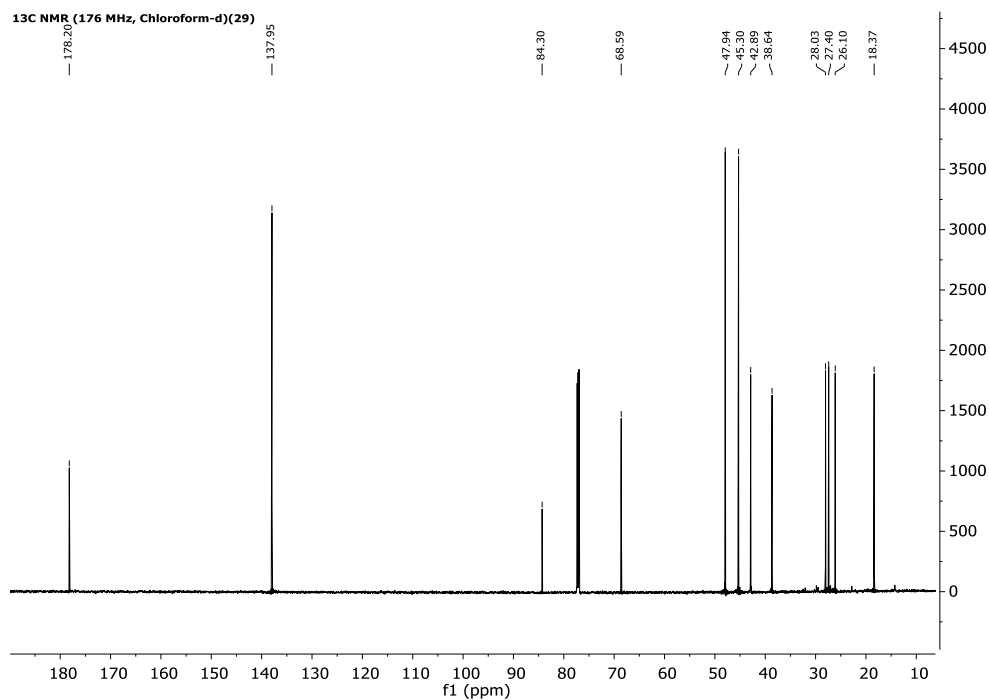


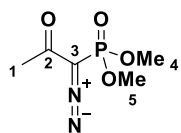


¹H NMR (700 MHz, Chloroform-d)(29)

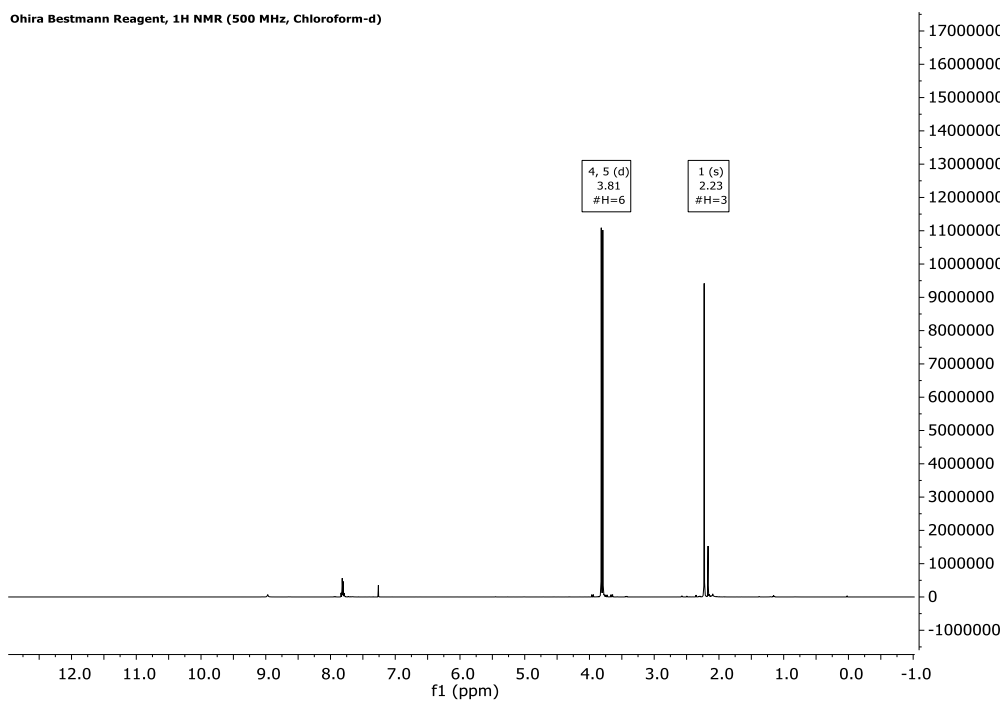


¹³C NMR (176 MHz, Chloroform-d)(29)

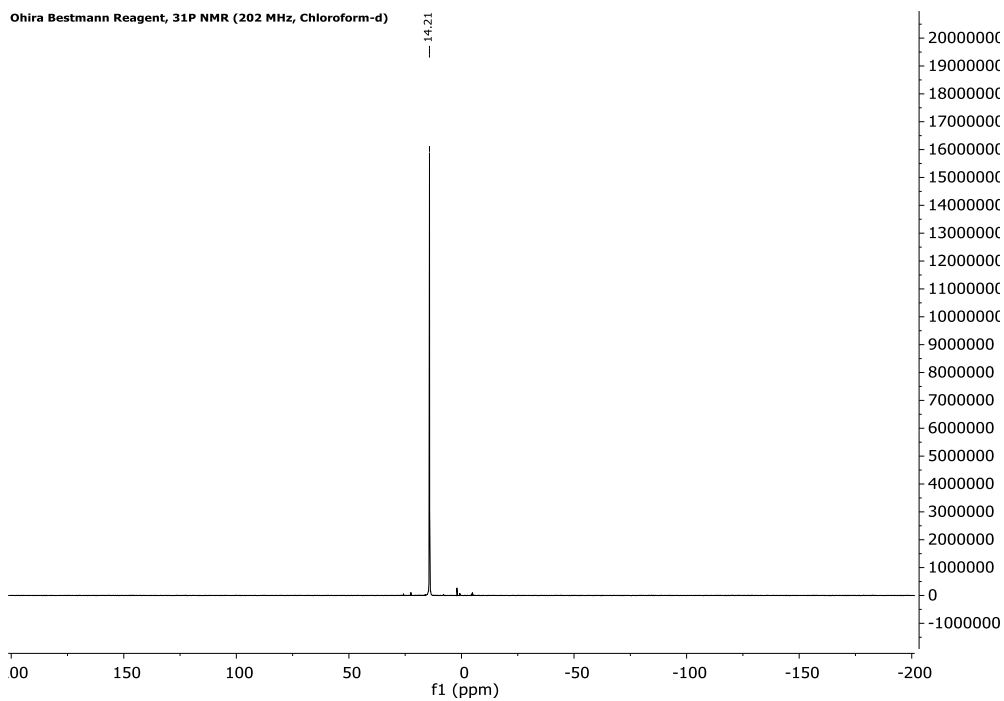




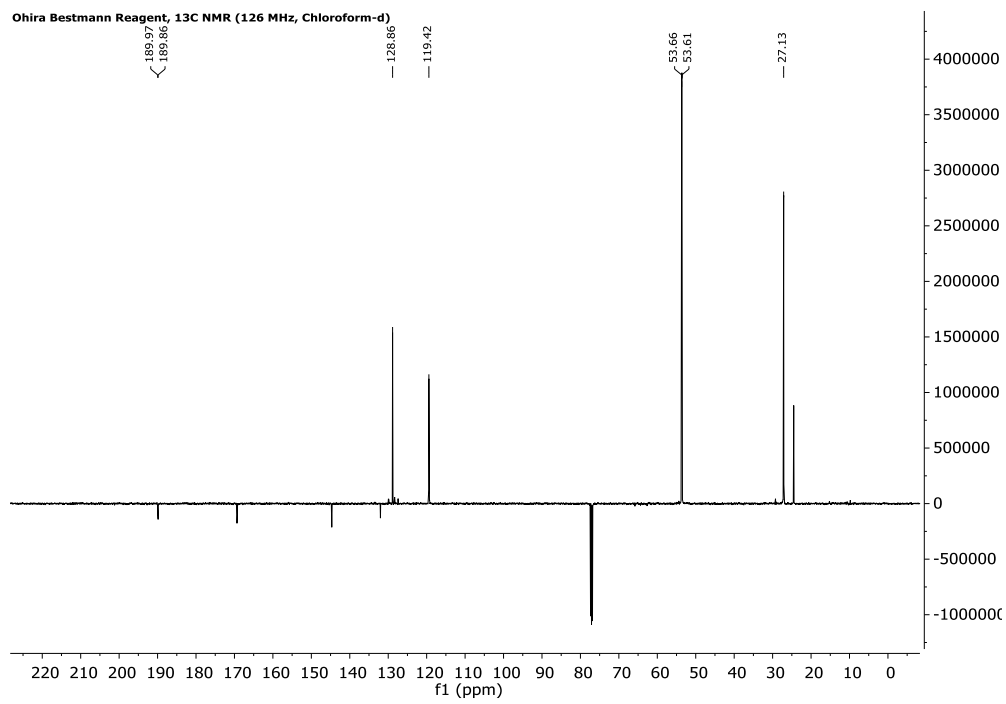
Ohira Bestmann Reagent, ¹H NMR (500 MHz, Chloroform-d)

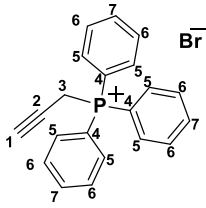


Ohira Bestmann Reagent, ³¹P NMR (202 MHz, Chloroform-d)

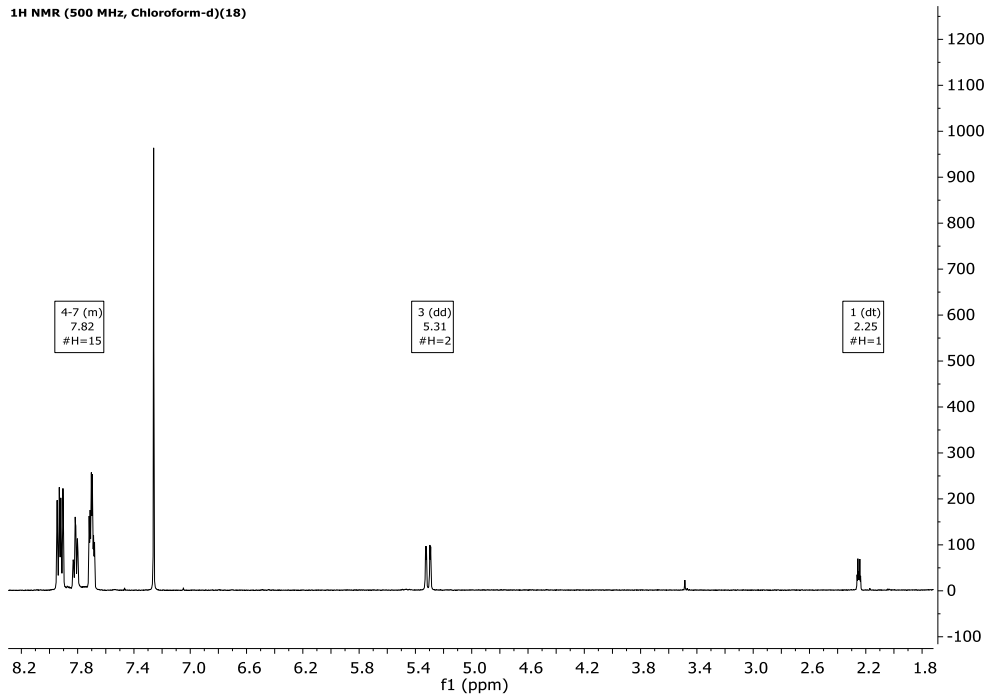


Ohira Bestmann Reagent, ¹³C NMR (126 MHz, Chloroform-d)

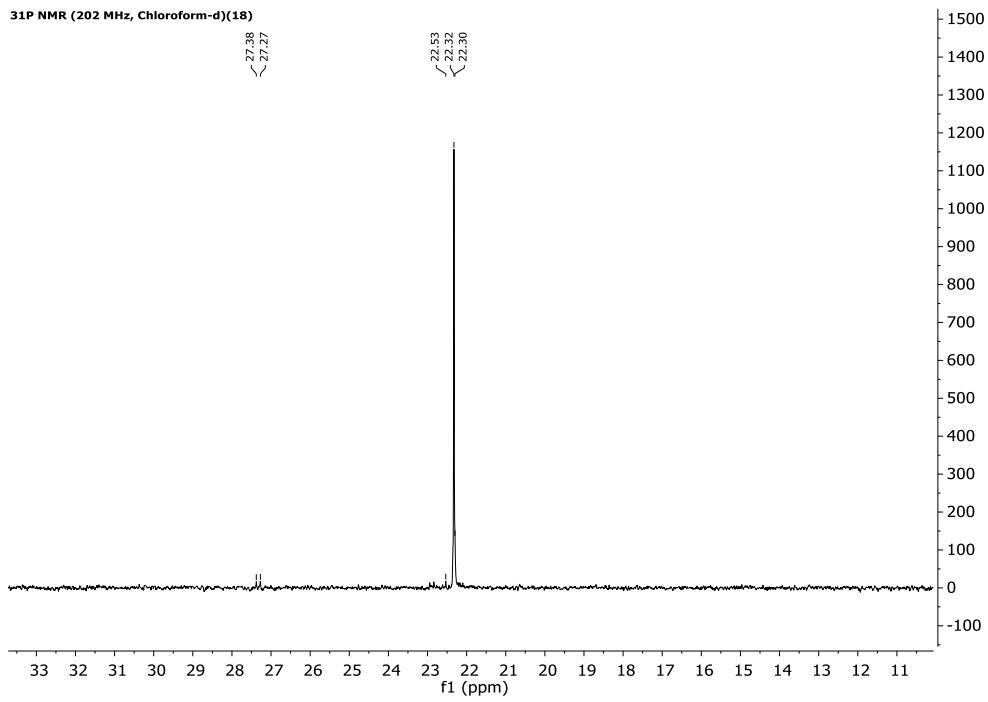


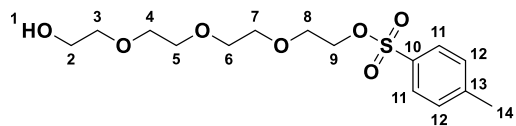


¹H NMR (500 MHz, Chloroform-d)(18)

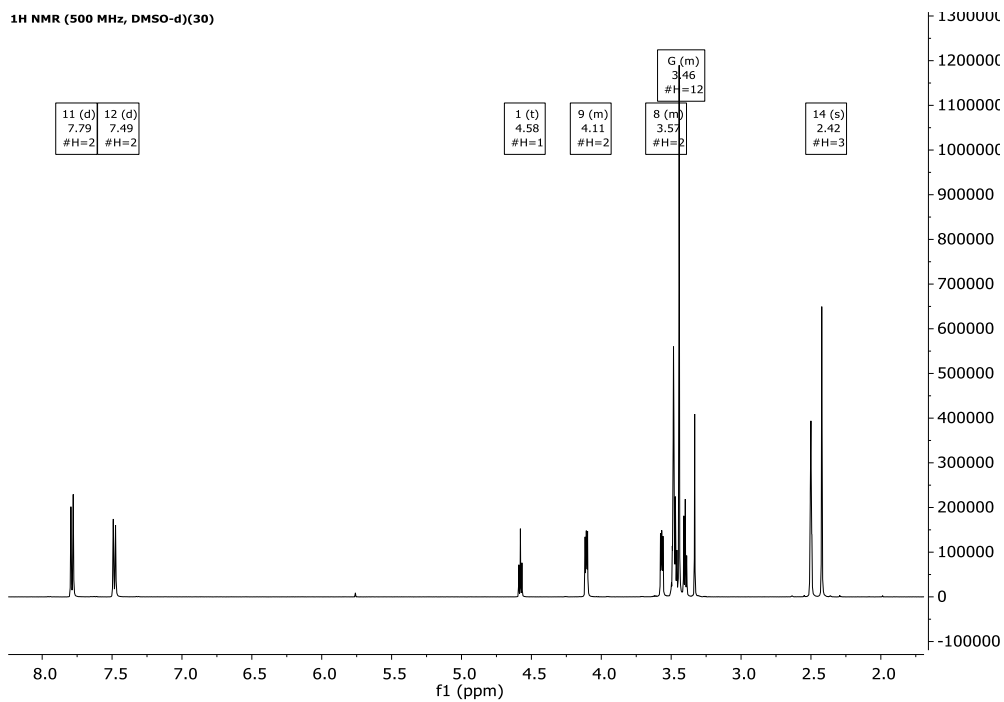


³¹P NMR (202 MHz, Chloroform-d)(18)

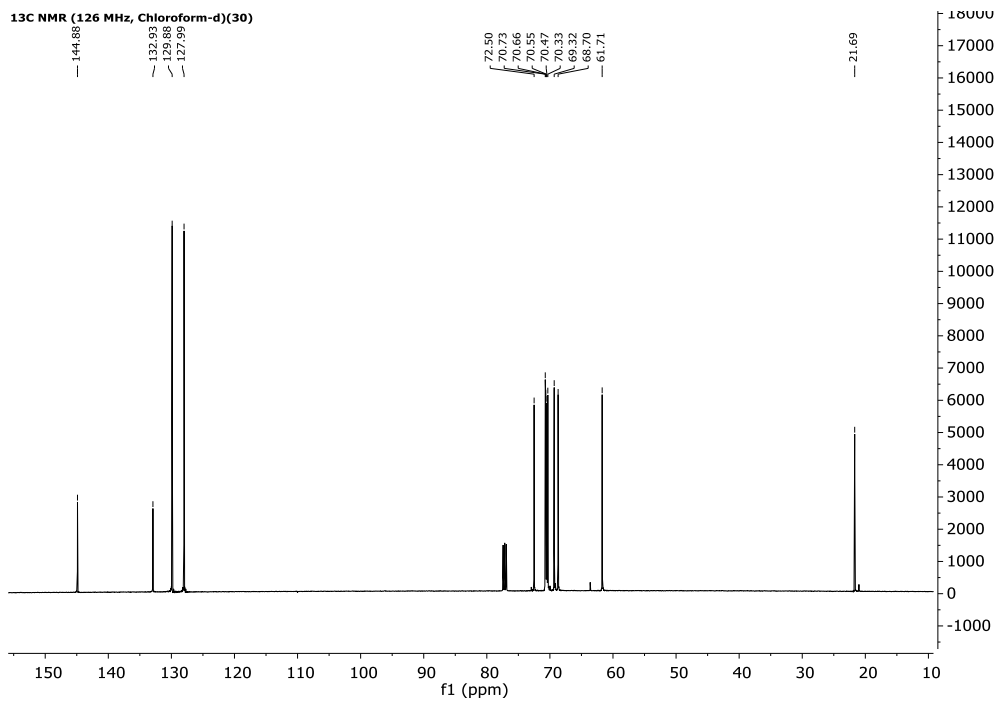


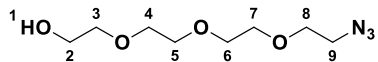


¹H NMR (500 MHz, DMSO-d)(30)

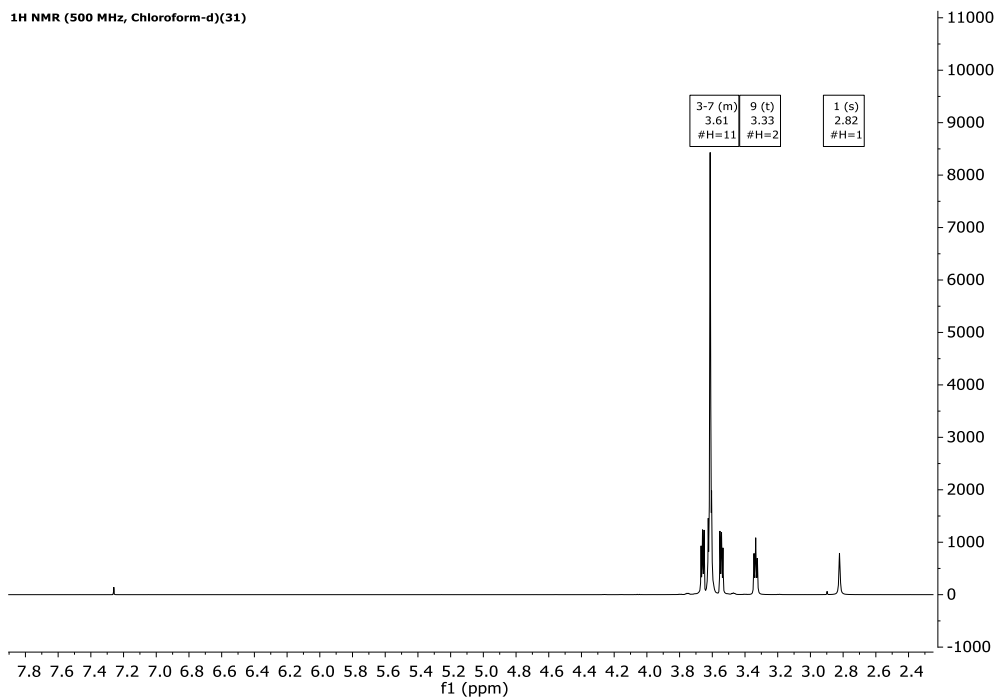


¹³C NMR (126 MHz, Chloroform-d)(30)

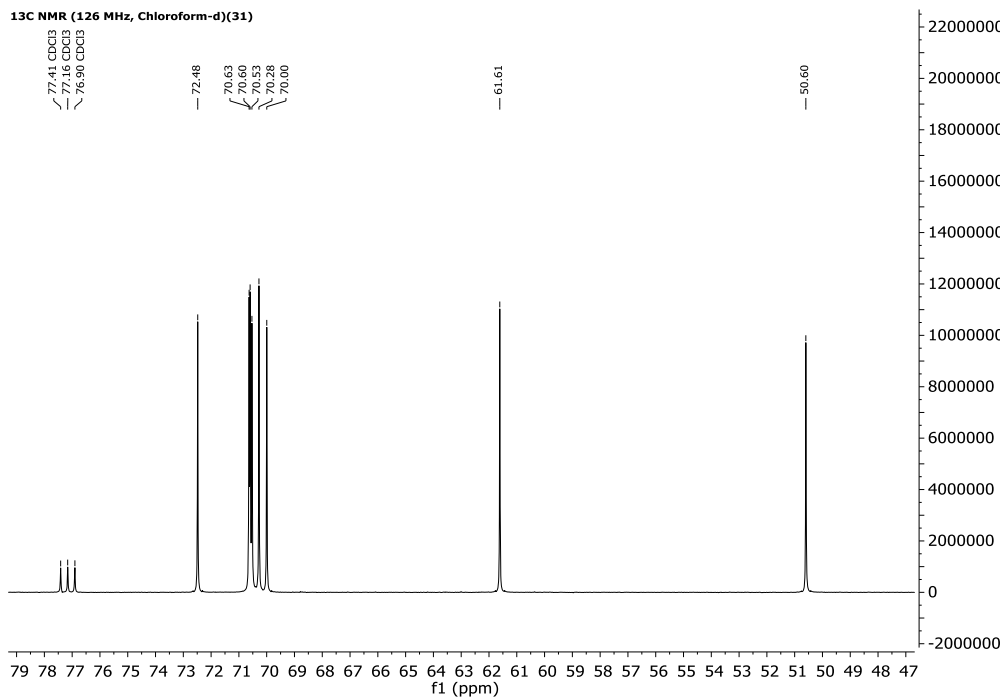


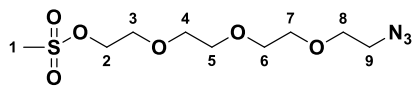


¹H NMR (500 MHz, Chloroform-d)(31)

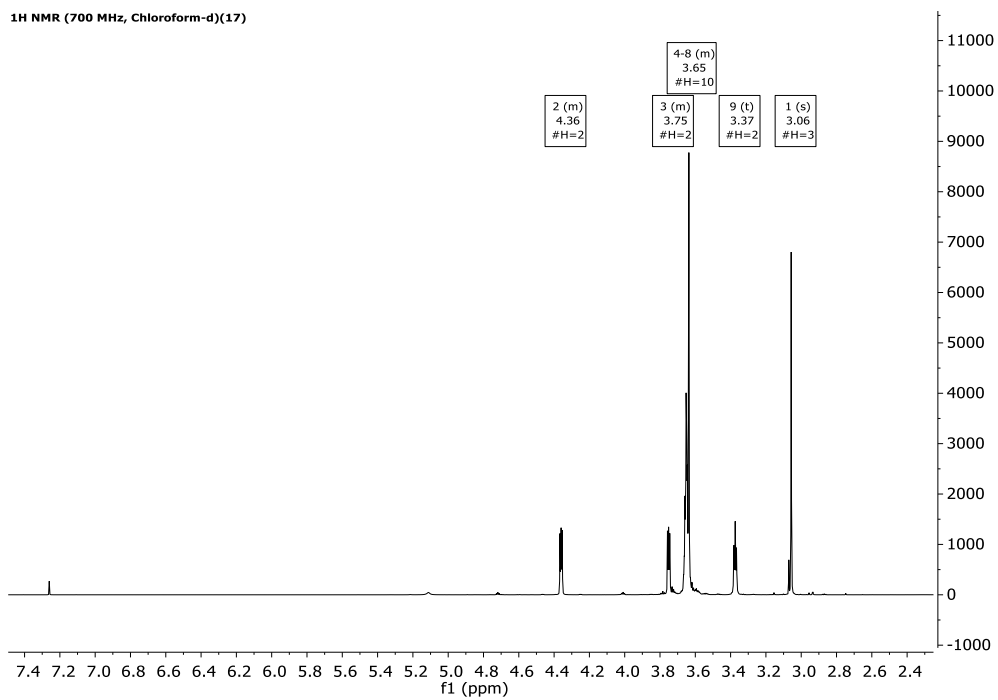


¹³C NMR (126 MHz, Chloroform-d)(31)

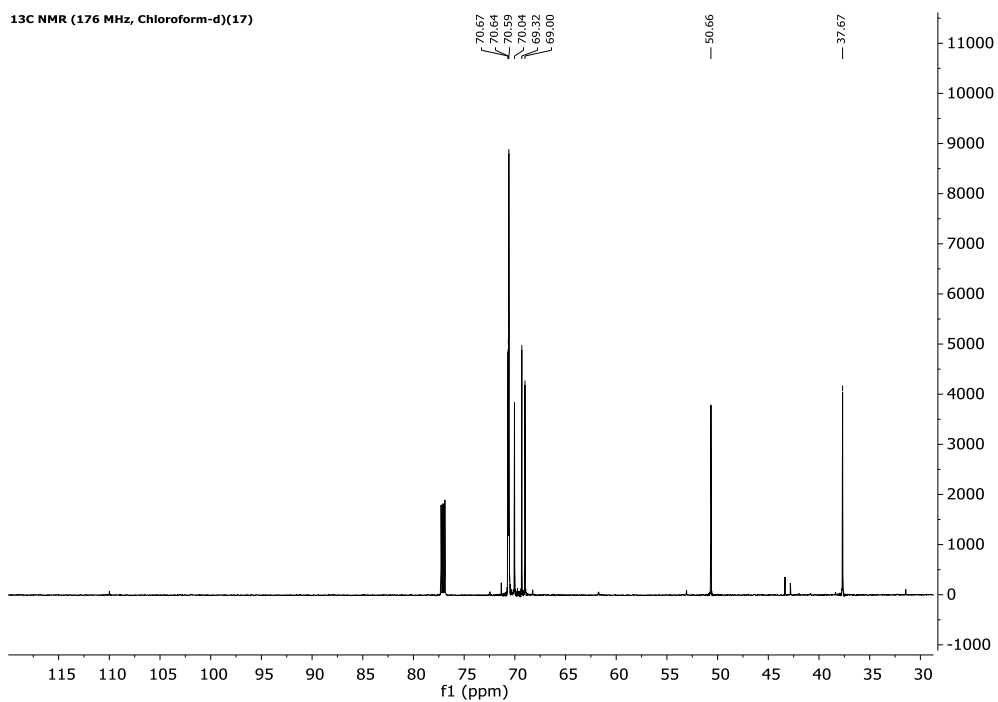


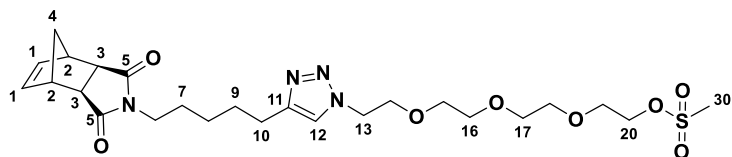


¹H NMR (700 MHz, Chloroform-d)(17)

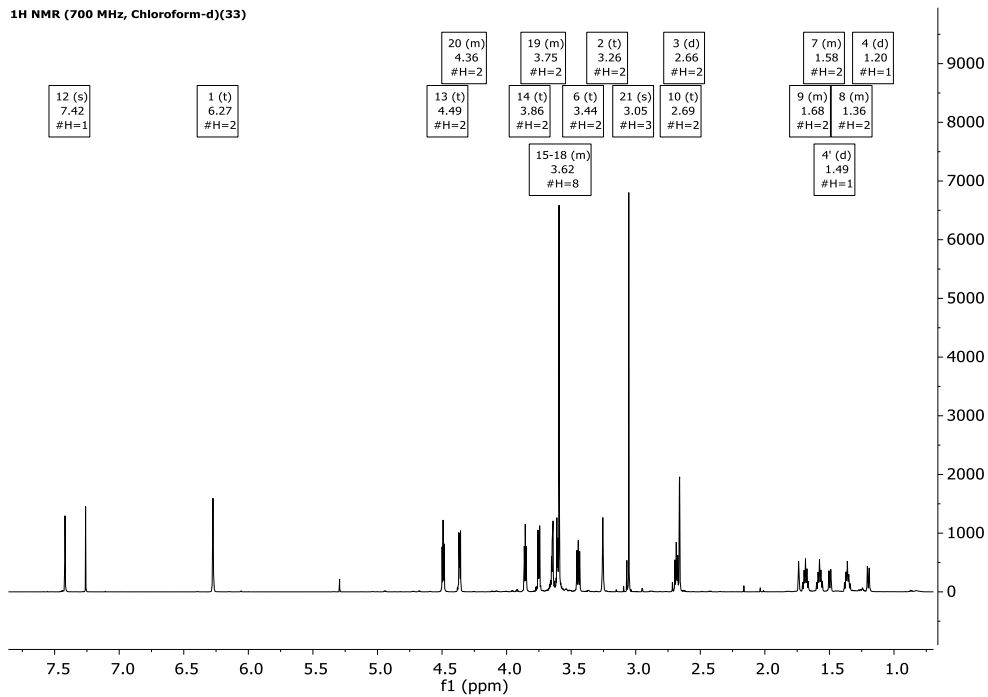


¹³C NMR (176 MHz, Chloroform-d)(17)

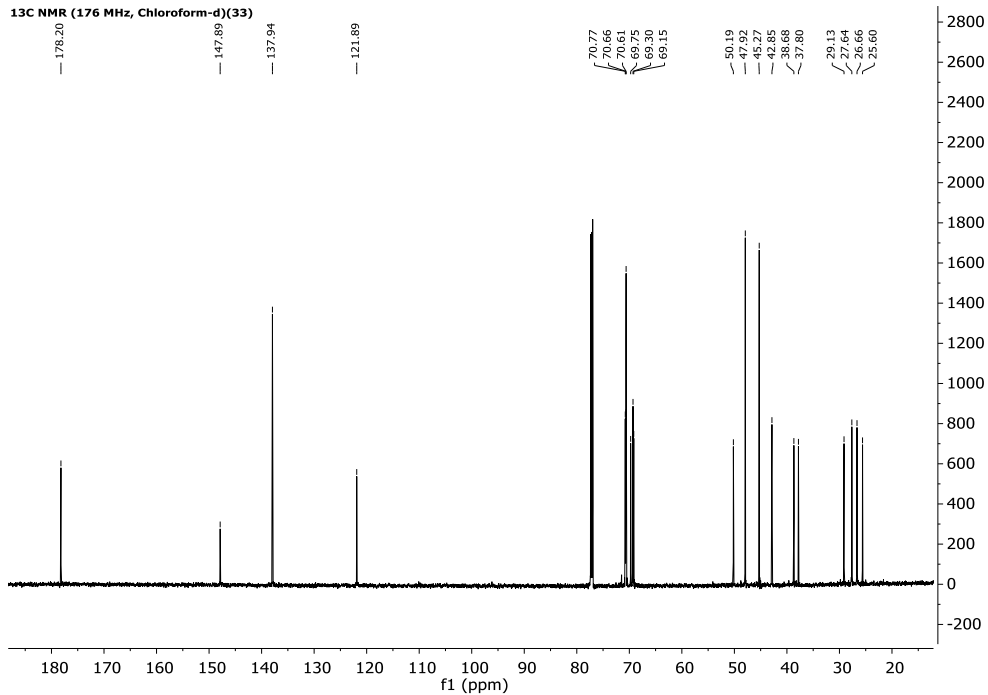


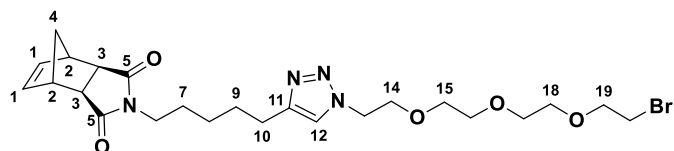


¹H NMR (700 MHz, Chloroform-d)(33)

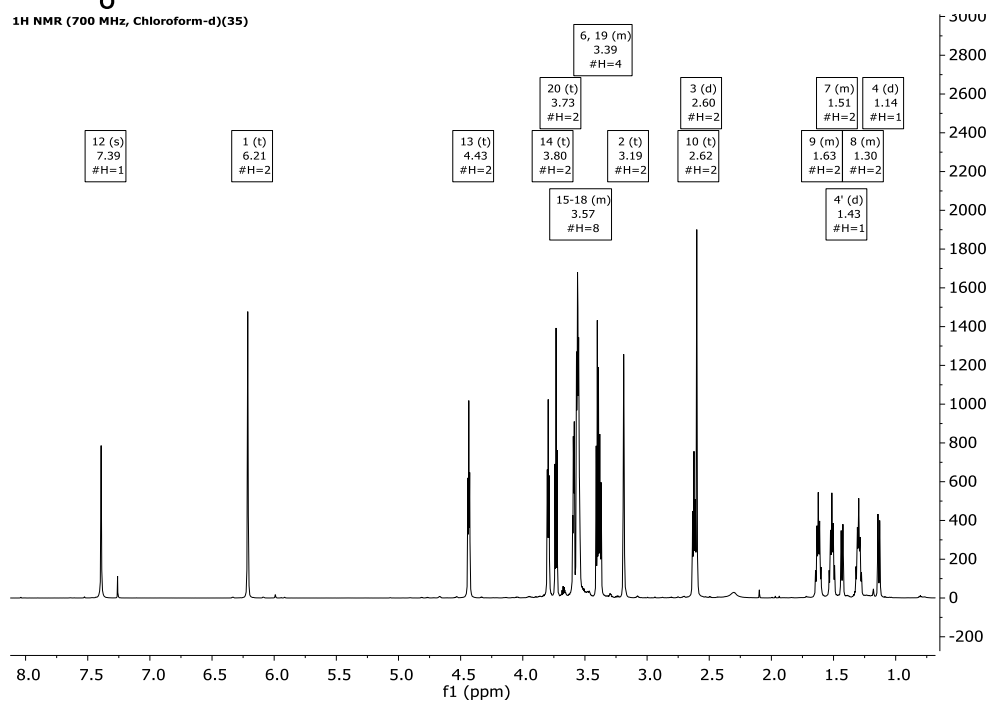


¹³C NMR (176 MHz, Chloroform-d)(33)

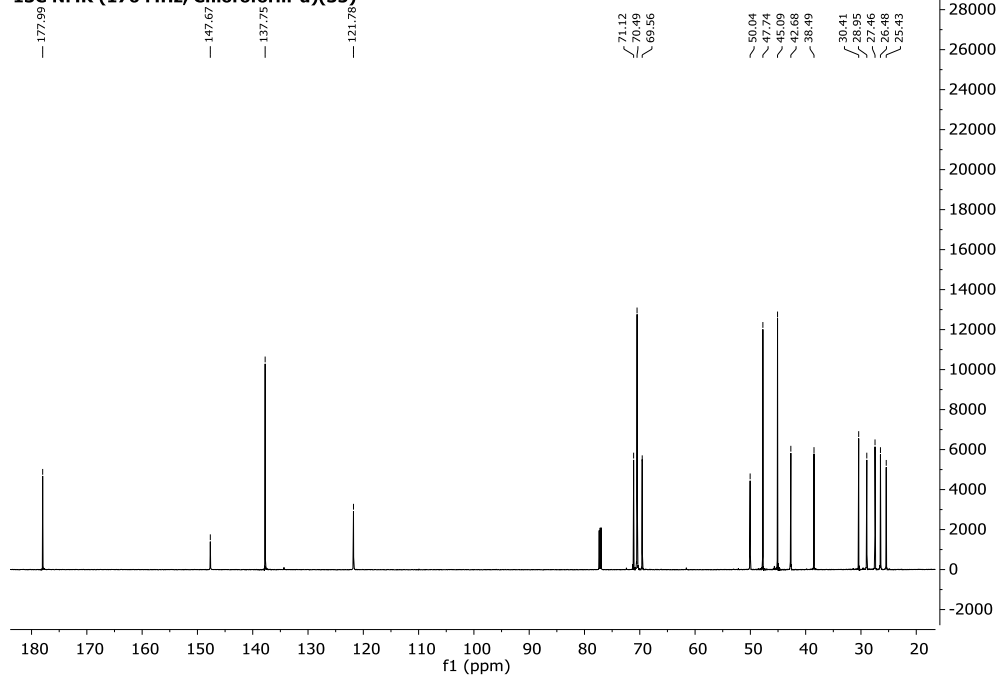


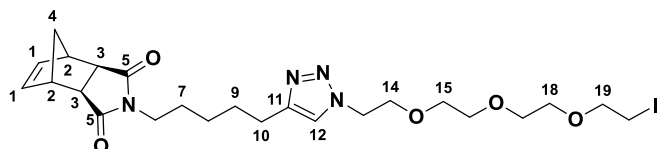


¹H NMR (700 MHz, Chloroform-d)(35)

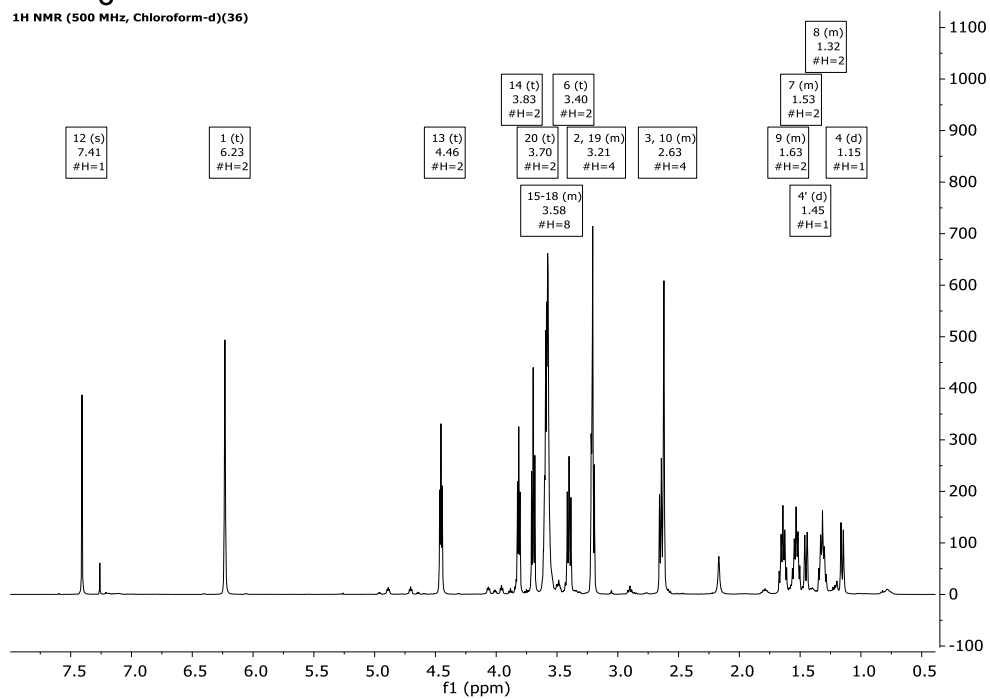


¹³C NMR (176 MHz, Chloroform-d)(35)

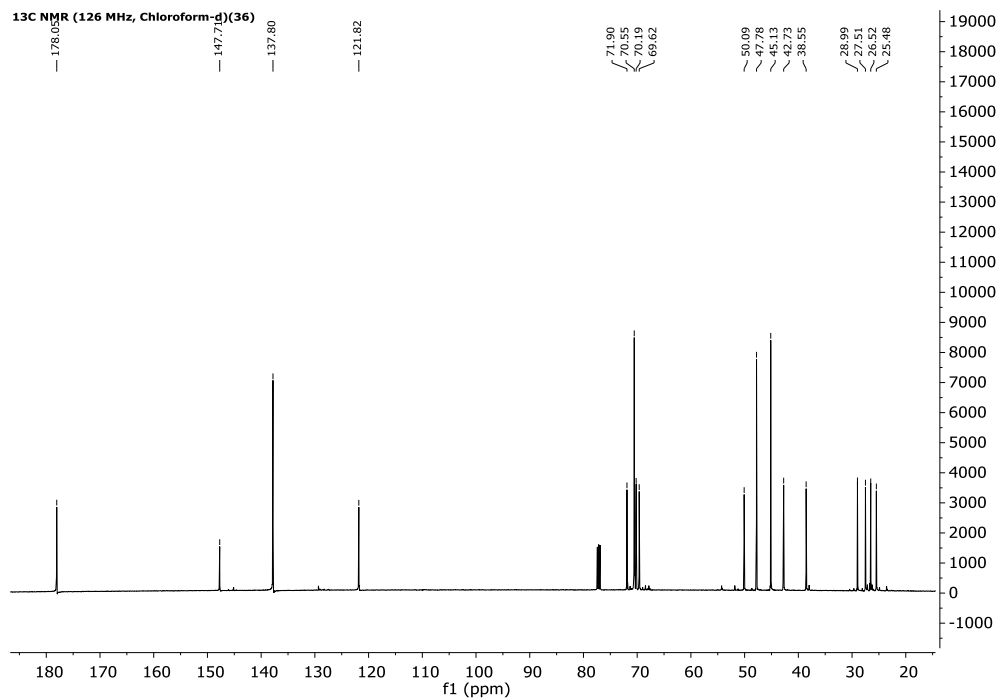


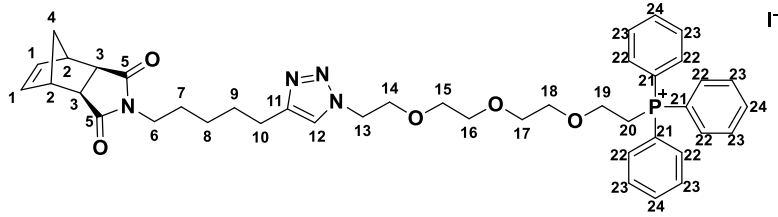


¹H NMR (500 MHz, Chloroform-d)(36)

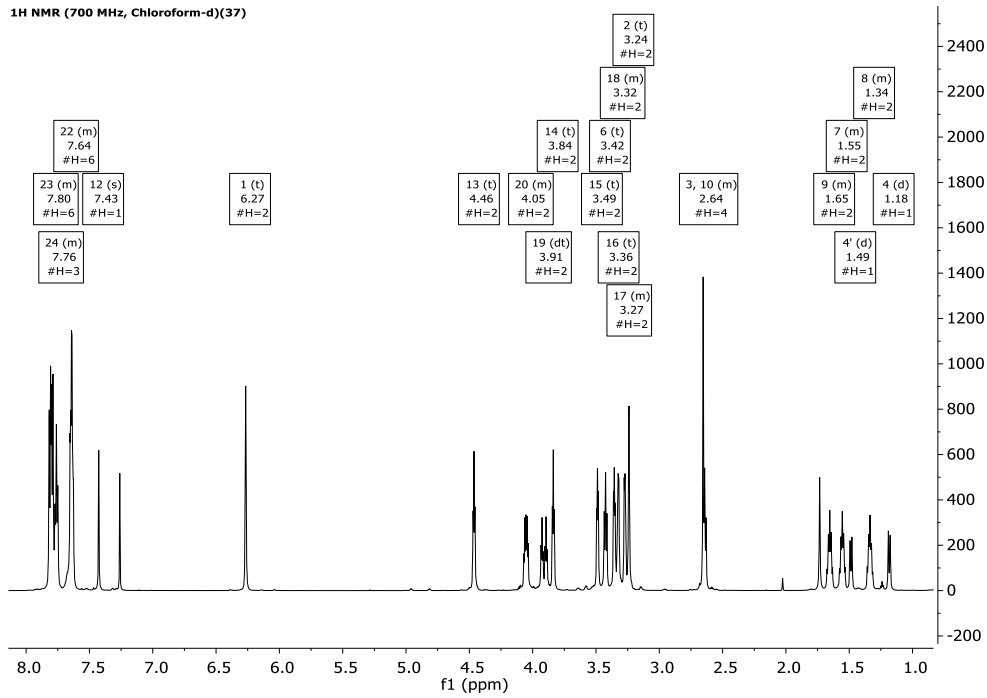


¹³C NMR (126 MHz, Chloroform-d)(36)

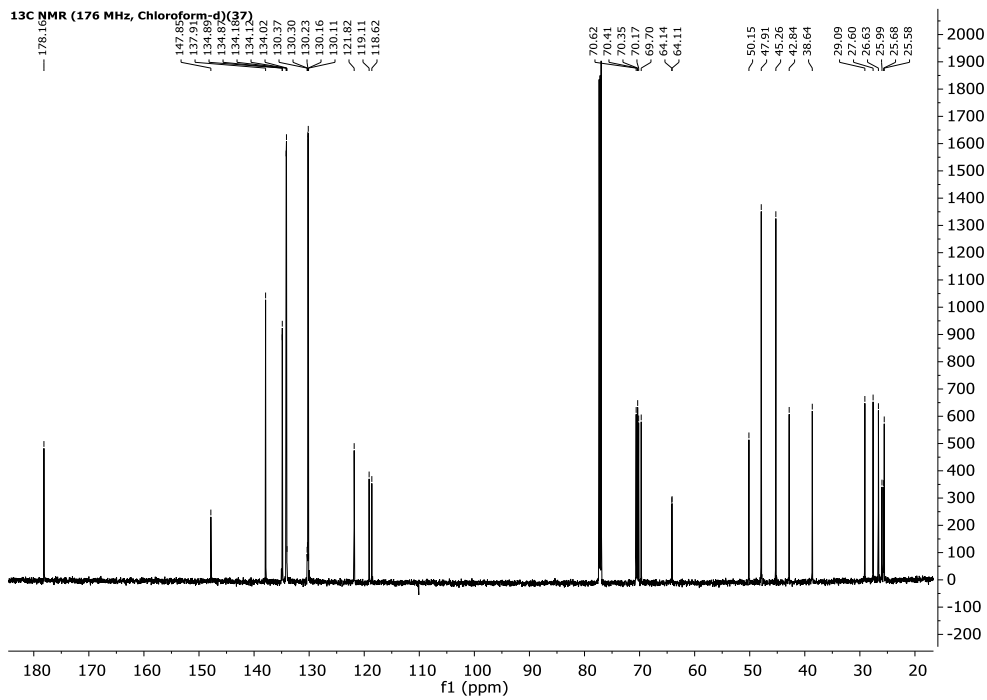




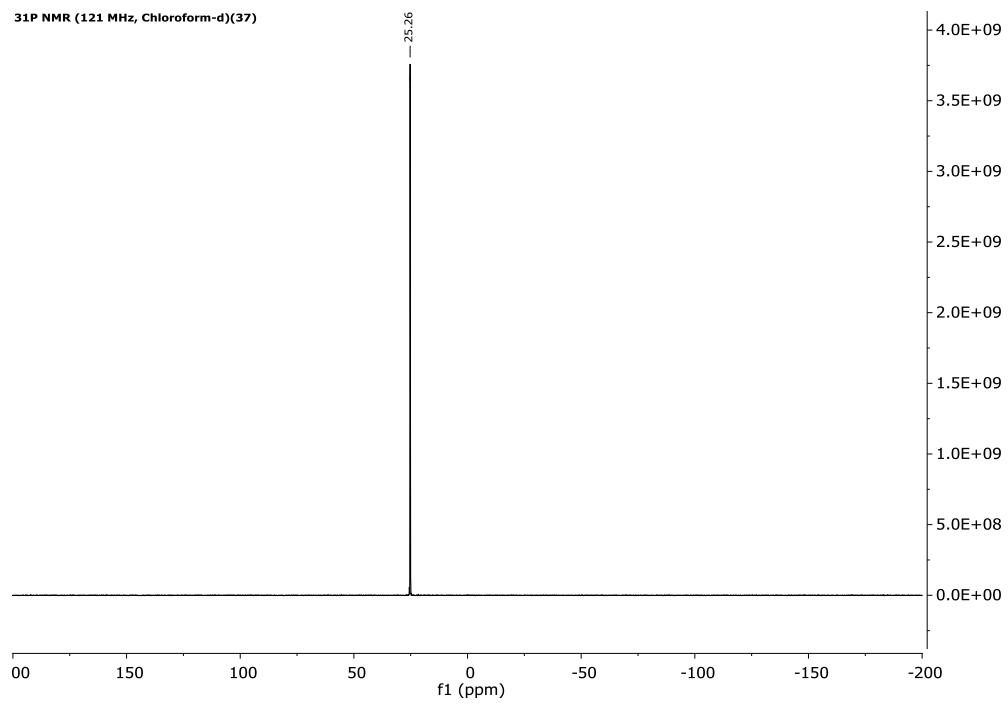
¹H NMR (700 MHz, Chloroform-d)(37)

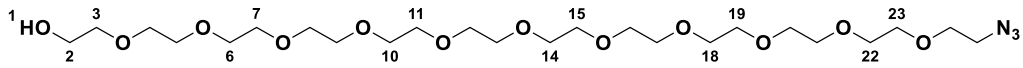


¹³C NMR (176 MHz, Chloroform-d)(37)

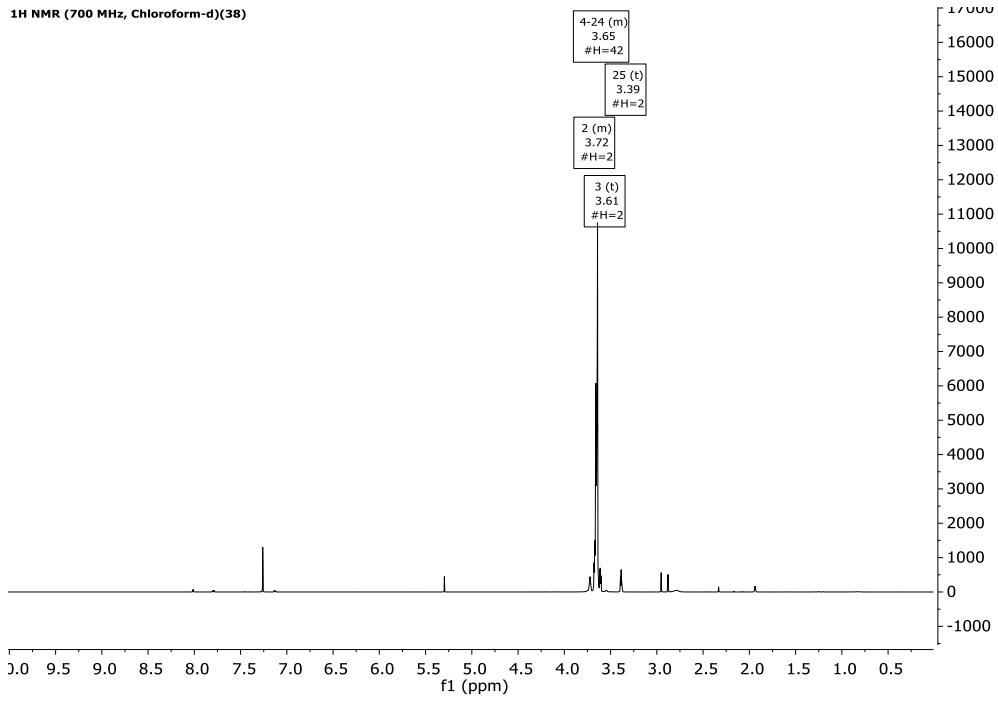


31P NMR (121 MHz, Chloroform-d)(37)

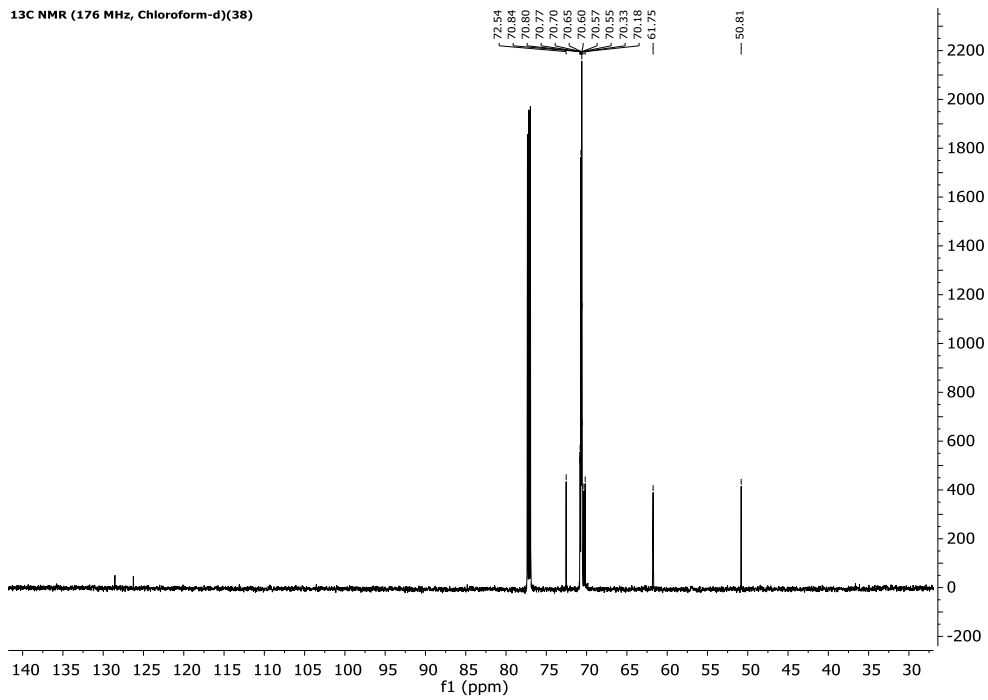


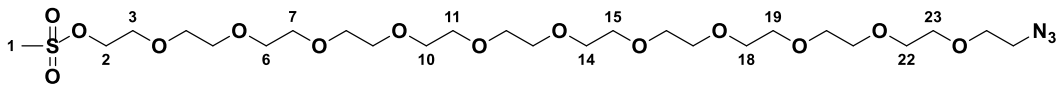


¹H NMR (700 MHz, Chloroform-d)(38)

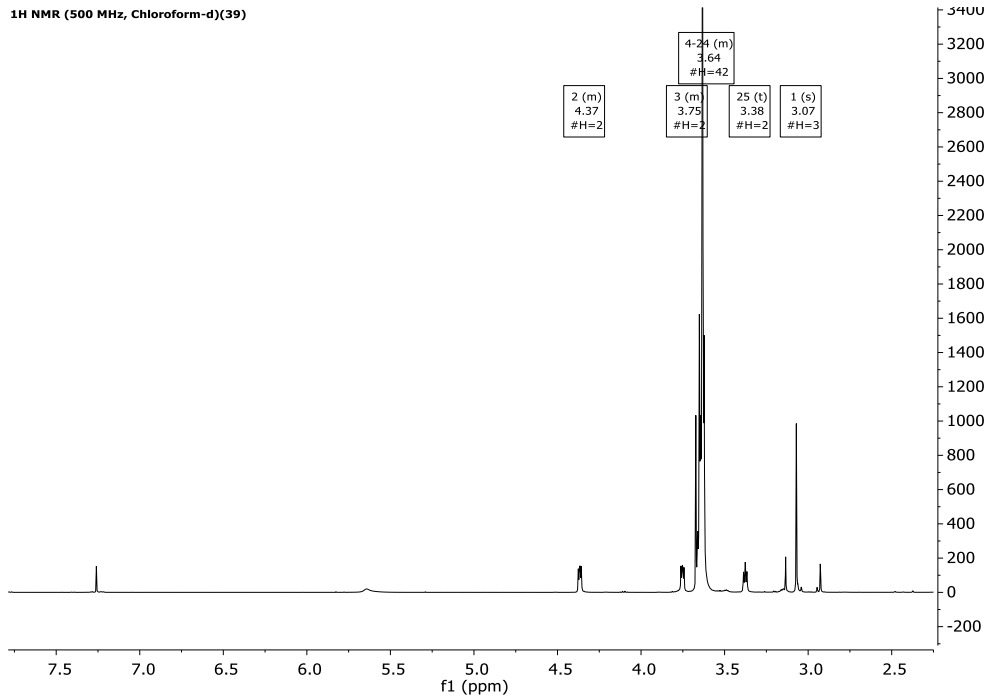


¹³C NMR (176 MHz, Chloroform-d)(38)

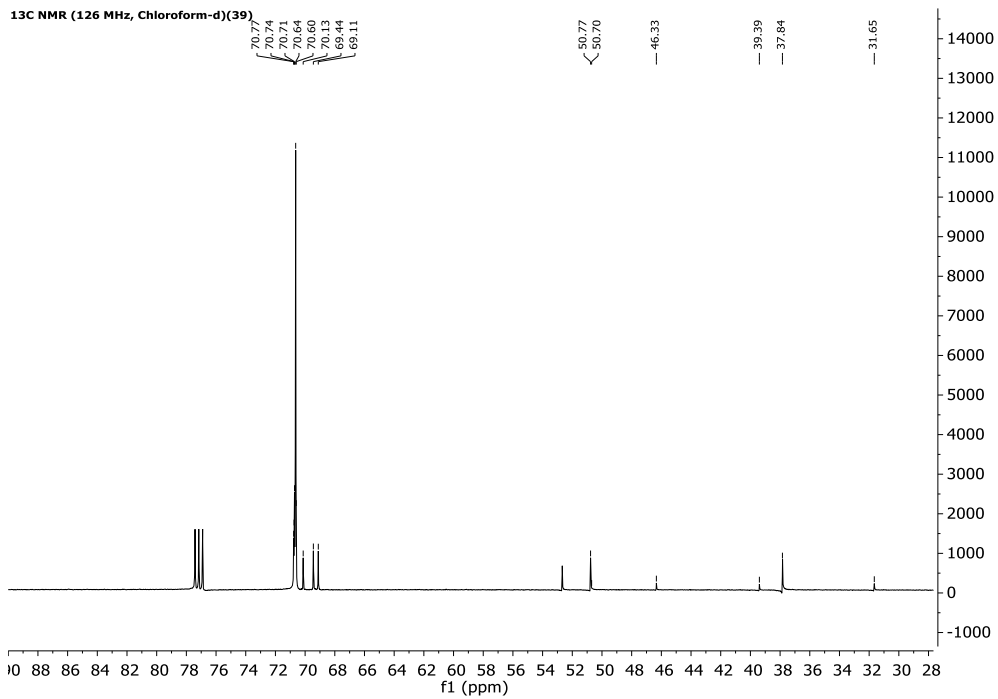


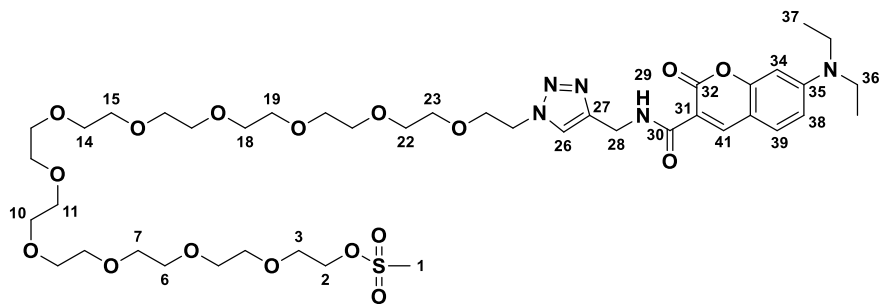


¹H NMR (500 MHz, Chloroform-d)(39)

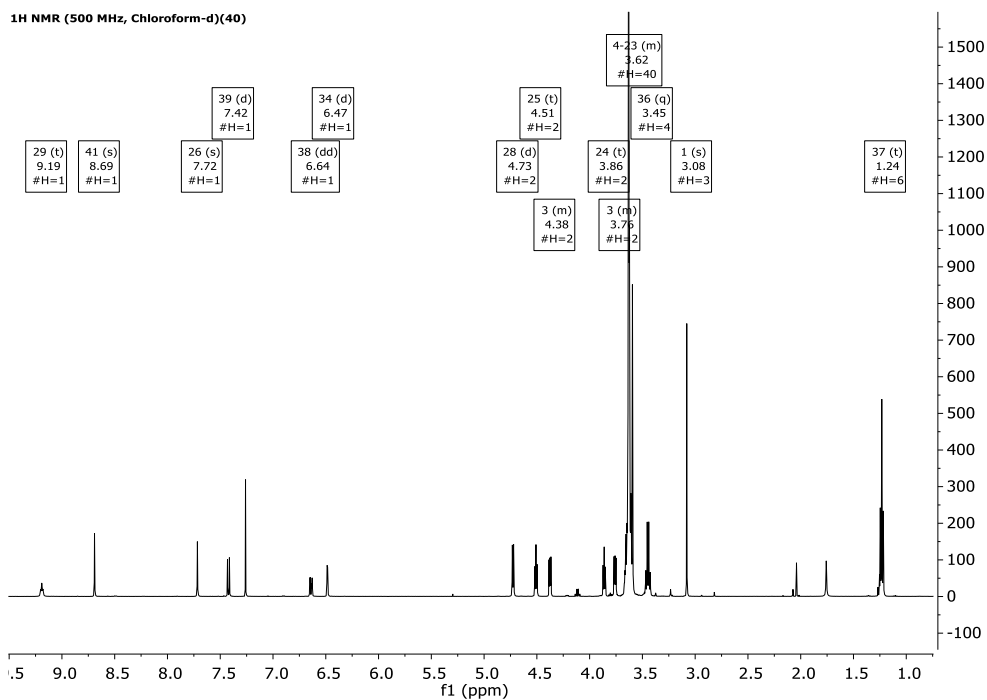


¹³C NMR (126 MHz, Chloroform-d)(39)

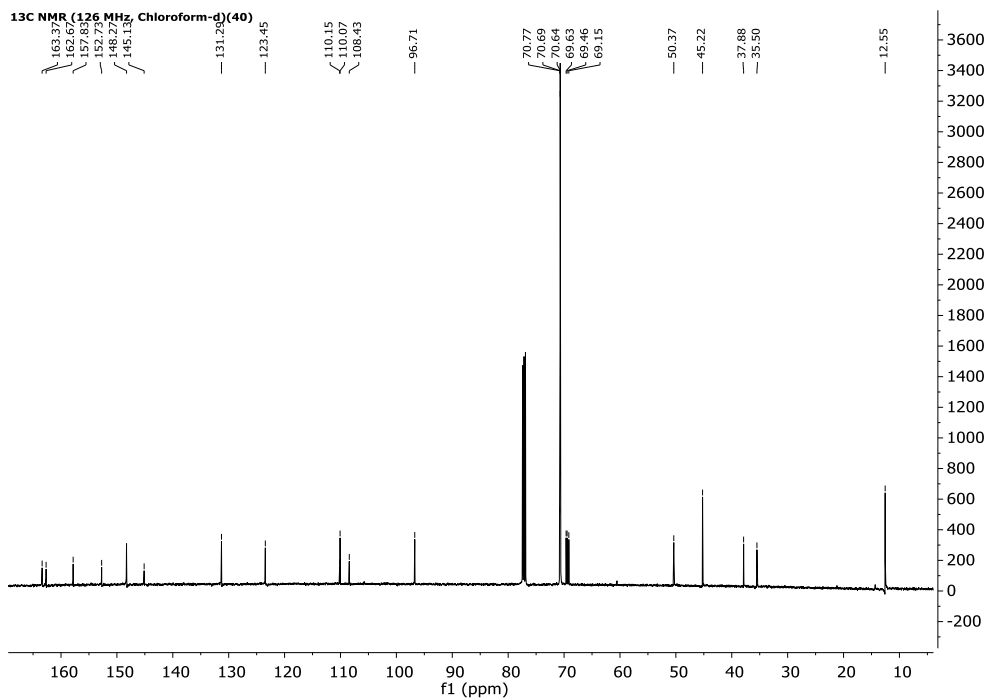


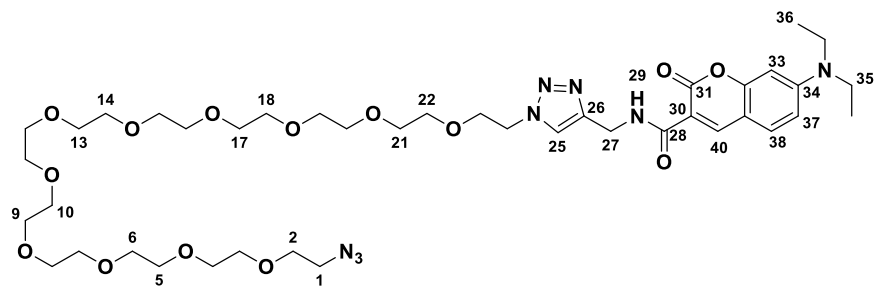


¹H NMR (500 MHz, Chloroform-d)(40)

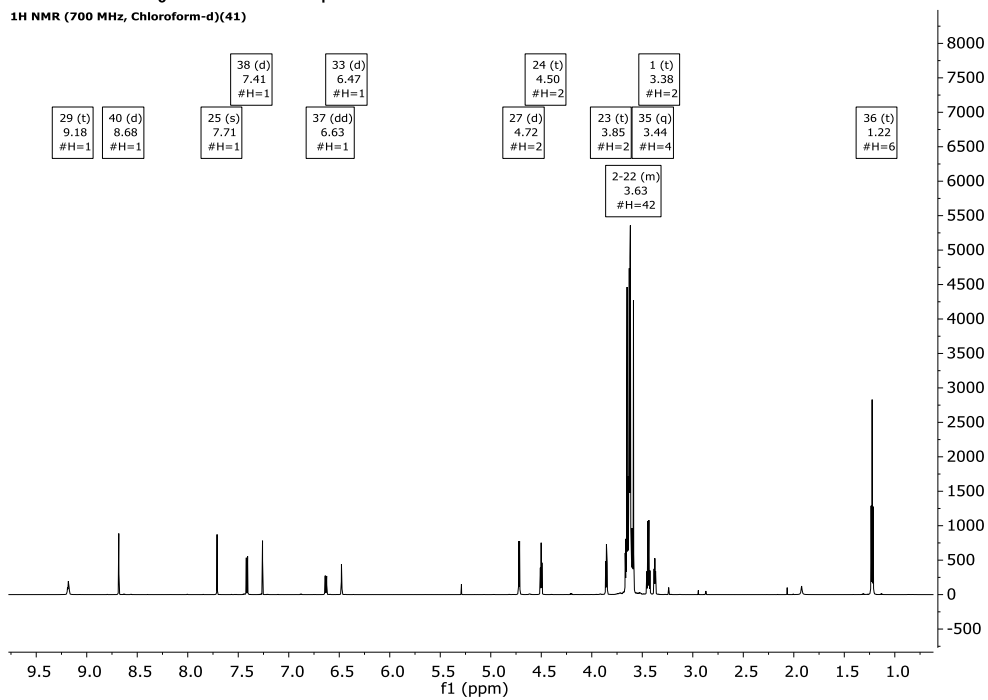


¹³C NMR (126 MHz, Chloroform-d)(40)

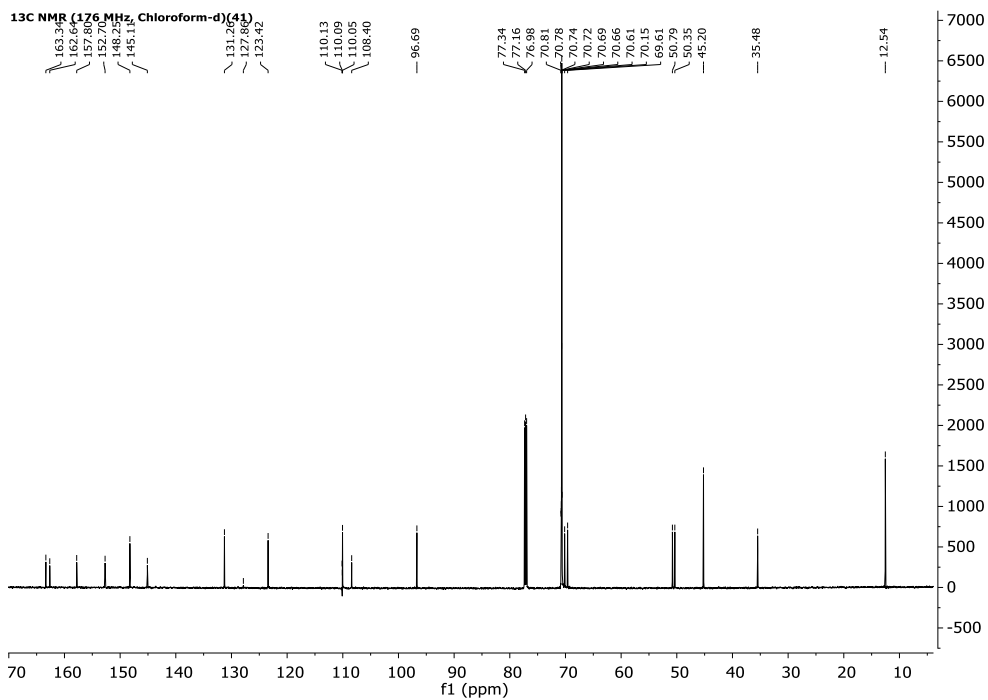


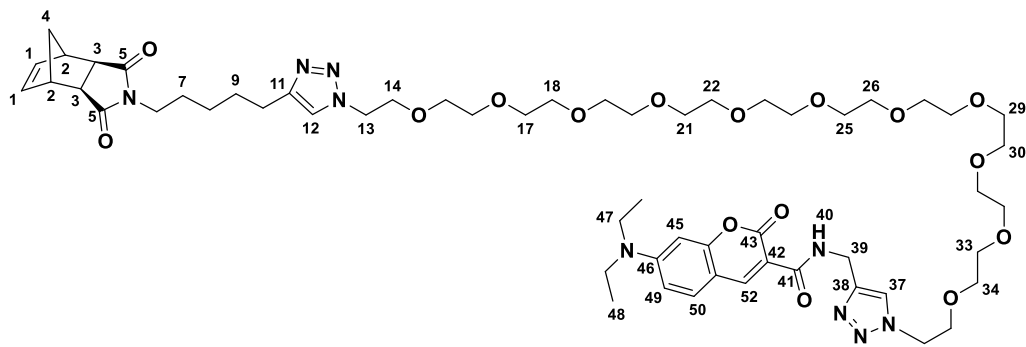


¹H NMR (700 MHz, Chloroform-d)(41)

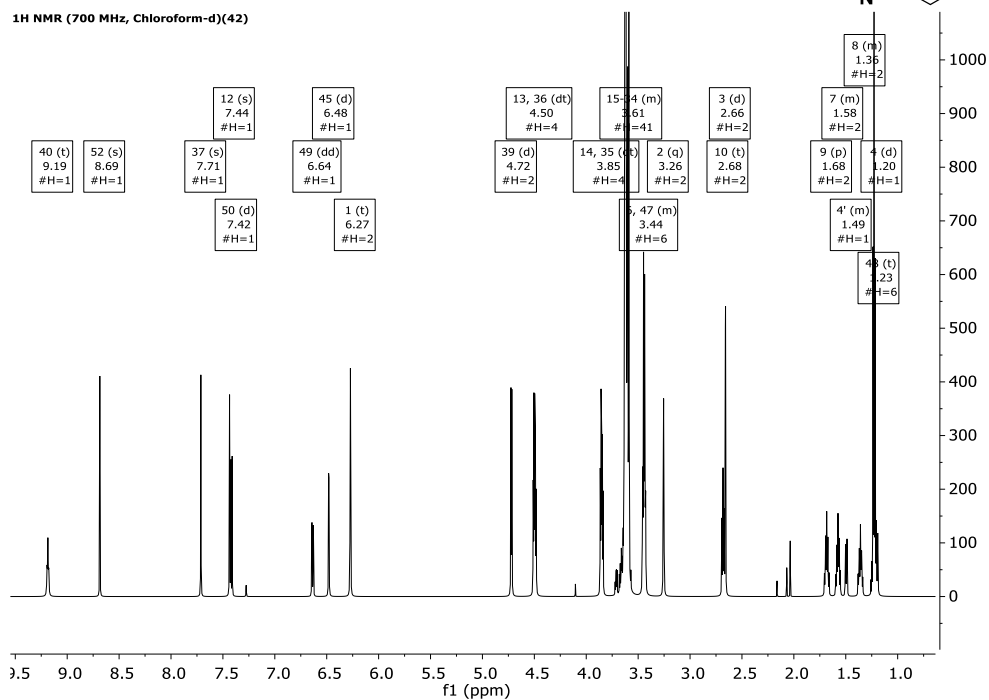


¹³C NMR (176 MHz, Chloroform-d)(41)

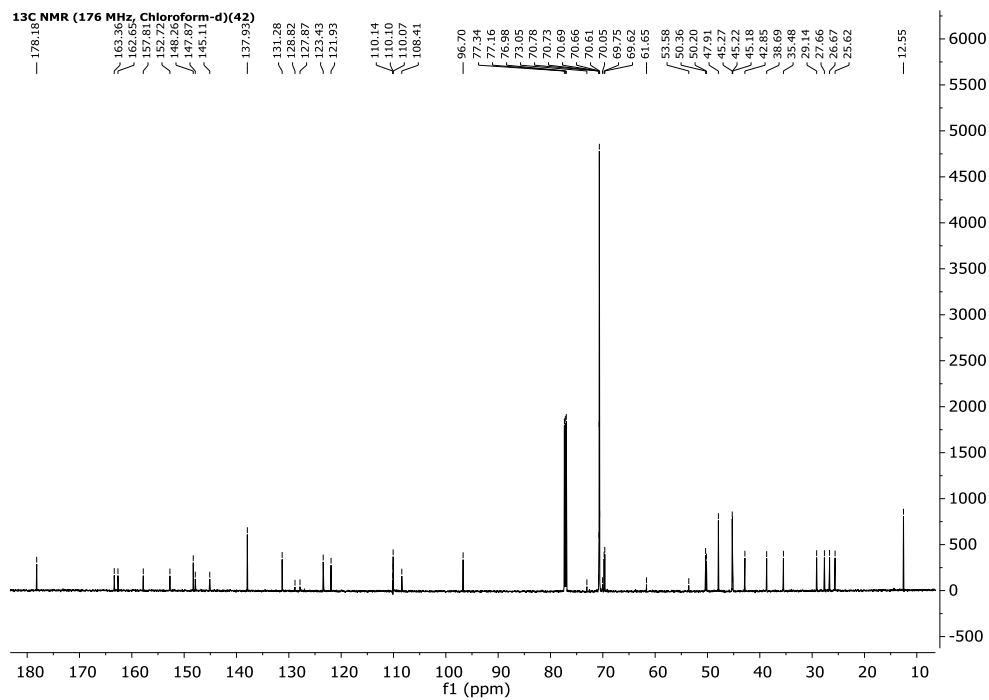


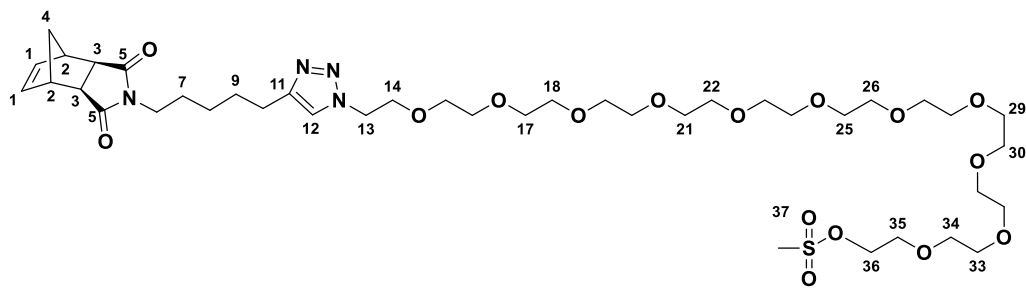


¹H NMR (700 MHz, Chloroform-d)(42)

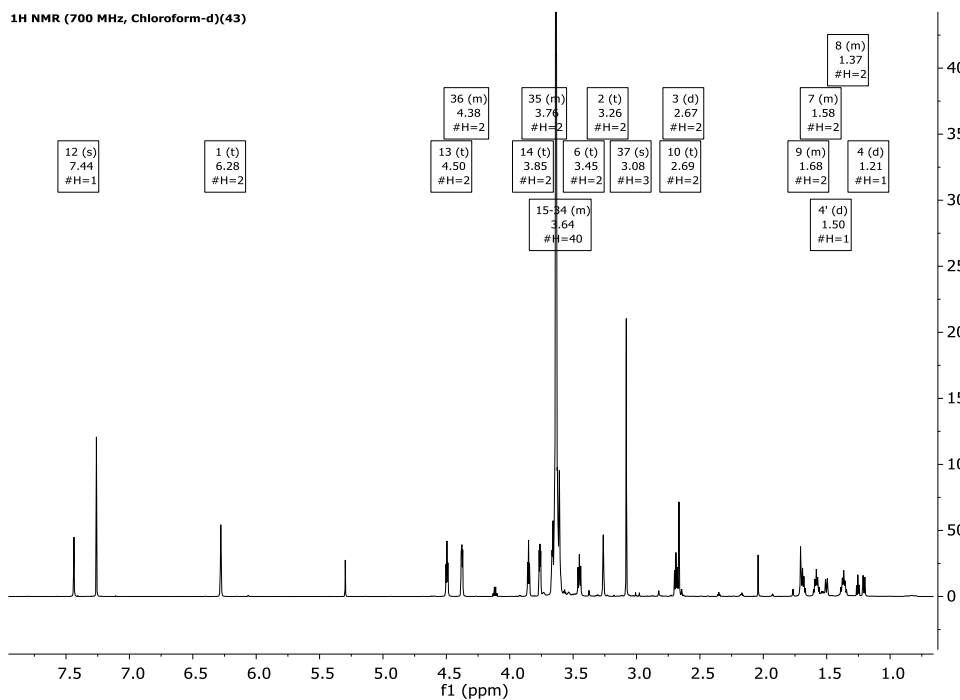


¹³C NMR (176 MHz, Chloroform-d)(42)

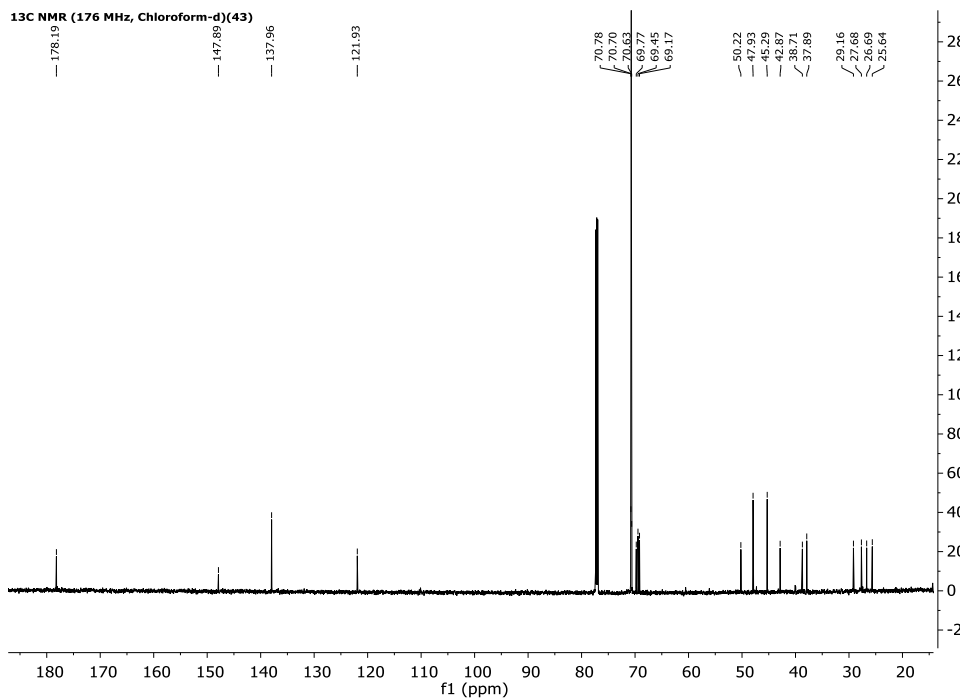


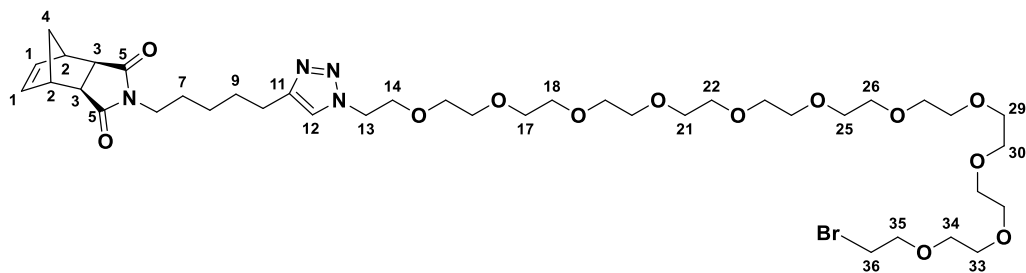


¹H NMR (700 MHz, Chloroform-d)(43)

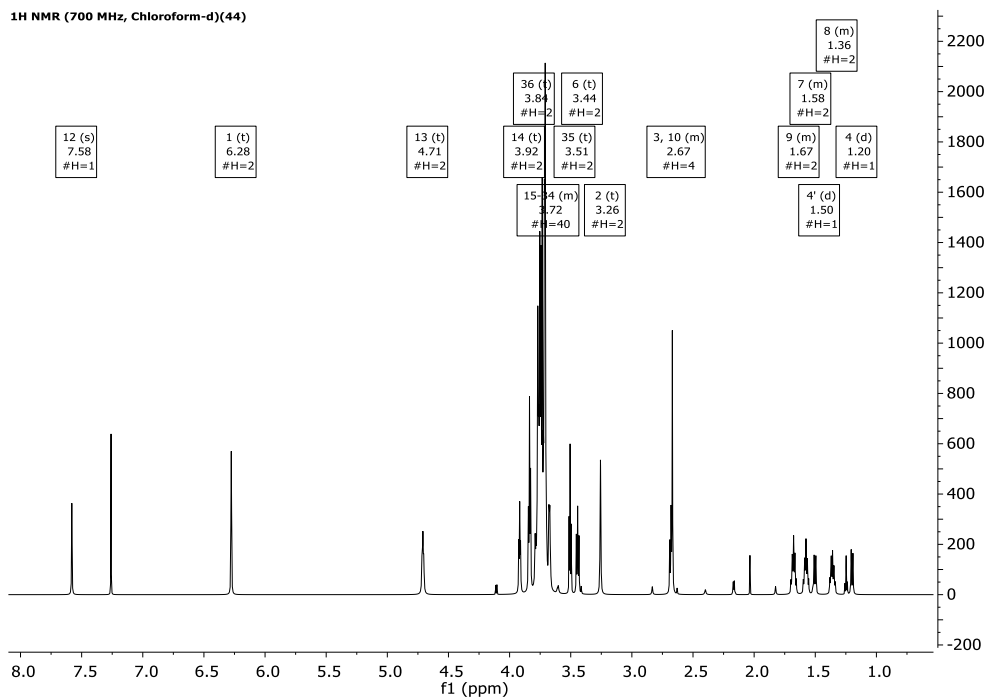


¹³C NMR (176 MHz, Chloroform-d)(43)

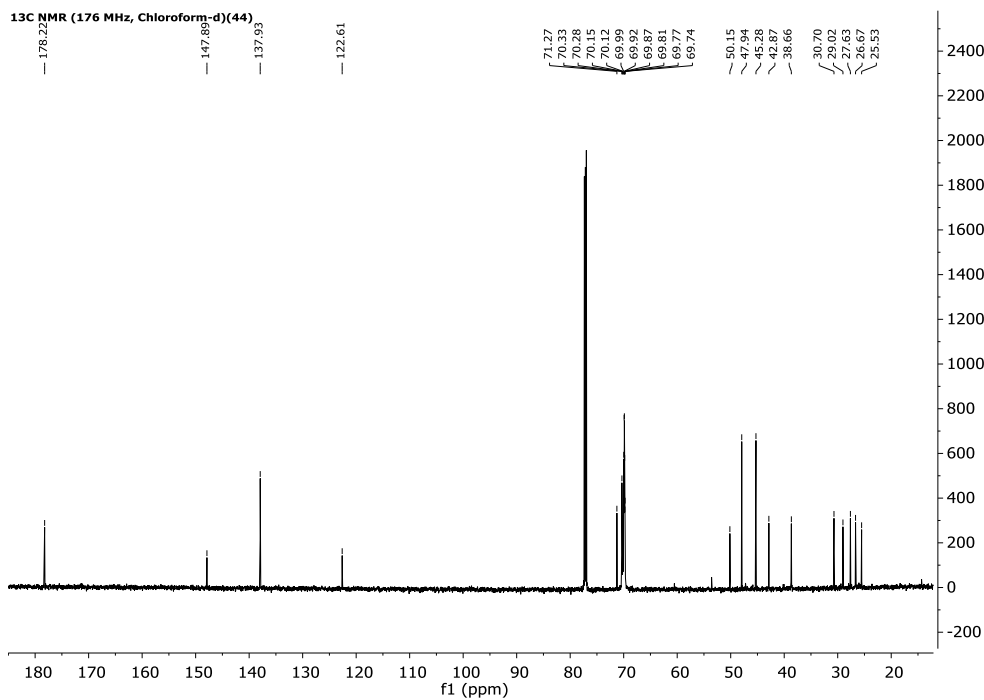


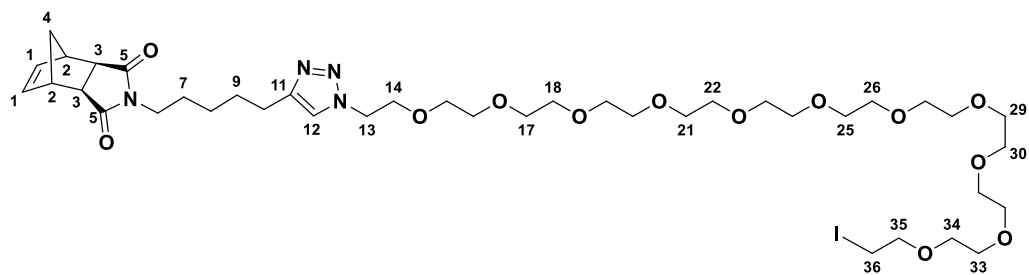


¹H NMR (700 MHz, Chloroform-d)(44)

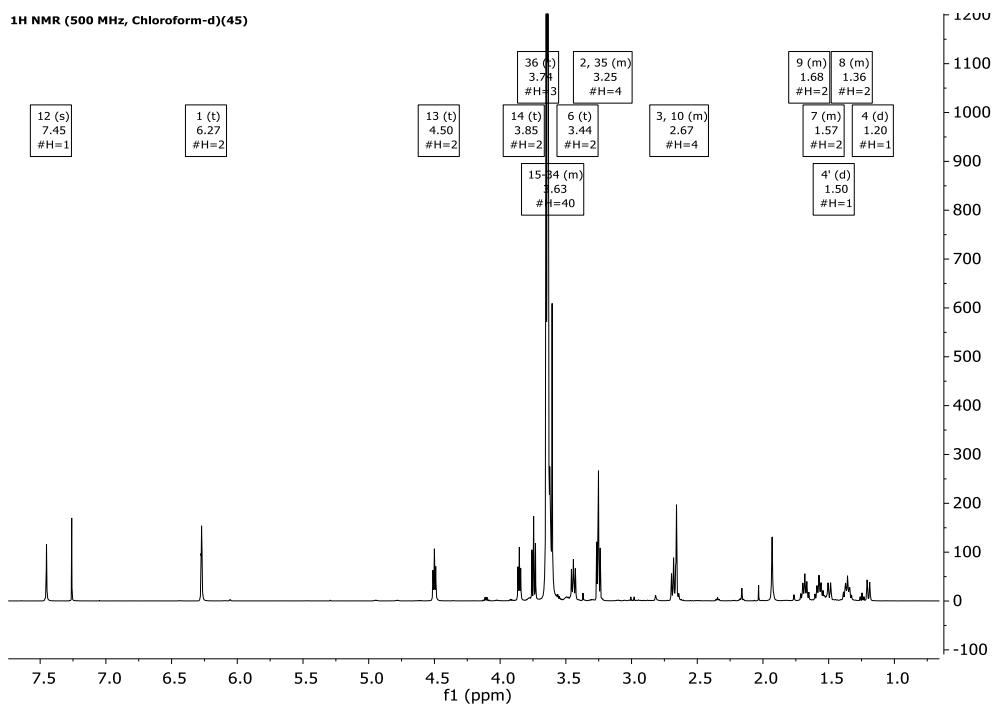


¹³C NMR (176 MHz, Chloroform-d)(44)

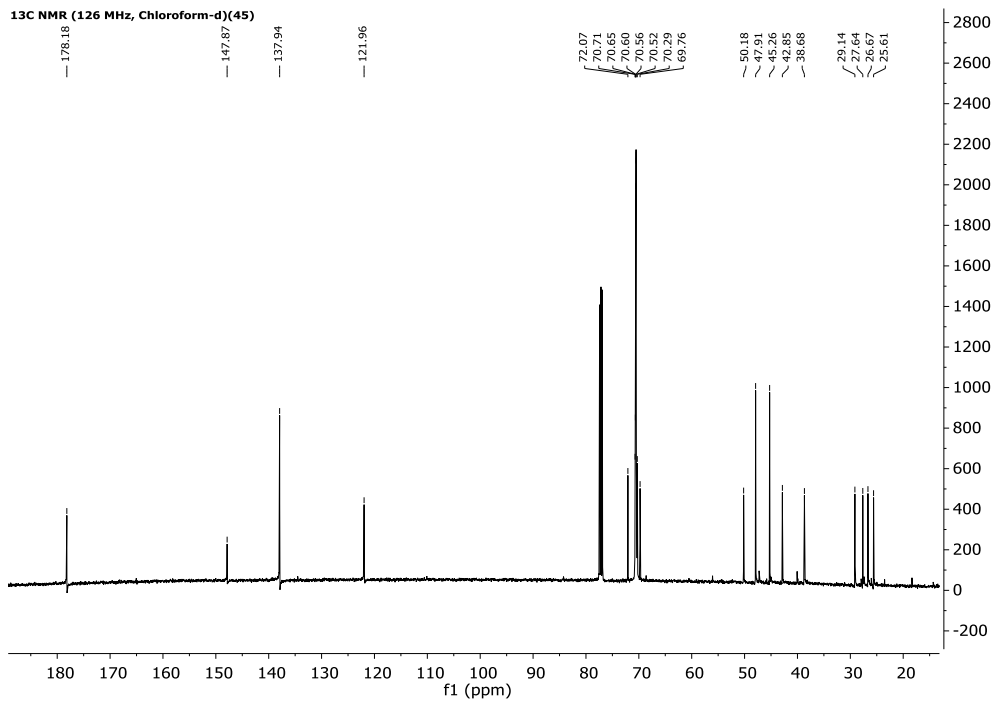


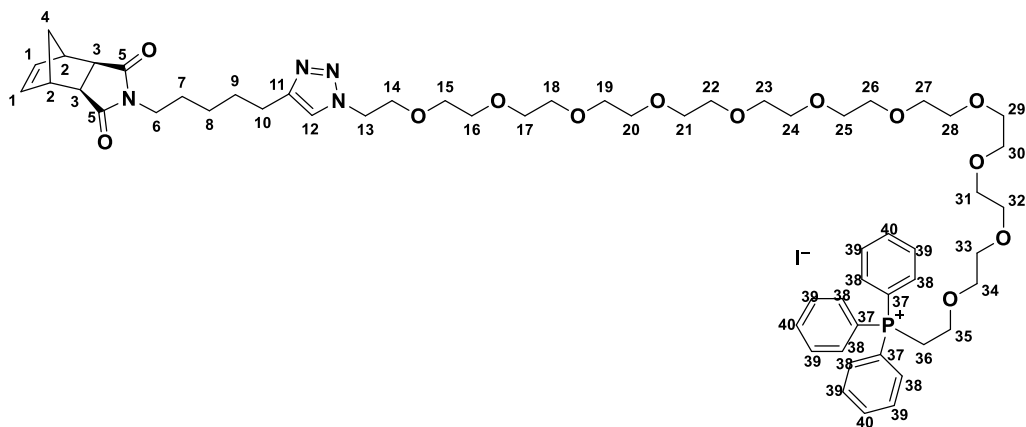


¹H NMR (500 MHz, Chloroform-d)(45)

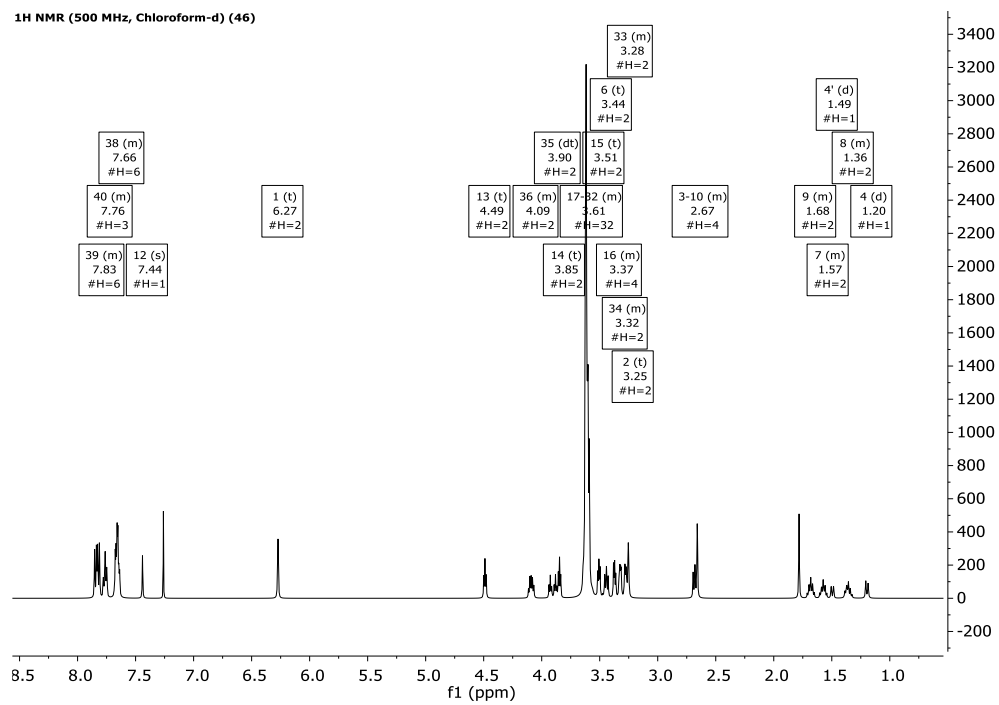


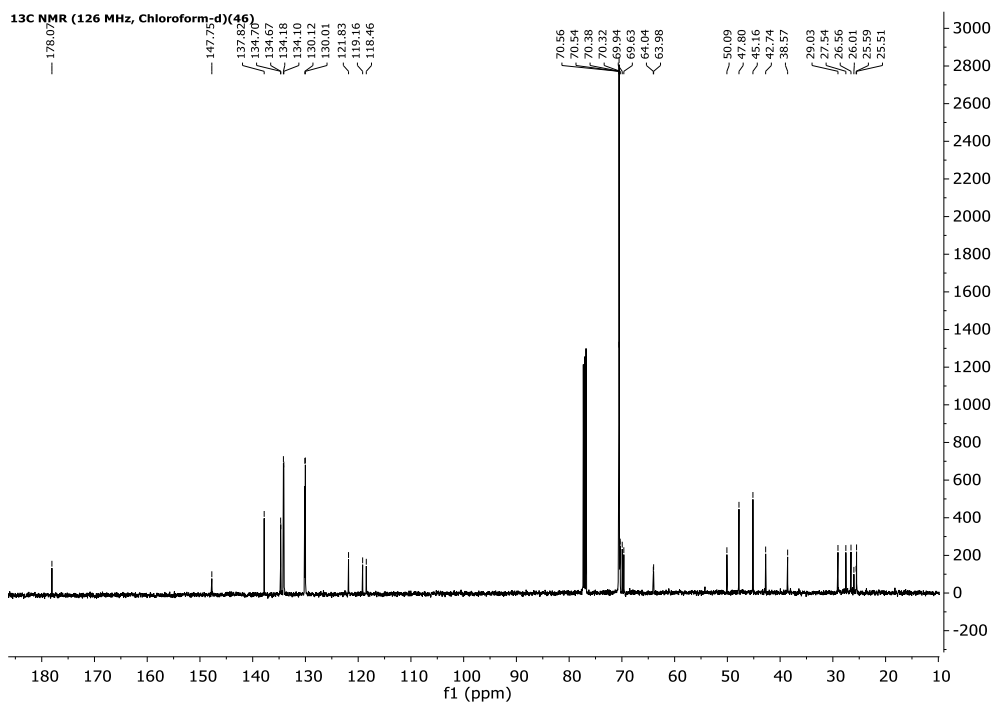
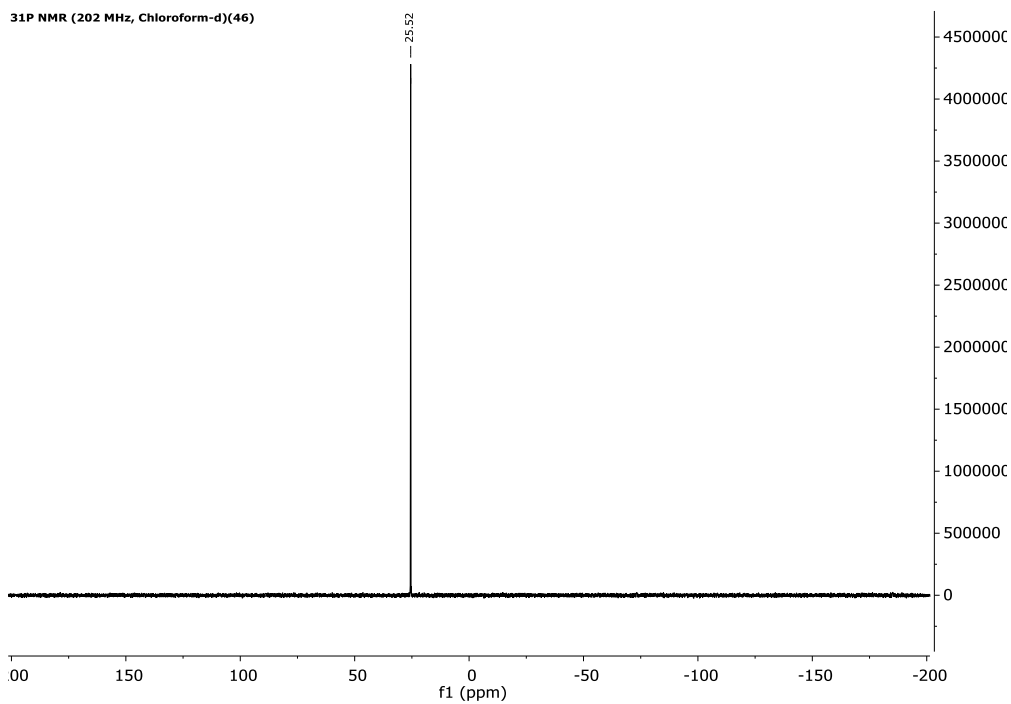
¹³C NMR (126 MHz, Chloroform-d)(45)

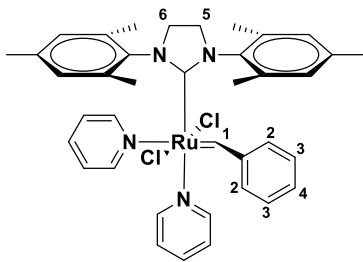




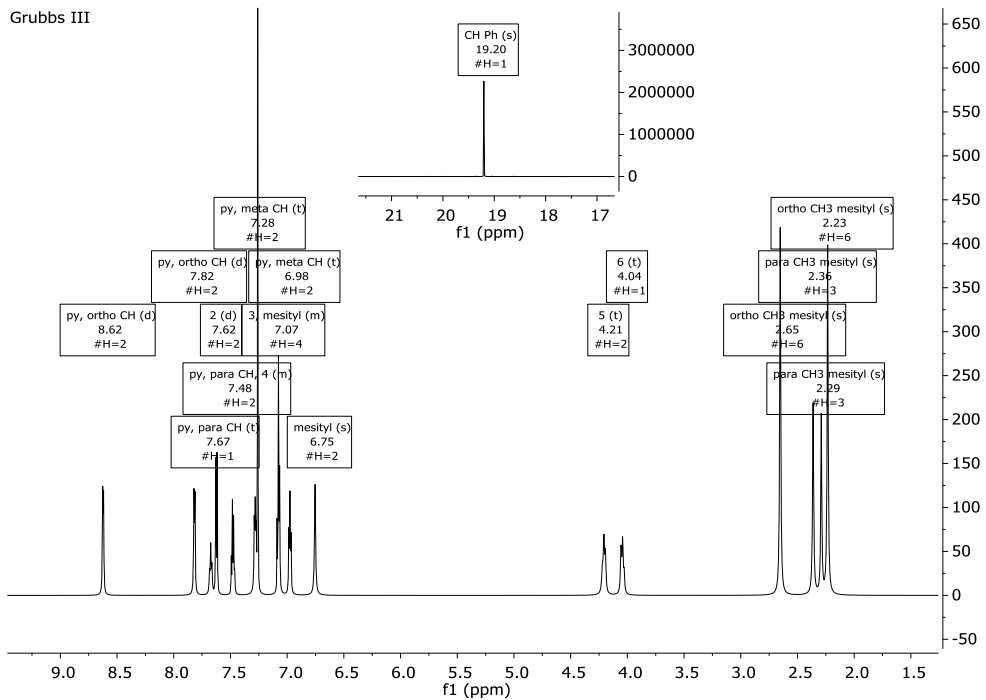
¹H NMR (500 MHz, Chloroform-d) (46)

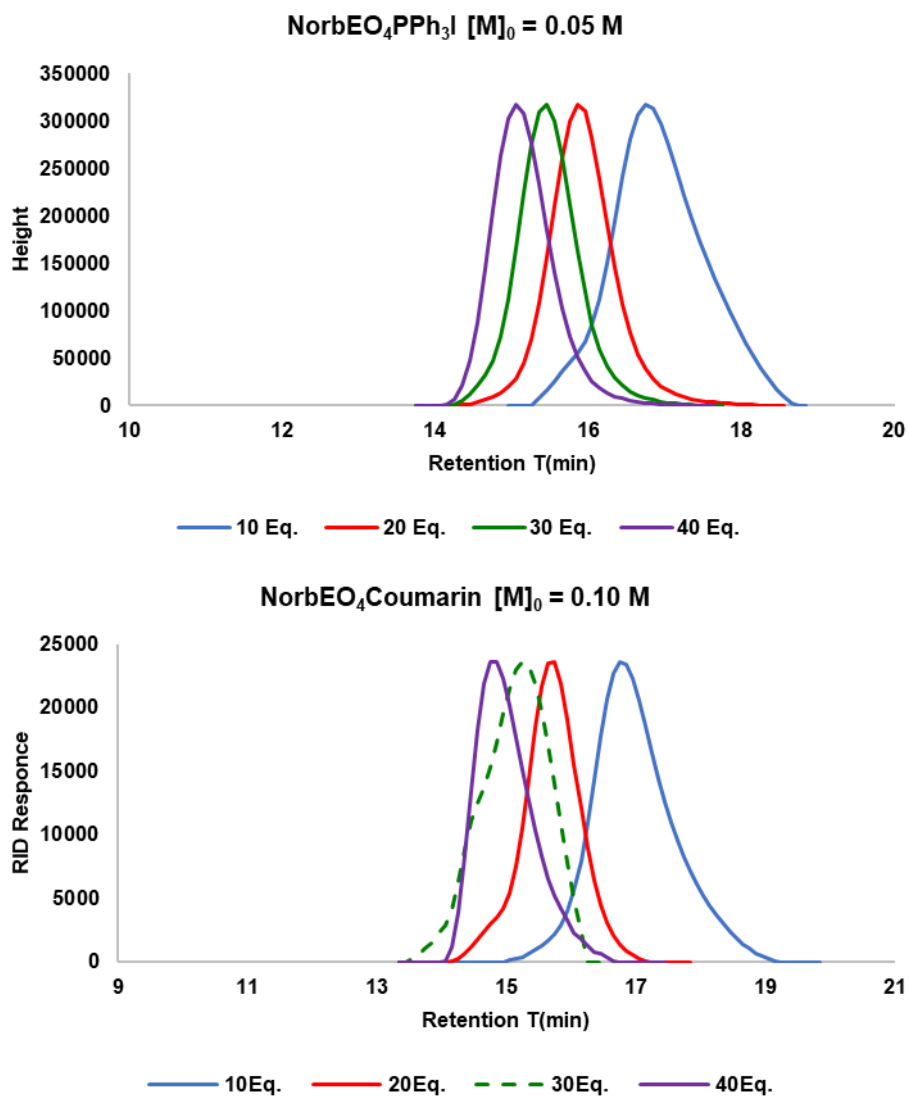




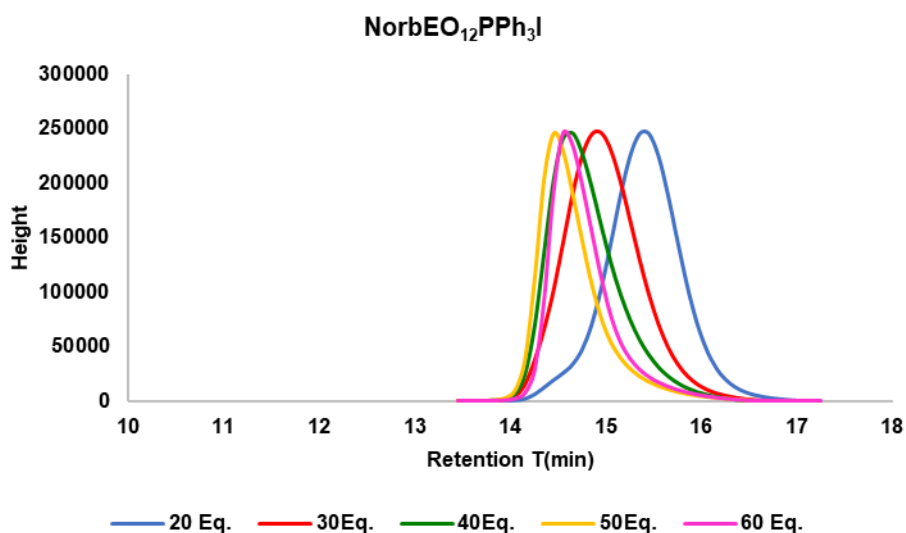
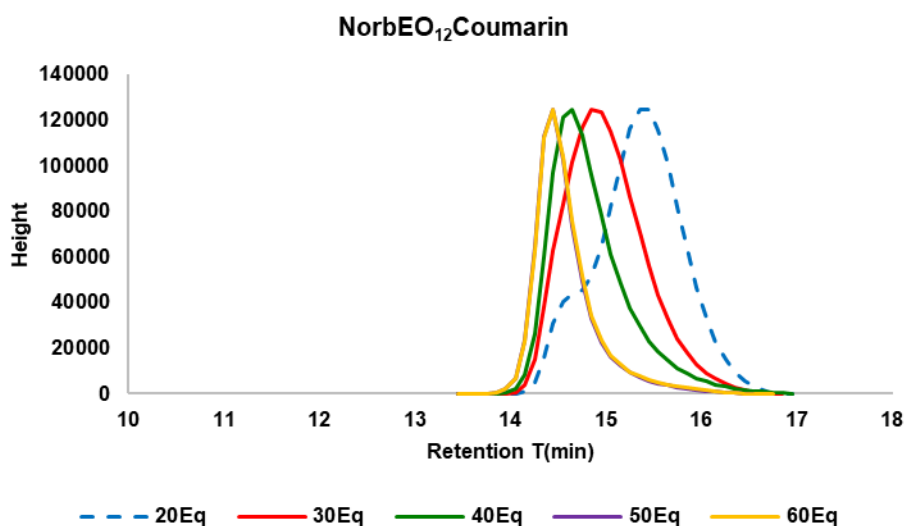


Grubbs III

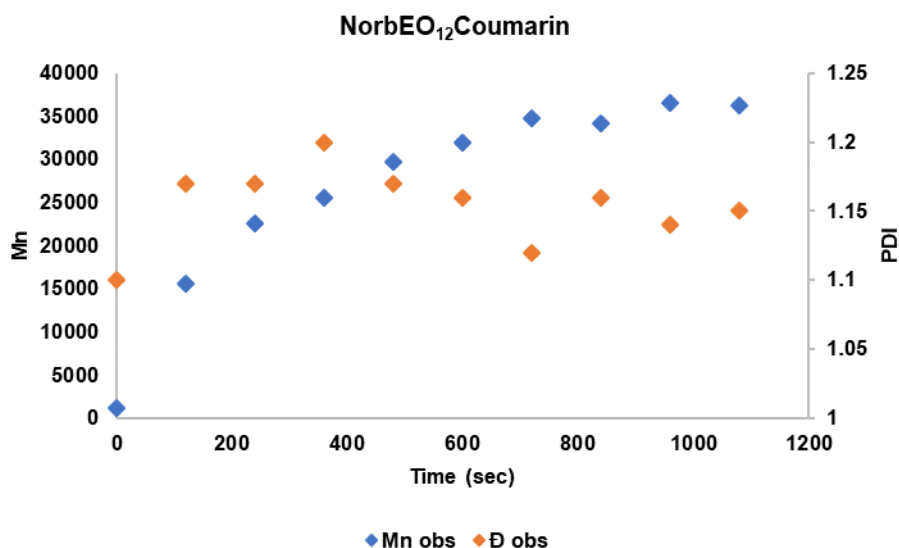
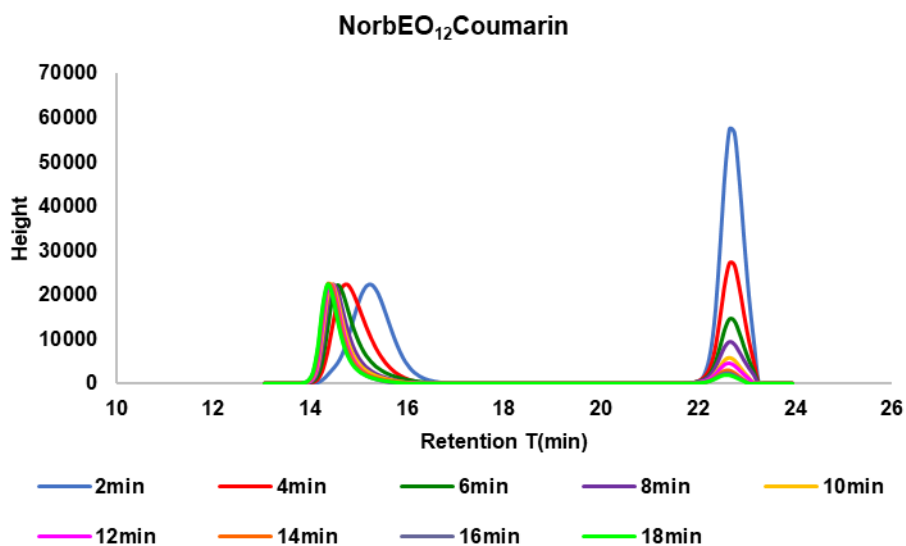




Appendix 1: GPC traces of samples of final product of homo-polymerization after quenching with EVE. The GPC traces were acquired at 30 °C using LiBr in DMF (0.2 M) as the eluting solvent with a flow-rate of 0.8 mL/min.



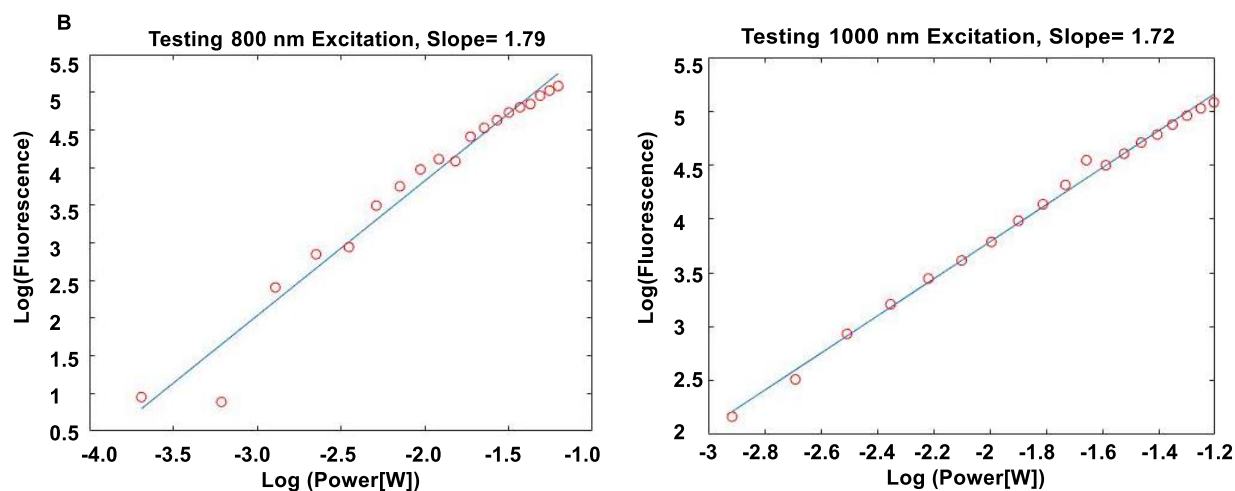
Appendix 2: GPC traces of samples of final product of homo-polymerization of second-generation homo-polymers after quenching with EVE. The GPC traces were acquired at 30 °C using LiBr in DMF (0.2 M) as the eluting solvent with a flow-rate of 0.8 mL/min.



Appendix 3: (Top) GPC traces of ¹H NMR samples of aliquots withdrawn from of the homopolymerization of **NorbEO₁₂Coumarin** reaction mixture at 2 min (120 sec) intervals. The GPC samples were prepared by quenching of the ¹H NMR sample with EVE, evaporation and redissolution in DMF. The traces were acquired at 30 °C using LiBr in DMF (0.2 M) as the eluting solvent with a flow-rate of 0.8 mL/min. (Bottom) Further analysis of the GPC traces reveal the anticipated increase in Mn over time as a result of insertion of monomer molecules into the growing polymer chain (blue diamond). The analysis also reveals the increase in Đ marked by broadening of the product peak of a factor of 1.01-1.06 overtime (orange diamond).

Monomer	Time (min)	Mn _{Obs.} kDa	D _{Obs.}	Broad. F.
<i>NorbEO₁₂Coumarin</i>	0	1.2	1.10	1.00
	2	16	1.17	1.06
	4	23	1.17	1
	6	26	1.2	1.03
	8	30	1.17	1.00
	10	32	1.16	1.00
	12	34	1.12	1.00
	14	35	1.16	1.04
	16	36	1.14	1.00
	18	36	1.15	1.01

Appendix 4: Mn and *D* values of the ¹H NMR kinetic study samples of homo-polymerization of **NorbEO₁₂Coumarin** obtained by GPC after quenching with EVE, evaporation and redissolution in DMF. Mn values of the propagating chain increased over time as a result of insertion of monomer molecules into the growing polymer chain so as the *D* values by a factor of 1.01-1.06 overtime.



Appendix 5: Line plots of the logarithmic value of laser power, of a Ti-shapphire laser, against logarithmic values of the corresponding fluorescence output, of block-co-polymer I 10 μ M solution in deionized water, showing a line plots of a slope of ≈ 1.79 (A) and 1.72 (B) obtained at excitation wavelengths of 800 and 1000 nm respectively. Together with figure 43 (B and C) show that block-co-polymer I obeys the two-photon quadratic rule and establishes $\lambda = 830$ nm as the optimal two-photon excitation wavelength for block-co-polymer I.

11 References

1. Elsabahy, M.; Wooley, K. L. *Chem. Soc. Rev.* **2012**, *41*, 2545-2561.
2. Roney, C.; Kulkarni, P.; Arora, V.; Antich, P.; Bonte, F.; Wu, A.; Mallikarjuana, N. N.; Manohar, S.; Liang, H. F.; Kulkarni, A. R.; Sung, H. W.; Sairam, M.; Aminabhavi, T. M. *J. Control Release* **2005**, *108*, 193-214.
3. Shen, Z.; Nieh, M.-P.; Li, Y. *Polymers*. **2016**, *8*, 83-101.
4. Zhu, B.; Eurell, T.; Gunawan, R.; Leckband, D. *J. Biomed. Mater. Res.* **2001**, *56*, 406-416.
5. Jeon, S. I.; Lee, J. H.; Andrade, J. D.; De Gennes, P. G. *J. Colloid. Interf. Sci.* **1991**, *142*, 149-158.
6. Říhová, B.; Kovář, M. *Adv. Drug. Deliver. Rev.* **2010**, *62*, 184-191.
7. Johnson, J. A.; Lu, Y. Y.; Burts, A. O.; Lim, Y.-H.; Finn, M. G.; Koberstein, J. T.; Turro, N. J.; Tirrell, D. A.; Grubbs, R. H. *J. Am. Chem. Soc.* **2011**, *133*, 559-566.
8. Abbott, N. J.; Rönnbäck, L.; Hansson, E. *Nat. Rev. Neurosci.* **2006**, *7*, 41-53.
9. Sahni, J. K.; Doggui, S.; Ali, J.; Baboota, S.; Dao, L.; Ramassamy, C. *J. Control. Release.* **2011**, *152*, 208-231.
10. Muirhead, K. E. A.; Borger, E.; Aitken, L.; Conway, S. J.; Gunn-Moore, F. J. *Biochem. J.* **2010**, *426*, 255-270.
11. Powell, A. J.; Read, J. A.; Banfield, M. J.; Gunn-Moore, F.; Yan, S. D.; Lustbader, J.; Stern, A. R.; Stern, D. M.; Brady, R. L. *J. Mol. Biol.* **2000**, *303*, 311-327.
12. Nsiah-Sefaa, A.; McKenzie, M. *Bioscience. Rep.* **2016**, *36*, 313-332.
13. Wang, Z.; Guo, W.; Kuang, X.; Hou, S.; Liu, H. *Asian. J. Pharm. Sci.* **2017**, *12*, 498-508.
14. Sakhrani, N. M.; Padh, H. *Drug. Des. Devel. Ther.* **2013**, *7*, 585-599.
15. Shargel, L.; Wu-Pong, S.; Yu, A. B. C. *Applied Biopharmaceutics & Pharmacokinetics*, 5th ed.; McGraw Hill Professional: New York, 2004; pp 96-116.
16. Yan, X.; Scherphof, G. L.; Kamps, J. A. *J. Liposome. Res.* **2005**, *15*, 109-139.
17. Owens, D. E.; Peppas, N. A. *Int. J. Pharm.* **2006**, *307*, 93-102.
18. Keller, F.; Hann, A. *Clin. J. Am. Soc. Nephrol.* **2018**, *13*, 1413-1420.
19. Beck, A.; Goetsch, L.; Dumontet, C.; Corvaia, N. *Nat. Rev. Drug. Discov.* **2017**, *16*, 315-337.
20. Smith, R. A. J.; Porteous, C. M.; Gane, A. M.; Murphy, M. P. *Proc. Natl. Acad. Sci. USA.* **2003**, *100*, 5407-5412.
21. Ruttala, H. B.; Ramasamy, T.; Poudal, B. K.; Choi, Y.; Choi, J. Y.; Kim, J.; Ku, S. K.; Choi, H.-G.; Yong, C. S.; Kim, J. O. *Oncotarget.* **2017**, *8*, 14925-14940.

22. Li, M.; Zhang, W.; Wang, B.; Gao, Y.; Song, Z.; Zheng, Q. C. *Int. J. Nanomed.* **2016**, *11*, 5645-5669.
23. Yoong, S. L.; Yoong, B. S.; Zhou, Q. L.; Chin, C. F.; Li, J.; Venkatesan, T.; Ho, H. K.; Yu, V.; Ang, W. H. *Biomaterials.* **2014**, *35*, 748-759.
24. Antonenko, Y. N.; Nechaeva, N. L.; Baksheeva, V. E.; Rokitskaya, T. I.; Plotnikov, E. Y.; Kotova, E. A.; Zorov, D. B. *Biochim. Biophys. Acta.* **2015**, *1848*, 1277-1284.
25. Tolan, D.; Gandin, V.; Morrison, L.; El-Nahas, A.; Marzano, C.; Montagner, D.; Erxleben, A. *Sci. Rep.* **2016**, *6*, 29367-29380.
26. Hong, R. L.; Huang, C. J.; Tseng, Y. L.; Pang, V. F.; Chen, S. T.; Liu, J. J.; Chang, F. H. *Clin. Cancer. Res.* **1999**, *5*, 3645-3652.
27. Johnson, J. A.; Lu, Y. Y.; Burts, A. O.; Xia, Y.; Durrell, A. C.; Tirrell, D. A.; Grubbs, R. H. *Macromolecules.* **2010**, *43*, 10326–10335.
28. Arima, H.; Motoyama, K. *Sensors-Basel.* **2009**, *9*, 6346-6361.
29. Hua, S. *Front. Pharmacol.* **2015**, *6*, 219-223.
30. Kumar, P. S.; Pastoriza-Santos, I.; Rodríguez-González, B.; Javier García de Abajo, F.; Liz-Marzán, L. M. *Nanotechnology.* **2008**, *19*, 015606-015612.
31. Akbarzadeh, A.; Samiei, M.; Davaran, S. *Nanoscale. Res. Lett.* **2012**, *7*, 144-157.
32. Aharoni, A.; Mokari, T.; Popov, I.; Banin, U. *J. Am. Chem. Soc.* **2006**, *128*, 257-264.
33. Sajanalal, P. R.; Sreeprasad, T. S.; Samal, A. K.; Pradeep, T. *Nano. Rev.* **2011**, *2*, 5883-5945.
34. Mahou, R.; Wandrey, C. *Polymers* **2012**, *4*, 561-589.
35. Davis, F. F. *Adv. Exp. Med. Biol.* **2003**, *519*, 51-58.
36. Garay, R. P.; Labaune, J. P. *Open. Conf. Proc. J.* **2011**, *2*, 104-107.
37. Abuchowski, A.; McCoy, J. R.; Palczuk, N. C.; van Es, T.; Davis, F. F. *J. Biol. Chem.* **1977**, *252*, 3582-3586.
38. Filpula, D.; Zhao, H. *Adv. Drug. Deliver. Rev.* **2008**, *60*, 29-49.
39. Sheth, S. R.; Leckband, D. *Proc. Natl. Acad. Sci. USA.* **1997**, *94*, 8399–8404.
40. Heuberger, M.; Drobek, T.; Spencer, N. D. *Biophys. J.* **2005**, *88*, 495–504.
41. Gurumoorthy, A. V. P.; Khan, K. H. *Rec. Res. Sci. Technol.* **2011**, *3*, 80-86.
42. Abuchowski, A.; van Es, T.; Palczuk, N. C.; Davis, F. F. *J. Biol. Chem.* **1977**, *252*, 3578-3581.
43. Ozin, G. A.; Arsenault, A. *Nanochemistry Basics.* In *Nanochemistry: A Chemical Approach to Nanomaterials*; Royal Society of Chemistry: Cambridge, UK, 2005; pp 1-44.
44. Jhaveri, A. M.; Torchilin, V. P. *Front. Pharmacol.* **2014**, *5*, 77-103.

45. Huang, G.; Khemtong, C.; Bey, E. A.; Boothman, D. A.; Sumer, B. D.; Gao, J. Theranostic Polymeric Micelles for Cancer Imaging and Therapy. In *Multifunctional Nanoparticles for Drug Delivery Applications*; Svenson, S., Prud'homme, R. K., Eds.; Springer: New York, 2012; pp 257-276.
46. Zhao, X.; Poon, Z.; Engler, A. C.; Bonner, D. K.; Hammond, P. T. *Biomacromolecules*. **2012**, *13*, 1315–1322.
47. Garg, S. M.; Vakili, M. R.; Lavasanifar, A. *Colloid. Surface. B*. **2015**, *132*, 161-170.
48. Lu, J.; Owen, S. C.; Shoichet, M. S. *Macromolecules*. **2011**, *44*, 6002–6008.
49. Hejl, A.; Scherman, O. A.; Grubbs, R. H. *Macromolecules*. **2005**, *38*, 7214–7218.
50. Feng, K.; Xie, N.; Chen, B.; Tung, C.-H.; Wu, L.-Z. *Biomacromolecules*. **2016**, *17*, 538–545.
51. Sowers, M. A.; McCombs, J. R.; Wang, Y.; Paletta, J. T.; Morton, S. W.; Dreaden, E. C.; Boska, M. D.; Ottaviani, M. F.; Hammond, P. T.; Rajca, A.; Johnson, J. A. *Nature. Commun.* **2014**, *5*, 5460-5469.
52. Rajca, A.; Kathirvelu, V.; Roy, S. K.; Pink, M.; Rajca, S.; Sarkar, S.; Eaton, S. S.; Eaton, G. R. *Chemistry*. **2010**, *16*, 5778-5782.
53. Suriboot, J.; Bazzi, H. B.; Bergbreiter, D. E. *Polymers*. **2016**, *8*, 140-163.
54. Suriboot, J.; Hu, Y.; Malinski, T. J.; Bazzi, H. S.; Bergbreiter, D. E. *ACS. Omega*. **2016**, *1*, 714–721.
55. Yin, L.; Ding, J.; He, C.; Cui, L.; Tang, C.; Yin, C. *Biomaterials*. **2009**, *30*, 5691-5700.
56. Pearson, H. A.; Peers, C. *J. Physiol.* **2006**, *575*, 5-10.
57. LaFerla, F. M.; Green, K. N.; Oddo, S. *Nat. Rev. Neurosci.* **2007**, *8*, 499-509.
58. Yan, S. D.; Fu, J.; Soto, C.; Chen, X.; Zhu, H.; Al-Mohanna, F.; Collison, K.; Zhu, A.; Stern, E.; Saido, T.; Tohyama, M.; Ogawa, S.; Roher, A.; Stern, D. *Nature*. **1997**, *389*, 689-695.
59. He, X.-Y.; Schulz, H.; Yang, S.-Y. *J. Biol. Chem.* **1998**, *273*, 10741–10746.
60. He, X.-Y.; Merz, G.; Mehta, P.; Schulz, H.; Yang, S.-Y. *J. Biol. Chem.* **1999**, *274*, 15014–15019.
61. He, X.-Y.; Merz, G.; Yang, Y.-Z.; Mehta, P.; Schulz, H.; Yang, S.-Y. *Eur. J. Biochem.* **2001**, *268*, 4899–4907.
62. Lustbader, J. W.; Cirilli, M.; Lin, C.; Xu, H. W.; Takuma, K.; Wang, N.; Caspersen, C.; Chen, X.; Pollak, S.; Chaney, M.; Trinchese, F.; Liu, S.; Gunn-Moore, F.; Lue, L.-F.; Walker, D. G.; Kuppusamy, P.; Zewier, Z. L.; Arancio, O.; Stern, D.; Yan, S. S.; Wu, H. *Science*. **2004**, *304*, 448-452.
63. Kunau, W. H.; Dommès, V.; Schulz, H. *Prog. Lipid. Res.* **1995**, *34*, 267-342.
64. Harmen, D. *J. Gerontol.* **1956**, *11*, 298-300.

65. Gladyshev, V. N. *Antioxid. Redox. Signal.* **2014**, *20*, 727–731.
66. Camello-Almaraz, C.; Gomez-Pinilla, P. J.; Pozo, M. J.; Camello, P. J. *Am. J. Physiol. Cell. Physiol.* **2006**, *291*, 1082-1088.
67. Chen, X.; Yan, S. D. *J. Alzheimers. Dis.* **2007**, *12*, 177–184.
68. Allen, B. G.; Spitz, D. R. Physiologic and Pathologic Functions. In *Mitochondria and Cell Death*; Hockenbery, D. M., Ed.; Humana Press: New York, 2016; pp 111-130.
69. Murphy, M. P. *Biochem. J.* **2009**, *417*, 1–13.
70. Fujii, J.; Iuchi, Y.; Okada, F. *Reprod. Biol. Endocrin.* **2005**, *3*, 43-53.
71. Kaake, R. M.; Wang, X.; Huang, L. *Mol. Cell. Proteomics.* **2010**, *9*, 1650–1665.
72. Spickett, C. M. *Redox. Biol.* **2013**, *1*, 145-152.
73. Kissinger, C. R.; Rejto, P. A.; Pelletier, L. A.; Thomson, J. A.; Showalter, R. E.; Abreo, M. A.; Agree, C. S.; Margosiak, S.; Meng, J. J.; Aust, R. M.; Vanderpool, D.; Li, B.; Tempczyk-Russell, A.; Villafranca, J. E. *J. Mol. Biol.* **2004**, *342*, 943-952.
74. Falkowska, A.; Gutowska, I.; Goschorska, M.; Nowacki, P.; Chlubek, D.; Baranowska-Bosiacka, I. *Int. J. Mol. Sci.* **2015**, *16*, 25959–25981.
75. Rule, J. D.; Moore, J. S. *Macromolecules.* **2002**, *35*, 7878-7882.
76. Stawikowski, M.; Fields, G. B. *Curr. Protoc. Protein. Sci.* **2002**, *Chapter 18*, Unit 18.1.
77. Beija, M.; Afonso, C. A. M.; Martinho, J. M. G. *Chem. Soc. Rev.* **2009**, *38*, 2410–2433.
78. Leriche, G.; Chisholm, L.; Wagner, A. *Bioorg. Med. Chem.* **2012**, *20*, 571-582.
79. Ballatori, N.; Krance, S. M.; Marchan, R.; Hammond, C. L. *Mol. Aspects. Med.* **2009**, *30*, 13-28.
80. Kim, K.; Park, H.; Lim, K. M. *Toxicol. Res.* **2015**, *31*, 97-104.
81. Ash, C.; Dubec, M.; Donne, K.; Bashford, T. *Lasers. Med. Sci.* **2017**, *32*, 1909-1918.
82. Wawro, A. M.; Muraoka, T.; Kinbara, K. *Polym. Chem.* **2016**, *7*, 2389-2394.
83. Vivek, A. V.; Dhamodharan, R. *J. Polym. Sci. A1.* **2007**, *45*, 3818-3832.
84. Riva, R.; Schmeits, S.; Jérôme, C.; Jérôme, R.; Lecomte, P. *Macromolecules* **2007**, *40*, 796-803.
85. Bielawski, C. W.; Grubbs, R. H. *Prog. Polym. Sci.* **2007**, *32*, 1–29.
86. Slugov, C. Synthesis of Homopolymers and Copolymers. In *Handbook of Metathesis*; Grubbs, R. H., Khosravi, E., Eds.; Wiley-VCH: Weinheim, Germany, 2015; Vol. 3, pp 1-24.
87. Matson, J. B.; Grubbs, R. H. *J. Am. Chem. Soc.* **2008**, *130*, 6731–6733.

88. Madkour, A. E.; Koch, A. H. R.; Lienkamp, K.; Tew, G. N. *Macromolecules* **2010**, *43*, 4557–4561.
89. Ren, L.; Zhang, J.; Bai, X.; Hardy, C. G.; Shimizu, K. D.; Tang, C. *Chem. Sci.* **2012**, *3*, 580–583.
90. Hollauf, M.; Zach, P. W.; Borisov, S. M.; Müller, B. J.; Beichel, D.; Tscherner, M.; Köstler, S.; Hartmann, P.; Knall, A.-C.; Trimmel, G. *J. Mater. Chem. C* **2017**, *5*, 7535–7545.
91. Lin, T.-P.; Chang, A. B.; Chen, H.-Y.; Liberman-Martin, A. L.; Bates, C. M.; Voegtle, M. J.; Bauer, C. A.; Grubbs, R. H. *J. Am. Chem. Soc.* **2017**, *139*, 3896–3903.
92. Shibuya, Y.; Nguyen, H. V.-T.; Johnson, J. A. *ACS. Macro. Lett.* **2017**, *6*, 963–968.
93. Liu, J.; Gao, A. X.; Johnson, J. A. *J. Vis. Exp.* **2013**, *80*, 50874-50881.
94. Louie, J.; Grubbs, R. H. *Organometallics*. **2002**, *21*, 2153-2164.
95. Love, J. A.; Morgan, J. P.; Trnka, T. M.; Grubbs, R. H. *Angew. Chem. Int. Ed.* **2002**, *41*, 4035–4037.
96. Holland, M. G.; Griffith, V. E.; France, M. B.; Desjardins, S. G. *J. Polym. Sci. Pol. Chem.* **2002**, *41*, 2125-2131.
97. Radzinski, S. C.; Foster, J. C.; Chapleski, J. . R. C.; Troya, D.; Matson, J. B. *J. Am. Chem. Soc.* **2016**, *138*, 6998–7004.
98. Alonso-Villanueva, J.; Rodríguez, M.; Vilas, J. L.; Laza, J. M.; León, L. M. *J. Macromol. Sci. A*. **2010**, *47*, 1130-1134.
99. Kumar, D. R.; Lidster, B. J.; Adams, R. W.; Turner, M. L. *Polym. Chem.* **2017**, *8*, 3186-3194.
100. Choi, T.-L.; Grubbs, R. H. *Angew. Chem. Int. Ed.* **2003**, *42*, 1743 – 1746.
101. Walsh, D. J.; Lau, S. H.; Hyatt, M. G.; Guironnet, D. *J. Am. Chem. Soc.* **2017**, *139*, 13644–13647.
102. Bielawski, C. W.; Grubbs, R. H. *Angew. Chem. Int. Ed.* **2000**, *39*, 2903-2906.
103. Conrad, J. C.; Camm, K. D.; Fogg, D. E. *Inorg. Chim. Acta.* **2006**, *359*, 1967–1973.
104. Elias, H. G. Polymerization Equilibria. In *Macromolecules*; Springer, Boston, MA: New York, 1984; pp 557-581.
105. Sawada, H. *J. Macromol. Sci. C*. **1969**, *3*, 313-338.
106. Sawada, H. *J. Macromol. Sci. C*. **1972**, *8*, 235-288.
107. Schleyer, P. R.; Williams, J. E.; Blanchard, K. R. *J. Am. Chem. Soc.* **1970**, *92*, 2377–2386.
108. Kurzhals, S.; Binder, W. H. Combination of Olefin Metathesis Polymerization with Click. In *Handbook of Metathesis*; Grubbs, R. H., Khosravi, E., Eds.; Wiley-VCH: Weinheim, Germany, 2015; Vol. 3, pp 207-227.

109. Fischmeister, C.; Bruneau, C. *Beilstein. J. Org. Chem.* **2011**, *7*, 156–166.
110. Matson, J. B.; Grubbs, R. H. *Macromolecules.* **2010**, *43*, 213–221.
111. Meldal, M.; Tornøe, C. W. *Chem. Rev.* **2008**, *108*, 2952–3015.
112. Flewelling, R. F.; Hubbell, W. L. *Biophys. J.* **1986**, *49*, 531-540.
113. Neumcke, B.; Lauger, P. *Biophys. J.* **1969**, *9*, 1160-1170.
114. Neumcke, B.; Walz, D.; Lauger, P. *Biophys. J.* **1970**, *10*, 172-182.
115. Asin-Cayuela, J.; Manas, A.-R. B.; James, A. M.; Smith, R. A. J.; Murphy, M. P. *FEBS. Lett.* **2004**, *571*, 9-16.
116. Le Trionnaire, S.; Perry, A.; Szczesny, B.; Szabo, C.; Winyard, P. G.; Whatmore, J. L.; Wood, M. E.; Whiteman, M. *Med. Chem. Commun.* **2014**, *5*, 728-736.
117. Trendeleva, T. A.; Rogov, A. G.; Cherepanov, D. A.; Sukhanova, E. I.; Il'yasova, T. M.; Severina, I. I.; Zvyagilskaya, R. A. *Biochemistry-Moscow.* **2012**, *77*, 1021-1028.
118. Trnka, J.; Elkalaf, M.; Anděl, M. *PLoS. One.* **2015**, *10*, 121837-121851.
119. Leo, S.; Szabadkai, G.; Rizzuto, R. *Ann. N. Y. Acad. Sci.* **2008**, *1147*, 264-274.
120. Peroni, E.; Caminati, G.; Baglioni, P.; Nuti, F.; Chelli, M.; Papini, A. M. *Bioorgan. Med. Chem. Lett.* **2002**, *12*, 1731-1734.
121. Jung, H. S.; Kwon, P. S.; Lee, J. W.; Kim, J. I.; Hong, C. S.; Kim, J. W.; Yan, S.; Lee, J. Y.; Lee, J. H.; Joo, T.; Kim, J. S. *J. Am. Chem. Soc.* **2009**, *131*, 2008–2012.
122. Fischer, A.; Cremer, C.; Stelzer, E. H. K. *Appl. Optics.* **1995**, *34*, 1989-2003.
123. Gao, H.; Yang, Z.; Cao, S.; Xi, Z.; Zhang, S.; Pang, Z.; Jiang, X. *Nanotechnology* **2012**, *23*, 435101-435110.
124. Diaspro, A.; Sheppard, C. J. R. Two-Photon Excitation Fluorescence Microscopy. In *Confocal and Two-Photon Microscopy: Foundations, Applications and Advances* ; Diaspro, A., Ed.; Wiley-Liss. Inc: New York, 2002; pp 39-73.
125. Soeller, C.; Cannell, M. B. *Microsc. Res. Techniq.* **1999**, *47*, 182-195.
126. Sheppard, C.; Gu, M. *Optik.* **1990**, *86*, 104-106.
127. Born, M.; Wolf, E. Elements of The Theory of Diffraction. In *Principles of Optics: electromagnetic theory of propagation, interference and diffraction of light*, Seventh Edition ed.; Cambridge University Press: New York, 1999; pp 412-516.
128. Wolleschensky, R.; Dickinson, M. E.; Fraser, S. E. Group-Velocity Dispersion and Fiber Delivery in Multiphoton Laser Scanning Microscopy. In *Confocal and Two-Photon Microscopy: Foundations, Applications and Advances*; Diaspro, A., Ed.; Wiley-Liss, Inc.: New York, 2002; pp 171-190.

129. Girkin, J. M.; Wokosin, D. L. Practical Multiphoton Microscopy. In *Confocal and Two-Photon Microscopy: Foundations, Applications and Advances*; Diaspro, A., Ed.; Wiley-Liss, Inc.: New York, 2002; pp 207-235.
130. König, K.; Tirlapur, U. K. Cellular and Subcellular Perturbations During Multiphoton Microscopy. In *Confocal and Two-Photon Microscopy: Foundations, Applications and Advances*; Diaspro, A., Ed.; Wiley-Liss, Inc.: New York, 2002; pp 191-205.
131. Liao, Y.-C.; Venkatesan, P.; Wei, L.-F.; Wu, S.-P. *Sensor. Actuat. B-Chem.* **2016**, *232*, 732-737.
132. Song, A.; Wang, X.; Lam, K. S. *Tetrahedron. Lett.* **2003**, *44*, 1755–1758.
133. He, X.; Shang, Y.; Zhou, Y.; Yu, Z.; Han, G.; Jin, W.; Chen, J. *Tetrahedron.* **2015**, *71*, 863-868.
134. Lafaye, K.; Bosset, C.; Nicolas, L.; Guérinot, A.; Cossy, J. *Beilstein. J. Org. Chem.* **2015**, *11*, 2223–2241.
135. Schwabacher, A. W.; Lane, J. W.; Schiesher, M. W.; Leigh, K. M.; Johnson, C. W. *J. Org. Chem.* **1998**, *63*, 1727–1729.
136. Okoth, R.; Basu, A. *Beilstein J. Org. Chem.* **2013**, *9*, 608–612.
137. Schweizer, E. E.; Goff, S. D.; Murray, W. P. *J. Org. Chem.* **1977**, *42*, 200–205.
138. Bouzide, A.; Sauvé, G. *Org. Lett.* **2002**, *4*, 2329–2332.
139. Clayden, J.; Greeves, N.; Warren, S. Nucleophilic Substitution at Saturated Carbon. In *Organic Chemistry*, Second Edition ed.; Oxford University Press: Oxford, 2012; pp 328-359.
140. Castañeda, F.; Aliaga, C.; Acuña, C.; Silva, P.; Bunton, C. A. *Phosphorus, Sulfur, and Silicon.* **2008**, *183*, 1188–1208.
141. Larson, E. M.; Doughman, D. J.; Gregerson, D. S.; Obritsch, W. F. *Invest. Ophthalmol. Vis. Sci.* **1997**, *38*, 1929-1933.
142. Aguilar, M. R.; Gallardo, A.; Fernández, M. M.; Román, J. S. *Macromolecules.* **2002**, *35*, 2036–2041.
143. Gouranlou, F. *Asian. J. Chem.* **2007**, *19*, 1757-1760.
144. Mosmann, T. *J. Immunol. Methods.* **1983**, *65*, 55-63.
145. Conchello, J.-A.; Lichtman, J. W. *Nat. Methods.* **2005**, *2*, 920–931.
146. Gustafsson, O. J.; Arentz, G.; Hoffmann, P. *Biochim. Biophys. Acta.* **2015**, *559-580*, 1854.
147. Wyatt, P. J. *Anal. Chim. Acta.* **1993**, *272*, 1-40.
148. Lowry, G. V.; Hill, R. J.; Harper, S.; Rawle, A. F.; Hendren, C. O.; Klaessig, F.; Nobbmann, U.; Sayreh, P.; Rumble, J. *Environ. Sci.: Nano* **2016**, *3*, 953-965.

149. European Medicines Agency. https://www.ema.europa.eu/documents/scientific-guideline/international-conference-harmonisation-technical-requirements-registration-pharmaceuticals-human-use_en-21.pdf (accessed Jan 14, 2019).
150. Singh, A. K. Experimental Methodologies for the Characterization of Nanoparticles. In *Engineered Nanoparticles: Structure, Properties and Mechanisms of Toxicity*; Academic Press, 2016; pp 125-170.
151. Zorova, L. D.; Popkov, V. A.; Plotnikov, E. Y.; Silachev, D. N.; Pevzner, I. B.; Jankauskas, S. S.; Babenko, V. A.; Zorov, S. D.; Balakireva, A. V.; Juhaszova, M.; Sollott, S. J.; Zorov, D. B. *Anal. Biochem.* **2018**, *552*, 50-59.
152. Heiskanen, K. M.; Bhat, M. B.; Wang, H. W.; Ma, J.; Nieminen, A. L. *J. Biol. Chem.* **1999**, *274*, 5654-5658.
153. Chen, Y. S.; Kuo, P. Y.; Shie, T. L.; Yang, D. Y. *Tetrahedron.* **2006**, *62*, 9410-9416.
154. Muirhead, K. E.; Froemming, M.; Li, X.; Musilek, K.; Conway, S. J.; Sames, D.; Gunn-Moore, F. J. *ACS. Chem. Biol.* **2010**, *5*, 1105-1114.
155. Helms, H. C.; Abbott, N. J.; Burek, M.; Cecchelli, R.; Couraud, P. O.; Deli, M. A.; Förster, C.; Galla, H. J.; Romero, I. A.; Shusta, E. V.; Stebbins, M. J.; Vandenhaute, E.; Weksler, B.; Brodin, B. *J. Cereb. Blood. Flow. Metab.* **2016**, *36*, 862-890.
156. Aryal, M.; Arvanitis, C. D.; Alexander, P. M.; McDannold, N. *Adv. Drug. Deliver. Rev.* **2014**, *72*, 94-109.
157. Sheikov, N.; McDannold, N.; Sharma, S.; Hynynen, K. *Ultrasound. Med. Biol.* **2008**, *34*, 1093-1104.
158. Liu, J.; Burts, A. O.; Li, Y.; Zhukhovitskiy, A. V.; Ottaviani, M. F.; Turro, N. J.; Johnson, J. A. *J. Am. Chem. Soc.* **2012**, *134*, 16337-16344.
159. Yuan, H.; He, R.; Wan, B.; Wang, Y.; Pauli, G. F.; Franzblau, S. G.; Kozikowski, A. P. *Bioorg. Med. Chem. Lett.* **2008**, *18*, 5311-5315.
160. Sanford, M. S.; Love, J. A.; Grubbs, R. H. *Organometallics.* **2001**, *20*, 5314-5318.
161. Perkins, J. College of Imaging Arts & Sciences. <https://cias.rit.edu/faculty-staff/101/faculty/340> (accessed June 12, 2015).
162. Saraiva, C.; Praça, C.; Ferreira, R.; Santos, T.; Ferreira, L.; Bernardino, L. *J. Control. Release.* **2016**, *235*, 34-47.
163. Verhoef, J. J. F.; Anchordoquy, T. J. *Drug. Deliv. Transl. Res.* **2013**, *3*, 499-503.
164. Zhang, P.; Sun, F.; Liu, S.; Jiang, S. *J. Control. Release.* **2016**, *244*, 184-193.
165. Two-Photon fluorescence microscopy. <http://microscopy.berkeley.edu/courses/tlm/2P/index.html> (accessed August 21, 2018).
166. Ireland, B. J.; Dobigny, B. T.; Fogg, D. E. *ACS. Catal.* **2015**, *5*, 4690-4698.

167. Lummiss, J. A. M.; Ireland, B. J.; Sommers, J. M.; Fogg, D. E. *Chemcatchem*. **2014**, *6*, 459-463.
168. Chatterjee, A.; Seth, D. *Photochem. Photobiol.* **2013**, *89*, 280-293.
169. Chatterjee, A.; Maity, B.; Seth, D. *RSC. Adv.* **2014**, *4*, 34026–34036.
170. Nowak, P. M.; Woźniakiewicz, M.; Piwowarska, M.; Kościelniak, P. *J. Chromatogr. A*. **2016**, *1446*, 149-157.
171. Gross, K. C.; Seybold, P. G. *Int. J. Quantum. Chem.* **2000**, *80*, 1107–1115.
172. Sutthasupa, S.; Shiotsuki, M.; Masuda, T.; Sanda, F. *J. Am. Chem. Soc.* **2009**, *131*, 10546–10551.
173. Fluorescence SpectraViewer. <https://www.thermofisher.com/uk/en/home/life-science/cell-analysis/labeling-chemistry/fluorescence-spectraviewer.html> (accessed September 17, 2018).
174. What a Drug Does to the Body and What the Body Does to a Drug. <https://www.aegislabs.com/pharmacogenetics1> (accessed September 22, 2018).
175. Xie, Y.; Deng, S.; Chen, Z.; Yan, S.; Landry, D. W. *Bioorg. Med. Chem. Lett.* **2006**, *16*, 4657-4660.